Doctoral Dissertation
Doctoral Program in Civil and Environmental Engineering (37th Cycle)

Non-linear analysis and dynamic monitoring methods for the safety assessment of bridges and viaducts

Mario Ferrara
* * * * * *

Supervisors
Prof. Luca Giordano,Supervisor
Prof. Gabriele Bertagnoli, Co-Supervisor

Politecnico di Torino
May 15, 2025

I hereby declare that the contents and organisation of this dissertation constitute my own original work and does not compromise in any way the rights of third parties, including those relating to the security of personal data.

…….....

Mario Ferrara

Turin, May 15, 2025

Summary

Infrastructure assets, such as bridges and tunnels, are crucial for a Country's economic and social development. In Western countries, much of this infrastructure was developed post-World War II and has now reached or exceeded its design life. Due to degradation and design or construction deficiencies usual at the time of construction, the safety and functionality of these assets are now at risk.

Currently, the primary needs regarding these infrastructures involve assessing their safety and interpreting their structural behaviour using Structural Health Monitoring (SHM) systems. For safety assessments, increasingly sophisticated numerical models are required. For interpreting structural behaviour, either purely data-driven or model-driven methodologies can be employed, often involving the creation of digital twin models. These models are particularly essential for complex structures.

This thesis fits into the previously discussed context by investigating, through real case studies, the potential of non-standard approaches for the safety assessment and interpretation of the structural behaviour of existing bridges and viaducts.

It first focuses on the safety assessment of existing bridge decks, specifically three girder decks made of prestressed reinforced concrete, which are a common typology in existing infrastructures.

The assessment is conducted using different methods: Courbon theory, linear elastic finite element (FE) analysis, and nonlinear FE analysis (NLFEA) according to three global safety formats.

The decks are initially modelled using Courbon's theory and then with a linear elastic FE model composed of beam elements only.

In both cases, safety is evaluated by comparing design resistant and acting moments in the sections of interest, using partial safety factors for local approaches.

Subsequently, nonlinear 3D FE models are applied, implementing global safety formats that yield varying safety margins compared to local methods.

The first two local approaches employed in safety assessments are notably conservative, leading to a reduced safety margin. In contrast, global approaches—relying on global safety formats—tend to yield higher safety margins. However, the extent of this improvement depends significantly on the specific global safety format adopted.

Moreover, the safety level is evaluated in relation to structural damage through global nonlinear 3D numerical analyses, considering various damage scenarios. These numerical studies assess the structural performance of the deck under ultimate limit state conditions for each scenario, establishing a correlation between safety loss and the extent of damage. Based on this, a threshold-based approach is proposed, in which specific static parameters are used to monitor the progression of damage within the structure.

Several key considerations emerge from this first aspect—namely, the safety assessment of existing bridge decks. Chief among them is that increasing the complexity of analysis and modelling generally leads to improved safety margins. Certain modelling aspects, such as the accurate representation of boundary conditions and constraint stiffness, are critical to the final safety assessment. Finally, while structural damage does reduce load-bearing capacity, the resulting loss in strength typically exceeds the corresponding reduction in stiffness. This discrepancy suggests that static parameters are not well-suited for reliable damage detection.

The second focus of the thesis is the interpretation of the structural behaviour of existing bridges and viaducts through the analysis of Structural Health Monitoring (SHM) data, with a specific emphasis on dynamic behaviour.

The dynamic behaviour of the structures under investigation is determined using Operational Modal Analysis (OMA) methods. Over the past decade, rapid technological advancements and the reduction in sensor costs have enabled the monitoring of increasingly complex structures. In this context, the development of finite element models (FEM) has become essential for interpreting monitoring data and understanding structural behaviour. These models also play a crucial role in verifying the safety of the monitored structures.

In the second part of the thesis, three viaducts—each representing a different structural typology—are examined. A digital twin is developed for each structure, and model updating is carried out using a range of approaches, from fully manual calibration to optimization techniques based on genetic algorithms. This process

highlights both common and structure-specific modelling challenges, which must be carefully addressed to ensure that the numerical models reliably represent the actual behaviour of the structures.

Several key considerations emerge from this second aspect—namely, the interpretation of structural behaviour through the analysis of Structural Health Monitoring (SHM) data and the subsequent model updating of digital twins. The most critical point is that structural models used for interpreting SHM data differ significantly from those developed for design purposes, owing to their distinct objectives. Key divergences between design models and simulation models include the characterization of bearing friction and deformability, the global deformability of the soil-structure system, the estimation of permanent loads, and the specification of material properties. Among these, certain factors—such as bearing behaviour or global system deformability—tend to play a dominant role across multiple structural types, while others are more relevant to specific configurations.

Acknowledgment

Arrivato a questo punto, sento la necessità di ringraziare le persone più importanti che mi hanno sostenuto ed aiutato, ognuna a modo suo, durante questo percorso.

Il ringraziamento più grande va a Gabriele e Luca. Li ringrazio per aver creduto in me fin dal primo giorno. Li ringrazio per avermi trasmesso la loro conoscenza e la passione per questa disciplina, prima come docenti, poi come supervisors. Li ringrazio per avermi fatto diventare un ingegnere consapevole e un ingegnere migliore.

Ringrazio i miei genitori. Che seppur a chilometri di distanza non mi hanno mai fatto mancare il loro supporto e sanno sempre farmi sentire la loro vicinanza.

Ringrazio Daniele e Chiara, compagni fedeli di mille avventure in montagna. Grazie a voi e alla montagna le fatiche del dottorato sono state parecchio alleviate.

Ringrazio Melissa, Giacomino e la casa di via Olmo 83, un rifugio sicuro all'inizio della scrittura di questa tesi, quando mi sentivo bloccato. Il ringraziamento più grande va a Melissa, che ha accolto il mio bagaglio di tenebre e che ha portato un raggio di luce nella mia vita.

Per ultimo, ma non meno importanti, ringrazio Marco e Silvia, che da dieci lunghi anni mi supportano e credono in me.

I would like to dedicate
this thesis to my parents

Contents

List of Tables

List of Figures

Chapter 1

Introduction

1.1. Research context

Civil infrastructures are still an extremely important asset for the economic development of modern Countries. In Western Countries, most of the infrastructure assets were built after World War II. Especially, in Italy, 24% of bridges in service were built before 1961 and 28% of bridges in service were built between 1961 and 1982 [1]. These structures are close to reaching their service life and, in many cases, they exceeded it. They may present risks with respect to structural safety or anomalies in their structural behaviour due to aging, exposure to aggressive environments, poor maintenance and defects in design and/or construction.

In recent decades, several bridge collapses have occurred in Italy, the most relevant are reported in chronological order according to [2].

The Petrulla viaduct [2][3] in Sicily, that consists in a series of 12 simply supported girder deck, each of them with a 40 m span. On July 7, 2014, one span collapsed Figure 1-1. The breakage occurred in mid-span section of the deck. The deck, 11.30 m wide, was made of four precast and prestressed concrete longitudinal beams equally spaced by 2.85 m and five transverse beams. The investigation, conducted after the collapse, evidenced an exceeding state of material decay for the reinforcement components: diffused oxidation in the prestressing cables, severe corrosions of the metallic sheathing and large absence of the protective grout inside the cables. The investigations have evidenced several construction deficiencies, in particular related to finishing operations of the prestressing system. Under these circumstances, humidity found a preferential way into the cables, and its continuous content variation generated an aggressive environment for steel oxidation. Other additional deficiencies for this particular degradation scenario were addressed to: not sufficient cover due to malposition of the prestressing cables; not adequate workability and fluidity of the concrete; inadequate waterproofing covering of the joints.

Figure 1-1: Collapse of a span of the Petrulla viaduct [3].

The collapse of the Annone [2][4] overpass, Lecco, occurred on October 18, 2016 Figure 1-2. The bridge was built between the 1960 and 1962, with a Gerber scheme. The central deck, 24.60 m long and 4.40 m wide, was constituted by five precast and prestressed longitudinal beams. Gerber supports were 0.575 m high, with ordinary reinforcement. Before the collapse, the bridge was subjected to several impacts by underlying moving vehicles [4]. After these events, the gerber saddle was repaired with rebars and CFRP system. However, those interventions could not renovate the shear fracture propagated over the gerber saddle and significant presence of humidity was often detected when inspected. This was mainly due to the produced misalignment in the dapped-end due to the retrofitting, which constituted a stagnation point for running water. The collapse occurred when a 107.6 t heavy 8-axels truck went across the deck with a low moving speed. Once the load was carried entirely by the central beam, the external repaired dapped end corbel collapsed due to the vertical reaction established for supporting the beam. Investigation [4] have demonstrated that this failure was compromised by: an initial design flaws in the dapped-end corbel that significantly reduced the ultimate load; the presence of a shear fracture along the dapped end corbel promoted the oxidation of the reinforcement bars in the joint; the eccentricity produced by a transit misaligned by the carriageway central line significantly increased the loading in the external dapped end joint.

Figure 1-2: Collapse of the Annone overpass.

the collapse of the Fossano [2] overpass on April 18, 2017 Figure 1-3. The structure was a simply supported beam, 30.80 m long and 8.90 m wide, constituted by a multiple-box post-tensioned beam and by an in-situ casted slab. In the longitudinal direction, the bridge was built in 3 segment, the central one 11.50 m long and the lateral ones 9.35 m long. The connection between the segments was realized by an in-situ casted concrete joint 0.5 m wide. Post tensioning system constituted in 8 parabolic cables, each of them made by 19 0.8'' strands. Visual inspections consented to affirm that the collapse mechanism was triggered by a shear failure in one of the joints due to the absence of the equilibrating action of the prestressing. This means that in some part between the support and the intact joint, the cables were damaged. Visual inspections immediately also demonstrated that the cables did not have sufficient grout protection in the collapsed joint area. The vulnerabilities of this structure can be summarized as follows: absence of ductility and structural robustness, there is no redundancy in the prestressing device; inadequate grout injection inside the cables, which led the water to a preferential way inside the sheathing; total non-accessibility for structural inspections.

Figure 1-3: Collapse of the Fossano overpass.

On August 14, 2018, the Tower 9 of the Polcevera bridge, collapsed on the underlying industrial hub, Polcevera river and rail track of the city of Genoa Figure 1-4. Starting from the design (1960), the structural system that realized the tower relied on the balanced compressive force along the lateral columns coming from the stays. The assembled framed tower, plus a four-point supported deck, exhibits a complete absence of robustness and structural redundancy, which means that in case of failure of one of the components, there was no control in preventing a catastrophic collapse. The structures were designed by using the simplest possible schemes, in order to have easier calculation to be made. Consequently, no ductility expedient, at any scale, was adopted to exclude fragile collapse [5][6]. Polcevera bridge has been continuously investigated and consolidated over the years. Along the 70s, the designer himself, started with regular visual inspections, while over the '80s a distributed restoration of the concrete components was carried out starting from the towers and then moving through the deck. In 1993, a detailed inspection through the insertion of an endoscopy inside the stays of the Tower 11, evidenced a severe oxidation of the metallic protective membrane and of the strands themselves. Additionally, significant presence of humidity and absence of grout

were reported. Moreover, some of the strands appeared slacked or sheared, sign of a tensile rupture due to steel cross-section reduction. All the described conditions led the structure to a quickened state of material decay and the entire sets of stays of the Tower 11 were replaced with an external prestressing system. After this massive intervention many other maintenance and monitoring activities have been performed over the viaduct. Most of the monitoring regarded the health condition of the strands of the remaining towers [7], while the repairing affected the carriageway slabs. When Tower 9 collapsed, a replacement intervention of its strands was planned for the following two months, and ongoing maintenance was present on the deck.

Figure 1-4: Collapse of the Polcevera bridge.

On April 2020, the 260 m reinforced concrete arch bridge of Caprigliola suddenly collapsed into the Magra river [8] Figure 1-5. The arch bridge of Caprigliola spanned above the Magra river and was erected in the early 1900s. It consisted of five variable-thickness slender reinforced concrete spans resting on four 51 m-spaced piers; the deck was supported by columns resting on the arches. The bridge of Caprigliola was one of the first RC bridges ever built in Italy, and detained the record of longest bridge in the world for almost a decade, with its 260 m. It was re-built after the World War II on the existing masonry piers and abutments. The global structural conditions of the bridge had been assessed through an in-situ inspection only a few months before the collapse, after a crack was noticed on the surface asphalt following heavy rain. However, the latter was considered not to be a danger to the structure, which was thus cleared for further use. Although several different hypotheses on potential triggering factors that might have induced the observed collapse have been formulated, attributed to e.g. material deterioration, foundation settlements, overloading. To date, the real causes are still unknown.

Figure 1-5: Collapse of the Caprigliola bridge.

In 2020 and 2022, the Italian Ministry of Infrastructures published two documents called *Guidelines For Risk Classification and Management, Safety Assessment and Monitoring of Existing Bridges* [9], [10]. In these documents, the focus was placed on existing bridges and how to verify them with respect to safety and the proper strategies for maintenance and monitoring.

To date, the biggest challenges for designers and researchers concern the structural health monitoring and the assessment of the safety of these structures.

Structural Health Monitoring (SHM) is a discipline that has become increasingly important within civil engineering in recent decades. The main purpose of structural monitoring systems is to assess the performance of a structure over time and check for possible deterioration phenomena in progress that lead to a decay in structural performance. To date, different SHM methodologies exist: dynamic monitoring, static monitoring, data-driven monitoring methods, and model-driven monitoring methods. Choosing the most appropriate type of monitoring for a structure is not an obvious choice, as the monitoring needs for each structure may be different and each structure has complexities to take into account. For these reasons, to date, it is challenging to define a univocal monitoring approach.

The safety assessment of complex structures, like viaducts, based on traditional approaches often leads to results that are too conservative and therefore to the adoption of retrofitting actions that result in unnecessary economic effort. For this reason, an increasingly sophisticated numerical modelling and numerical analysis approach to the safety assessment is required. To date, the application of safety format to the results of Non-Linear Numerical Analysis (NLNAs) is undoubtedly one of the most refined approaches that can be employed.

This thesis focuses on the two key issues mentioned. The dynamic behaviour of different types of bridges will be analysed and the influence of key parameters in model updating of the digital twin of these structures for model-driven monitoring techniques will be examined. Moreover different methodologies for safety assessment of existing structures will be analysed and compared.

1.2. Safety assessment of existing structures

The structural safety assessment can be performed with simpler or more refined methodologies. In this context, *fib Model Code 2010* [11] and *Muttoni and Ruiz* [12] suggests an approach based on level of approximation (LoA). Low LoA are based on well-established theoretical foundations, requiring limited computational effort, and are in favour of safety. Higher LoA require increasing computational effort, deeper user experience, and are less pro-safety than low LoA. High LoA is beneficial in cases in which a more accurate estimate of structural response can lead to significant economic savings, especially for existing structures.

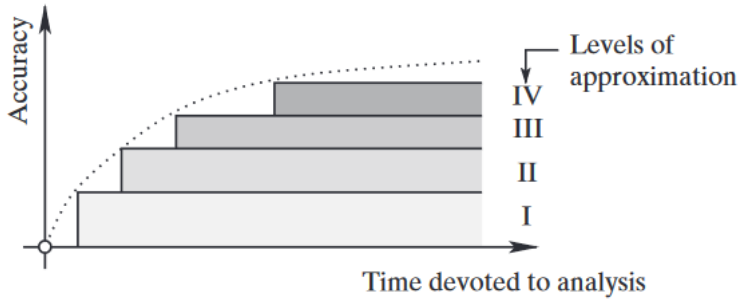

Figure 1-6: Level of approximation approach according to [11] and [12].

Target reliability for new and existing structures

The most common measure of the structural reliability is represented by the probability of failure P_f. An alternative measure of the structural reliability is represented by the reliability index β, which formally can be defined as the negative value of the inverse of the standard normal variable corresponding to the probability of failure P_f as shown in Figure 1-7. The bigger is the reliability index β, the more reliable is the structure (i.e. lower P_f).

Another fundamental concept is that of limit state function. The limit state for a structure (i.e. Ultimate Limit State ULS or Serviceability Limit State SLS) can be outlined by the limit state function Z which, in general, is defined in the following form as a function of main random variables X_i:

$$Z = g(X_i) = 0 \tag{1.1}$$

The limit state function Z is defined, so that:

$$\begin{cases} Z \geq 0 \rightarrow safe\ region \\ Z < 0 \rightarrow failure\ region \end{cases} \tag{1.2}$$

Then, the limit state function Z is defined in such a way that for a favourable configuration (i.e. safe region) of the structure the function is positive $Z \geq 0$, and for an unfavourable configuration (i.e. failure region) the function is negative $Z < 0$. Based to this definition, the probability of failure Pf can be calculated as:

$$P_f = P[Z < 0] \tag{1.3}$$

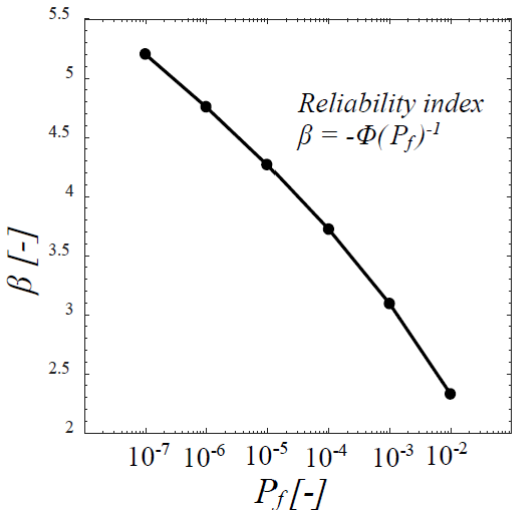

Figure 1-7: Relationship between the probability of failure P_f and reliability index β.

Structural reliability quantification can be performed by sophisticated estimation of the probability of failure of the structure P_f or by simplified approaches.

In general, the reliability method can be categorized in four levels from the most refined to the simplest:

- ***Level III methods (probabilistic)***. Implies the exact calculation of the probability of failure P_f or reliability index β.
- ***Level II methods (probabilistic)***. Perform reliability analysis using only the moments of basic variables. The first and the second order moments are adopted in most of the cases. The limit state function is linearized around predefined points, commonly represented by the mean value (*Cornell 1967* [13]) of the joint probabilistic distribution of basic variables and by the design point (*Hasofer and Lindt 1974* [14]). Due to these two approximations, the two above methods are called "*First Order Second Moment – FOSM*" or "*First Order Reliability Methods – FORM*".
  According to *Cornell 1967* [13] the target reliability index (β) is defined as the distance between the mean value μ_z of the limit state function from the failure condition expressed in number of standard deviation of the limit state function σ_z (Figure 1-8 (a)).
  According to *Hasofer and Lindt 1974* [14] The reliability index β is defined as the closest distance between the mean value of the joint probabilistic distribution of basic variables in the standard normal space and the multidimensional limit state surface. The explanation is shown in Figure 1-8 (b) in the case of two random variable R and E with linear limit state function.

Any point of the limit state function can be considered as a critical structural configuration. The best solution with level II methods is achieved performing the linearization of the limit state function around the *design point*. In the details, the point having coordinates (R_d, E_d) closest to the mean point of coordinates (μ_R, μ_E).

In Figure 1-8 (b) α_R and α_E denotes the *First Order Reliability Method – FORM – sensitivity factors* of the random variables R and E; where R denotes the distribution of resistances and E denotes the distribution of the actions. The sensitivity factors α_R and α_E may be evaluated as the direction cosines of the design point Figure 1-8 (b): $\alpha_R = \frac{\sigma_R}{\sqrt{\sigma_E^2+\sigma_R^2}}$; $\alpha_E = \frac{\sigma_E}{\sqrt{\sigma_E^2+\sigma_R^2}}$; $\alpha_E^2 + \alpha_R^2 = 1$. In the *EN 1990* [15] and *fib Model Code 2010* [11], an approximation of these values is performed according to *Konig and Hosser 1982* [16]. Specifically, the value of α_R is set equal to 0.8 and the value of α_E is set equal to -0.7. These values for α_R and α_E are defined for dominant random variables (i.e., failure mechanism governed by aleatory uncertainties and not epistemic uncertainties). In case of non-dominant random variables (as in the case of epistemic uncertainty) the value of FORM sensitivity factors can be pre-multiplied for 0.4.

- ***Level I methods (semi-probabilistic)***. The basic variables are represented by their characteristic value; the low quantile (i.e., 5%) in case of strength distributions and the high quantile (i.e., 95%) in case of distributions related to actions. Moreover, partial safety factors are introduced with values that are based on Level II calculations. The basic verification, introduced by *EN 1990* [15], consist of verifying whether the limit state is not exceeded when all basic variables in the limit state equation are replaced by so called design values. The design resistance R_d should be at least equal to the design value of the load effect E_d: $R_d \geq E_d$.
- ***Level 0 methods (deterministic)***. Purely deterministic methods. These methods does not allow to quantify the level of reliability and may underestimate the structural safety without any control about it. The basic verification is performed basing on the following equation: $R_{Nom} \geq \gamma \cdot E_{Nom}$. Where R_{Nom} represents the nominal strength of the structure calculated with the nominal material properties; γ represents a safety coefficient that is a function of the failure mechanism considered and E_{Nom} is the nominal value of the action on the structure considering the nominal value of the actions.

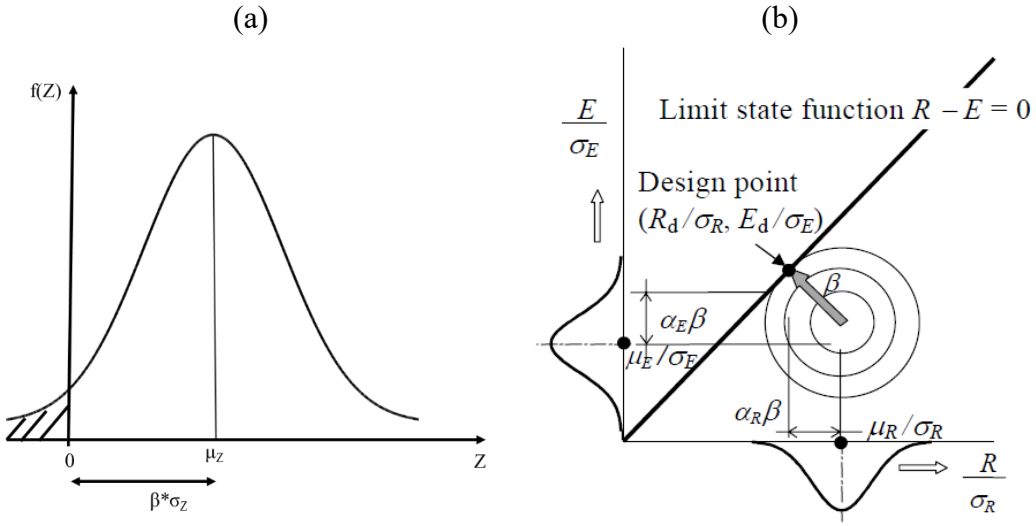

Figure 1-8: Definition of reliability index β. (a) According to Cornell [13]. (b) According to Hasofer and Lindt [14].

Starting from the level III to the level 0 the implementation of probability theory and the computational effort for estimation of the structural reliability decreases significantly.

The concept of target reliability index was introduced by *Hasofer and Lindt 1974* [14]. In 1986 *Madsen et al.* [17] publish a book reviewing key aspects in safety assessment including: analysis of uncertainties in loads and materials through probabilistic theories; approaches to represent uncertainties in load and strength models; performance and service life analysis of structures; and techniques for assessing the safety of structures, including deterministic and probabilistic methods.

Target reliability index values are given in international standards such as *EN 1990* [15] or *fib Model Code 2010* [11] and in scientific literature such as *fib Bulletin 80* [18].

The definition of the target levels of reliability has to consider the possible consequences of structural failure, both, in terms of human fatalities and economic implications. Furthermore, the selection of level of reliability should consider the cost required for safety measures able to reduce the probability of failure.

The reliability analysis of existing structures differs from new ones in different aspects:

- the economic cost to increase the safety level of existing structures is generally higher than the one needed to increase the safety of a new structure during its design;
- the remaining service life of existing structures is shorter than that of new structures (50 - 100 years).

The optimal value of the reliability index is obtained by minimizing the total cost that is a function of the reliability index. The total cost in the case of new

structures is given by the cost of construction plus the cost of consequences in case of structural collapse ($P_f D$). The total cost in the case of existing structures is given by the cost of upgrading plus the cost of consequences in case of structural collapse ($P_f D$). In Figure 1-9 this procedure is represented for both new and existing structures.

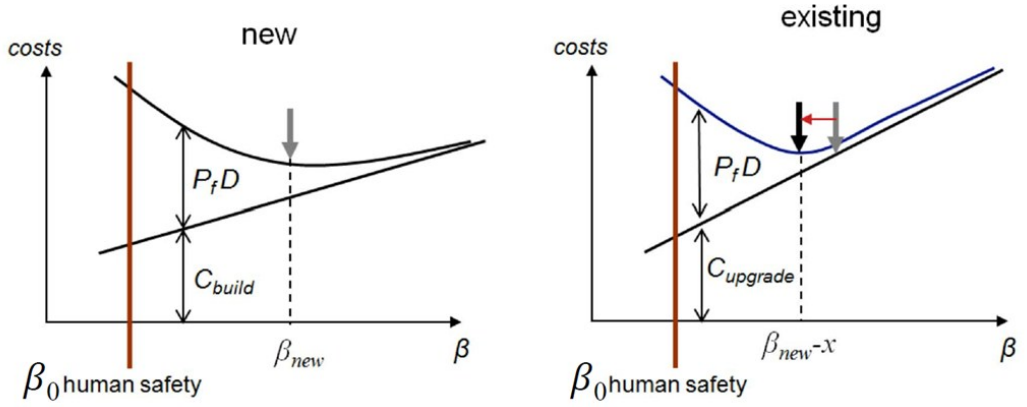

Figure 1-9: Differences in cost optimization between the design of new structures and upgrading of existing structures [18].

The target levels of reliability should be differentiated among new and existing structures. The cost for upgrading an existing structure may be higher than the cost for build a new structure with appropriate safety measures. For this reason, optimum target reliability indexes for existing structures have to be lower than the ones for new structures. Moreover, target reliability of existing structures should be based on their residual service life. The methodology to derive target reliability indexes accounting for these aspects related to existing structures is outlined in *fib Bulletin 80* [18]. It is critical to emphasize that the approach provided by *fib Bulletin 80* [18] is only and exclusively valid for existing undamaged and/or undegraded structures. This is a key point, as some deterioration, like corrosion of post-tensioned tendons may be present in existing structures, but often remains undetectable on the most common visual inspections.

Table 1-1 shows the target reliability indexes for new and existing structures according to *fib Model Code 2010* [11].

Table 1-1: Target reliability index according to fib Model Code 2010 [11] for new and existing structures.

Limit states	Target reliability index β	Reference period
New structures		
Serviceability (SLS)		
Reversible	0.0	Service life
Irreversible	1.5	50 years
Irreversible	3.5	1 year
Ultimate (ULS)		
Low consequences of failure	3.1	50 years
	4.1	1 year
Medium consequences of failure	3.8	50 years
	4.7	1 year
High consequences of failure	4.3	50 years
	5.1	1 year
Existing structures		
Serviceability (SLS)	1.5	Residual service life
Ultimate (ULS)	3.1 – 3.8	50 years
	3.4 – 4.1	15 years
	4.1 – 4.7	1 year

1.3. Structural Health Monitoring of existing structures

The main purpose of a Structural Health Monitoring (SHM) system is to assess the condition of the structure at the time of the installation of the monitoring system and from that point on, to evaluate any changes in structural response over time.

The monitoring system provides a "snapshot" of the state of the structure at the instant of its installation. Any change in structural response from that point onward indicates that a variation in structural parameters is undergoing and some sort of degradation may be in progress. SHM obviously provides no information about any damage occurred before installation. For this reason, supporting the interpretation of monitoring data through appropriate numerical models of the structure, so-called "*Digital-Twins*", is the increasingly common practice in SHM, especially for challenging structures.

In the first instance, SHM can be classified into two major families: *static monitoring* and *dynamic monitoring*. The first deals with the analysis of static data collected on the structure (rotations, displacements, deformations, etc.) . The sampling period is higher than the time needed by achieving a significative variation of some variable loads. Therefore the effect of quick varying loads is not accurately perceived.

The second deals with the analysis of dynamic data (accelerograms). Sampling data frequency is higher than the highest frequency of variation of any significative variable load. The choice of monitoring instrumentation and the type of monitoring depends on the parameters that are considered interesting by the designer.

Therefore, a proper design of the monitoring system is required. Generally, a combined approach between static and dynamic monitoring is used.

The objectives of SHM strategies can be divided into the following five levels according to *Chem and Ni* [19].

- ***Level 1***. Detection of damage, providing a qualitative indication of the possible presence of damage in the structure;
- ***Level 2***. Localization of damage, giving information on the probable location of the damage in the structure;
- ***Level 3***. Classification of damage, giving insight into the possible type of damage;
- ***Level 4***. Damage assessment, giving an estimate of the probable extent of damage;
- ***Level 5***. Prognosis of damage, giving information on structural safety, such as estimating the useful life of the structure following damage.

The levels, in the order in which they were previously exposed, represent increasing knowledge of structural damage. A high-order level generally requires the information necessary for the determination of the lowest order. As the order increases, the complexity of algorithms for data analysis and the number of sensors needed will also increase.

1.4. Objectives of the Dissertation

Within this context, the thesis aims to investigate the advantages, limitations, and distinctions among various modelling approaches through the analysis of real-world case studies.

In the domain of safety assessment, linear elastic modelling techniques are compared with approaches based on three-dimensional nonlinear finite element analysis (3D NLFEA). These methods differ significantly in terms of complexity, computational demands, and associated economic costs. A comparative study on a real case demonstrates the advantages—particularly in terms of improved safety margins—that arise as model complexity increases. These benefits, however, are strongly dependent on the assumptions underlying the nonlinear modelling and on the theoretical framework of the safety format employed. Additionally, a second case study explores the correlation between structural damage and changes in stiffness, using static parameters that are directly measurable on the structure.

In the area of structural monitoring, the focus shifts to dynamic monitoring and the updating of digital twins. Through three case studies involving different bridge and viaduct typologies, the thesis examines the differences between numerical models used for structural safety assessment and those designed for interpreting monitoring data. For each structural type, the influence of various modelling parameters on dynamic behaviour is analysed. Some parameters—such as global stiffness or support conditions—emerge as critical across multiple structural types,

while others are relevant only in specific configurations. These findings help define the priorities and strategies for effective digital twin updating.

1.5. Organization of Dissertation

This thesis presents a comprehensive framework for the structural safety assessment and monitoring of existing bridges. Its primary objective is to highlight key aspects of numerical modelling and the in-service behaviour of these structures, with particular emphasis on how such factors influence both safety evaluations and the interpretation of monitoring data.

Chapter 2 reviews the state of the art in the safety assessment of existing structures. It introduces the methodologies proposed in fib Bulletin 80—specifically, the Deterministic Verification Method (DVM) and the Advanced Partial Factor Method (APFM). The chapter then examines the guidelines outlined in the Italian technical framework for the safety assessment of existing bridges. Finally, three global safety formats used for evaluating existing structures are presented and discussed.

Chapter 3 provides an overview of Structural Health Monitoring (SHM), with a primary focus on dynamic monitoring. It outlines the theoretical background of dynamic monitoring and describes two widely used Operational Modal Analysis (OMA) techniques: the SSI-Covariance method and the PolyMAX method. A brief discussion on static monitoring is also included. The chapter concludes with an introduction to digital twin model updating, emphasizing the application of genetic algorithms.

Chapter 4 presents the first case study on safety assessment, involving two bridge decks. Their safety is evaluated using five distinct approaches: two local and three global. The local approaches involve modelling based on Courbon's theory and an elastic finite element model. The global approaches are based on 3D nonlinear numerical analyses, each assessed using a different global safety format. The chapter highlights the differences in safety outcomes depending on the modelling approach and safety format adopted.

Chapter 5 introduces a second case study concerning the safety assessment of a bridge deck. Using a global safety format applied to a 3D nonlinear analysis, the chapter correlates the level of structural degradation with the overall safety margin. Furthermore, it explores the relationship between structural damage and threshold values of measurable static parameters such as displacements and rotations.

Chapter 6 examines the interpretation of dynamic monitoring data in three different bridge structures. The chapter focuses on the model updating process for digital twins, identifying the parameters that most significantly affect the dynamic behaviour of each numerical model. These parameters are optimized using genetic algorithms to improve the accuracy and reliability of the updated digital models.

Chapter 2

State of the art on safety assessment of existing RC bridge

2.1. Chapter introduction

This chapter will provide a state of the art on different strategies for safety assessment of existing bridges.

In general, in professional activity, safety assessments are performed according to *fib Model Code 2010* [11] and *EN 1990* [15] by referring to local approaches through the partial factor format (Figure 2-1 (a)), comparing the value of a design agent action E_d and a design resistant action R_d, checking that $R_d \geq E_d$.

This method has the advantage of requiring low computational effort, but it has the disadvantage of being on safety side, and this in the case of existing structures can lead to the need for retrofitting interventions even where not strictly necessary, using unnecessary economic resources. For this reason, an alternative method that is increasingly being used - due to the increase in computing power available today - is the application of global safety format to the results of Non-Linear Finite Element Analysis (NLFEAs). This second option requires the analysis of the structure through a global approach (Figure 2-1 (b)).

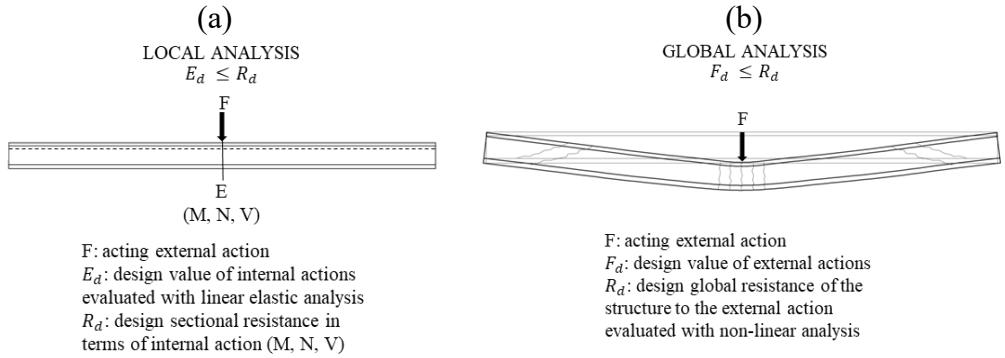

Figure 2-1: Generic comparison between local structural analysis (a) and global structural analysis (b).

2.2. fib Bulletin 80

fib Bulletin 80 [18] proposes two methods to calculate the partial safety factor for exiting RC structures: the *Design Value Method* (DVM) and the *Adjusted Partial Factor Method* (APFM). The DVM allows to recalculate the partial safety

factors for material resistances and actions through a consistent probabilistic models derived by the prior knowledge, test results, and observations related to the existing structure under investigation. The APFM, that is the simplest approach, allows to update the partial safety factors defined by standards for new structures, by means of *adjustment coefficients* accounting for the prior knowledge, test results, and observations related to the existing structure.

The basis of the two methods is that the existing structures have already fulfilled part of their service life and only need to be evaluated for the remaining part. In addition, as specified in the section 1.2, the costs for retrofitting existing structures may be higher than the costs of building new structures. Thus, target reliability levels for existing structural systems should be reconsidered.

As specified in section 1.2 the two approaches can only be applied to existing structures that are undamaged and do not exhibit deterioration.

An application of the two methods proposed by *fib Bulletin 80* to an existing bridge and a discussion of these is provided by *Gino et al.* [20].

Basics of the partial factor format

The evaluation of structural reliability according to *fib Bulletin 80* [18] is based on the partial factor format defined according to the Level I (semi-probabilistic approach), as specified in section 1.2. Therefore, the application of partial safety factors is adopted both resistance side (R_d) and action side (E_d).

The design value of the resistance of a structural component R_d can be evaluated, according to *EN 1990* [15], as:

$$R_d = R\left\{\eta_i \cdot \frac{X_{k,i}}{\gamma_{M,i}}; a_d\right\} \tag{2.1}$$

$$\gamma_{M,i} = \gamma_{Rd1} \cdot \gamma_{Rd2} \cdot \gamma_{m,i} \tag{2.2}$$

$$\gamma_{m,i} = \frac{X_{k,i}}{X_{d,i}} = \frac{1 - 1.645 \cdot V_{X_i}}{1 - \alpha_R \cdot \beta \cdot V_{X_i}} \tag{2.3}$$

where η_i represents the conversion factor; $X_{k,i}$ and $X_{d,i}$ are, respectively, the characteristic (i.e., 5% quantile) and the design values of material proprieties; V_{X_i} is the coefficient of variation of the material propriety; a_d is the design values of geometrical parameters; γ_m is the partial safety factor for the material uncertainty assuming a normal distribution; γ_M is the partial safety factor that takes into account material uncertainties, geometric uncertainties, and model uncertainties; γ_{Rd1} is the partial safety factor for model uncertainties *EN 1992-1* [21]; γ_{Rd2} is the partial safety factor for geometrical uncertainties *EN 1992-1* [21].

The design value of the action E_d can be evaluated as:

$$E_d = E\{\gamma_{G,j} G_{k,j}; \gamma_P P; \gamma_{Q,1} Q_{k,1}; \gamma_{Q,i} \psi_{0,i} Q_{k,i}\} \; i > 1; j \geq 1 \tag{2.4}$$

$$\gamma_{g,j} = \frac{G_{d,i}}{G_{k,i}} = \frac{1 - \alpha_R \cdot \beta \cdot V_{G_j}}{1 - k \cdot V_{G_j}} \tag{2.5}$$

$$\gamma_{q,j} = \frac{F^{-1}_{Q,j,t_{ref}}\left[\Phi\left(-\alpha_E \cdot \beta, t_{ref}\right)\right]}{Q_{k,j}} \tag{2.6}$$

$$\gamma_{G,j} = \gamma_{Ed} \cdot \gamma_{g,j} \tag{2.7}$$

$$\gamma_{Q,j} = \gamma_{Ed} \cdot \gamma_{q,j} \tag{2.8}$$

$$\gamma_P = 1 \tag{2.9}$$

Where:

- $G_{k,i}$ and $G_{d,i}$ represent, respectively, the characteristic and the design values of the permanent actions;
- V_{G_j} is the coefficient of variation of the permanent actions; *P* represents the prestressing actions;
- $Q_{k,1}$ is the characteristic value of the dominant external action for the selected loading configuration;
- $\psi_{0,i}Q_{k,i}$ are the combination values of the non-dominant actions for the selected loading configuration;
- t_{ref} is the reference period;
- $F^{-1}_{Q,j,t_{ref}}$ is the inverse of the cumulative probabilistic distribution of maxima of variable action related to t_{ref};
- Φ is the normal distribution; γ_{Ed} is the modal uncertainty partial safety factor for actions according to *EN 1990* [15];
- $\gamma_{G,j}$, $\gamma_{Q,j}$ and γ_P are the partial safety factors accounting for model and aleatory uncertainties for permanent, variable and prestressing, respectively.

The level of reliability is defined by the reliability index β. The FORM sensitivity factors α_R and α_E are set equal to 0.8 and -0.7 for dominant variables, respectively, and equal to 0.4 and -0.32 for non-dominant variables according to *EN 1990* [15] and *fib Model Code 2010* [11].

Target levels of reliability for existing bridges according to fib Bulletin 80

As anticipated in section 1.2, target reliability values for existing structures should be revised with respect to the ones conceived for new structures.

The target reliability indices are evaluated accounting for both economic and human safety criteria. In detail, the assumption of constant annual target probability of failure within the residual service life of the structure t_{ref}. For this hypothesis *fib Bulletin 80* [18] is not directly applicable for cases of bridges subjected to active deterioration processes, as mentioned in section 1.2; where, the probability of failure over the years cannot be considered constant. In the case of degraded structures, the target reliability index should be calculated on an annual basis [22] and should be interpreted as a target limit for every individual year during the design or remaining working life of the structure. If the annual failure probability is an increasing function of time, like in the case when aging processes like corrosion and future uncertain trend are relevant the last year of the design service life may be decisive [22].

The optimization concerning the economic criteria is performed accounting for the consequence of structural failure in terms of economic losses, social inconvenience, environmental effects, and costs of safety measures adopted to reduce the probability of failure.

The consequences related to structural failure are accounted through the reliability differentiation approach according to *EN 1990* [15] and *fib Model Code 2010* [11]. Three consequence classes (i.e., CC1, CC2, and CC3) are defined with increasing economic, social, and environmental casualties due to structural collapse.

fib Bulletin 80 [18] suggests that target reliability levels for economic optimization for existing structures can be defined differentiating between two different values of the target reliability index β_t:

- $\beta_{0,t}$ target reliability index associated to the existing structure assessed in its current state, without any retrofitting. In the case of this target level of reliability is not fulfilled, the retrofitting of the structure is required;
- $\beta_{up,t}$ target reliability index to be satisfied after the retrofitting of the existing structure.

The human safety requirements for existing bridges are identified in compliance to the individual and group risk criteria. The group risk criteria allow to take into account the possible number of people at risk as a function of the potential collapsed span of the bridge S and the residual service life t_{ref}.

The potential collapsed span S should be identified by means of an engineering judgment accounting for the actual static scheme of the bridge and the predicted failure modes. However, the group risk criteria accounting for human safety are extremely approximate as it is derived from the relationship between the collapsed span of the bridge S and the number of casualties N, which is calibrated on the basis of limited data. The methodology proposed by *fib Bulletin 80* [18] to define the target reliability levels for existing bridges is shown in Table 2-1.

Table 2-1: Target reliability index for existing bridges according to fib Bulletin 80 [18].

Economical aspects: valid for existing building and bridges		
Consequence classes	$\boldsymbol{\beta_{0,t,economical}}$	$\boldsymbol{\beta_{up,t,economical}}$
CC1	1.8	2.8
CC2	2.3	3.3
CC3	2.8	3.8
Human safety requirement: valid for existing bridges		
Consequence classes	$\boldsymbol{\beta_{0,t,human\ safety}}$	$\boldsymbol{\beta_{up,t,human\ safety}}$
CC1/CC2	$-\Phi^{-1}\left[\frac{2.75 \cdot 10^{-5} \cdot (0.09 \cdot S)^{-2} \cdot t_{ref}}{0.055}\right]$	
Target reliability index for existing bridges		
Consequence classes	$\boldsymbol{\beta_{0,t}}$	$\boldsymbol{\beta_{up,t}}$
CC1/CC2	$max\begin{pmatrix}\beta_{0,t,economical};\\ \beta_{0,t,human\ safety}\end{pmatrix}$	$max\begin{pmatrix}\beta_{up,t,economical};\\ \beta_{up,t,human\ safety}\end{pmatrix}$
CC3	1.8	2.8
t_{ref} is the residual service life; S is the collapsed span of the bridge accounting for individual and group risk criteria; Φ is the cumulative standard normal distribution function.		

The Design Value Method

The Design Value Method (DVM) [18] allows to recalculate the partial safety factors $\gamma_{M,i}$, $\gamma_{G,j}$ and $\gamma_{Q,j}$ from the actual probabilistic distribution of the variables X_i, G_j, and Q_j under consideration.

The partial safety factors can be defined according to target reliability levels related to existing structures and to the expected residual service life t_{ref}.

The DVM leads to results, in terms of values of partial safety factors, discordant to the ones derived by *EN 1990* [15] *fib Model Code 2010* [11] and *EN 1992-1* [21] performing the same assumptions concerning the probabilistic model for the involved random variables, especially, concerning the partial safety factors for variable actions.

The adjusted partial factor method

The adjusted partial factor method (APFM) [18], [23] allows to define the partial factors for existing structures ($\gamma_{Existing}$) adjusting the partial factors $\gamma_{M,i}$, $\gamma_{G,j}$ and $\gamma_{Q,j}$ related to new structures (γ_{New}) proposed by *EN 1990* [15] *EN 1992-1* [21] and *fib Model Code 2010* [11] through adjustment factors ω as follows:

$$\gamma_{Existing} = \omega \cdot \gamma_{New} \tag{2.10}$$

The adjustment factor ω accounts for the different target reliability level, the residual service life t_{ref} of the existing structure, prior ad new information from in situ and laboratory tests and measurements.

Comparing this method to the DVM, both are based on the same fixed values of the FORM sensitivity factors. The APFM may be considered as the easiest one to be applied in practice and often leads to conservative values of partial safety factors if compared to the DVM.

2.3. Italian Guidelines For Risk Classification and Management, Safety Assessment and Monitoring of Existing Bridges

The Italian Guidelines [9], [10] are compliant with the Italian standard for constructions [24] (i.e., NTC in Italian) which provide the load combination and the safety checks for bridge design. Existing bridges must be evaluated according to NTC as well if they are structurally changed or damaged during their service life. The It. Guidelines state the necessity of classifying the whole existing stock of bridges according to a simplified risk analysis. On the basis of estimated risk, the classification should permit to define an attention class of the bridge. In the case of high attention class bridges or particular structural systems, a safety assessment in accordance with the code must be carried out. In addition to the NTC, the It. Guidelines include new traffic load models and reduced safety partial factors that allow practitioners to assess the safety assessment of the bridge in a given reference period.

The It. Guidelines establish a multi-hazard methodology to combine structural, seismic, geotechnical and hydraulic hazards for the preliminary assessment of the bridge risk class. A multilevel approach is also provided to define priority schemes for the bridge network according to the following list:

- Level 0: data mining is performed to collect relevant information on all bridges in the Italian inventory: location, structural scheme, year of construction, design standards in force at the time of construction, retrofit interventions during the lifetime, etc.
- Level 1: a visual inspection is performed to detect possible damage (e.g., concrete cracks, steel corrosion, etc.) and hazard scenarios (e.g., active landslides, etc.) to generate an inspection report.
- Level 2: the combination of hazard, vulnerability and exposure data provide a simplified assessment of the bridge risk class classified from low to high with a total of five classes (low, medium-low, medium, medium-high, high).
- Level 3: is applied in the case of medium and medium-high risk class: a preliminary structural safety assessment is carried out based on a comparison of the effect of the traffic loads provided by the current standards and those in force at the time of construction.
- Level 4: is applied in case of high hazard class or assessment not met at Level 3. A detailed safety assessment is carried out according to current standards. It should be mentioned that in case of structural damage or

deterioration, a detailed assessment should always be carried out to define the safety level of the bridge and the need for retrofit according to current standards.

An applicative case for detailed safety assessment through guidelines can be found in *Cosenza et al.* [25].

Detailed safety assessment

The approach of the *It. Guidelines* [9], [10] is in line with the *fib Bulletin 80* [18] method described in section 2.2, aiming to provide a minimum target reliability β_0 during the reference period t_{ref} adopting reduced safety factors.

The It. Guidelines introduce the concept of the performance class of the existing bridge: *code-compliant*, *fully operational* or *partially operational*. In the case of a partially operational bridge, either the standards or suitably developed traffic loads may be applied for safety assessment, depending on the judgment of the local authority. The detailed safety assessments presented in the It. Guidelines aim to determine the performance class the bridge can provide, shown below in descending order of safety:

- ***Code-compliant***: Standards levels of safety are met based on standards traffic loads and standards safety factors. Reduced permanent load safety factor may be adopted under appropriate scenarios to be checked. The reference period, target reliability, design loads and load combinations are established according to the standards as for the design of new bridge.
- ***Fully-operational***: standard safety levels are fulfilled by adopting reduced safety factors calibrated for $\beta = \beta_0$ and $t_{ref} = 30$ years.
- ***Partially-operational***: standard safety levels are fulfilled by adopting reduced safety factors calibrated for $\beta = \beta_0$ and $t_{ref} = 5$ years. Two different configurations for traffic loads can be adopted: new traffic loads according to actual moving vehicles on Italian roadways; standards traffic loads are adopted with a physical limitation on the number and/or position of lanes.

2.4. Non-linear finite elements analysis of reinforced concrete structures

In common applications, assessment and design of reinforced concrete structures can be performed efficiently by means linear elastic analysis. This solution generally provides safe solutions within the limit states approach. In some cases, the use of linear analysis may not be sufficient in order to fulfil the safety requirements and deeper investigations may be required, in particular, for economic reasons.

In the last decades, Non-Linear Finite Element Analyses (NLFEAs) have increasingly become the most common and practical tool able to simulate the actual

mechanical behaviour of structural systems. In this context, several guidelines for NLFEAs, as *fib Bulletin 45* [26], have been defined in order to provide efficient methodologies devoted to calibrate NLFE models.

The NLFE method turns out to be an efficient tool when it is necessary to perform assessment/design of reinforced concrete structures having complex geometry, poorly detailed or locally damaged structural members (e.g. localized cracking or local damaging due to impacts). The use of NLFE models for design and assessment should be always performed by engineers confident with the approach. In fact, the user can be misled from the apparent precise results obtained by the NLFEA simulations.

In the follow, basic notions of solution methods and modelling of nonlinear material properties are provided.

Solution methods

The structural system can be solved by the following system of equilibrium equations:

$$\lambda p - f(q) = 0 \tag{2.11}$$

$$K(q)q - f(q) = 0 \tag{2.12}$$

where q is the vector of nodal displacements; p is the vector of external loads; λ is the multiplier of the vector of external loads; $K(q)$ is the stiffness matrix of the system, in general as a function of the displacements vector q; $f(q)$ is the vector of internal forces as a function of the nodal displacements.

The system of nonlinear equations can only be solved by numerical calculation. The commonest method of numerical solution is the Newton-Raphson method, shown below.

Newton-Raphson method

The Newton-Raphson method is an iterative approach able to solve non-linear systems of equations by means progressive linear approximations.

With the set $(q_0, \lambda p)$ defined as the current trial displacement condition and the vector of loads, respectively, the solution can be calculated iteratively by adding the change in displacements δq_i to the current displacement condition evaluated as:

$$\delta q_i = \left(K_T^i\right)^{-1} r(q_i) \tag{2.13}$$

where K_T^i is the tangent stiffness matrix determined for the current state and $r(q_i)$ is the vector of out of balance forces.

In this method, within every iteration step the current stiffness matrix is defined and the linearized equations are solved considering the increment δq_i. For this

reason, the method results to be very efficient, even though may require more computational time.

Convergence criteria

The solution of a structural system by means of NLFEA leads to solutions which are an approximation of the exact one. The exact solution is the one that corresponds to an out of balance force equal to zero: $r(q_i) = 0$.

The solutions obtained by NLFEA are always in presence of a certain amount of out of balance force. For this reason, it is necessary to define criteria (i.e. convergence criteria) able to discern if the iterative solution process has reached the required level of accuracy.

In general, the quantities monitored to check the progressive convergence of the solution procedure are the differences between two consecutive iterations of: the out of balance forces, the displacements and the deformation energy.

Non-linear modelling of concrete

The fundamental hypotheses for non-linear modelling of reinforced concrete adopted in this dissertation are outlined in this section.

Specifically, the most common modelling hypotheses for 3D brick element models are reported. The software DIANA FEA is used for non-linear modelling [27],[28],[29].

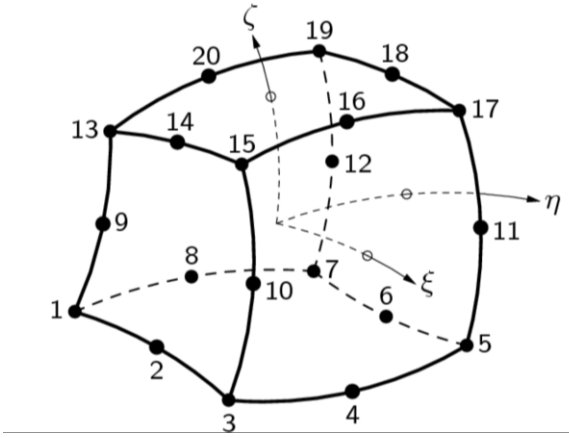

Figure 2-2: 20 nodes brick element [28].

Twenty-node solid isoparametric elements are used for three-dimensional modelling of concrete elements, as shown in Figure 2-2. The use of brick elements offers several advantages, particularly in contexts where precision and realism in structural behaviour are essential—such as accurate stress analysis and realistic modelling. This approach also allows for the selective removal of concrete elements to represent concrete cover spalling, as well as the removal of portions of reinforcement, such as the bottom legs of stirrups or sections of longitudinal bars affected by corrosion. They are based on quadratic interpolation and Gauss integration. The polynomials for the translations u_{xyz} can be expressed as:

$$u_i(\xi,\eta,\zeta) = a_0 + a_1\xi + a_2\eta + a_3\zeta + a_4\xi\eta + a_5\eta\zeta + a_6\xi\zeta + a_7\xi^2 + a_8\eta^2 + a_9\zeta^2 + a_{10}\xi\eta\zeta + a_{11}\xi^2\eta + a_{12}\xi^2\zeta + a_{13}\xi\eta^2 + a_{14}\xi\zeta^2 + a_{15}\eta^2\zeta + a_{16}\eta\zeta^2 + a_{17}\xi^2\eta\zeta + a_{18}\xi\eta^2\zeta + a_{19}\xi\eta\zeta^2 \quad (2.14)$$

This rectangular brick element approximates the following strain and stress distribution over the element volume: the strain ε_{xx} and stress σ_{xx} vary linearly in x direction and quadratically in y and z direction; the strain ε_{yy} and stress σ_{yy} vary linearly in y direction and quadratically in x and z direction; the strain ε_{zz} and stress σ_{zz} vary linearly in z direction and quadratically in x and y direction. The number of integration points used for each direction is 3.

The mesh refinement should be calibrated case by case limiting the dependence of results from the mesh size.

A Smeared Cracking model with fixed crack direction (Figure 2-3) is used for concrete *Cervera and Chiumenti 2006* [31], the crack direction is defined at first cracking and does not change during the following load steps. The constitutive law is based on the *Total Strain Crack model* associated to the *Modified Compression Field Theory Vecchio and Collins 1986* [32] and extended to three-dimensional problems according to *Selby and Vecchio 1993* [33].

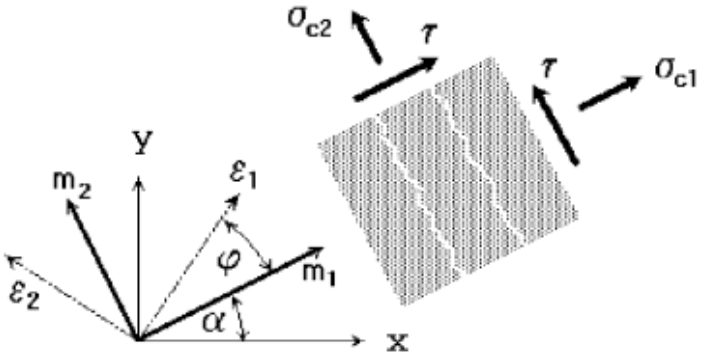

Figure 2-3: Fixed crack model.

A linear-ultimate crack strain model is used for concrete subjected to tensile stresses, with a linear tension softening branch after reaching peak tensile strength *Castaldo et al. 2018* [34] (Figure 2-4), to take in account the *tension stiffening effect* due to interaction of cracked concrete and reinforcement. Tensile behaviour of concrete is an extremely impactful parameter in the results of nonlinear numerical analyses. In *Castaldo et al 2018 [34]* a study is conducted by simulating experimental evidence on different structures through NLFEA. Three different nonlinear modelling software and three different constitutive tensile concrete constitutive law are used for each software: elastic-brittle behaviour; elastic-plastic behaviour; and linear-ultimate crack strain behaviour. The first two represent the two limit behaviours, the third represents the real behaviour, intermediate to the two tensile limit behaviours. The study shows that the ultimate load using the three different tensile concrete models shows engineering variability that is negligible;

what varies significantly, however, is the ultimate deformation. For ductile-type collapse mechanisms, the best constitutive law for tensile concrete is the linear-ultimate crack strain behaviour with ultimate strain ranging from 2 to 10 times the maximum elastic strain.

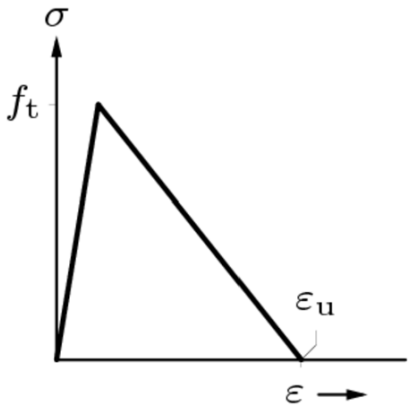

Figure 2-4: stress-strain relationship for concrete in tension [29].

The stress-strain relationship for concrete in compression is based on EN 1992-1-1 [21] Figure 2-6 and is written in Equation (2.15).

$$\frac{\sigma}{f_c} = \frac{\left(\frac{E_c}{E_s}\right)\cdot\left(\frac{\varepsilon}{\varepsilon_c}\right)}{1 + A\cdot\left(\frac{\varepsilon}{\varepsilon_c}\right) + B\cdot\left(\frac{\varepsilon}{\varepsilon_c}\right)^2 + C\cdot\left(\frac{\varepsilon}{\varepsilon_c}\right)^3} \tag{2.15}$$

$$A = \frac{\left[\frac{E_c}{E_u} + (p^3 - 2p^2)\cdot\frac{E_c}{E_s} - (2p^3 + 3p^2 + 1)\right]}{[(p^2 - 2p + 1)\cdot p]} \tag{2.16}$$

$$B = \left[\left(2\frac{E_c}{E_s} - 3\right) - 2A\right] \tag{2.17}$$

$$C = \left[\left(2 - \frac{E_c}{E_s}\right) + A\right] \tag{2.18}$$

$$E_s = \frac{f_c}{\varepsilon_c} \tag{2.19}$$

$$E_u = \frac{f_u}{\varepsilon_u} \tag{2.20}$$

$$p = \frac{\varepsilon_u}{\varepsilon_c} \tag{2.21}$$

where E_c is the zero-stress tangent Young modulus; E_s is the secant Young modulus of concrete corresponding to peak strength; E_u is the secant Young modulus of concrete corresponding to ultimate strength; ε is the strain; ε_c is the peak strain; ε_u is the ultimate strain; σ is the stress; f_c is the peak strength; f_u is the ultimate

strength and p is the ratio between ultimate and peak strain. The mono-axial constitutive law of concrete in compression (Equation (2.15)) is modified taking into account variation of the peak compressive and ultimate strength and relative strains in function of generalized tri-axial state of stress. This phenomenon can lead to compression softening when the material is subjected to tensile stresses orthogonal to the main direction of compression or to compression hardening when the material gets close to hydrostatic state of stress.

A reduction of compressive strength due to lateral cracking, based on the model proposed in *Vecchio and Collins 1993* [35] (Figure 2-5), is implemented and the confinement model, based on the model proposed in *Selby and Vecchio 1997* [36], is adopted. Cracked reinforced concrete in compression has been observed to exhibit lower strength and stiffness than uniaxially compressed uncracked concrete. The so-called compression softening effect responsible is thought to be related to the degree of transverse cracking and straining present. It significantly influences the strength, ductility and load-deformation response of a concrete element. The compressive strength of cracked concrete can be calculated according to Equation (2.22)

$$f_c^{ef} = f_c \cdot \beta_{\sigma_{cr}} \tag{2.22}$$

$$\beta_{\sigma_{cr}} = \frac{1}{1 + K_c} \leq 1 \tag{2.23}$$

$$K_c = 0.27 \cdot \left(-\frac{\alpha_{lat}}{\varepsilon_0} - 0.37 \right) \tag{2.24}$$

where: f_c^{ef} is the compressive strength in biaxial tension-compression; f_c is the mono-axial cylindrical compressive strength; $\beta_{\sigma_{cr}}$ is the reduction factor for compressive strength due to orthogonal tensile strains and α_{lat} is the lateral tensile strain.

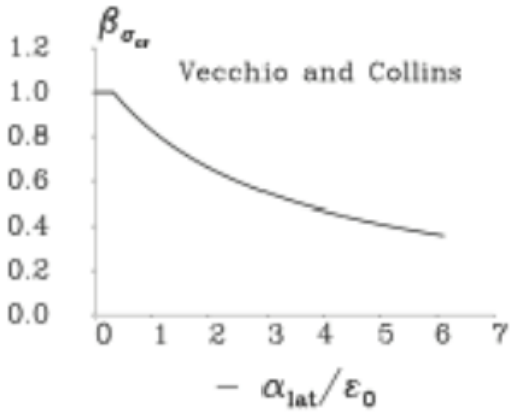

Figure 2-5: Reduction factor due to lateral cracking [35].

A constant shear retention factor $\beta = 0.2$ is used to model the shear stiffness after cracking. The shear retention factor, refers to the amount of shear transfer

across a crack. A shear retention factor of 0 refers to no aggregate interlock, whereas 1 represents full aggregate interlock. This parameter becomes crucial in brittle-type collapse mechanisms and should be carefully calibrated; it has a less impactful effect in ductile-type collapse mechanisms and can take values between 0.15 and 0.2 [37].

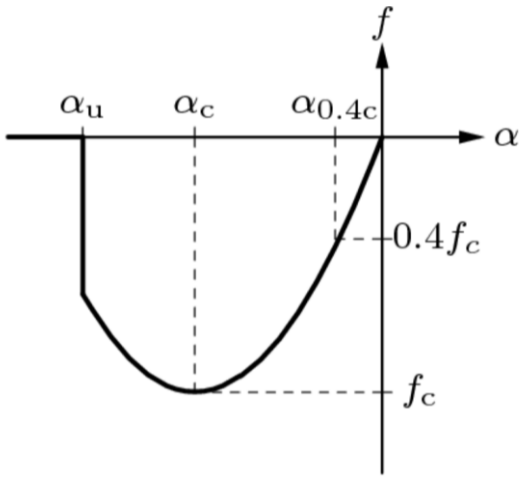

Figure 2-6: stress-strain relationship for concrete in compression according to [21].

Non-linear modelling of reinforcement

In this thesis both ordinary reinforcement, pre-tension and post-tension reinforcement are modelled as embedded type elements Figure 2-7.

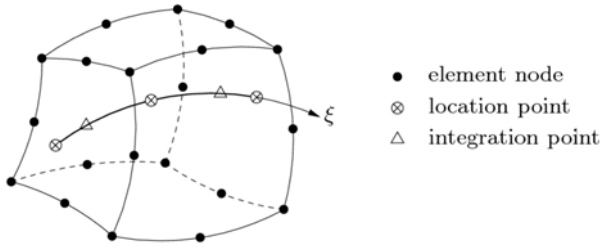

Figure 2-7: Embedded reinforcement in 3D brick element [28].

Embedded reinforcements add stiffness to the finite element model. Their main characteristics are:

- reinforcements are embedded in structural elements, the so-called *mother elements*.
- they do not have degrees of freedom of their own.
- reinforcement strains are computed from the displacement field of the mother elements. This implies *perfect bond* between the reinforcement and the surrounding material.

Elastic-plastic stress-strain relationships with linear isotropic hardening law after yielding, based on Von-Mises plasticity [38],[39] are used for both the ordinary and prestressing reinforcements Figure 2-8.

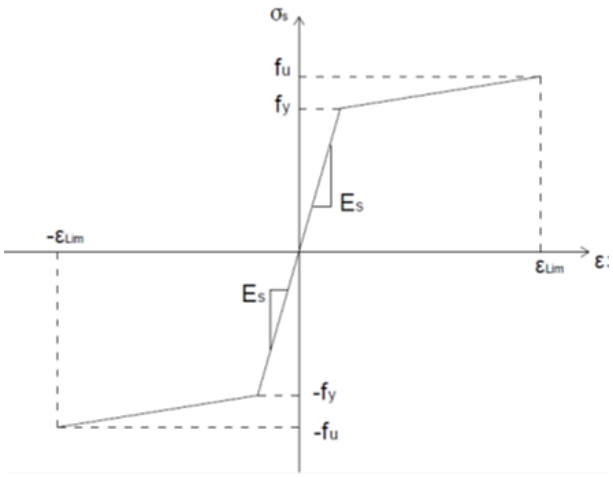

Figure 2-8: stress-strain relationship for embedded reinforcement.

2.5. Safety formats for non-linear analysis of reinforced concrete structures

The Global Resistance Format (GRF) deals with uncertainties associated with structural behaviour according to the limit state approach at the level of overall structural resistance (global strength). The sources of uncertainty are integrated into an overall design resistance R_d and can be considered through global safety factors. Global safety factors reflect the uncertainty in determining the overall structural response that depends on the random variability of the basic variables and epistemic uncertainties.

The GRF was introduced to allow structural design and assessment using non-linear analysis. In fact, refined mechanical and geometric non-linear models are generally based on a global structural level, and GRF is an efficient format for performing safety assessments.

According to GRF, the representative variable of overall strength is the structural strength R. The safety condition is represented by the following equations:

$$R_d = \frac{R_m}{\gamma_R \cdot \gamma_{Rd}} \tag{2.25}$$

where R_d is the design value of the global structural resistance according to specified target reliability index β; R_m is the mean value of the global resistance; γ_R is denoted as the global resistance safety factor, which account for material aleatory uncertainties; γ_{Rd} represents the resistance model uncertainty safety factor, which account for the resistance model uncertainty.

Global safety factors differ from the partial safety factors adopted within local analysis by partial factor format. In fact, global safety factors refer to the global structural response evaluated through mean values of material properties, instead, partial safety factors refer just to each material property (i.e. concrete compressive

strength, reinforcement yielding strength) evaluated with its characteristic value for local verification of structural members.

In scientific literature and codes, different safety formats based on GRF has been proposed. In the present dissertation, the following safety formats are considered:

- Partial Factor Method (PFM) (*fib Model Code 2010* [11]);
- Method of Estimating of the Coefficient of Variation of the structural resistance (ECoV) (*fib Model Code 2010* [11]);
- Global Resistance Factor (GRF) (*fib Model Code 2010* [11]).

Partial Factor Method (PFM)

According to the partial factor method (PFM) proposed by *fib Model Code 2010* [11], the design resistance R_d is obtained by means of a single NLFEA, which is performed using the design values (evaluated according to the partial factor format proposed by *fib Model Code 2010* [11], *EN 1990* [15] and *fib Bulletin 80* [18]) of the material resistances f_d:

$$R_d = \frac{R_{NLFEA}(f_d)}{\gamma_{Rd}} \tag{2.26}$$

where $R_{NLFEA}(f_d)$ represents the global bearing capacity of the structure estimated by means of a non-linear analysis; γ_{Rd} is the NLFE resistance model uncertainty safety factor. The NLFE resistance model uncertainty safety factor is adopted equal to 1.15 in accordance with [34], assuming the epistemic uncertainties non-dominant. Higher values of resistance model uncertainty safety factor could be necessary. To this scope, only considering explicitly the mechanical and geometrical uncertainties in addition to the "between" (different solution strategies used to analyse one RC structure) and "within" (one solution strategy used to analyse different RC structures) epistemic uncertainties [40]-[43], it is possible to identify the dominant or non-dominant role of the aleatory uncertainties with respect to epistemic ones and specify the appropriate values of both the model uncertainty safety factor [44].

Estimation of Coefficient of Variation method (ECoV)

Following the estimation of the coefficient of variation (ECoV) method, as suggested by *fib Model Code 2010* [11], the design global resistance is obtained as:

$$R_d = \frac{R_{NLFEA}(f_m)}{\gamma_R \cdot \gamma_{Rd}} \tag{2.27}$$

where R_d is the design value of the structural resistance; $R_{NLFEA}(f_m)$ denotes the structural resistance predicted by a NLFEA performed introducing the mean values of the material properties in the structural model; γ_R is the global resistance safety

factor accounting for the uncertainties related to the material properties (i.e., aleatory uncertainties); γ_{Rd} is the NLFE resistance model uncertainty safety factor. For the NLFE resistance model uncertainty safety factor the considerations made in the previous paragraph are valid.

Assuming a lognormal distribution for the global load bearing capacity of the structure, the global resistance factor γ_R can be written as:

$$\gamma_R = exp(\alpha_R \cdot \beta \cdot V_R) \tag{2.28}$$

where V_R is the coefficient of variation of the distribution of the global structural resistance. In the ECoV method, the value of V_R can be estimated, with a simplified approach, using a lognormal distribution for representing the variability of global structural resistance:

$$V_R = \frac{1}{1.65} \cdot ln\left(\frac{R_{NLFEA}(f_m)}{R_{NLFEA}(f_k)}\right) \tag{2.29}$$

where $R_{NLFEA}(f_k)$ is the structural resistance predicted by a NLFEA performed using the characteristic values of the material properties to define the structural model.

Global resistance factor method (GRF)

According to the global resistance factor (GRF) method, presented in *fib Model Code 2010* [11] and *EN1992-2* [30], the global resistance is defined as follows:

$$R_d = \frac{R_{NLFEA}(f_{cmd}, f_{ym})}{\gamma_{Gl}} \tag{2.30}$$

The value of the global safety factor γ_{Gl} is set equal to 1.27, therefore equal to the global resistance factor γ_R assuming a unitary value of γ_{Rd}.

The mean value of the yield stress f_{ym} has to be considered for reinforcing steel in the estimation of the representative value of the global resistance:

$$f_{ym} = 1.1 \cdot f_{yk} \tag{2.31}$$

where f_{yk} is the characteristic yield stress. In addition, a reduced value f_{cmd} for the concrete compressive strength has to be used to equalize the partial factor for both steel and concrete failure, as follows:

$$f_{cmd} = 0.85 \cdot f_{ck} \tag{2.32}$$

where f_{ck} denotes the characteristic value of the concrete compressive strength.

New approaches within the Global Resistance Format

In 2024, Gino et al. [44] proposed a new approach based on the ultimate strain of the main reinforcement governing the collapse mechanism of the structure for the evaluation of the global design strength of the structure within the GRF. The peak reinforcement strain serves as a response indicator representative of the structural failure mode to assess the global safety.

The design strength is evaluated in accordance with GRF as:

$$R_d = \frac{R_{NLFEA}(f_{rep}; a_{rep})}{\gamma_R \cdot \gamma_{Rd}} \tag{2.33}$$

R_{NLFEA} represents the global structural resistance estimated through NLNAs; f_{rep} and a_{rep} are, respectively, the representative values of materials and geometric properties adopted in the NLNAs.

The term γ_R denotes the global resistance safety factor related to the uncertainties of material properties and geometry (i.e., aleatory uncertainties). It can be determined under the assumption of a lognormal probabilistic distribution for the overall structural strength as:

$$\gamma_R = \frac{exp(\alpha_R \cdot \beta \cdot V_R)}{\delta_R} \tag{2.34}$$

where: β is the target reliability index; α_R is the first order reliability method sensitivity factor assumed equal to 0.8 in the hypothesis of dominating aleatory uncertainties with respect to the epistemic ones; δ_R groups the influence related to the bias factors of geometrical properties deviations $\delta_{R,g}$ and to the mean-to-mean deviation $\delta_{R,m}$, and can be computed as:

$$\delta_R = \delta_{R,m} \cdot \delta_{R,g} \tag{2.35}$$

Both terms $\delta_{R,m}$ and $\delta_{R,g}$ it has been shown that they can be taken equal to 1 [44].

The term V_R represents the coefficient of variation (CoV) of the global structural resistance (assumed as log-normally distributed variable), inclusive of the influence of aleatory uncertainties related to both materials and geometrical properties. This value can be estimated as:

$$V_R = \sqrt{V_{R,m}^2 + V_{R,g}^2} \tag{2.36}$$

where: $V_{R,m}$ represents the CoV of the global structural resistance associated to the aleatory uncertainty of material properties while, $V_{R,g}$ denotes the CoV related to

the aleatory uncertainty of geometrical properties. The value of $V_{R,g}$ can be considered reasonably equal to 0.05.

Therefore, the only parameter to be calculated is $V_{R,m}$ which in accordance with [44] can be defined as a function of the maximum strain of the main reinforcement at the time of collapse as:

$$V_{R,m} = V_c \cdot \left(\frac{\varepsilon_{s,max}}{\varepsilon_y} + 1 \right)^{\eta} \; with \; V_y \leq V_{R,m} \leq V_c \tag{2.37}$$

where: $\varepsilon_{s,max}$ is the maximum strain of the main reinforcement at the time of collapse; ε_y is the yelding strain of the reinforcement; V_c is the CoV of the concrete strength; V_y is the CoV of the reinforcement strength and η suggested as -0.4 by [44].

Chapter 3

State of the art on Structural Health Monitoring of existing bridge

3.1. Chapter introduction

This chapter provides a state of the art on Structural Health Monitoring (SHM) of existing bridges. The aim is to present a comprehensive overview of this discipline that can be considered quite young if compared to other fields of civil engineering, but which has become extremely popular and useful in order to be able to assess the health of such structures.

As mentioned in Chapter 1, SHM techniques can be divided into two families: static monitoring and dynamic monitoring. Historically, dynamic monitoring techniques have always played the most important role within SHM techniques, which is why more space is devoted to them below. In addition to the basics of SHM a brief mention of model updating techniques of the so-called Digital-Twin will be reported.

3.2. Structural Health Monitoring

SHM techniques were first applied in the automotive and aerospace fields, but due to their multidisciplinary nature and potential, they have been widely used and adapted to the fields of civil engineering in recent decades [19].

The SHM process requires the observation and assessment of the health of a structure over time. The process of observation and sampling of the data necessary to carry out the analyses, can be done periodically hand-made or continuously being automatized, as it has become increasingly common in recent years.

In the second case the amount of data sampled is not negligible and appropriate arrangements for data storage must be followed [45].

Continuous SHM based on sensors installed within the structures overcomes the limitations related to visual inspections, that imply a number of non-negligible approximations [19].

Nowadays the practice considered to be the most reliable to assess the health of a structural system, is in most cases a visual inspection [19]. While this type of investigation is immediate and requires no special complexity, it nevertheless has numerous limitations. Their effectiveness is strongly related to the experience of

the personnel performing them. The level of accuracy that can be guaranteed is limited, considering that only damage that is actually visible can be assessed. Damage to elements that are not accessible for inspection could lead to an unreliable assessment of the health of the structure. Moreover, in the case where a damage is evidenced on the structure its evaluation can only be done qualitatively.

A structural monitoring system generally consists of a number of key components: sensors, data acquisition, data transmission, data processing, data storage, and structure health assessment. Each of these phases plays a key role.

The development of an SHM-based method generally depends on two key factors: the technology of the used hardware (sensors, cables, acquisitors, telecommunication devices) and the software/algorithms used to manage and interpret the sampled data [19].

The original idea behind SHM is that a change in structural conditions (e.g., changes in mass or stiffness) would lead to a change in the dynamic properties of the system (e.g., natural frequencies, damping, or modal shapes). A detailed state of the art on SHM has been published by *Doebling et al.* [46] in 1996. In this research work, authors have summarized the most significant contributions found in literature by 1996, including some early papers published on the topic.

In 1999 *Peeters and De Roeck* [47] publish an article about an annual monitoring of the Z24 bridge, a case study that analyses the structural response of a bridge under real conditions. The objective of the study is to evaluate the behaviour of the bridge in terms of deformation and vibration, and identify possible structural problems. Sensors were used to collect data on both the dynamic and static behaviour of the structure. The methodology includes statistical analysis of the collected data. The results showed the effectiveness of monitoring to identify phenomena such as variable loading and environmental conditions affecting the structure.

In 2000 *Brincker et al.* [48] present research on modal identification of "output-only" systems. The main goal is to develop methods to identify modal properties (natural frequencies, modal shapes, and damping) using only output data. The data analysed come from measurements made with accelerometers, recording responses to environmental or operational excitation. The authors use spectral analysis techniques, such as the Fourier Transform, to identify dominant frequencies. The authors makes use of statistical methods to improve the reliability of modal estimates. This may include approaches such as Cross Correlation Analysis and Coherence Analysis, which help determine the relationship between measured responses. A mathematical model describing the dynamics of the system is developed. The authors propose the use of optimization algorithms to fit the model to the observed data.

In addition to dynamic monitoring, other alternative techniques have been developed over the years. Special interest has been deserved for the static monitoring, in which the observed quantities evolve slowly in time (few months or few years). The most common monitored parameters are displacements, tilts, deformations, cracks amplitude etc. They can be used to evaluate variations in the

behaviour of the analysed structure. A great number of methods and technologies are available for monitoring such quantities.

In 2006, DeWolf et al. [49] published an extensive report regarding a large-scale research program starting from 1994. Four bridges of different structural type were instrumented with a long-term monitoring system, with the aim of better understand the behaviour of bridges under operating conditions. Strain and acceleration were monitored by using tiltmeters, strain gages and accelerometers. Results showed how both static and dynamic measurements provided useful information for characterizing each bridge and its behaviour.

3.3. Dynamic monitoring

Dynamic monitoring of a structure is the process that leads to the evaluation of structural characteristics through the study of natural or induced vibrations.

Vibrations can be applied by appropriate external forcing, or can be induced by environmental excitation. In the first case, the excitation that produce the structural vibrations is known; in the second case, it is unknown. From these two different cases, two different types of modal analysis are developed: *Experimental Modal Analysis* (EMA) when a known forcer is used, and *Operational Modal Analysis* (OMA) when an unknown forcer is used.

EMA allows the identification of the modal parameters of a system by measuring the vibrations of a structure subjected to a known exciting force. EMA methods have been widely used over the years, especially in the automotive and aerospace fields. However, the application of methods based on EMA becomes difficult in civil engineering, as the size of the structures to be tested can be very large and the range of resonant frequencies is limited [45]. For these reasons, the application of a forcing that can be controlled and measured in big civil structures like bridges is complicated and expensive.

The difficulties in applying EMA can be overcome by the application of methods based on OMA. These methods allows the determination of the modal parameters of a system by measuring structural vibrations only [45]. In other words, it is based on knowing only the output parameters of the structure, using as input, i.e., forcing of the structure, all the forcings by which it is excited, i.e., the normal operating loads of the structure itself. One of the most important advantages of applying OMA is to be able to apply methodologies for monitoring the health of a structure. In practice, a series of accelerometers are installed on the structure and an algorithm to extract structural parameters in continuous time from accelerometric data should be developed, so that their evolution over time can be evaluated [45]. Attention should be paid to the quality of the signal coming from the accelerometers and the influence of environmental parameters on the measurement to prevent wrong assessment of dynamic parameters.

Signal processing

Signal processing plays a key role in extracting useful and correct information from data recorded by a network of sensors. Indeed, processing vibration signals in an appropriate way is essential for obtaining the most accurate representation of the real behaviour of the structure. In particular, signal processing refers to all the numerical and technical operations needed for translating the analog signal, corresponding to the dynamic response of the structure over time, to data suitable for subsequent analysis, such as modal identification processes.

Signal processing is particularly tricky when passing from time to the frequency domain. Indeed, vibration signals are defined as mathematical functions of time. However, they are commonly studied through mathematical models in which frequency is considered the reference variable. This conversion (time to frequency) involves a series of inevitable approximations in the transition from a digital signal to a frequency spectrum, which must be taken into account for obtaining a result without undetermined errors.

Sampling frequency

The real signal is a continuous signal in time, sampling transforms a continuous signal in time into a discrete signal [45]. So the real continuous signal, is transformed into a discrete-time signal by measuring the continuous signal function every t_s seconds , where t_s is the sampling period. Thus, simply the sampling frequency will be given by $f_s = 1/t_s$.

The sampling rate value choice, therefore, plays a key role in dynamic monitoring. It is generally a compromise between the need to have the reproduction of a sufficiently accurate discrete-time signal, and the need to limit the amount of sampled data as much as possible [45]. It is essential to know the range of frequencies of interest to be investigated so as to set the appropriate sampling frequency in accordance with the Nyquist criterion that is, the maximum frequency that can be analysed is equal to half the sampling frequency.

Aliasing

Aliasing is the effect of inadequate sampling rate for the discrete-time signal to accurately reconstruct the continuous-time signal. The effects of aliasing are shown in figure Figure 3-1. To avoid the occurrence of errors due to aliasing, it is necessary to comply with Nyquist's criterion [45].

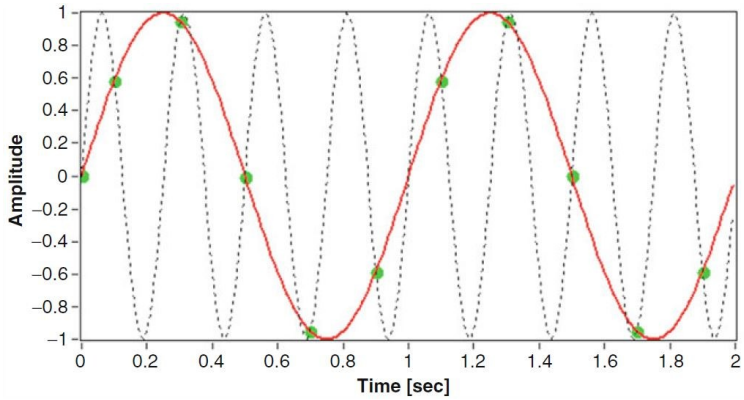

Figure 3-1: Aliasing. Real signal dashed line, signal with aliasing continuous line [45].

Correlation functions

Correlation functions play a key role in the analysis of systems based on output response only. In fact, under the assumption of stationary and random structure response, second-order statistics contain all physical information [45].

Given two sampled functions $x_k(t)$ and $y_k(t)$ of two stationary and random processes, the mean value of the two functions, regardless of time t, is given by:

$$\mu_x = E[x_k(t)] = \int_{-\infty}^{+\infty} xp(x)dx \tag{3.1}$$

$$\mu_y = E[y_k(t)] = \int_{-\infty}^{+\infty} yp(x)dx \tag{3.2}$$

The assumption of stationary and random process provides covariance functions that are also independent of time.

$$C_{xx}(\tau) = E[(x_k(t) - \mu_x)(x_k(t+\tau) - \mu_x)] \tag{3.3}$$

$$C_{yy}(\tau) = E\big[\big(y_k(t) - \mu_y\big)\big(y_k(t+\tau) - \mu_y\big)\big] \tag{3.4}$$

$$C_{xy}(\tau) = E\big[(x_k(t) - \mu_y)(y_k(t+\tau) - \mu_y)\big] \tag{3.5}$$

If the values of the mean are both equal to zero, then the covariance function coincides with the correlation function.

$$R_{xx}(\tau) = E[x_k(t)x_k(t+\tau)] \tag{3.6}$$

$$R_{yy}(\tau) = E[y_k(t)y_k(t+\tau)] \tag{3.7}$$

$$R_{xy}(\tau) = E[x_k(t)y_k(t+\tau)] \tag{3.8}$$

R_{xx} and R_{yy} are defined as auto-correlation functions of $x_k(t)$ and $y_k(t)$; R_{xy} is defined as the cross-correlation function between $x_k(t)$ and $y_k(t)$.

When the mean value is non-zero, the covariance functions and correlation functions are related by the following equations:

$$C_{xx}(\tau) = R_{xx}(\tau) - \mu_x^2 \tag{3.9}$$

$$C_{yy}(\tau) = R_{yy}(\tau) - \mu_y^2 \tag{3.10}$$

$$C_{xy}(\tau) = R_{xy}(\tau) - \mu_x \mu_y \tag{3.11}$$

Taking into consideration that two stationary and random processes are uncorrelated if $C_{xy}(\tau)$ for each τ and that this implies that $R_{xy}(\tau) = \mu_x \cdot \mu_y$ for each τ, if μ_x or μ_y is equal to zero, the two processes are uncorrelated when $R_{xy}(\tau) = 0$ for each τ.

Considering that the cross-correlation and cross-covariance functions are bounded by the following inequality:

$$\left|C_{xy}(\tau)\right|^2 \leq C_{xx}(0) C_{yy}(0) \tag{3.12}$$

$$\left|R_{xy}(\tau)\right|^2 \leq R_{xx}(0) R_{yy}(0) \tag{3.13}$$

And noting that:

$$|C_{xx}(\tau)| \leq C_{xx}(0) \tag{3.14}$$

$$|R_{xx}(\tau)| \leq R_{xx}(0) \tag{3.15}$$

The maximum value of the auto-correlation and auto-covariance functions is for $\tau = 0$; which corresponds to the mean square of the data.

$$R_{xx}(0) = E[x_k^2(t)] \quad C_{xx}(0) = \sigma_x^2 \tag{3.16}$$

In practice, sampled data can be treated as stationary if the properties evaluated over small time intervals do not vary significantly from one interval to the next. The direct estimate of correlation is given by:

$$\hat{R}_{xx}(r\Delta t) = \frac{1}{N-r} \sum_{n=1}^{N-r} x_n x_{n+r} \qquad r = 0,1,2 \ldots, m \tag{3.17}$$

It is valid for a zero-averaged stationary process sampled with a sampling period Δt. Provides the estimate of the auto-correlation at a time-lag $r\Delta t$.

Spectra density functions

Given two sampled signals $x_i(t)$ and $y_i(t)$ of finite duration T, the Fourier transform of the signals, which exists as a consequence of their finite duration [45], is given by:

$$X_i(f,T) = \int_0^T x_i(t)e^{-i2\pi ft}dt \tag{3.18}$$

$$Y_i(f,T) = \int_0^T y_i(t)e^{-i2\pi ft}dt \tag{3.19}$$

The auto- and cross-spectral density functions (PSD) are defined as:

$$G_{xx}(f) = 2\lim_{T\to\infty}\frac{1}{T}E[|X_i(f,T)|^2] \qquad 0 < f < +\infty \tag{3.20}$$

$$G_{yy}(f) = 2\lim_{T\to\infty}\frac{1}{T}E[|Y_i(f,T)|^2] \qquad 0 < f < +\infty \tag{3.21}$$

$$G_{xy}(f) = 2\lim_{T\to\infty}\frac{1}{T}E[X_i^*(f,T)Y_i(f,T)] \quad 0 < f < +\infty \tag{3.22}$$

where * denotes the complex conjugate value, since the Fourier transform of the signal returns values in the complex field.

In practical applications, the PSD can be obtained in accordance with the so-called Welch procedure [45], based on the direct transformation of the signal from the time domain to the frequency domain by FFT (Fast Fourier Transform), and then evaluating the PSD with the formulations seen above.

The PSD can be estimated by dividing the signal into n continuous segments, each of period $T = N \cdot t_s$ Where: t_s is the sampling period and N is the number of data sampled within each segment.

$$\hat{G}_{xx}(f) = \frac{2}{nNt_s}\sum_{i=1}^{n}|X_i(f)|^2 \tag{3.23}$$

The number of data sampled (N) within each segment determines the frequency resolution of the spectral density estimation. The number of segments chosen for estimation, on the other hand, affects the error in spectral density estimation.

Direct computation of the Fourier transform of the signal is very advantageous from a computational point of view. Specific strategies, however, are required to eliminate the error originating from the fact that the estimation is based on signals of finite length. A sampled signal $x(t)$ can be viewed as an unbounded signal $v(t)$ multiplied by a rectangular window in time $u(t)$:

$$x(t) = u(t)v(t) \qquad u(t) = \begin{cases} 1 & 0 \le t \le T \\ 0 & elsewhere \end{cases} \tag{3.24}$$

Thus, the Fourier transform of $x(t)$ will be given by the convolution of the transform of $u(t)$ and $v(t)$. The Fourier transform of a rectangular window is a cardinal sine function shown in Figure 3-2, with side lobes characterized by a fairly large amplitude relative to the main central lobe.

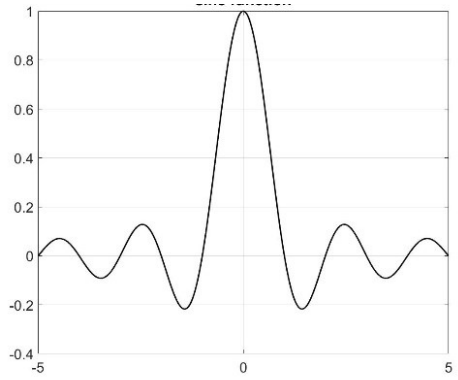

Figure 3-2: Cardinal sine function.

The large width of the side lobes allows the energy of a certain frequency to diffuse to neighboring frequencies, causing a large error in spectral energy estimation. This phenomenon is known as leakage and leads to even very significant errors in the estimation of the spectral energy density [45].

In order to eliminate the errors produced by leakage, the sampled signals are made periodic through the application of appropriate windows in the time domain, which taper the data to the edge of the time interval considered. There are different types of windows, the one used the most is the Hanning window [45] shown in Figure 3-3, obtained as.

$$u_{Hanning}(t) = \begin{cases} 1 - \cos^2\left(\frac{\pi t}{T}\right) & 0 \leq t \leq T \\ 0 & elsewhere \end{cases} \tag{3.25}$$

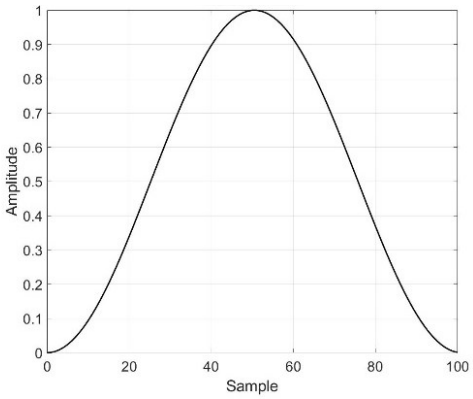

Figure 3-3: Hanning window.

The estimated auto- and cross-PSDs can be assembled within a PSD matrix. One dimension of the matrix represents the frequencies at which the spectral densities are estimated. Thus, for a given frequency value, the resulting submatrix of size N x N, where N denotes the number of channels from which the data are collected, has real values on the main diagonal and off the main diagonal complex conjugate values.

Dynamic models

Some of the most commonly used mathematical models to describe the dynamic behaviour of a structure will be described in the follow. Each model is of course approximated and subjected to limitations on its applicability.

Dynamic behaviour can be described through a set of differential equations in the time domain (Spatial Model) or through a set of algebraic equations in the frequency domain (Modal Model) [45].

Spatial Model

The dynamic behaviour of a Multi-Degree-Of-Freedom dynamic system (MDOF) traditionally is expressed through a system of linear differential equations of the second order, which in matrix form is expressed as follows:

$$[M]\{\ddot{y}(t)\} + [C]\{\dot{y}(t)\} + [K]\{y(t)\} = \{f(t)\} \tag{3.1}$$

where $\{\ddot{y}(t)\}$ $\{\dot{y}(t)\}$ and $\{y(t)\}$ are the vectors of accelerations, velocities and displacements, respectively; $[M]$ $[C]$ and $[K]$ are the mass, damping and stiffness matrices; $\{f(t)\}$ is the vector of the forcing. Equation (3.1) is valid for a linear, invariant ($[M]$, $[C]$ and $[K]$ are constant), observable system with viscous damping. It describes the dynamic behaviour of a system with N degrees of freedom, where N is the dimension of $\{y(t)\}$ and its derivatives. The equation of motion, which is coupled in this formulation, can be decoupled under the assumption of viscous damping and by using the principle of orthogonality between modes of vibration, by solving an eigenvalue problem, as shown in the next sub-section.

Modal model

Solving an eigenvalue problem, it is possible to decouple Equation (3.1) by transforming it into a set of algebraic equations, where each equation represents a Single-Degree-Of-Freedom (SDOF) system. This indicates that a MDOF system, can be analysed as a combination of several SDOF systems.

The transformation described above can be imposed through:

$$\{y(t)\} = [\Phi]\{q(t)\};\ \{\dot{y}(t)\} = [\Phi]\{\dot{q}(t)\};\ \{\ddot{y}(t)\} = [\Phi]\{\ddot{q}(t)\} \tag{3.2}$$

where the vector of displacements $\{y(t)\}$ has been transformed into a new vector $\{q(t)\}$ of which the components are referenced to modal coordinates (i.e., a new principal coordinate system in which the equations of motion are decoupled). $[\Phi]$ is the modal matrix of dimension N x N, containing on the columns the N modes of the system. Taking into account Equation (3.2), Equation (3.1) can be rewritten as:

$$[M][\Phi]\{\ddot{q}(t)\} + [C][\Phi]\{\dot{q}(t)\} + [K][\Phi]\{q(t)\} = \{f(t)\} \tag{3.3}$$

Multiplying all by $[\Phi]^T$ results in:

$$[\Phi]^T[M][\Phi]\{\ddot{q}(t)\} + [\Phi]^T[C][\Phi]\{\dot{q}(t)\} + [\Phi]^T[K][\Phi]\{q(t)\} = [\Phi]^T\{f(t)\} \tag{3.4}$$

where the matrix of modal mass $[\bar{M}]$, damping $[\bar{C}]$ and stiffness $[\bar{K}]$ are diagonal due to the orthogonality properties of the modes.

$$[\bar{M}] = [\Phi]^T[M][\Phi] \tag{3.4a}$$

$$[\bar{C}] = [\Phi]^T[C][\Phi] \tag{3.4b}$$

$$[\bar{K}] = [\Phi]^T[K][\Phi] \tag{3.4c}$$

Equation (3.4) becomes:

$$[\bar{M}]\{\ddot{q}(t)\} + [\bar{C}]\{\dot{q}(t)\} + [\bar{K}]\{q(t)\} = \{\bar{F}(t)\} \tag{3.5}$$

Dividing Equation (3.5) by the modal mass results in:

$$\ddot{q}_i(t) + 2\zeta_i\omega_i\dot{q}_i(t) + \omega_i^2 q_i(t) = \frac{\bar{F}_i(t)}{\bar{M}_i}; i = 1, 2, \dots, n \tag{3.6}$$

$$\omega_i^2 = \frac{\bar{K}_i}{\bar{M}_i};\ \zeta_i = \frac{\bar{C}_i}{2\bar{M}_i\omega_i} \tag{3.7}$$

where ω_i represents the pulsation of the i-th mode of vibration and ζ_i represents the damping of the i-th mode.

In this way, the differential equations in geometric coordinates expressed in Equation (3.1) are decoupled and transformed into n algebraic equations in modal coordinates, where each equation represents a SDOF system.

State-space model

The state-space model is used to transform the second-order problem, governed by the differential equations of motion expressed in Equation (3.1), into two first-order problems, governed by the equation of state and the observability equation, as shown below.

The equation of state can be obtained from Equation (3.1) through some mathematical manipulations. When the forcing vector $\{f(t)\}$ is factorized into the matrix $[\bar{B}]$ defining the geometrical position of the excitations and the vector $\{u(t)\}$ describing the temporal variation. Thus, Equation (3.1) can be rewritten as:

$$[M]\{\ddot{y}(t)\} + [C]\{\dot{y}(t)\} + [K]\{y(t)\} = [\bar{B}]\{u(t)\} \tag{3.8}$$

Or equivalently:

$$\{\ddot{y}(t)\} + [M]^{-1}[C]\{\dot{y}(t)\} + [M]^{-1}[K]\{y(t)\} = [M]^{-1}[\bar{B}]\{u(t)\} \tag{3.9}$$

The state vector can be defined as:

$$\{s(t)\} = \begin{Bmatrix}\{\dot{y}(t)\}\\ \{y(t)\}\end{Bmatrix} \tag{3.10}$$

Substituting Equation (3.10) into Equation (3.9) results in:

$$\{\dot{s}(t)\} = \begin{bmatrix}-[M]^{-1}[C] & -[M]^{-1}[K]\\ [I] & [0]\end{bmatrix}\{s(t)\} + \begin{bmatrix}[M]^{-1}[\bar{B}]\\ [0]\end{bmatrix}\{u(t)\} \tag{3.11}$$

From Equation (3.11) the state matrix $[A_c]$ and input matrix $[B_c]$ can be defined as:

$$[A_c] = \begin{bmatrix}-[M]^{-1}[C] & -[M]^{-1}[K]\\ [I] & [0]\end{bmatrix} \tag{3.12}$$

$$[B_c] = \begin{bmatrix}[M]^{-1}[\bar{B}]\\ [0]\end{bmatrix} \tag{3.13}$$

The state equation can be written as:

$$\{\dot{s}(t)\} = [A_c]\{s(t)\} + [B_c]\{u(t)\} \tag{3.14}$$

In the general case, the observability equation can be written as:

$$\{y_l(t)\} = [C_a]\{\ddot{y}(t)\} + [C_v]\{\dot{y}(t)\} + [C_d]\{y(t)\} \tag{3.15}$$

under the assumption that measurements of the structural response are taken at l locations and the sensors are accelerometers, velocimeters, and displacement transducers; $\{y_l(t)\}$ is the vector of measured outputs; $[C_a]$, $[C_v]$ and $[C_d]$ are the output location matrices for accelerations, velocities, and displacements. It is worth emphasizing that, while a real structure is characterized by an infinite number of DOFs, in a practical vibration test this number decreases down to a few dozens or even less. Substituting the expression of $\{\ddot{y}(t)\}$ obtained in Equation (3.9) into Equation (3.15) the following equation can be obtained:

$$\begin{aligned}\{y_l(t)\} = {} & ([C_v] - [C_a][M]^{-1}[C])\{\dot{y}(t)\} \\ & + ([C_d] - [C_a][M]^{-1}[K])\{y(t)\} \\ & + ([C_a][M]^{-1}[\bar{B}])\{u(t)\}\end{aligned} \tag{3.16}$$

The observability equation then becomes:

$$\{y(t)\} = [C_c]\{s(t)\} + [D_c]\{u(t)\} \tag{3.17}$$

$$[C_c] = \left[[C_v] - [C_a][M]^{-1}[C][C_d] - [C_a][M]^{-1}[K]\right] \tag{3.18}$$

$$[D_c] = [C_a][M]^{-1}[\bar{B}] \tag{3.19}$$

$[C_c]$ is the output matrix, $[D_c]$ is the direct transmission matrix.

The state equation (3.14) and the observability equation (3.17) define the continuous-time model in the state space. An important characteristic of this model is the existence of an infinite number of equivalent state-space representations for a given system: each one is referred to as a realization. As a consequence, the experimental test allows establishing only one of these infinite realizations.

Taking into account that the real measurements are taken in discrete time, the continuous-time model must be converted to a discrete-time model. For a given sampling period Δt, the continuous-time equations can be discretized and solved at all discrete time instants. An assumption about the behaviour of the time-dependent variables between two samples has to be made to this aim. For instance, the Zero Order Hold (ZOH) assumption states that the input is piecewise constant over the sampling period. Under this assumption the continuous-time state space model can be converted to the discrete-time state-space model:

$$\{s_{k+1}\} = [A]\{s_k\} + [B]\{u_k\} \tag{3.20}$$

$$\{y_k\} = [C]\{s_k\} + [D]\{u_k\} \tag{3.21}$$

where $\{s_k\} = \{s_k(k\Delta t)\}$ is the discrete-time state vector yielding the sampled displacements and velocities; $\{u_k\}$ and $\{y_k\}$ are the sampled input and sampled output, respectively; $[A]$ is the discrete state matrix; $[B]$ is the discrete input matrix; $[C]$ is the discrete output matrix and $[D]$ is the direct transmission matrix.

The relationships between continuous-time and discrete-time matrices are given below:

$$[A] = e^{[A_c]\Delta t} \tag{3.22}$$

$$[B] = ([A] - [I])[A_c]^{-1}[B_c] \tag{3.23}$$

$$[C] = [C_c] \tag{3.24}$$

$$[D] = [D_c] \tag{3.25}$$

Thus, the ZOH sampling does not influence these last two matrices. As an alternative, assuming a piecewise linear behaviour between two subsequent samples—First Order Hold (FOH) assumption—different, more complex relations between continuous-time and discrete-time state-space matrices can be derived *Franklin et al. 2006* [50].

The model expressed by Equation (3.20) and Equation (3.21) is a deterministic model since the system is driven by a deterministic input only. Stochastic components must be necessarily included in order to describe actual measurement data. When stochastic components are included in the model, the following discrete-time combined deterministic-stochastic state-space model is obtained:

$$\{s_{k+1}\} = [A]\{s_k\} + [B]\{u_k\} + \{w_k\} \tag{3.26}$$

$$\{y_k\} = [C]\{s_k\} + [D]\{u_k\} + \{v_k\} \tag{3.27}$$

where $\{w_k\}$ is the process noise due to disturbances and model inaccuracies and $\{v_k\}$ is the measurement noise due to sensor inaccuracies. The state equation models the dynamic behaviour of the system; the observation equation defines that part of the dynamic response of the system that can be observed in the output of the model.

In the context of OMA, structures are excited by unknown inputs. Since the information about the input $\{u_k\}$ is not available, the measured system response $\{y_k\}$ is generated only by the two stochastic processes $\{w_k\}$ and $\{v_k\}$, and the following discrete-time stochastic state-space model is obtained:

$$\{s_{k+1}\} = [A]\{s_k\} + \{w_k\} \tag{3.28}$$

$$\{y_k\} = [C]\{s_k\} + \{v_k\} \tag{3.29}$$

In the absence of $\{u_k\}$, its role is implicitly modeled by process noise and measurement noise. In particular, the process noise becomes the input that drives the dynamics of the system, while the measurement noise accounts for the direct disturbance of the response of the system. Thus, when a stochastic state-space model is adopted, the objective is the determination of the order n of the unknown system and of a realization of the matrices $[A]$ and $[C]$ from a large number of measurements of the output $\{y_k\}$ generated by the system itself. The state matrix $[A]$ transforms the current state of the system $\{s_k\}$ in the next state $\{s_{k+1}\}$, while the product of the observation matrix $[C]$ with the state vector provides the observable part of the dynamics of the system. More precisely, the response vector $\{y_k\}$ is given by the observable part of the state plus the measurement noise. The process noise and the measurement noise are both immeasurable. They are assumed to be zero mean, stationary white noise processes with covariance matrices given by:

$$E\left[\begin{Bmatrix}\{w_p\}\\ \{v_p\}\end{Bmatrix}\langle\{w_p\}^T \quad \{v_p\}^T\rangle\right] = \begin{cases}\begin{bmatrix}[Q^{ww}] & [S^{wv}]\\ [S^{wv}]^T & [R^{vv}]\end{bmatrix} & p = q\\ [0] & p \neq q\end{cases} \tag{3.30}$$

where p and q are two arbitrary time instants. The estimation of the matrices $[Q^{ww}]$, $[R^{vv}]$ and $[S^{wv}]$ is also part of the process. The assumption of white noise for $\{w_k\}$ and $\{v_k\}$ is fundamental in the proof of SSI methods [51]. Thus, if the unmeasured input includes some dominant frequency components, they appear as poles of the state matrix $[A]$ together with the eigenvalues of the system. This is equivalent to the identification of the dynamic properties of both the structure under investigation and the excitation system forming the combined system (driven by stationary, zero mean Gaussian white noise as input) that is the generally assumed objective of identification in Operational Modal Analysis (OMA).

In agreement with the stochastic framework, the system response in the state-space model is represented by a zero mean Gaussian process. The output covariance matrices are given by:

$$[R_i] = E[\{y_{k+i}\}\{y_k\}^T] \tag{3.31}$$

and they carry all the information to describe the process. A covariance equivalent model can be then defined as the estimated state-space model characterized by correct covariance and, therefore, able to describe the statistical properties of the system response. The estimator producing this model is referred to as an optimal estimator.

The state $\{s_k\}$ is also a zero mean Gaussian process described by its covariance (which is independent of the time instant k):

$$[\Sigma] = E[\{s_k\}\{s_k\}^T] \tag{3.32}$$

and it is uncorrelated with the process noise and the measurement noise:

$$E[\{s_k\}\{w_k\}^T] = [0] \tag{3.33}$$

Taking into account the previous assumptions about the noise terms, the system response and the state, mathematical manipulations of the state space equations ((3.28) and (3.29)) lead to the following fundamental relations:

$$[\Sigma] = [A][\Sigma][A]^T + [Q^{ww}] \tag{3.34}$$

$$[R_0] = [C][\Sigma][C]^T + [R^{vv}] \tag{3.35}$$

$$[G] = [A][\Sigma][C]^T + [S^{wv}] \tag{3.36}$$

$$[R_i] = [C][A]^{i-1} + [G] \tag{3.37}$$

where:

$$G = E[\{s_{k+1}\}\{y_k\}^T] \tag{3.38}$$

is the next state-output covariance matrix (covariance between the response of the system $\{y_k\}$ and the updated state vector $\{s_{k+1}\}$). The last property expressed by Equation (3.37) is very important. In fact, since the output covariance sequence $[R_i]$ can be directly estimated from the measured data Equation (3.31), its decomposition according to Equation (3.37) permits the estimation of the state-space matrices and the solution of the system identification problem.

The stochastic state-space model in Equation (3.28) and Equation (3.29) can be expressed in an alternative form through the introduction of the so-called Kalman filter [52].

For a given time instant t_k, suppose that the system matrices $[A]$, $[C]$, $[Q^{ww}]$, $[R^{vv}]$, $[S^{wv}]$ and all previous measurements $[Y^{k-1}]$ are known:

$$[Y^{k-1}] = [\{y_0\}, \{y_1\}, \cdots, \{y_{k-1}\}]^T \tag{3.39}$$

A classical estimation problem concerns the ability to optimally predict the response measurements. Thus, an optimal predictor can be defined as the one minimizing the error between the predicted and measured response. The system response can be optimally predicted if an optimal predictor of the states is available. The quality of the predictor of the states is quantified by the state prediction error:

$$\{\varepsilon_k\} = \{s_k\} - \{\widehat{s_k}\} \tag{3.40}$$

which represents the part of $\{s_k\}$ that cannot be predicted by the one-step-ahead predictor of the state vector $\{\widehat{s_k}\}$. This is defined as the conditional mean of $\{s_k\}$ given all previous measurements:

$$\{\widehat{s_k}\} = E\left[\{s_k\}[Y^{k-1}]\right] \tag{3.41}$$

In a similar way it is possible to define the innovation:

$$\{e_k\} = \{y_k\} - \{\widehat{y_k}\} \tag{3.42}$$

as the part of the measured response $\{y_k\}$ that cannot be predicted by the onestep-ahead predictor $\{\widehat{y_k}\}$. This is defined as the conditional mean of $\{y_k\}$ given all previous measurements:

$$\{\widehat{y_k}\} = E\left[\{y_k\}[Y^{k-1}]\right] = E\left[([C]\{s_k\} + \{v_k\})|[Y^{k-1}]\right] = [C]\{\widehat{s_k}\} \tag{3.43}$$

The last part of Equation (3.43) is obtained by taking into account Equation (3.29) and assuming no correlation between the measurement noise $\{v_k\}$ at instant t_k and the previous measurements $[Y^{k-1}]$. Since $\{y_k\}$ is assumed zero mean and Gaussian distributed, $\{e_k\}$ is a zero mean Gaussian white noise process.

The Kalman filter for linear and time-invariant systems relates the predictors given by Equation (3.41) and Equation (3.43) as follows:

$$\{\hat{s}_{k+1}\} = [A]\{\hat{s}_k\} + [K_k]\{e_k\} \tag{3.44}$$

$$\{e_k\} = \{y_k\} + [C]\{\hat{s}_k\} \tag{3.45}$$

The matrix $[K_k]$ is referred to as nonsteady state Kalman gain. Given the initial state estimate $\{\hat{s}_0\} = \{0\}$, the initial covariance of the state estimate $[P_0] = E[\{\hat{s}_0\}\{\hat{s}_0\}^T]$ and the output measurements $[Y^{k-1}]$, the nonsteady-state Kalman state estimate at time t_k can be obtained from the following recursive formulas providing the Kalman state estimate, the Kalman gain, and the Kalman state covariance, respectively:

$$\{\hat{s}_k\} = [A]\{\hat{s}_{k-1}\} + [K_{k-1}](\{y_{k-1}\} - [C]\{\hat{s}_{k-1}\}) \tag{3.46}$$

$$[K_{k-1}] = ([G] - [A][P_{k-1}][C]^T)([R_0] - [C][P_{k-1}][C]^T)^{-1} \tag{3.47}$$

$$\begin{aligned}[P_k] = [A][P_{k-1}][A]^T \\ + ([G] \\ - [A][P_{k-1}][C]^T)([R_0] - [C][P_{k-1}][C]^T)^{-1}([G] \\ - [A][P_{k-1}][C]^T)^T\end{aligned} \tag{3.48}$$

Equation (3.48) is also known as the Ricatti equation. The Kalman filter provides the state estimate $\{\hat{s}_k\}$ at instant t_k given the previous state estimate $\{\hat{s}_{k-1}\}$ and the measurements $\{y_{k-1}\}$. Obtained the Kalman state covariance matrix $[P_k]$ as a solution of the Ricatti equation:

$$[P_k] = E[\{\hat{s}_k\}\{\hat{s}_k\}^T] \tag{3.49}$$

the covariance of the innovation can be computed, taking into account Equation (3.45), as:

$$E[\{e_k\}\{e_k\}^T] = [R_0] - [C][P_k][C]^T \tag{3.50}$$

When the measurements are Gaussian distributed, the Kalman filter provides an optimal prediction of the states. It is worth pointing out that the Kalman state covariance is not steady at startup, since the Kalman filter experiences a transient phase. However, under certain assumptions about the state matrix ($[A]$ is stable, that is to say the real parts of all its eigenvalues are negative), the steady state is quickly reached and the state covariance matrix and the Kalman gain become constant (independent of time: $[P_k] = [P]$ and $[K_k] = [K]$). In steady-state:

$$\{\hat{s}_{k+1}\} = [A]\{\hat{s}_k\} + [K]\{e_k\} \tag{3.51}$$

$$\{e_k\} = \{y_k\} + [C]\{\hat{s}_k\} \tag{3.52}$$

The steady-state Kalman gain $[K]$ is obtained by finding the solution $[P]$ of the algebraic Ricatti equation:

$$[P] = [A][P][A]^T + ([G] - [A][P][C]^T)([R_0] - [C][P][C]^T)^{-1}([G] - [A][P][C]^T)^T \tag{3.53}$$

and substituting it into the following equation:

$$[K] = ([G] - [A][P][C]^T)([R_0] - [C][P][C]^T)^{-1} \tag{3.54}$$

Then, the covariance matrix of the innovation can be computed:

$$E[\{e_k\}\{e_k\}^T] = [R_0] - [C][P][C]^T \tag{3.55}$$

The closed form solution for the Kalman gain given by the Ricatti equation makes the Kalman filter very attractive. However, in the context of dynamic identification the system matrices $[A]$, $[C]$, $[Q^{ww}]$, $[R^{vv}]$, $[S^{wv}]$ are not known. Thus, the state sequence has to be determined directly from the output data through geometric manipulations without solving the Ricatti equation.

Operational Modal Analysis (OMA)

The term Operational Modal Analysis (OMA) refers to the class of modal identification methods based solely on response measurements. The earliest applications of OMA can be dated back to the beginning of modal testing in the

1960s. Early applications of OMA were mainly based on the analysis of Power Spectral Density (PSD) and the identification of Operational Deflection Forms (ODF). ODS is a technique used in dynamic systems analysis to visualize and analyse deformations of structures during their operation. This methodology is particularly useful for identifying how a structure is deformed under operational loads, allowing information on vibration modes.

In the 1990s, several time-domain methods in combination with correlation functions were developed and applied, leading to so-called Natural Excitation Techniques (NExT) for output-only modal verification Juang et al. [53]. NExT-type methods were very popular at the beginning of OMA. However, these methods have been progressively abandoned in favour of the more robust subspace methods [45]. The three main methods in this class are: Least Squares Complex Exponential (LSCE) method; Ibrahim Time Domain (ITD) method and Eigensystem Realization Algorithm (ERA) method. The LSCE method is basically a curve-fitting algorithm aimed at the extraction of the modal parameters from correlation functions. The LSCE method is a two-stage method for OMA, where mode shapes are estimated only in a second stage of analysis following the identification of the physical poles. The ITD method is a global modal identification procedure based on processing of all the measured correlation functions at once [45]. ERA method relies on the system realization theory [52].

In the same period began to emerge the use of ARMA models for modal parameter estimation (*Andersen et al.* [54]) firstly introduced in the late 1970s. The use of ARMA models for output-only modal identification has been attempted in the past, but they never became popular in this field due to a number of drawbacks (convergence problems, excessive computational time) [45].

New effective output-only modal identification techniques became available in the late 1990s, such as Frequency Domain Decomposition (FDD) and Stochastic Subspace Identification (SSI), which overcame the limitations of earlier techniques in dealing with closely spaced modes and noise [45].

The OMA is based on the following assumptions:

- **Linearity.** The response of the structure to a given combination of inputs is equal to the same combination of the corresponding outputs;
- **Stationarity.** The dynamic characteristics of the structure do not change over time, so the coefficients of the differential equations governing the dynamic response of the structure are independent of time;
- **Observability.** The sensor layout is designed appropriately to observe the modes of interest.

OMA is based on the dynamic response of the structure under consideration to uncontrollable and unknown loads, such as environmental and operational loads. Consequently, some assumptions about the input are necessary. If the structure is excited by white noise, that is, the input spectrum is constant, all modes are equally excited and the output spectrum contains all information about the structure. However, this is rarely the case, since the excitation has its own spectral

distribution. The modes are then weighted according to the spectral distribution of the input, and both the properties of the input and the modal parameters of the structure are observed in the response. Thus, in the general case, it is assumed that the structure is excited by unknown forces that are the output of the so-called excitation system loaded with white noise. Under this assumption, the measured response can be interpreted as the output of the combined system, formed by the excitation system and the structure under investigation in series, to a stationary Gaussian white noise with zero mean. In this context, the measured response includes information about the excitation system and the structure under investigation, but the modal parameters of the structure are preserved and identifiable, and the characteristics of the excitation system have no influence on the accuracy of the modal parameter estimates *Ibrahim et al.* [55]. Discrimination between structural modes and the properties of the excitation system is possible because the structural system has a narrow-band response and time-invariant properties, while the excitation system has a broad-band response and can have time-varying or time-invariant properties.

Classification of OMA Techniques

Different criteria can be applied to the classification of OMA methods. Each criterion highlights a specific aspect common to the different analysis methods and is useful in guiding the user toward choosing the most appropriate analysis method, depending on the advantages and limitations associated with specific assumptions and data processing procedures.

A first distinction is between parametric and nonparametric methods. If a model is fitted to the data, the technique is called parametric. These procedures are more complex and computationally demanding than nonparametric methods. However, they usually show better performance than nonparametric techniques, which are faster and easier to use. Nonparametric techniques, on the other hand, are particularly useful during field trials to get a quick view of measurement effectiveness and dynamic identification results.

The most common classification is based on the implementation domain. OMA methods based on the analysis of response time histories or correlation functions are called time domain methods. On the other hand, methods based on spectral density functions are called frequency domain methods.

Methods in the time domain are usually better conditioned than frequency domain methods. This is mainly related to the effect of frequency powers in the frequency domain equations [45].

The strategy adopted to handle noisy measurements is another discriminating aspect between time-domain and frequency-domain methods. Time domain methods are usually better suited to handle noisy data and can avoid some signal processing errors. Time domain methods exploit Singular Value Decomposition (SVD) to reject noise. Averaging, on the other hand, is the strategy adopted by frequency domain methods to handle noisy measurements.

The following paragraphs will describe the two most widely used methods for dynamic identification of civil structures:

- a parametric time domain method Covariance-Driven Stochastic Subspace Identification (SSI-Cov);
- a parametric method in the frequency domain Poly-Reference Least Squares Complex Frequency Method also known as PolyMAX.

Furthermore, these will be the two methods used in this dissertation for dynamic identification.

Covariance-Driven Stochastic Subspace Identification (SSI-Cov)

The SSI-Cov method addresses the problem of stochastic realization, that is, the problem of identifying a stochastic model of the state space from output-only data. The origin of the method can be traced back to the theory of system realization for deterministic (input-output) cases and the concept of minimum realization developed by *Ho and Kalman 1996* [56]. An in-depth discussion of system realization theory can be found in [57].

The fundamental hypothesis of this method is that the system under investigation should be observable and controllable. For the system (of order *N*) to be observable and controllable, the observability and controllability matrices of the system must have rank *N*. In practice, the order of the system is unknown, and an accurate determination of it is very complex because of the uncertainty and noise that accompanies sampling. For this reason, a conservative approach to estimating the order of the system is to overestimate the order of the system. This will cause the occurrence of nonphysical modes, so nonphysical modes must be separated from physical modes by specific expedients.

The application of the SSI-Cov method starts with determining the correlation between the outputs as follow:

$$\left[\hat{R}_i\right] = \frac{1}{N-i}\left[Y_{(1:N-i)}\right]\left[Y_{(i:N)}\right]^T \tag{3.24}$$

where $[Y]$ is the matrix of sampled data, of size l (number of sensors) by N (number of sampled data); $\left[Y_{(1:N-i)}\right]$ is the matrix obtained from the matrix of collected data ($[Y]$) by removing the last i sampled data; $\left[Y_{(i:N)}\right]$ is the matrix obtained from the matrix of collected data ($[Y]$) by removing the first i sampled data; $\left[\hat{R}_i\right]$ represents the estimation of the correlation matrix at time lag i based on a finite number of data.

The correlations estimated at different time lags are collected in the following block Toeplitz matrix (signal processing methods involving Toeplitz matrices are explored in [58]):

$$\left[T_{1|i}\right] = \begin{bmatrix} \left[\hat{R}_i\right] & \left[\hat{R}_{i-1}\right] & \cdots & \left[\hat{R}_1\right] \\ \left[\hat{R}_{i+1}\right] & \left[\hat{R}_i\right] & \ddots & \left[\hat{R}_2\right] \\ \vdots & \vdots & \ddots & \vdots \\ \left[\hat{R}_{2i-1}\right] & \left[\hat{R}_{2i-2}\right] & \cdots & \left[\hat{R}_i\right] \end{bmatrix} \tag{3.25}$$

Each correlation matrix has dimension l x l, therefore, the block matrix has dimension $l \cdot i$ x $l \cdot i$.

For the correct identification of a system of order N, the following condition must be fulfilled:

$$l \cdot i \geq N \tag{3.26}$$

In practice, the order N of the system is, of course, unknown. Thus, an estimate of the number of modes in the frequency range under observation can be obtained in several ways, for instance as the number of peaks in the trace of the PSD matrix or in the singular value plots given by the Singular Value Decomposition (SVD) of the PSD matrix. SVD is a matrix decomposition technique used in linear algebra. It allows a matrix to be expressed as the product of three matrices: an orthogonal matrix whose columns are the left singular vectors; a diagonal matrix whose elements on the diagonal are the singular values, sorted in descending order; an orthogonal matrix whose columns are the right singular vectors.

The block matrix can be decomposed through a SVD, obtaining:

$$\left[T_{1|i}\right] = [U][\Sigma][V]^T = \begin{bmatrix} [U_1] & [U_2] \end{bmatrix} \begin{bmatrix} [\Sigma_1] & [0] \\ [0] & [0] \end{bmatrix} \begin{bmatrix} [V_1]^T \\ [V_2]^T \end{bmatrix} \tag{3.27}$$

where singular values equal to zero are omitted. Considering that the output data are sampled in discrete time, so the problem under consideration is a discrete-time problem and not a continuous-time problem, singular values equal to zero will not be found, but a number of singular values equal to the size of the matrix $\left[T_{1|i}\right]$, therefore, $l \cdot i$ singular values will be obtained.

$$\left[T_{1|i}\right] = [O_i][\Gamma_i] = [U_1][\Sigma_1][V_1]^T \tag{3.28}$$

where $[O_i]$ is the observability matrix of size $l \cdot i$ x N; $[\Gamma_i]$ is the controllability matrix of size N x $l \cdot i$; $[U_1]$ of size $l \cdot i$ x N; $[\Sigma_1]$ diagonal matrix of size N x N containing in the main diagonal the singular values arranged in descending order; $[V_1]$ of size N x $l \cdot i$.

It is then possible to obtain the observability and controllability matrices by splitting the SVD into two parts, as follows:

$$[O_i] = [U_1][\Sigma_1]^{1/2}[T] \tag{3.29}$$

$$[\Gamma_i] = [T]^{-1}[\Sigma_1][V_1]^T \tag{3.30}$$

$[T]$ is a non-singular matrix that plays the role of similarity. Thus the matrix can be chosen simply equal to an identity matrix.

The output matrix $[C]$ (from the analysis in state-space) can be simply obtained from the first l rows of the observation matrix $[O_i]$.

The state matrix can be obtained by following several approaches. One of these is based on the decomposition of a block matrix offset by one time lag with respect the block matrix $[T_{1|i}]$ presented earlier, this matrix will be denoted by $[T_{2|i+1}]$.

The state matrix can then be obtained as follows:

$$[A] = [O_i]^{+}[T_{2|i+1}][\Gamma_i]^{+} \tag{3.31}$$

As an alternative, the state matrix $[A]$ can be estimated by exploiting the shift structure of the observability matrix. Pre- and post-multiplying the matrix $[T_{1|i}]$ by the invertible weighting matrices $[W_1]$ and $[W_2]$, computing the SVD of the weighted Toeplitz matrix and omitting the zero singular values yield the observability matrix *Yi and Yun 2004* [59].

Obtained the matrices $[A]$ and $[C]$ the modal parameters of the system can then be derived. In particular, from the decomposition to the eigenvalues of the matrix $[A]$. The (complex conjugate) discrete-time pairs of poles lie on the diagonal of the matrix of eigenvalues. The eigenvalues must be converted from discrete time to continuous time as follows:

$$\lambda_r = \frac{\ln(z_r)}{t_s} \tag{3.32}$$

z_r represents the eigenvalue derived from the decomposition to the eigenvalues of the discrete-time state matrix, λ_r is its continuous-time transformation.

It is then possible to derive the modal parameters of the system as follow:

$$f_r = \frac{|\lambda_r|}{2\pi} \tag{3.33}$$

$$f_{r,d} = \frac{Im(\lambda_r)}{2\pi} \tag{3.34}$$

$$\zeta_r = -\frac{Re(\lambda_r)}{|\lambda_r|} \tag{3.35}$$

f_r represents the natural frequency; $f_{r,d}$ represents the damped frequency and ζ_r represents the damping.

The eigenvectors obtained from the decomposition to the eigenvalues of the state matrix returns the modal forms for the different identified modes.

The modes identified by this procedure are not all physical modes, so physical modes should be separated from spurious modes. Only the poles that exhibit

stability between different model orders represent physical modes. The most commonly used stability criteria, as reported in [45], generally are as follows:

$$\frac{|f(n) - f(n+1)|}{f(n)} < 0.01 \tag{3.36}$$

$$\frac{|\zeta(n) - \zeta(n+1)|}{\zeta(n)} < 0.05 \tag{3.37}$$

$$1 - MAC(\{\Phi(n)\}, \{\Phi(n+1)\}) < 0.02 \tag{3.38}$$

where MAC measures the similarity between two modal shapes. It varies between 0 and 1; 0 represents no correspondence between modal shapes, 1 represents maximum correspondence between modal shapes. The MAC between two modal shapes, in the most general case of complex-valued vectors, is calculated as follows:

$$MAC(\{\Phi_1\}, \{\Phi_2\}) = \frac{|\{\Phi_1\}^H \cdot \{\Phi_2\}|^2}{(\{\Phi_1\}^H \cdot \{\Phi_1\}) \cdot (\{\Phi_2\}^H \cdot \{\Phi_2\})} \tag{3.39}$$

Plotting the poles identified for the different modal orders in a stabilization diagram, it will be possible to see that the stable poles, coincident at the frequencies proper to the system under consideration, will align.

Poly-Reference Least Squares Complex Frequency Method (PolyMAX)

The poly-reference version of the Least Squares Complex Frequency (LSCF) estimator is based on a Right Matrix Fraction Description (RMFD). The development of this method was motivated by some inherent limitations of the LSCF estimator based on the common denominator model. In particular, they concern the identification of closely spaced modes and the reduction in the quality of the fit when the polynomial model is converted to a modal model *Peeters and Van der Auweraer 2005* [60].

The method is based on the right fraction of the FRF (Frequency Response Function) matrix.

$$[H(\omega)] = [B_R(\omega)][A_R(\omega)]^{-1} \tag{3.40}$$

The FRF matrix is the matrix that relates the inputs that force the system to the system response. In the case of OMA, the system inputs are unknown, so the analogy between PSD matrix and FRF is used.

The common denominator model (also known as the scalar matrix fraction model) of the FRF, represents a special case of the right fraction of a matrix, in which the numerator is a matrix polynomial while the denominator is a polynomial characterized by scalar coefficients.

$$[H(\omega)] = \frac{[B(\omega)]}{[A(\omega)]} = \frac{\sum_{j=0}^{n}[\beta_j(\omega)]\Omega^j(\omega)}{\sum_{j=0}^{n}\alpha_j\Omega^j(\omega)} \tag{3.41}$$

In the PolyMAX method, the PSD matrix at each discrete frequency f (of size $N_{sensors}$ x $N_{sensors}$) at which it is estimated ($f = 1, \dots, N_f$) is modeled through the right fraction of the matrix [61].

$$\left[G_{YY}(\omega_f)\right] = \left[B\left(\Omega_f, [\theta]\right)\right]\left[A\left(\Omega_f, [\theta]\right)\right]^{-1} \tag{3.42}$$

where $[\theta]$ is the matrix of unknown parameters. For each output channel o ($o = 1, \dots, l$).

$$\langle B_o\left(\Omega_f, [\theta]\right)\rangle = \sum_{j=1}^{n}\langle B_{o,j}\rangle\Omega_f^j \tag{3.43}$$

Equation (3.43) represents the polynomial of the numerator matrix. $\langle\cdot\rangle$ indicates a row vector.

$$\left[A\left(\Omega_f, [\theta]\right)\right] = \sum_{j=0}^{n}[A_j]\Omega_f^j \tag{3.44}$$

Equation (3.44) represents the polynomial of the denominator matrix.

The 1 x l matrix $\langle B_{o,j}\rangle$ and the l x l matrix $[A_j]$ are the unknown parameters to be estimated. The polynomial coefficients can be collected into a single complex-valued matrix as follows:

$$[\theta] = \begin{bmatrix}[\beta_1]\\ \vdots \\ [\beta_l]\\ [\alpha]\end{bmatrix} \tag{3.45}$$

where:

$$[\beta_o] = \begin{bmatrix}\langle B_{o,0}\rangle\\ \vdots \\ \langle B_{o,n}\rangle\end{bmatrix} \tag{3.46}$$

$$[\alpha] = \begin{bmatrix}[A_0]\\ \vdots \\ [A_n]\end{bmatrix} \tag{3.47}$$

where n represents the model order.

The basis of the polynomial can be expressed in the continuous Laplace ($\Omega_f = i\omega_f$) domain or in the discrete z domain $z_f = e^{i\omega_f t_s}$. Formulation in the z domain is recommended to improve numerical conditioning.

The following formulation for the error:

$$\langle E_o(\omega_f, [\theta])\rangle = \langle B_o(\Omega_f, [\theta])\rangle - \langle \hat{G}_o(\omega_f)\rangle[A(\Omega_f, [\theta])] \tag{3.48}$$

It is adopted in order to obtain a linear least squares problem. It is defined by minimizing the following cost function:

$$\ell([\theta]) = \sum_{o=1}^{l}\sum_{f=1}^{N_f} tr\left(\langle E_o(\omega_f, [\theta])\rangle^H \langle E_o(\omega_f, [\theta])\rangle\right) \tag{3.49}$$

The minimization of the cost function expressed in Equation (3.49) corresponds to the solution of the following matrix equation:

$$[J][\theta] = [0] \tag{3.50}$$

where the Jacobian matrix $[J]$ is given by:

$$[J] = \begin{bmatrix} [\Gamma_1] & [0] & \dots & [0] & [\Upsilon_1] \\ [0] & [\Gamma_2] & \dots & [0] & [\Upsilon_2] \\ \vdots & \vdots & \ddots & \vdots & \vdots \\ [0] & [0] & \cdots & [\Gamma_l] & [\Upsilon_l] \end{bmatrix} \tag{3.51}$$

where:

$$[\Gamma_o] = \begin{bmatrix} \langle 1 & z_1 & \dots & z_1^n\rangle \\ \langle 1 & z_2 & \dots & z_2^n\rangle \\ & & \vdots & \\ \langle 1 & z_{N_f} & \dots & z_{N_f}^n\rangle \end{bmatrix} \tag{3.52}$$

$$[\Upsilon_o] = \begin{bmatrix} -\langle 1 & z_1 & \dots & z_1^n\rangle \otimes \langle \hat{G}_o(\omega_1)\rangle \\ -\langle 1 & z_2 & \dots & z_2^n\rangle \otimes \langle \hat{G}_o(\omega_2)\rangle \\ & & \vdots & \\ -\langle 1 & z_{N_f} & \dots & z_{N_f}^n\rangle \otimes \langle \hat{G}_o\left(\omega_{N_f}\right)\rangle \end{bmatrix} \tag{3.53}$$

where $\otimes$ denotes the Kronecker product. The matrices $[\Gamma_o]$ and $[\Upsilon_o]$ have dimensions N_f x $(n+1)$ and N_f x $(n+1)\cdot l$, respectively.

It is possible to show that:

$$\ell([\theta]) = \sum_{o=1}^{l}\sum_{f=1}^{N_f} tr\left(\langle E_o(\omega_f,[\theta])\rangle^H \langle E_o(\omega_f,[\theta])\rangle\right) = tr([\theta]^H[J]^H[J][\theta]) \tag{3.54}$$

It is also possible to reduce the size of the matrix equation through the definition of the normal equations:

$$[J]^H[J][\theta] = \begin{bmatrix} [R_1] & \cdots & [0] & [S_1] \\ \vdots & \ddots & \vdots & \vdots \\ [0] & \cdots & [R_l] & [S_l] \\ [S_1]^H & \cdots & [S_l]^H & \sum_{o=1}^{l}[T_o] \end{bmatrix} \begin{bmatrix} [\beta_1] \\ \vdots \\ [\beta_l] \\ [\alpha] \end{bmatrix} = [0] \tag{3.55}$$

where:

$$[R_o] = Re([\Gamma_o]^H[\Gamma_o]) \tag{3.56}$$

$$[S_o] = Re([\Gamma_o]^H[\Upsilon_o]) \tag{3.57}$$

$$[T_o] = Re([\Gamma_o]^H[\Gamma_o]) \tag{3.58}$$

$[R_o]$, $[S_o]$ and $[T_o]$ have dimensions $(n+1)$ x $(n+1)$, $(n+1)$ x $(n+1)\cdot l$ and $(n+1)\cdot l$ x $(n+1)\cdot l$; respectively.

The coefficients $[\beta_o]$ can be eliminated from Equation (3.55) by taking into account that:

$$[\beta_o] = -[R_o]^{-1}[S_o][\alpha] \tag{3.59}$$

As a final result the normalized reduced equations are obtained as:

$$2\sum_{o=1}^{l}([T_o] - [S_o]^H[R_o]^{-1}[S_o])[\alpha] = [M][\alpha] = [0] \tag{3.60}$$

where $[M]$ is a square matrix of size $(n+1)\cdot l$ x $(n+1)\cdot l$.

Parameter redundancy can be removed by requiring that a matrix of denominator coefficients be equal to the identity matrix.

$$[A_n] = [I_l] \tag{3.61}$$

where $[I_l]$ has dimension l x l.

The least squares solution is given by:

$$[\alpha] = \begin{bmatrix} -\left[M_{(1:nl,1:nl)}\right]^{-1}\left[M_{(1:nl,(nl+1):(n+1)l)}\right] \\ [I_l] \end{bmatrix} \tag{3.62}$$

The matrix $\left[M_{(1:nl,1:nl)}\right]$ is the submatrix of $[M]$ obtained from the first $n \cdot l$ rows and the first $n \cdot l$ columns; the matrix $\left[M_{(1:nl,(nl+1):(n+1)l)}\right]$ is the submatrix of $[M]$ obtained from the first $n \cdot l$ rows and the last $n \cdot l$ columns. The coefficients $[\alpha]$ and the coefficients $[\beta_o]$ can be obtained from Equation (3.59).

The roots of the denominator polynomial $\left[A\left(\Omega_f, [\theta]\right)\right]$ are the eigenvalues of the following matrix:

$$[A] = \begin{bmatrix} [0] & [I] & \cdots & [0] & [0] \\ [0] & [0] & \cdots & [0] & [0] \\ \vdots & \vdots & \ddots & \vdots & \vdots \\ -[A_0]^T & -[A_1]^T & \cdots & -[A_{n-2}]^T & -[A_{n-1}]^T \end{bmatrix} \tag{3.63}$$

The matrix $[A]$ is a square matrix of dimension $n \cdot l$ x $n \cdot l$ and models a dynamical system with $n \cdot l/2$ modes. Its z_r eigenvalues must be converted to the poles expressed in the Laplace domain as follow:

$$z_r = e^{\lambda_r \mathrm{t_s}} \Rightarrow \lambda_r = \frac{ln(z_r)}{t_s} \tag{3.64}$$

where t_s indicates the sampling period.

It is then possible to derive the frequencies, damped frequencies and damping as shown in Equations (3.33), (3.34) and (3.35), respectively.

By deriving the modal parameters for different orders of the model, the stabilization diagram can be constructed. The pole alignment indicates the modal parameters of the system under consideration.

Once the poles associated with the physical modes are selected, the LSFD estimator is used to obtain the corresponding mode shapes. The residue matrices can be calculated by minimizing the scatter between the experimentally estimated and modelled PSD matrix [62].

Considerations about modal shapes

The two OMA methods discussed above provide results in the form of complex eigenvalues and complex eigenvectors. Since mode shape estimates are in the form of complex vectors, a distinction is needed between normal modes, characterized by real-valued mode shape vectors, and complex modes.

In the case of normal (real) modes, the displacements at the various Degrees of Freedom (DOFs) reach their maximum at the same time and cross the equilibrium position at the same time. This is not the case for complex modes, where both the maximum and zero values of the modal displacements are reached at different instants of time for the various DOFs [63].

Complex modes can originate for a variety of reasons, such as gyroscopic effects, aerodynamic effects, nonlinearity, and nonproportional damping [63]. Close modes sometimes show significant complexity, too [64]. Complex modes are

often obtained from modal tests as a result of measurement noise (poor signal-to-noise ratio).

In practical applications a conversion of modes from complex to real is necessary. The simplest way to make it is to analyse the phase of each component of the mode shape and set it equal to 0° or 180° depending on its initial value. If the phase angle is in the first or fourth quadrant, it is set equal to 0°; it is set equal to 180° if it is in the second or third quadrant. Strictly, this approach should be applied only in the case of quasi-normal modes, when the phase angles differ no more than $\mp 10°$ from 0° to 180°. However, it is frequently extended to all phase angles [64].

3.4. Static Monitoring

Static parameters monitoring such as strains, deformations, tilts and displacements can provide useful information in alternative or complementary to dynamic monitoring for assessing the health of the structures.

Displacements can be handled as absolute or relative values, i.e. as georeferenced data (like GPS coordinates) or differential quantities with respect to a reference, such as the shape of the unloaded structure.

Measurement techniques include conventional surveying techniques and advanced methods *Catbas et al. 2012* [65], such as: laser Doppler vibrometers; GPS; image tracking; optical marker tracking; microwave interferometry and contacting displacement measurements.

Laser Doppler vibrometers are useful for bridge dynamic testing for both displacement and velocity measurements. The GPS system has been successfully applied for measuring displacements of large civil infrastructure, such as long span bridges, landslides and high rise structures (*Ni 2014* [66]). GPS is a promising but relatively expensive sensing technology.

Strain gauges are widely used to measure deformations of critical structural components, such as girders, reinforcement and concrete decks. The measured strain data can be used to calculate stresses and evaluate the load capacity of the structure. Only differential strain can be measured without knowing a reference value. Due to thermal effects, self-compensating type sensors are preferred in cases of temperature changes. Typical methods used to measure strain include: foil strain gauges or piezoelectric foil gauges; demountable strain gauges; strain transducers; vibrating wire gauges and fibre optic sensors, e.g. fibre Bragg grating (FBG). Electrical resistance strain gauges are cheap but often noisy. Vibrating wire strain gauges are popular because of their reliability and repeatability. The fiber-optic sensing method is an emerging technology; it can provide integrated, quasidistributed or fully distributed strain measurements.

Fibre optic sensors can be used for monitoring many physical or chemical quantities of civil structures *Glisic and Inaudi 2007* [67]. The current state of many critical concrete structures can be assessed through the detection and monitoring of cracking in concrete. So far, many optical crack sensors have been developed, such as sensing based on fibre breakage and point sensors, but they may be limited in their applications due to some disadvantages that these sensors have such as: their

degradation over time when subjected to harsh environmental conditions, which reduces their measurement reliability; nonlinear response due to the complexity of the fracture and damage accumulation mechanisms in the fibres themselves, this makes data interpretation difficult, especially if accurate calibration is not available; installation of the sensors can be complex, especially in existing structures, if the sensor is not placed properly, it may not detect damage adequately or may not be able to monitor critical areas effectively; they can be expensive, both in terms of purchase and installation. Distributed fibre optic sensors can overcome the previous limitations. They do not require prior knowledge of the crack locations, which is a major advantage over existing crack monitoring techniques *Casas and Cruz 2003* [68]. Furthermore, several cracks in concrete can be detected, located and monitored with a single fibre. The commonly used fibre optic sensors for strain sensing include Fabry– Pérot sensors and FBG sensors. Many small instruments using FBG sensors have been developed to be embedded into concrete and to monitor the strain.

In structural integrity assessment, the strain of concrete may not be as useful as the strain of tensed reinforcing bars (*Casas and Cruz 2003* [68]).

FBG sensors have a main limitation of dual sensitivity to temperature and strain. This creates a problem for sensors used for strain monitoring, since temperature variations along the fibre can lead to abnormal strain readings. To tackle the problem, reference gratings are used. Such reference gratings are in thermal contact with the structure, but do not respond to local strain changes. Thus, compensation can be achieved by subtracting the shift of the reference gratings from the shift of the sensing gratings.

Many fibre optic sensors are available for temperature monitoring. However, these sensors cannot be embedded, unless a box is used to isolate the sensor from any structural strain. Since FBG sensors have many advantages such as low self-weight, multiple measuring points, superior performance and better reliability, they can also be used for monitoring other quantities (*Casas and Cruz 2003* [68]), including inclination of structural components, vibration of the structure by measuring acceleration, force by using FBG load cells, ice detection on pavements and traffic conditions on bridges.

Direct stress measurement tools are relatively rare. Vibrating wire stress cells are often used to measure tunnel linings and concrete girder bridges (*Catbas et al. 2012* [65]). A form of stress cell that takes advantage of elastomagnetic effects can be used to monitor cable forces, such as for post-tensioning tendons and stays, main cables, and suspension bridge hangers.

Load cells are mechanical devices for measuring natural or mechanically induced loads on structures. There are different types of load cells, such as mechanical load cells (hydraulic or pneumatic), strain gauge-based load cells, and other load cells (e.g., fiber-optic and piezoresistive). Currently, the most commonly used load cells are transducers based on strain gauges and their principles.

Pressure measurement technology is similar to force measurement technology, such as using vibrating wire pressure sensors for static measurements and/or

piezoelectric pressure sensors for dynamic measurements, as described in detail in *Doebelin 1990* [69].

Inclinometers are used to measure inclination (tilt) of structural components due to distress in the system. For example, they are often utilised to assess fixity of bridge girders at supports and to monitor long term movements of bridge piers, abutments and girders. There are several types of inclinometers, including hydraulically and electrically based. The hydraulic inclinometers are simple, but not suitable for dynamic measurements.

In SHM systems for civil engineering structures, sensor measurements need to be pre-processed before their application to structural condition assessment. The preprocessing procedure includes data validation, normalisation, cleansing and fusion. First of all, the data obtained from sensing devices has to be inspected. The data validation process ensures that the sensor data possesses information relevant to subsequent analyses. For example, measured data may have anomalies because of electromagnetic interference, and it may have missing values because of disrupted transmission or a constant offset caused by drift *Farrar et al. 2003* [70]. Statistical inference techniques such as outlier analysis and novelty detection can be used in this data validation process.

Because data are often measured under varying environmental conditions, the ability to normalize the data becomes critical to the SHM strategy. For example, parameters such as tilts and/or displacements vary as temperature changes due to thermal effects.

Data cleaning is the process of selectively choosing data to accept or reject from the feature selection process for damage identification. The data cleaning process usually depends on the knowledge gained from people directly associated with data acquisition *Sohn et al. 2004* [71].

Data normalization is the process of distinguishing between changes in sensor readings caused by damage and those caused by different operational and environmental factors.

Data fusion is the process of combining information from various sensors in an effort to improve the reliability of the SHM process. The purpose of data fusion is to integrate data from a number of sensors with the goal of making a more robust and confident decision, compared to making a decision from a single sensor. In many cases, data fusion is done in a simple way, such as examining the relative information among several sensors *Sohn et al. 2004* [71]. However, in some cases, the data fusion process may require complex analysis of information from sensor arrays, such as that provided by artificial neural networks.

Static monitoring of structures requires a different approach than dynamic monitoring. In fact, if a periodic monitoring approach can be adopted for dynamic monitoring (i.e. periodically recording accelerations on the structure and deriving dynamic properties through OMA analyses). This is not possible for static monitoring because most of the quantities monitored are extremely sensitive to environmental effects (i.e., temperature or even humidity variations) and continuous, long-time monitoring is necessary to compensate this effect [72].

As low-cost sensor systems are now accessible and reliable, the amount of monitoring data is expected to dramatically increase in the next decade. Structural identification methodologies provide rational and systematic means for data interpretation. Successful data interpretation leads to the following advantages [65]:

- increased efficiency and effectiveness of visual inspection by providing information relating to what to look for and where;
- improved decision making for further instrumentation and testing;
- better estimations of structural reliability;
- better overall structural management for decisions such as replacement planning, retrofit strategies and maintenance budget expenditures;
- for civil infrastructure owners and designers, improved insight into what happens to structures during service;
- development of an integrated framework for structural condition assessment;
- increased generic knowledge of in-service structural behaviour that can be distilled into educational materials for students and practitioners;
- quantitative contribution to extending concepts of performance-based structural engineering.

Unfortunately, data interpretation challenges often create the final "bottleneck" that limits the potential of structural identification. Unlike many other areas of engineering, sensors in structural engineering rarely measure causes directly; causes must be inferred from measured effects. Even when causes can be measured in complex structures, it is almost never possible to directly measure every possible phenomenon of interest at every point.

Therefore, without appropriate methods for data interpretation, structural identification cannot provide useful engineering support. For this reason, data mining (*Tan et al. 2006* [73]; *Witten and Frank 2005* [74]) is a field of research that deals with finding patterns in data for the purpose of understanding and prediction. Data mining algorithms are particularly useful when dealing with such large amounts of data that human processing is impractical.

Static monitoring data are particularly well suited for processing with artificial intelligence tools. A comprehensive description of these techniques is provided by *Zinno et al.* [75].

3.5. Model Updating

Exponential technological development has made possible the monitoring of increasingly complex structures. In this perspective, the development of Finite Element (FE) models dedicated to interpreting monitoring data (dynamic or static) and understanding structural behaviour becomes essential.

Structural FE models designed to interpret data obtained from monitoring (SHM) should be different from the FE models that are commonly used in design. This difference is due to the different purpose for which they are developed. Design

is an activity that aims to produce safe structures; therefore, design assumptions can deviate from the actual behaviour of the structure as long as they remain on the safety side. Interpretation of monitoring data is, on the contrary a simulation of what is occurring in reality, therefore many physical phenomena such as tensile strength of concrete and masonry and friction in the bearings can be commonly neglected in design whereas may play a crucial role in the interpretation of monitoring results.

In recent decades, extensive research has been conducted on updating FE models using vibration measurements (*Mottershead and Friswell 1993* [76], *Friswell and Mottershead 1995* [77]). Existing model updating methods can be classified into two major groups: direct methods and iterative methods. Direct methods directly update the elements of the stiffness and mass matrices and are a one-step procedure (*Kabe 1985* [78]). These methods allow the updated analytical model to reproduce the measured modal vibration data, but do not guarantee that the updated model truly represents the physical properties of the actual structure in question. On the other hand, iterative parameter updating methods adopt parameter sensitivity to update the analytical model (*Link 1999* [79], *Modak et al. 2002* [80], *Mottershead et al. 2011* [81]). Such methods set the errors between analytical and measured data as an objective function and try to minimize the chosen objective function by adjusting the preselected set of physical parameters of the analytical model in question. Compared with direct methods, iterative methods, such as sensitivity-based methods and the dynamic perturbation method, are more popular because they can be conveniently implemented in existing FE codes (*Chen and Maung 2014* [82]). In addition, there is a readily available physical explanation for each structural update parameter, which is typically associated with the stiffness and mass of the analytical model element.

For a sensitivity-based update approach, its performance depends largely on the selection of an objective function and constraints, structural update parameters, and optimization techniques (*Brownjohn and Xia 2000* [83]). The objective function can be considered as the residuals between the measured modal data and the associated predictions of the initial FE model, e.g., the difference between the frequencies and mode shape measurements. The selection of structural parameters to be updated requires considerable physical knowledge of the structure being tested, so as to properly characterize the physical properties at the local level, for example in the connections of structural elements (*Palmonella et al. 2005* [84]). Bayesian updating procedures can be adopted to reduce the influence of uncertainties in structural parameters and vibration measurements and to improve the correlation between the tested structure and the associated FE model (*Simoen et al. 2013* [85]). Advanced global optimization techniques, such as the simulated annealing method and genetic algorithm, combined with sensitivity analyses, are powerful tools. These techniques are often used to obtain globally optimized structural update parameters for complex structural systems to avoid local optimal solutions. However, sensitivity analysis and optimization techniques used in sensitivity-based model updating procedures may not work well, as they require considerable computational effort in the model updating process. These problems arise especially in cases where the number of structural parameters chosen to be

updated is large and the discrepancy between the initial FE model and the actual structure tested is significant.

Numerical models present uncertainties. Modelling uncertainties can be generally divided into the uncertainties of the model parameters, the model structure, and the model code [86]. Uncertainty in model parameters is usually due to incorrect assumptions about model parameters, such as material properties. Uncertainty in the model structure results from incorrect assumptions about the mechanical properties and physical behaviour of the structure; in fact, modelling is always a simplified representation of reality that carries with it a number of simplifications. Such erroneous assumptions arise from various idealizations and simplifications of the structure [87].

A comprehensive overview of model updating is provided by Ereiz et al. [88].

Generally, the most impactful parameters in the calibration of simulation models are:

- The deformability of the foundation system. In structural models for safety assessment of structures, the foundation system is often considered to be an infinitely rigid constraint. This assumption, which may be acceptable in models for safety assessment, is not representative of the actual behaviour of the structure [89].
- The stiffness of the bearing devices between deck and substructure (piers/abutments). These devices play a key role that governs structural behaviour. Calibrating their stiffness is not a trivial task, as they are subject to different deterioration phenomena that greatly change their initial stiffness
- The stiffness of the materials [91].

The effect of these parameters can be considered individually in order to understand their influence on structural behaviour, but in reality, it is necessary to perform model updating by considering all parameters together. For this reason, the complexity of model updating can be considerable, and genetic algorithms are an excellent application solution [92].

Commonly, model updating is performed based on the dynamic response of the real structure; using the modal parameters obtained from the OMA analyses as the benchmark of the structure. Another approach may be to calibrate the numerical model according to the response of the structure under static load tests [93].

Optimization problem

The optimisation problem is often associated with the search for the global minimum or maximum, i.e. the search for the optimal solution among all available alternatives. Optimisation problems comprise three elements [94].

- **Decision variables**. These are the variables whose optimal configuration is to be determined. They are determined by the analysts a priori;

- **The objective function**. This indicates the relationship between the decision variables and the function whose values are to be maximised or minimised; it is the link between the problem and the solution. Consequently, if the objective function could be described by the equation $y = f(x)$, it is necessary to develop an approach that aims to identify the value of x that will result in the minimum or maximum value of y;
- **The admissible set**. Corresponds to the set of possible alternatives and/or combinations that the analyst can perform. The admissible set can be reduced to a subset of the entire space if constraints are present, otherwise it will consist of the entire n-dimensional space of real vectors. In this case it will be referred to as 'unconstrained optimisation'.

The optimisation problem can be described as a problem of finding the maximum or minimum value of the objective function in relation to the decision variables and the constraints it is subject to.

It is also necessary to know how solutions depend on the assumptions or data assigned a priori. Thus, the concept of sensitivity analysis was born, i.e. the ability to assess the effects of the chosen parameters to detect any outliers or erroneous values and to define optimisation strategies [95]. Sensitivity analysis discusses 'how' and 'how much' changes in the parameters of an optimisation problem change the optimal value of the objective function and the point at which the optimum is reached [95]. This approach improves the goodness-of-fit of the model by providing an understanding of how the model responds to input-related changes.

Sensitivity analysis is an aid, not a solution to the optimisation problem. Therefore, two optimisation techniques in particular are used to find the global minimum: the gradient method and heuristic methods.

- **Gradient method**. This is a technique that involves calculating the direction of maximum increase of the analysed function and moving in that direction until the minimum is reached.
- **Heuristic methods**. These methods facilitate a more efficient exploration of the search space and increase the probability of finding the global minimum.

The objective function

The objective function is a function describing the effectiveness of the FE model in replicating the characteristics of the real structural system. It represents the criterion by which the FE model is to be optimised, and can be defined as:

$$F = (p_m, p_c, p_s) \tag{3.65}$$

where p_m, p_c, p_s represent the decision variables, i.e. material properties, structure characteristics and node characteristics respectively. Several well-defined steps make up the optimisation process. First, it is necessary to define the model and the variables that characterise it. Next, the objectives to be achieved should be

established, i.e. the objective functions of the problem. Once these aspects have been defined, the FE model for the simulation is created and the analysis is performed. The results obtained allow the system to be validated or changed iteratively until the optimal solution is derived. In summary, the optimisation problem requires a precise characterisation of the issue addressed and a detailed evaluation of the possible solutions in order to determine the most advantageous one.

Genetic algorithms

Genetic algorithms are based on Darwin's evolutionary principle of 'the strongest creature survives'. Darwin demonstrated that the survival of any organism can be maintained by genetic heredity, such as reproduction, interbreeding and mutation. Therefore, Darwin's theory of evolution has been used by the computational optimisation algorithm to search for a solution to any real-world optimisation problem in a natural way [96].

Inspired by the Darwinian theory of evolution, the genetic algorithm performs analyses on a population of individuals, from which it extracts the set of probable solutions to a specific problem. Specifically, the algorithm is concerned with selecting the best group of individuals for each generation, which are then subjected to a series of genetic operators. The combination of these operations, including breeding, crossing and mutation, gives rise in return to a new generation. A set of elements is thus formed that progressively approaches the optimal solution to the problem. The mechanism of evolution is analogous to what happens in nature, where each species tends to preserve the best characteristics for its own survival and pass them on to the next generation. The choice of the best individuals takes place through the selection phase, which leads the algorithm, iteration after iteration, to search for optimal solutions.

The initial phase of the algorithm involves the random creation of a population of individuals, so the string comprising the initial variables of the problem, known as the genotype, will be composed of a series of randomly generated values. The next step in the process involves the evaluation of each individual. This is done by means of the fitness function or an objective or adaptation function. The fitness function can be single-objective or multi-objective and allows individuals within the population to be examined by analysing them according to one or more performance levels. A score, also called a rank, is assigned to each solution based on the quality of the solution found. The algorithm ends when one of the predefined termination conditions is met. These include determining the optimal solution, completing the maximum number of iterations specified by the programmer or achieving population uniformity. The latter is expressed through a convergence indicator that expresses the genetic variation present between individuals of the same genotype. The algorithm will therefore terminate when there is almost no progress in evolution. If this is negative, a new analysis is carried out.

The evaluation of each individual, performed by the fitness function, plays a very important role as the actual solution of each analysis can only be determined

if the correct scoring of each element is performed. Otherwise, the problem may converge to a local minimum, so that the exact solution may be found more quickly, or excessive variability may occur between individuals in the same population. Once individuals are chosen from the set of potential solutions, they are subjected to genetic operators in order to retain the best genes and optimise the remainder. Crossover, similarly to natural reproduction, crosses the genetic code of two individuals (parents) returning in output new elements (children) with combined characteristics. Merging can occur at one or more points in the code Figure 3-4. Mutation, as the term suggests, changes the attributes of a solution while preserving its initial genetic characteristics Figure 3-5. The combination of these two techniques makes it possible to preserve the best genes of the parents or the individual itself, and to modify the rest in such a way that they perform better overall. The population of the new generation is again examined, evaluated and iteratively manipulated until the a priori defined termination conditions are reached.

The calibration of the genetic algorithm is important in order to derive the optimal solution in the shortest possible time. The set of possible solutions is often very large, so that the use of the wrong number of generations and individuals can lead to local convergences, preceding the global one. Therefore, it is initially necessary to run several trials to calibrate the algorithm to the required problem.

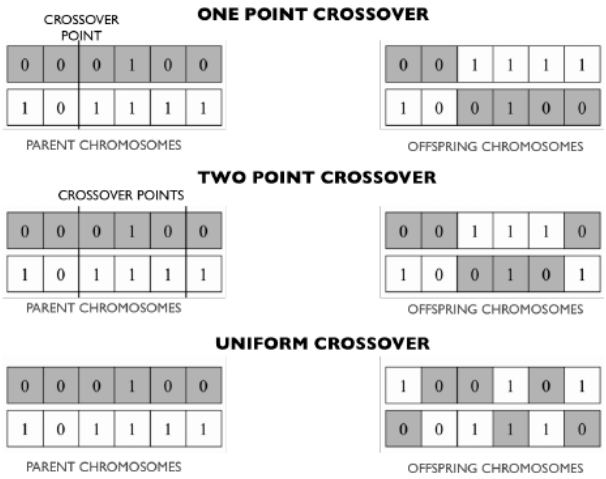

Figure 3-4: Genetic crossover operator.

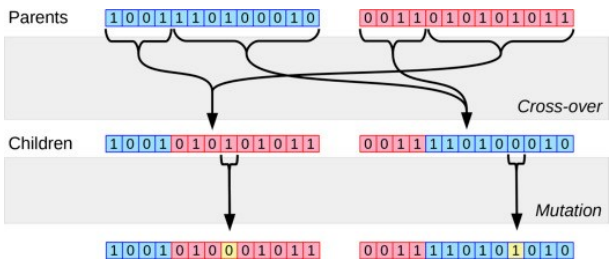

Figure 3-5: Genetic mutation operator.

Chapter 4

Case study: Safety assessment of existing bridge decks through different approaches

4.1. Chapter introduction

The safety assessment for bending and axial actions of two decks on an Italian highway is conducted using five different approaches. This study focuses exclusively on the decks; the assessment of other structural components—such as piers—is excluded, as these elements were retrofitted during the service life of the structure. Consequently, the decks are considered the most vulnerable structural components. Additionally, the analysis is limited to bending and axial actions, as modelling brittle failure mechanisms, such as shear, involves significantly greater uncertainties—particularly in nonlinear analyses—than those associated with axial behaviour.

In the first approach the decks are modelled according to Courbon theory [97]. The safety assessment is performed by comparing the design resisting and acting moments M_{Rd} and M_{Ed} in the section of interest. therefore, through an approach based on a local analysis using partial safety factors to calculate the design values [15].

In the second one the decks are modelled with an elastic girder finite element (FE) model and the safety assessment is performed as in the first case.

In the last three cases, the decks are modelled through a 3D non-linear finite element (NLFE) model, and the safety assessment is performed using the three global safety formats based on global analyses discussed in Section 2.5 of Chapter 2. A comparison of different safety formats, but on structures of lower complexity, is provided by Castaldo et al. [98].

As discussed in Section 2.3, according to the Italian Guidelines for Safety Assessment of Existing Bridges [9][10] the performance class of the existing bridge can be Code-compliant, Fully-operational or Partially-operational. In this study, the decks will be assessed referring to the Code-compliant performance class. It means that the safety level required to the existing bridge should be the same that is adopted for realization of new ones.

Lower partial safety factors are allowed in case of existing structures because the cost of safety measures becomes higher compared to the design, as discussed in Section 2.2 according to fib Bulletin 80 [18].

The proposed approach, however, is not directly applicable for cases of bridges subjected to active deterioration processes. In the absence of specific information on the state of deterioration of the decks or on any damage already present, a reduction of the partial factors is not followed.

4.2. Decks description and material characterisation

The first viaduct under investigation belongs to an Italian highway, built in the 1950s, some pictures of the real structure are shown in Figure 4-1. Its profile is shown in Figure 4-2. It is composed of six girder decks supported by 3D-framed piers.

There are two types of decks: 50 m long decks supported by the hammerhead of the taller piers and 20.8 m long decks supported directly by the shorter piers. In this study, the safety assessment is carried out for both types of decks.

Both decks types are girders with cast-in-situ reinforced concrete slab, prestressed reinforced concrete (PRC) longitudinal beams and PRC transverse beams. Each girder deck is 11 m wide and counts four longitudinal beams. The cast-in-situ RC slab is 10 cm thick. Details of the girder decks are shown in Figure 4-3 for the 20.8 m deck and in Figure 4-4 for the 50 m deck, respectively.

The spacing between the longitudinal beams is 2.80 m for both decks. All longitudinal beams have I shaped cross-section in both decks: they are 3 m deep in the 50 m deck with two half joints at the ends, while in the 20.8 m deck they are 1.3 m deep.

The PRC transverse beams are present at the ends and thirds of the span for the 20.8 m deck, while they have a regular spacing of 7.14 m for the 50 m deck.

Figure 4-1: Pictures of the viaduct.

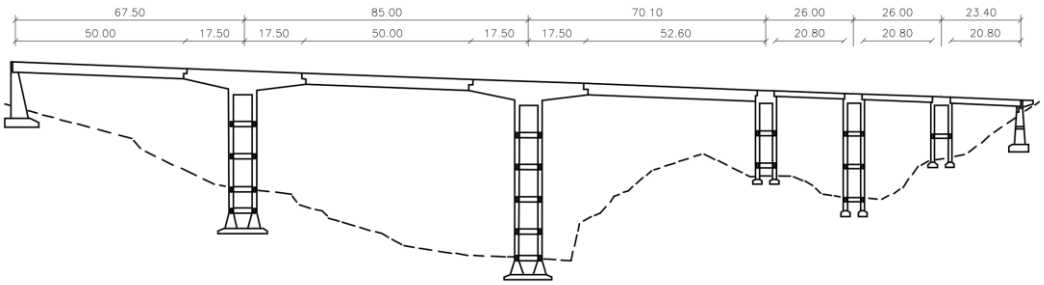

Figure 4-2: viaduct profile. Measures in metres.

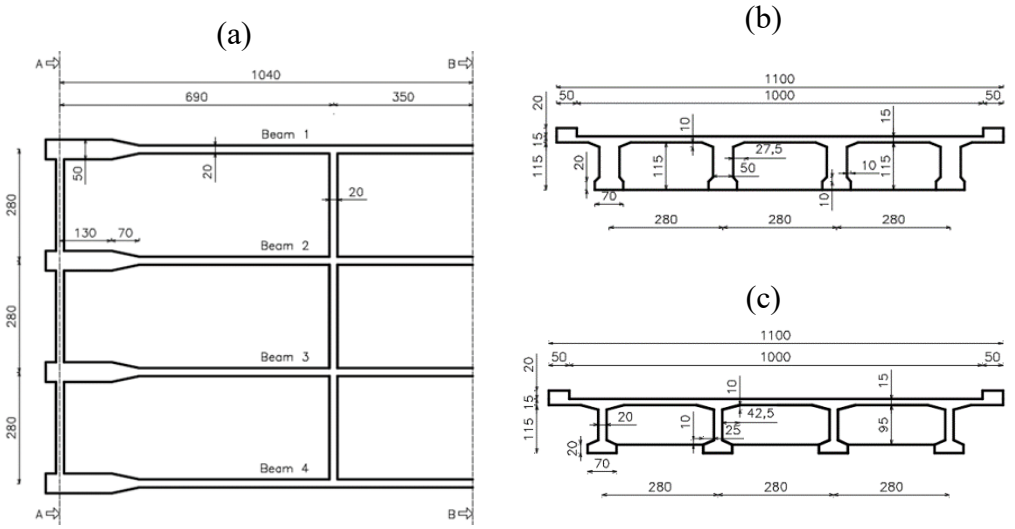

Figure 4-3: geometry of the 20.8 m deck: (a) planimetry; (b) cross section A-A; (c) cross section B-B. Measures in centimetres.

Reinforcement arrangement description

Ordinary and prestressing reinforcement are adopted in the realization of the girder decks, details on the arrangement of the reinforcement are provided in Annex A. Grouted post-tensioned tendons are used for the realization of the PRC beams of both the girder decks.

In the 20.8 m deck, ordinary reinforcement is present in the same amount for all four longitudinal beams. The amount of prestressing reinforcement changes between the beams, since Beam 1 is on the side of the low-speed traffic lane, while Beam 4 is on the side of the high-speed traffic lane. At the time of the construction of the deck, it was common in Italy to reduce the amount of prestressing as much as possible for economic reasons and many decks were designed without considering a possible inversion of the traffic lanes (e.g. for maintenance reasons). This deck is therefore not perfectly symmetrical with respect to the barycentric longitudinal axis. Details on the amount of prestressing reinforcement for the 20.8 m deck are given in Table 4-1.

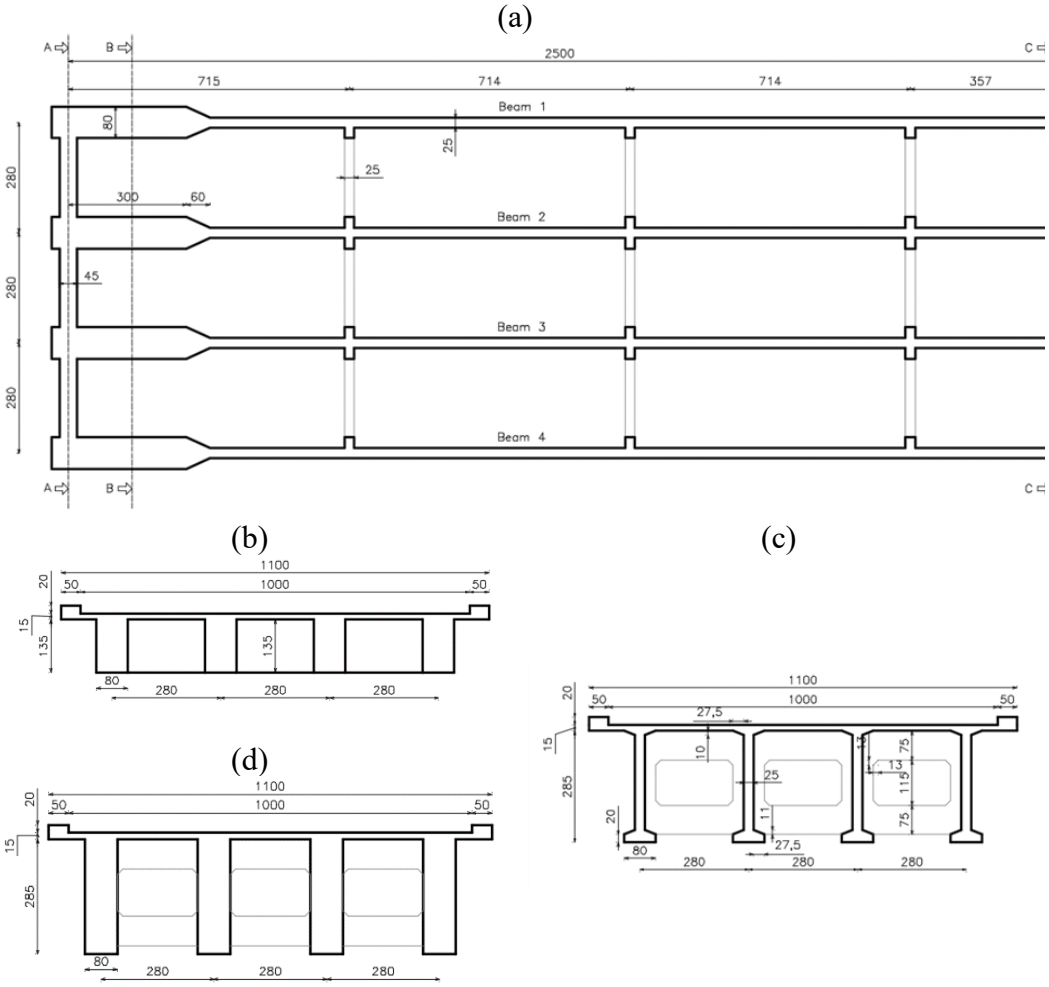

Figure 4-4: geometry of the 50 m deck: (a) planimetry; (b) cross section A-A; (c) cross section C-C; (d) cross section B-B. Measures in centimetres.

In the 50 m deck, ordinary reinforcement is the same for all four longitudinal beams. The amount of post-tensioning tendons is the same for the two edge beams and the two internal beams. Details of the quantity of post-tensioning tendons for the 50 m deck are given in Table 4-2. It follows that the 50 m deck is symmetrical with respect to the barycentric longitudinal axis.

Post-tensioned tendons are also present in transverse beams for both the decks. Two straight 16Φ6 tendons are present in each transverse beam, vertically centred in the web.

Material properties characterisation

Concrete, ordinary reinforcement and prestressing reinforcement specimens were taken in situ from the bridge decks in order to characterise their properties.

With regard to the tests on the concrete specimens, the maximum stress reached in the compression test was measured on sixteen cylindrical cores with a diameter of 63 mm or 85 mm: 6 taken from the 20.8 m deck (3 from the longitudinal beams and 3 from the slab); 10 taken from the 50 m deck (5 from the longitudinal beams and 5 from the slab). The maximum stress reached by the compression test was related to the compressive strength of the associated cylinder according to [99]-[100] taking into account the actual slenderness of the specimens. All other

fundamental properties of the concrete were derived from the compressive strength of the cylinder following the formulations proposed in *Fib* Model Code 2010 [11] and EN 1992-1-1 [21]. The values are shown in Table 4-3 and Table 4-4.

Table 4-1: Details of the post-tensioned tendons in the 20.8 m deck.

	Beam 1	Beam 2	Beam 3	Beam 4
Tendon 1	42 Φ 6	42 Φ 6	42 Φ 6	42 Φ 6
Tendon 2	42 Φ 6	42 Φ 6	42 Φ 6	42 Φ 6
Tendon 3	42 Φ 6	14 Φ 6	14 Φ 6	30 Φ 6
Total Area [mm²]	3563	2771	2771	3223

Table 4-2: Details of the post-tensioned tendons in the 50 m deck.

	Beam 1	Beam 2	Beam 3	Beam 4
Tendon 1	42 Φ 6	42 Φ 6	42 Φ 6	42 Φ 6
Tendon 2	42 Φ 6	42 Φ 6	42 Φ 6	42 Φ 6
Tendon 3	42 Φ 6	42 Φ 6	42 Φ 6	42 Φ 6
Tendon 4	42 Φ 6	42 Φ 6	42 Φ 6	42 Φ 6
Tendon 5	42 Φ 6	42 Φ 6	42 Φ 6	42 Φ 6
Tendon 6	42 Φ 6	20 Φ 6	20 Φ 6	42 Φ 6
Tendon 7	42 Φ 6	42 Φ 6	42 Φ 6	42 Φ 6
Tendon 8	42 Φ 6	42 Φ 6	42 Φ 6	42 Φ 6
Tendon 9	20 Φ 6	[-]	[-]	20 Φ 6
Total Area [mm²]	10066	8878	8878	10066

For the characterisation of the ordinary reinforcement, twenty specimens were taken from Φ8 and Φ12 steel bars. Finally, with regard to the prestressing reinforcement, thirty-two prestressing steel specimens were taken from post-tensioned tendons. The values are shown in Table 4-5 and Table 4-6.

The rheological characteristics of concrete (creep and shrinkage) and the relaxation factor of the steel were assumed from the literature [11],[21] as no specific tests were available. Furthermore, since the application of the ECoV safety format also requires an analysis performed with the characteristic values of material properties, these were obtained following the procedure proposed in [101] and Annex D of EN 1990 [15] assuming a lognormal distribution of material properties. The values are also shown in Table 4-3 - Table 4-6.

Table 4-3: Mechanical properties of concrete related to the 20.8 m deck.

Description	Symbol	Mean value	CoV	Characteristic value
Cylindrical compressive strength [MPa]	f_{cc}	36.0	12.3%	27.3
Tensile strength [MPa]	f_{ct}	2.8	*	2.2
Elastic modulus [MPa]	E_c	32945	*	30500

* Value of CoV not available. The other mechanical parameters were calculated with formulations according to [11].

Table 4-4: Mechanical properties of concrete related to the 50 m deck.

Description	Symbol	Mean value	CoV	Characteristic value
Cylindrical compressive strength [MPa]	f_{cc}	42.2	19.7%	28.5
Tensile strength [MPa]	f_{ct}	3.2	*	2.2
Elastic modulus [MPa]	E_c	34730	*	30483

* Value of CoV not available. Creep and shrinkage parameters were calculated with formulations according to [11].

Table 4-5: Mechanical properties of ordinary reinforcement.

Description	Symbol	Mean value	CoV	Characteristic value
Yield tensile strength [MPa]	σ_{ys}	540	6.4%	482
Ultimate tensile strength [MPa]	σ_{su}	722	6.4%	643
Ultimate strain [-]	ε_{su}	0.105	*	0.095
Elastic modulus [MPa]	E_s	200000	*	200000

* Value of CoV not available.

Table 4-6: Mechanical properties of post-tensioned tendons.

Description	Symbol	Mean value	CoV	Characteristic value
Yield tensile strength [MPa]	σ_{yp}	1618	6.4%	1445
Ultimate tensile strength [MPa]	σ_{up}	1679	6.4%	1494
Ultimate strain [-]	ε_{up}	0.05	*	0.045
Elastic modulus [MPa]	E_{sp}	195000	*	195000

* Value of CoV not available. Relaxation parameters were calculated with formulations according to [11].

For safety assessment, the design values of materials properties are derived according to [10] as follows:

$$f_d = min\left(\frac{f_m}{FC \cdot \gamma_m}; \frac{f_k}{FC}\right) \tag{4.1}$$

where f_d is the design value of the material property, f_m and f_k are its mean value and characteristic value respectively; γ_m is the partial safety factor for material strengths and FC is the confidence factor, which depends on the 'knowledge level' [10].

According to Italian standards [24], there are three levels of knowledge. The first (i.e. 'knowledge level 1') is to be used when information on material properties can only be found from the original calculation reports; in this case, the value of the confidence factor is 1.35. The second (i.e. 'knowledge level 2'), should be used when information on the material properties can be obtained from the original calculation report and limited on-site investigations; in this case, the value of the confidence factor is 1.2. The third (i.e. 'knowledge level 3'), should be used when

information on the strengths of materials can be obtained from the original calculation report and from extensive in-situ investigations; in this case, the value of the confidence factor is 1.0. In the case of bridges, the Italian standards [24] do not specify a specific number of experimental tests that must be available in order to fall within 'knowledge level 2' or 'knowledge level 3', and the choice of knowledge level is based on the judgment of engineers. In this case study, 'knowledge level 3' is assumed for concrete and ordinary reinforcing steel, but 'knowledge level 2' is conservatively considered for prestressing reinforcement, due to uncertainties resulting from the dispersion of laboratory test results.

On the basis of the formulation given in Equation (4.1), the following design values of the material properties are obtained: $f_{cd} = 23.9\ MPa$ for the concrete of the 20.8 m deck; $f_{cd} = 28.1\ MPa$ for the concrete of the 50 m deck; $f_{yd} = 470\ MPa$ and $f_{td} = 628\ MPa$ for the ordinary reinforcement of both decks; $f_{yd} = 1172\ MPa$ and $f_{td} = 1216\ MPa$ for the prestressing reinforcement of both decks.

Safety assessment requires knowledge of the mechanical properties of materials. Sampling campaigns (concrete cores, samples of reinforcement bars, strand wires and prestressing cables) are carried out to measure the statistical distribution of the strengths of the materials of which the structure is made.

It is clearly evident that the greater the extension of these campaigns, the better the accuracy of the data obtained. On the other hand, the effect of the choices made by the practitioners who assess the structure in clustering the data obtained from the inspection campaigns is less evident. For example, if there are three decks in a bridge which were designed to be made of the same concrete, but different clusters of strength values are obtained by the tests for the three decks, the practitioner may decide either to group all the data into a single cluster and obtain an average strength and high dispersion, or to create three clusters relating to the three decks obtaining different average strengths and lower dispersions. Nevertheless, the numerosity of the three clusters will be lower than that of the single cluster and consequently the estimation of resistance characteristic values for the lower numerosity clusters will be more penalising.

Table 4-7: Difference in mechanical properties depending on the cluster.

		Single cluster	**Cluster for 20.8m deck**	**Cluste for 50m deck**
Average yield stress [MPa]	f_{ym}	540	540	540
Average ultimate strength [MPa]	f_{tm}	722	716	725
Characteristic yield stress [MPa]	f_{yk}	482	449	498
Characteristic ultimate stress [MPa]	f_{tk}	643	601	660
Partial safety factor [-]	γ_s	1.15	1.15	1.15
Confidence factor [-]	FC	1.0	1.0	1.0
Design yield stress [MPa]	f_{yd}	470	449	470
Design ultimate stress [MPa]	f_{td}	628	601	630

An example is given in Table 4-7. A single cluster is considered for ordinary reinforcement steel for the 20.8m and 50m decks. An alternative choice could be to divide the same rebar test data into two clusters: one for the 20.8m decks and one

for the 50m decks. The choice of two different clusters did not lead to substantial variations in the mean material properties, but did lead to differences in the estimation of the characteristic properties and consequently in the design strengths. In fact, the calculation of the characteristic properties depends on the numerosity of the cluster, with small clusters being penalised.

Table 4-8: Mechanical properties of prestressing reinforcement specimens.

Position of the specimen	Specimen number	Yield stress [MPa]	Ultimate stress [MPa]
Beam 1 of the 50m deck	1	1515.3	1558.4
	2	1513.0	1564.3
	3	1513.4	1568.1
	4	1518.2	1561.5
	5	1511.8	1557.0
	6	1510.3	1560.7
	7	1509.6	1559.6
	8	1516.1	1567.5
Beam 1 of the 20.8m deck	9	1721.6	1794.5
	10	1719.8	1790.2
	11	1721.3	1788.1
	12	1725.9	1790.7
	13	1721.5	1788.2
	14	1722.9	1792.7
	15	1727.8	1787.7
	16	1726.0	1783.9
Beam 4 of the 20.8m deck	17	1519.9	1578.9
	18	1517.6	1580.5
	19	1518.5	1572.1
	20	1519.9	1580.7
	21	1512.6	1579.2
	22	1516.3	1572.3
	23	1517.9	1576.1
	24	1518.2	1573.5
Beam 4 of the 50m deck	25	1715.0	1789.3
	26	1719.5	1784.3
	27	1714.2	1788.1
	28	1715.6	1790.5
	29	1711.8	1788.0
	30	1712.2	1783.7
	31	1717.6	1779.7
	32	1716.2	1780.3

Another example is given in Table 4-8 and Table 4-9. For the prestressing reinforcement 32 specimens of steel were taken from the structure: 8 from Beam 4 of the 50m deck; 8 from Beam 4 of the 20.8m deck; 8 from Beam 1 of the 50m deck and 8 from Beam 1 of the 20.8m deck. From the results shown in Table 4-8, there would appear to be two classes of steel strength: a class with average yield strength around 1515 MPa and a class with average yield strength around 1715 MPa. Both classes are present on both decks; therefore, the use of two different steels on the two different decks cannot be assumed. In addition, there are no indications from

the deck design documentation to suggest the use of different classes of prestressing steel. The practitioner is therefore faced with the choice of clustering data from experimental tests on prestressing steel: two choices can be made:

1. group all the data into a single cluster;
2. group the data with an average yield strength of 1719 MPa (Cluster A) and the data with an average yield strength of 1515 MPa (Cluster B) separately.

The results of the two choices are shown in Table 4-9 . In all three clusters, a knowledge level 2 is assumed, i.e. a confidence factor FC=1.2, due to the lack of knowledge of the actual use of two different prestressing steel strength classes.

It can be seen that by separating the two resistance classes, the coefficient of variation of the cluster in both cases (i.e., Cluster A and Cluster B) is very low, less than 1%. Considering a single cluster, the value of the coefficient of variation is above 6%. The low statistical dispersion of Cluster A and Cluster B leads to characteristic resistance values very close to the mean value; on the other hand, the statistical dispersion of the single cluster leads to a considerable discrepancy between mean resistance value and characteristic resistance value.

Cluster A provides the highest average, characteristic and design resistance values. Cluster B provides the lowest average, characteristic and design resistance values. The single cluster provides average, characteristic and design resistance values between Cluster A and Cluster B.

In this case it was decided to use the results provided by the single cluster as there was no precise indication of the actual use of two different strength classes of prestressing steel.

Table 4-9: Difference in mechanical properties depending on the cluster for prestressing reinforcement.

		Single cluster	**Cluster A**	**Cluste B**
Average yield stress [MPa] (CoV)	f_{pm}	1618 (6.42%)	1719 (0.29%)	1516 (0.22%)
Average ultimate strength [MPa] (CoV)	f_{ptm}	1679 (6.63%)	1788 (0.23%)	1569 (0.53%)
Characteristic yield stress [MPa]	f_{pk}	1445	1711	1510
Characteristic ultimate stress [MPa]	f_{ptk}	1494	1780	1555
Partial safety factor [-]	γ_s	1.15	1.15	1.15
Confidence factor [-]	FC	1.2	1.2	1.2
Design yield stress [MPa]	f_{pyd}	1172	1246	1099
Design ultimate stress [MPa]	f_{ptd}	1216	1296	1137

4.3. Description of structural models for linear and non-linear analyses

In this section, a description of the structural models used for assessment under both the local and global approach is presented.

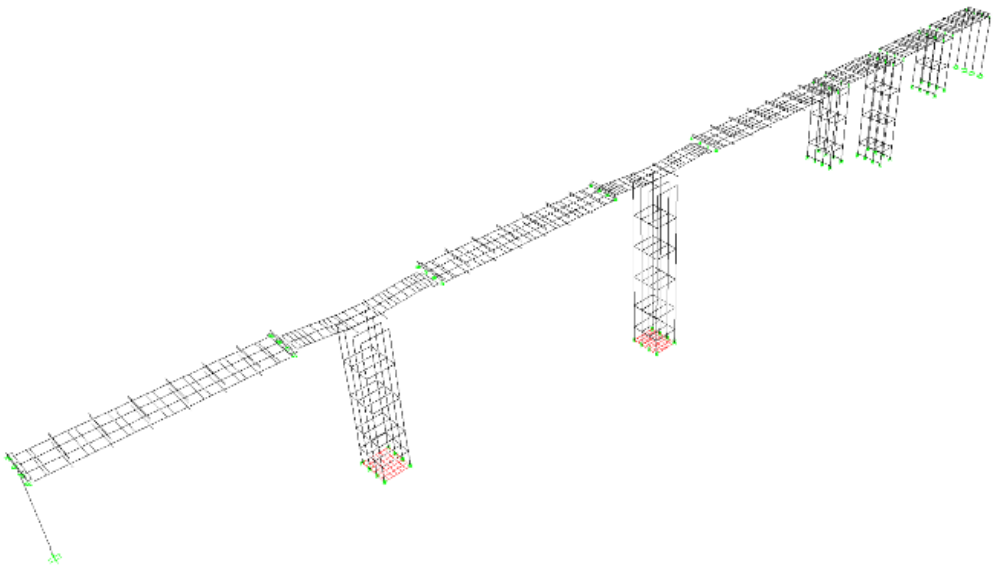

Figure 4-5: Linear elastic FE model.

The two decks are modelled using linear elastic and non-linear analyses. In detail, the following three different modelling approaches are considered:

- linear elastic analysis of decks according to Courbon theory. Courbon's simplificative hypothesis considers transverse beams with infinite flexural stiffness and longitudinal beams with zero torsional stiffness. This assumptions is valid in the case of steel or concrete beams with double-T beams and several rigid transverse beams. Almost all decks, such as those studied in this paper, fulfil Courbon's assumptions. This method allows a quick and simple manual calculation of the beam and was developed in the past, before the mass availability of finite element analysis. Today it is commonly used only for predimensioning or quick validation of software results.
- linear elastic analysis using a linear FE model created with the commercial software SAP2000 [102]. The entire viaduct is defined in the FE model, considering all structural elements to obtain a more refined reproduction of the boundary conditions of the decks, as illustrated in Figure 4-5.
- 3D NLFEAs carried out by modelling the decks in DIANA FEA software [27], [28], [29] to apply the three global safety formats. Modelling assumptions were discussed in Section 2.4 of Chapter 2. The dimensions of the 3D solid elements were chosen to respect an aspect ratio (AR) between 1 and 2 in the transverse direction and between 1 and 3 in the longitudinal direction. The dimensions of the elements were chosen to minimize mesh dependency issues through a convergence analysis of the results. The modelling results are shown in Figure 4-6.

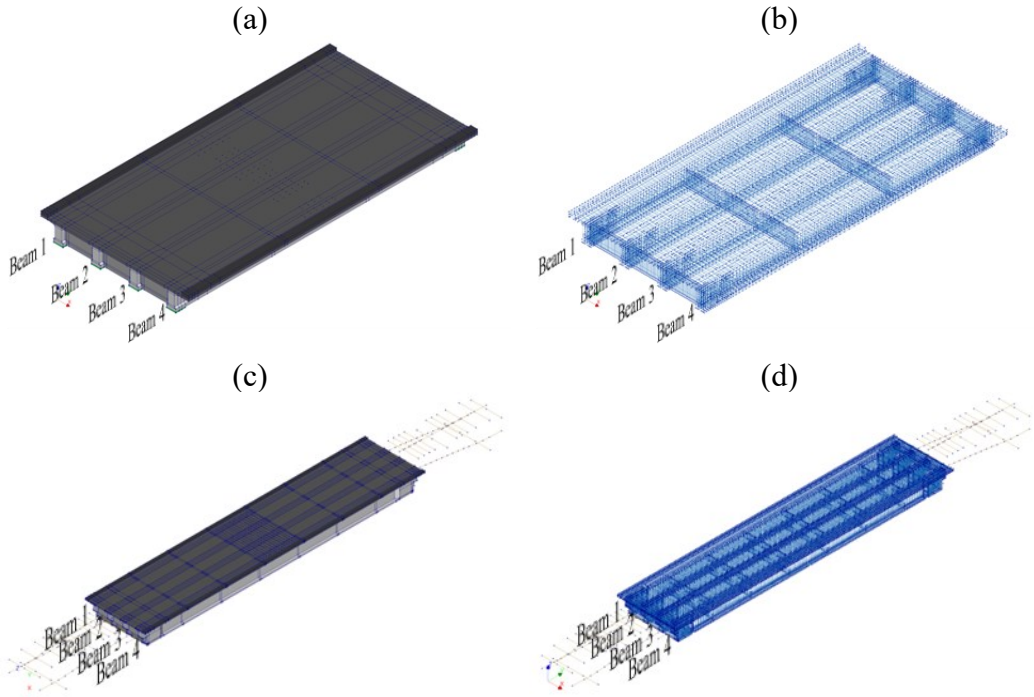

Figure 4-6: 3D NLFE models: (a) Concrete elements of the 20.8m deck; (b) Reinforcement elements of the 20.8m deck; (c) Concrete elements of the 50m deck; (d) Reinforcement of the 50m deck.

Influence of constraint conditions on ultimate strength of the decks in non-linear analyses

In this section, the influence of the constraint conditions on the ultimate strength of the decks is examined.

The different constraint conditions assumed are:

- **Constraint condition 1.** Rigid support plate made of 60 mm thick steel. Behaviour of the steel is elastic with elastic modulus $E = 210000\ MPa$. Constraints on vertical translations on side 1 and side 2 of the deck along the axis line at the base of the support plate. Constraint on longitudinal displacements only on side 1 of the deck along the axis line at the base of the support plate. Constraint to transverse translations only on beam 3 of the deck on side 1 and on side 2 along the axis line at the base of the support plate. Details in Figure 4-7.
- **Constraint condition 2.** Support plate made of 60 mm thick elastomeric material. The vertical and horizontal stiffnesses of the bearing plate are as follows: vertical stiffness $K_v = 9000\ kN/mm$; horizontal stiffness $K_H = 5\ kN/mm$. The stiffness values of the bearings were derived in accordance with [103] by knowing the plan dimensions and thickness of the elastomeric bearing. On both sides of the deck, the entire lower face of the elastomeric bearing was constrained to the three translations (vertical, longitudinal and transverse). Details in Figure 4-8.
- **Constraint condition 3.** Base plate made of elastomeric material 60 mm thick, resting on a steel plate with plan dimensions equal to the elastomeric

material plate and 60 mm thick. The constraint conditions applied to the base of the steel plate are the same as those described for constraint condition 1. Details in Figure 4-9.

- **Constraint condition 4.** Support plate made of elastomeric material, 60 mm thick, resting on a steel plate with plan dimensions equal to the elastomeric plate and 60 mm thick. The constraint conditions applied to the base of the steel support plate are as follows: vertical displacements constrained along the axis line of the plate base on side 1 and side 2 of the deck. Constrained longitudinal displacements along the axis line at the base of the steel support plate on side 1 and side 2 of the deck, thus, the longitudinal displacements of the deck depend only on the shear deformability of the elastomeric material. Transverse displacements constrained only on beam 3 along the axis line at the base of the steel support plate on side 1 and side 2 of the deck. Details in Figure 4-10.
- **Constraint condition 5.** In constraint condition 2, tensile stresses orthogonal to the bearing surfaces are reached on certain areas of the elastomer that are incompatible with both the actual tensile strength of the elastomer and the tensile strength of the concrete. An interface surface was therefore inserted between the upper face of the elastomeric pad and the concrete of the beams. This interface provides separation between the materials for tensile stresses greater than 1 MPa. The base of the elastomeric bearing is constrained as for constraint condition 2. For the 50-metre deck, in constraint condition 5, the 17.5 m cantilever beams extending from the piers (i.e. half of the hammer on each side), modelled with simple elastic beam elements. This additional choice was made in order to obtain a realistic description of the boundary support conditions of the 50 m simply supported deck. In fact, the results of a sensitivity analysis showed that the hammer deformability (especially the torsional one) cannot be neglected during the non-linear analysis of the deck.

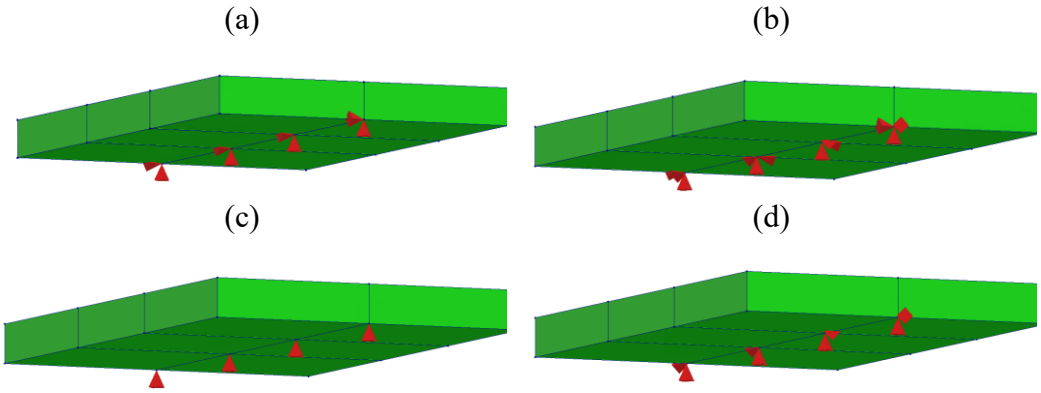

Figure 4-7: Constraint condition 1: 60 mm thick steel support. (a) Beam 1, Beam 2 and Beam 4 side 1 of the deck. (b) Beam 3 side 1 of the deck. (c) Beam 1, Beam 2 and Beam 4 side 2 of the deck. (d) Beam 3 side 2 of the deck.

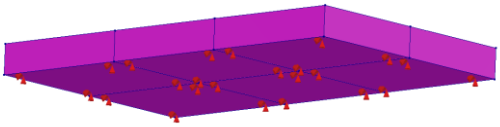

Figure 4-8: Constraint condition 2: 60 mm thick elastomeric bearing. Side 1 and side 2 of Beam 1, Beam 2, Beam 3 and Beam 4.

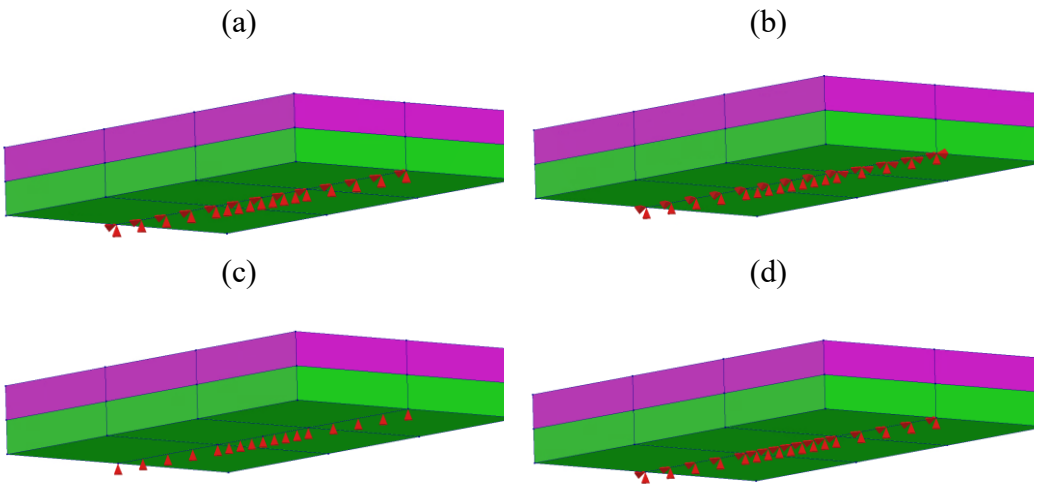

Figure 4-9: Constraint condition 3: 60 mm thick elastomeric bearing (magenta) on 60 mm tick steel plate (green). (a) Beam 1, Beam 2 and Beam 4 side 1 of the deck. (b) Beam 3 side 1 of the deck. (c) Beam 1, Beam 2 and Beam 4 side 2 of the deck. (d) Beam 3 side 2 of the deck.

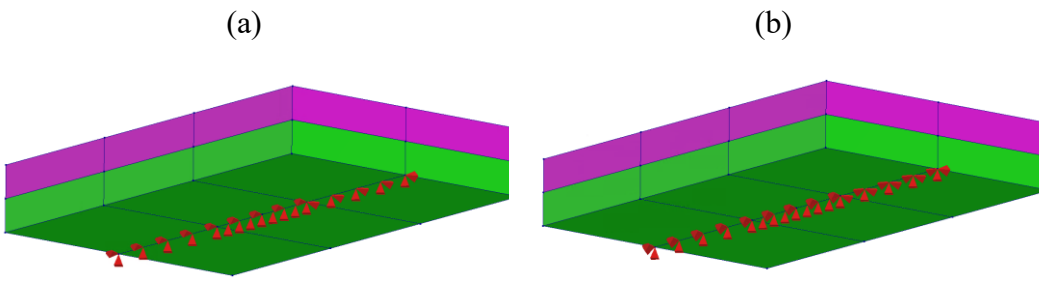

Figure 4-10: Constraint condition 4: 60 mm thick elastomeric bearing (magenta) on 60 mm tick steel plate (green). (a) Beam 1, Beam 2 and Beam 4 side 1 and side 2 of the deck. (b) Beam 3 side 1 and side 2 of the deck.

The comparison, in terms of load-displacement curve, for the different constraint conditions is shown in Figure 4-11, referring to the load multiplier of traffic loads. The influence of the constraint condition is much more pronounced for the 20.8m deck than for the 50m deck. Constraint condition 5 for the 50m deck leads to significantly greater displacements than the other four constraint conditions because the deformability of the cantilevers is included. Constraint condition 5 for both decks is the one considered.

(a)

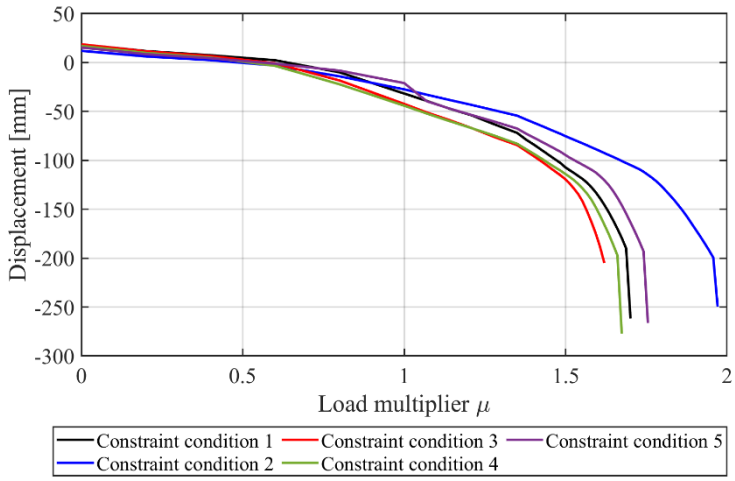

(b)

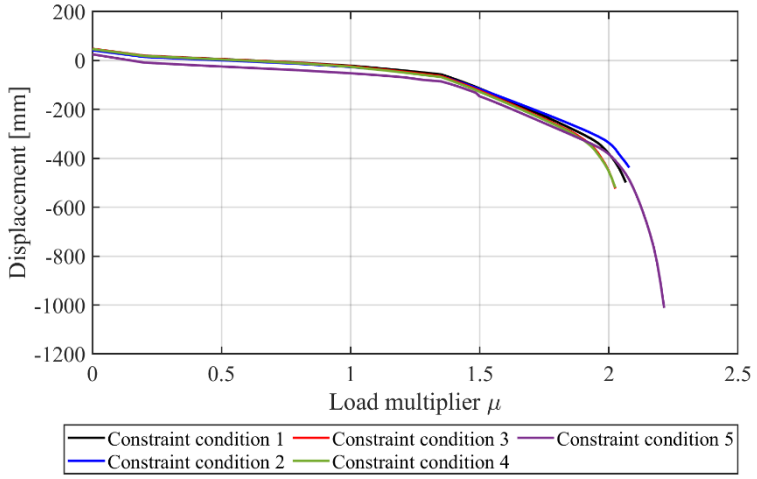

Figure 4-11: Comparison of load-displacement curves for different constraint conditions. (a) 20.8m deck; (b) 50m deck.

4.4. Analysis description and methodology

This section describes the methodologies followed and the analyses performed using linear models and non-linear global models.

Linear elastic analyses (local approach)

By adopting the linear elastic analysis (i.e. Courbon and FE elastic analyses), the safety assessment of the decks is carried out by calculating the ratio between the design resisting moment M_{Rd} and the design acting moment M_{Ed} according to standards [21],[24]. If this ratio is greater or equal to 1, the local verification is satisfied. This evaluation is performed for the deck edge beams (i.e. Beam 1 and Beam 4), since these beams present the maximum ratio between internal actions and the corresponding local resistances. The design acting moment is evaluated by

considering the following actions on the decks: permanent loads, traffic loads (Load Model 1 - LM1) and wind load according to [24]. The actions are combined according to the ULS combination [15],[24] presented in Equation (4.2):

$$F_d = \gamma_G \cdot G + \gamma_P \cdot P + \gamma_{QT} \cdot Q_T + \psi_W \cdot \gamma_{QW} \cdot Q_W \quad (4.2)$$

where F_d is the design action; γ_G is the partial factor of safety for structural and non-structural permanent loads (equal to 1,35); G is the structural and non-structural permanent loads; γ_P is the partial factor of safety for prestress (equal to 1); P is prestress action; γ_{QT} is the partial factor of safety for traffic loads (equal to 1 35); Q_T is the traffic loads; γ_{QW} is the partial safety factor for wind loads (equal to 1.50); Q_W is the wind action and ψ_W is the contemporaneity coefficient for wind actions (equal to 0.6 according to [24]). Temperature effects are considered negligible as the decks are simply supported. Seismic actions are not considered since it is a static analysis of the decks.

The traffic loads (LM1) are arranged on the decks to maximise the effects on the two edge beams (i.e. beam 1 and beam 4), as shown in Figure 4-12. To maximise the bending moment in the centre of the decks, the uniformly distributed loads must be applied along the entire length of the decks and the tandem loads are placed in the centre section of the decks.

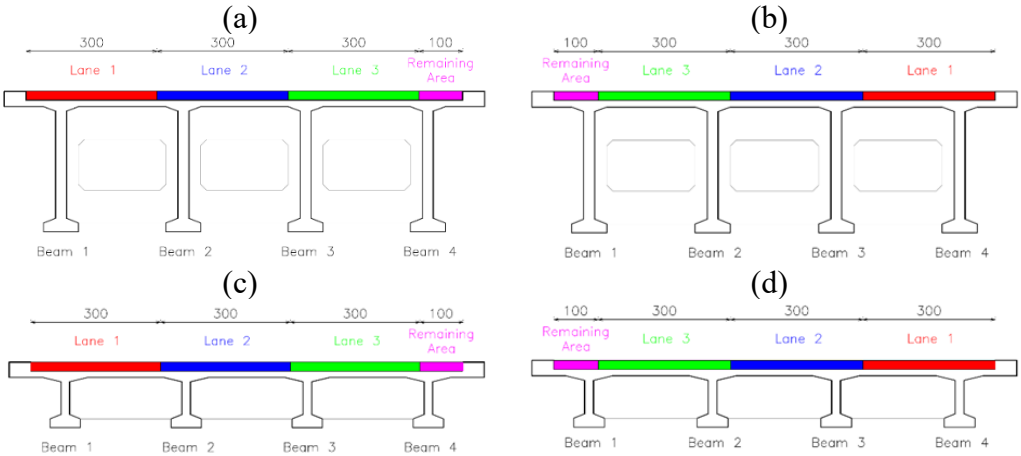

Figure 4-12: Arrangement of traffic loads on decks for the maximisation of effects on: (a) Beam 1 of the 50m deck; (b) Beam 4 of the 50m deck; (c) Beam 1 of the 20.8m deck; (d) Beam 4 of the 20.8m deck.

Non-linear analyses (global approach)

Non-linear analyses are developed to assess the safety of the decks through global safety formats discussed in Section 2.5 of Chapter 2.

First, a viscous-elastic analysis is performed from the time of construction to the current age of the decks (60 years). Rheological effects (shrinkage, creep and relaxation of prestressing reinforcement) are taken into account.

The construction phases of the decks last from 0 to 28 days and are the same for the 20.8 m deck and the 50 m deck. In the following 21900 days (60 years), only rheological effects occur. The most important effects of the construction phases on

the stresses in the concrete occur at 7 days, when the self-weight and post-tensioning of the deck are introduced, and at 28 days, when the permanent non-structural loads (the weight of the pavement and safety barriers) are introduced. These times were taken from the original calculation report.

Some results of the viscous-elastic analysis are shown in Figure 4-13 to Figure 4-18. In particular, the stresses in the concrete at the upper and lower fibres of the four longitudinal deck beams in the midspan section are shown in Figure 4-13,-Figure 4-14 and Figure 4-15-Figure 4-16, respectively. The stresses in the post-tensioned tendons are shown in Figure 4-17-Figure 4-18.

From the figures, it can be seen that the stresses in the mid-span cross-section reduce over time due to creep, shrinkage and relaxation: -1.0% and -0.8% losses in the concrete at the top fibre for the 20.8 m deck and the 50 m deck, respectively; -37.1% and -30.9% losses in the concrete at the bottom fibre for the 20.8 m deck and the 50 m deck, respectively; -8.7% and -8.6% post-tensioned tendons for the 20.8 m deck and the 50 m deck, respectively.

These values are calculated between 28 days (end of construction phases) and 21900 days (current age). After 60 years of construction, the stresses in the concrete and post-tensioning ties are different in the four beams of the 20.8 m deck due to the different amount of prestressing reinforcement. The differences are minimal for the 50 m deck. For the 50 m deck, the differences are very small due to the prestressing in the transverse beams. Therefore, the differences in stresses between the beams are more pronounced for the 20.8 m deck than for the 50 m deck.

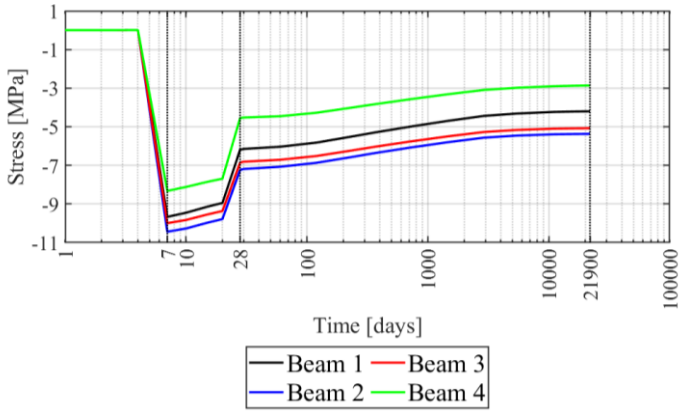

Figure 4-13: stresses at the bottom fibre of the midspan of the beams of 20.8m deck.

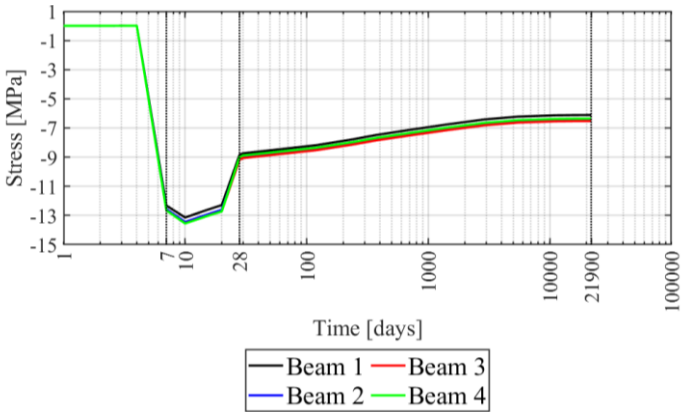

Figure 4-14: stresses at the bottom fibre of the midspan of the beams of 50m deck.

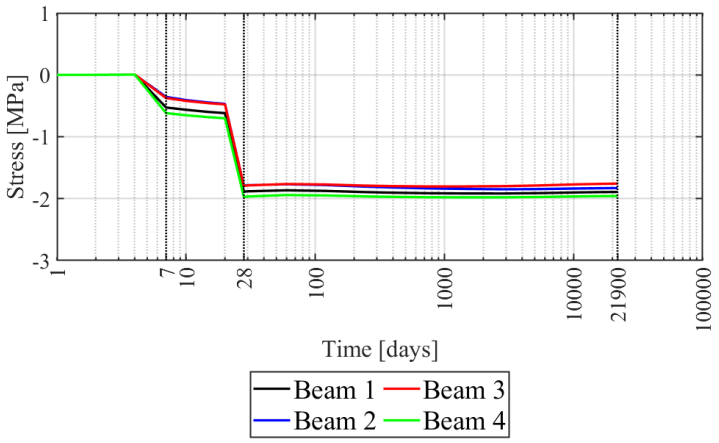

Figure 4-15: stresses at the top fibre of the midspan of the beams of 20.8m deck.

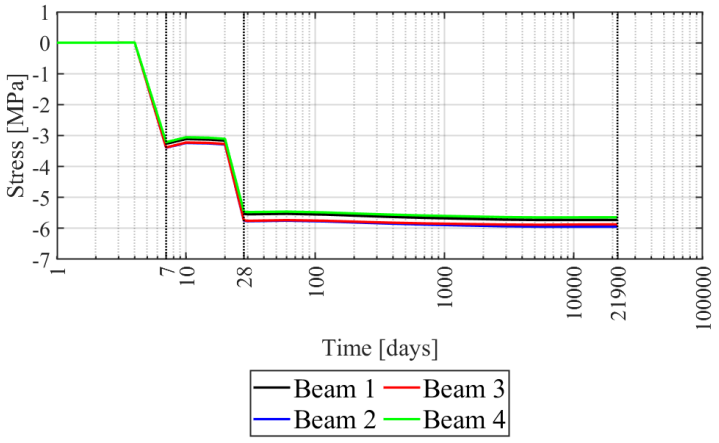

Figure 4-16: stresses at the top fibre of the midspan of the beams of 50m deck.

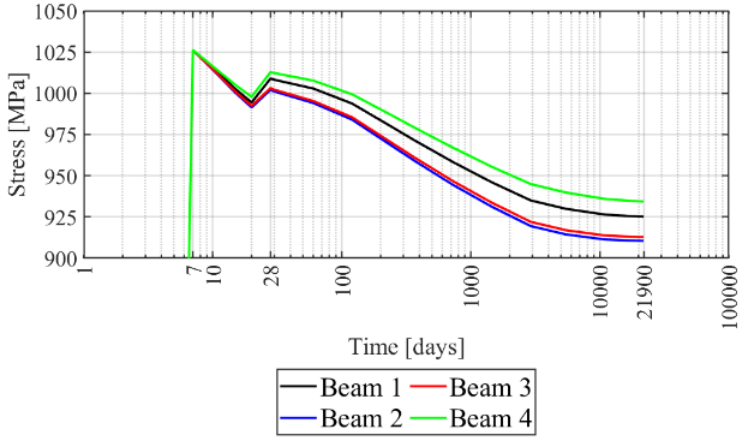

Figure 4-17: stresses in the post-tensioned tendons of the midspan of the beams of 20.8m deck.

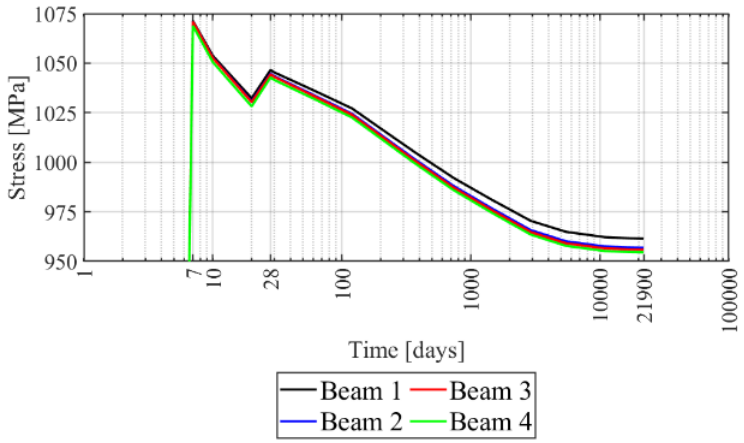

Figure 4-18: stresses in the post-tensioned tendons of the midspan of the beams of 50m deck.

Table 4-10: Loads acting on the decks.

Description	Symbol	Value
Self-weight of longitudinal beams [kN/m^3]	$G_{1,LB}$	25
Self-weight of transverse beams [kN/m^3]	$G_{1,TB}$	25
Self-weight of slab [kN/m^3]	$G_{1,S}$	25
Pavement weight [kN/m^2]	$G_{2,P}$	3
Barriers weight [kN/m]	$G_{2,B}$	2
Tensioning stress of the post-tensioned tendon of the longitudinal beams [MPa]	P_{CLB}	1190
Tensioning stress of the post-tensioned tendon of the transverse beams [MPa]	P_{CTB}	1190
Traffic load [kN/m^2 or kN]	Q	According to [24]
Wind load [kN/m^2]	W	According to [24]

Table 4-11: Loads applied from the construction time to the current age of the deck.

Time [days]	Active loads
0	-
7	$G_{1,LB} + G_{1,TB} + G_{1,S} + P_{CLB} + P_{CTB}$
28	$G_{1,LB} + G_{1,TB} + G_{1,S} + P_{CLB} + P_{CTB} + G_{2,P} + G_{2,B}$
⋮	⋮
>21900	$G_{1,LB} + G_{1,TB} + G_{1,S} + P_{CLB} + P_{CTB} + G_{2,P} + G_{2,B} + Q + W$

When the current age of the deck is reached, the traffic loads (i.e. Load Model 1 - LM1) are applied, arranged as shown in Figure 4-12. At this point, all loads are combined according to the ULS combination, presented in Equation (4.2), and from this condition they are monotonically and proportionally increased until the structure collapses. Table 4-10 shows the loads considered in the NL analysis and Table 4-11 lists the time-stepping followed in the viscous-elastic and NL analyses.

For both decks, Figure 4-19 shows the time history of the load multiplier during the viscous-elastic analysis from time 0 to 60 years and during the non-linear analysis performed at 60 years to bring the deck to collapse.

In detail, after 21900 days, the loads are increased until the design ULS load combination is reached (i.e., Equation (4.2)) and this step was performed in 1.5 virtual days. Therefore, it is assumed that the loads increase by 10% for each virtual day.

The overall structural strength of the decks is determined as a function of the different multipliers of ultimate loads μ (i.e. permanent loads, traffic loads and wind loads) obtained through the 3D NLFEAs. With reference to each specific action (i.e. permanent loads, traffic loads and wind loads), the safety verification, within the global approach, can be performed by comparing the design load multiplier μ_d determined using the specific safety format with the relevant partial safety factor γ according to the ULS combination [24]. If the value of μ_d, for all concurrent actions, is greater or equal to the corresponding γ, the global safety verification is satisfied. Note that since the partial safety factor γ_G and γ_{QT} are both equal to the value of 1.35 [24], the slope of both the solid black and dashed red lines, relating to the load increment for permanent and traffic loads respectively, is the same, as shown in Figure 4-19.

Based on the above considerations, Equation (2.30), within the GRF method [7], becomes:

$$\mu_d = \frac{\mu_{NLFEA}(f_{cmd}, f_{ym})}{\gamma_{Gl}} \tag{4.3}$$

where μ_d is the design load multiplier; $\mu_{NLFEA}(f_{cmd}, f_{ym})$ is the ultimate load multiplier expected from a 3D NLFEA γ_{Gl} and is the overall safety factor of 1.27.

Consequently, Equation (2.26), within the PF method, becomes:

$$\mu_d = \frac{\mu_{NLFEA}(f_d)}{\gamma_{Rd}} \tag{4.4}$$

where μ_d is the design load multiplier; $\mu_{NLFEA}(f_d)$ is the ultimate load multiplier predicted by a 3D NLFEA with the design values of the material properties in the structural model; γ_{Rd} is the NLFE model uncertainty safety factor, equal to 1.15 [104].

Finally, Equation (2.27), within the ECoV method, becomes:

$$\mu_d = \frac{\mu_m}{\gamma_R \cdot \gamma_{Rd}} \tag{4.5}$$

where μ_d is the design load multiplier; μ_m is the ultimate load multiplier predicted by a 3D NLFEA with the mean values of the material properties in the structural model. The term γ_R can be expressed through Equation (2.28) where V_R can be estimated as:

$$V_R = \frac{1}{1.65} \cdot ln\left(\frac{\mu_m}{\mu_k}\right) \tag{4.6}$$

where μ_k is the ultimate load multiplier predicted by a NLFEA performed using the characteristic values of the material properties; γ_{Rd} is the global safety factor of the model uncertainties (i.e., epistemic uncertainties) equal to 1.15 [104].

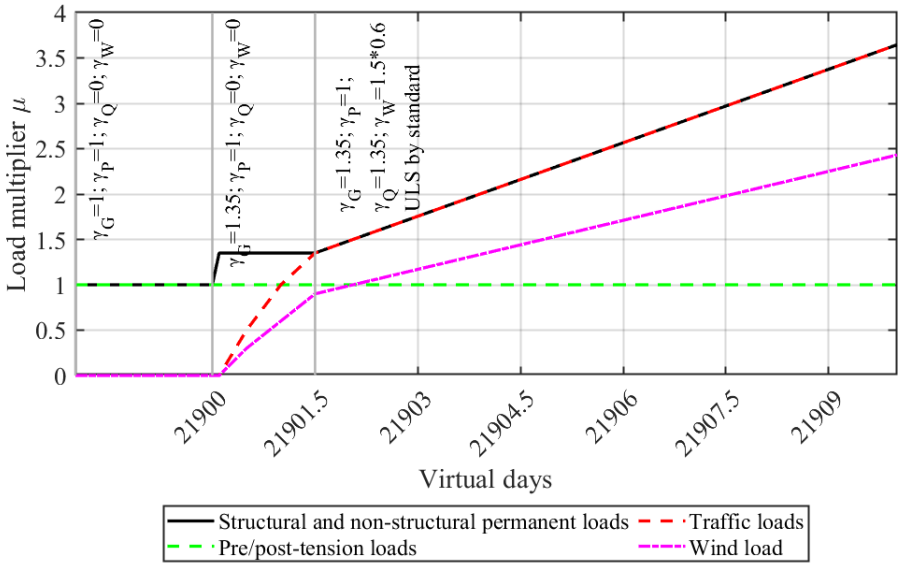

Figure 4-19: Time-History of the load multiplier: viscous-elastic analysis from time 0 to 60 years (21900 days) and non-linear analysis after 60 years. The data are related to both the decks.

4.5. Results and discussion

This section deals with the results obtained following the different methods (i.e., linear and non-linear analyses) previously described for both the local and global evaluation of the safety of the two decks.

Results from linear elastic analyses

The results of the local verifications of the linear elastic analysis (i.e. Courbon and linear FE analysis) are discussed in the following paragraphs.

Table 4-12 shows the design moments acting on the edge beams of the decks (i.e. Beam 1 and Beam 4) with reference to the midspan cross-section for the traffic load arrangement shown in Figure 4-12. The linear FE model gives a lower design moment (M_{Ed}) in the midspan section than that calculated according to Courbon theory: -12% for the 20.8 m deck and -16% for the 50 m deck. Table 4-13 shows the design resisting moment (M_{Rd}) on the edge beams (i.e. Beam 1 and Beam 4) of the decks with reference to their midspan cross-section. The design resistance of Beam 1 is different from that of Beam 4 in the 20.8 m deck because the prestressing reinforcement of the two beams is different, as shown in Table 4-1. On the contrary, the design resistance of both Beam 1 and Beam 4 is the same for the 50 m deck, due to the same amount of prestressing reinforcement in the beams, (see Table 4-2). Table 4-14 shows the results of local verifications with linear elastic analysis in terms of the safety margin calculated as the ratio between the design acting moment

(M_{Ed}) and the design resisting moment (M_{Rd}). Both decks were not verified with the Courbon method and only the 50 m deck results verified with FE linear analysis. In each case, the use of a FE model increases the coefficient of safety compared to the Courbon theory by approximately 14% for the 20.8 m deck and 19% for the 50 m deck.

Table 4-12: Design acting moment obtained from linear analyses.

M_{Ed} [kNm]	20.8m deck	50m deck
FE model	6433	32225
Courbon theory	7337	38369

Table 4-13: Design resisting moment.

M_{Rd} [kNm]	20.8m deck	50m deck
Beam 1	5544	34828
Beam 4	5075	

Table 4-14: Results of the local verifications with linear elastic analyses.

		Safety margin	
		20.8m deck	50m deck
FE model	Beam 1	0.86	1.08
	Beam 4	0.79	
Courbon theory	Beam 1	0.76	0.91
	Beam 4	0.69	

Results from NLFEAs

For each deck, four different NLFEAs were run to implement the three different safety formats for the safety assessment:

- two non-linear analyses for the application of the ECoV safety format. One with the average material properties (Model a) and one with the characteristic material properties (Model b);
- a non-linear analysis for the GRF method, considering the average properties of the reinforcing steel and the characteristic properties of the concrete (model c);
- a non-linear analysis for the PF method considering the design properties of the materials (model d).

The failure mode for all four models for both decks is the same: concrete crush in top fiber in the midspan of the edge beam (beam 1) as shown in Figure 4-20 for the 20.8m deck and in Figure 4-21 - Figure 4-22 for the 50m deck.

The 20.8 m deck collapses when the two central transverse beams reach cracking; at this point their function of redistributing the transverse load is limited and the concrete in the upper fibre of the edge beam (beam 1) reaches its ultimate

compressive strain. The 50 m deck collapses due to reaching the ultimate compressive stress on the upper fibre of the edge beam (beam 1).

It is interesting to note the differences in the stress distribution in the midspan section of the 50 m deck, shown in Figure 4-21and in Figure 4-22, due to the different nature of the supports. In Figure 4-21, the deck is modelled considering the presence of the cantilever beams on which it rests; therefore, the support is more deformable. In Figure 4-22, the deck is modelled without considering the presence of the cantilevers on which it rests; therefore the support is very rigid as if it was resting directly on the piers.

A more deformable support area allows for a more uniform distribution of loads in the different beams. Therefore, decks supported by cantilevered beams (such as the 50 m deck) require adequate modelling of the boundary conditions.

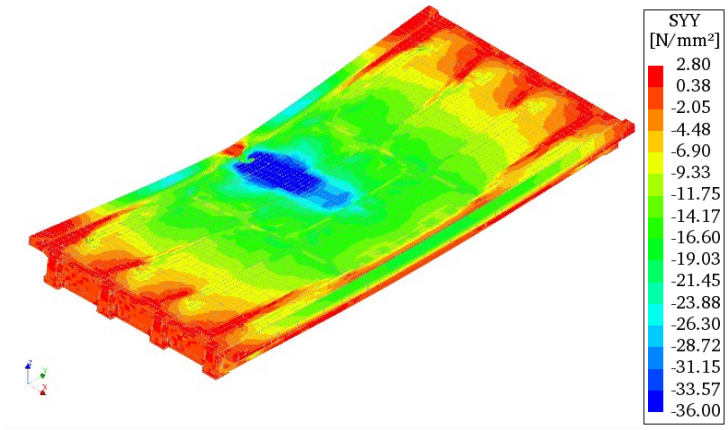

Figure 4-20: Failure mode of 20.8m deck.

A comparison of the results of the four different NL models as a function of the traffic load multiplier μ is presented in Figure 4-23 to Figure 4-30 for the midspan cross-section of the most loaded edge beam. In detail, Figure 4-23 and Figure 4-24 show the stress in the lower fibre; Figure 4-25 and Figure 4-26 show the stress in the upper fibre; Figure 4-27 and Figure 4-28 show the stress in the post-tensioned tendons. Figure 4-29 and Figure 4-30 show the load-displacement multiplier curve.

Table 4-15 shows the ultimate load multipliers μ_{NLFEA} for permanent loads, traffic loads and wind loads obtained from the NLFEA for the four models defined with different values representing the material properties according to the adopted safety formats.

Table 4-16 shows the global resistance safety factor γ_R, global safety factor for the model uncertainties γ_{Rd} and the global safety factor γ_{Gl} used to calculate the design load multiplier μ_d determined according to the specific safety formats (Eq.(4.3), Eq.(4.4) and Eq.(4.5)).

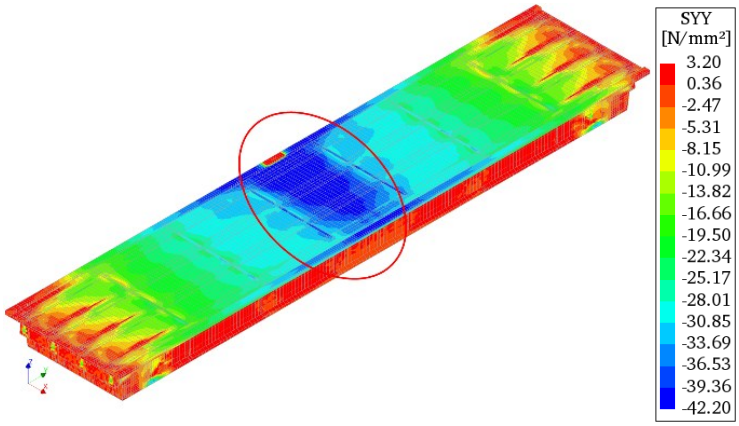

Figure 4-21: Failure mode of 50m deck on cantilever.

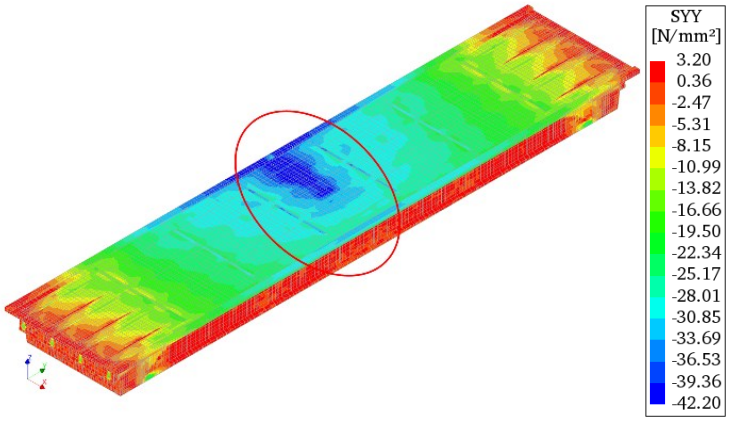

Figure 4-22: Failure mode of 50m deck on rigid support.

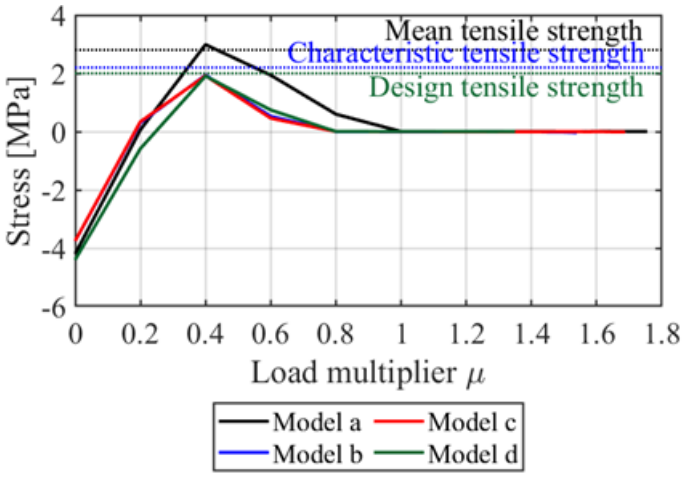

Figure 4-23: Stresses in the bottom fiber of the edge beam of the 20.8m deck.

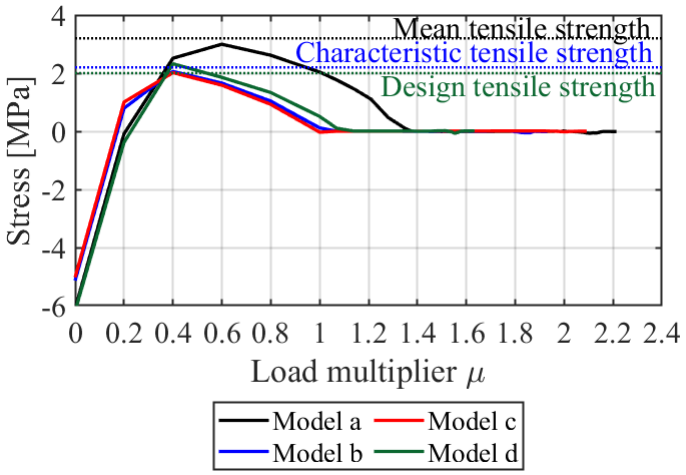

Figure 4-24: Stresses in the bottom fiber of the edge beam of the 50m deck.

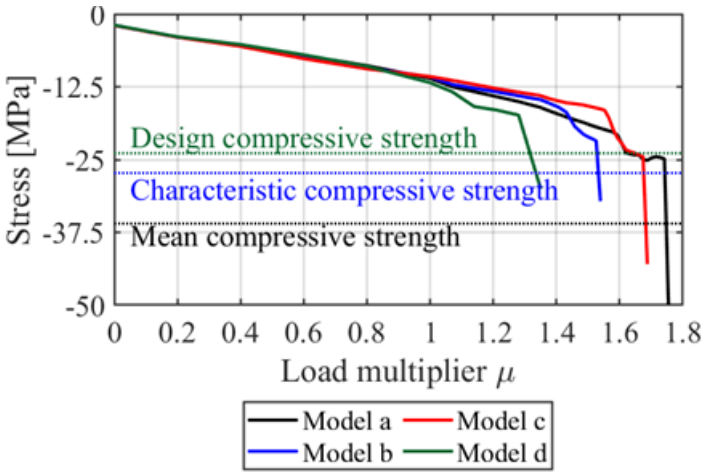

Figure 4-25: Stresses in the top fiber of the edge beam of the 20.8m deck.

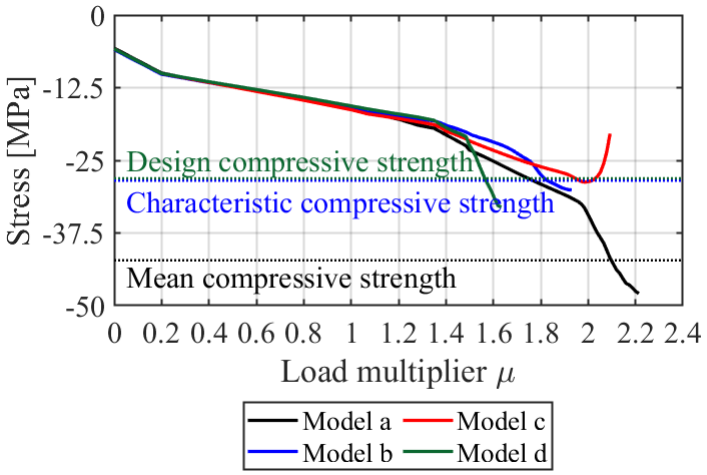

Figure 4-26: Stresses in the top fiber of the edge beam of the 50m deck.

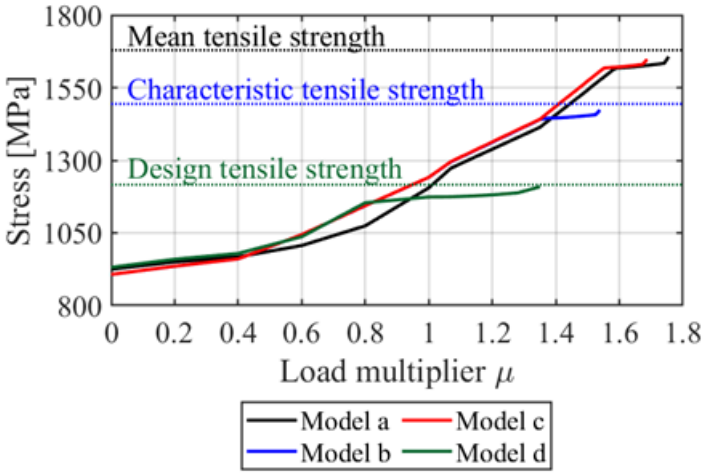

Figure 4-27: Stresses in the post-tensioned tendons of the edge beam of the 20.8m deck.

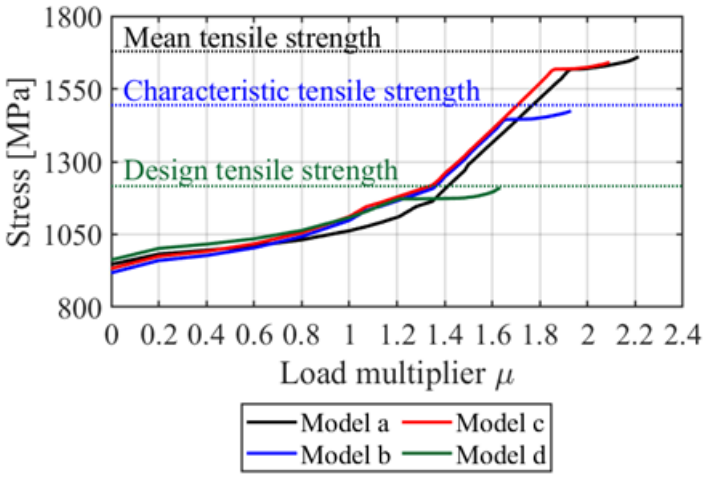

Figure 4-28: Stresses in the post-tensioned tendons of the edge beam of the 50m deck.

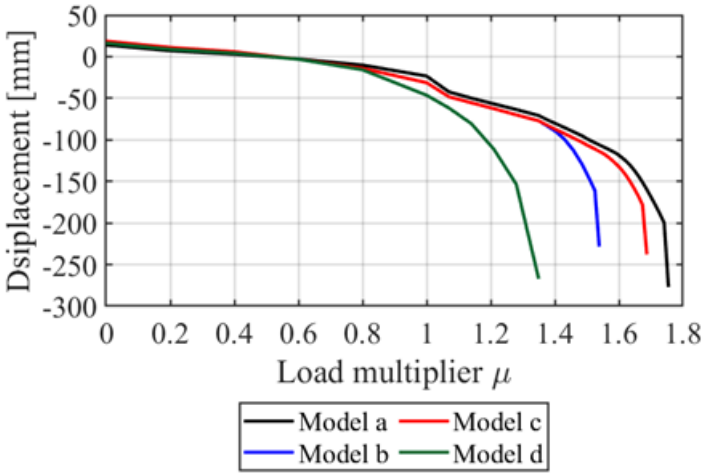

Figure 4-29: Load-displacement curve of the edge beam of the 20.8m deck.

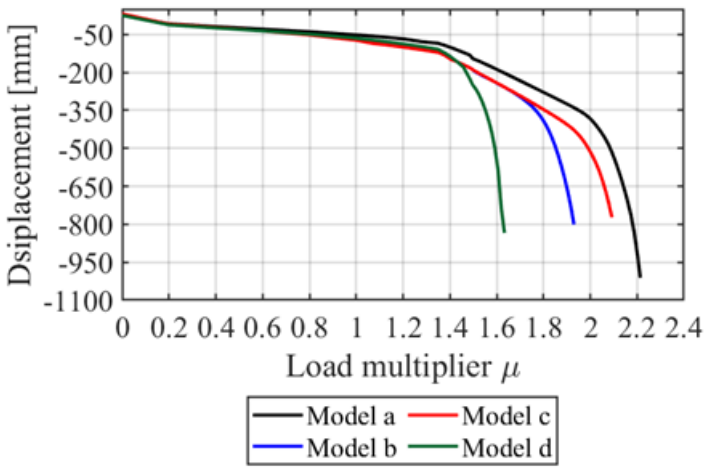

Figure 4-30: Load-displacement curve of the edge beam of the 50m deck.

The safety verification can be exploited by determining the safety margin as the ratio of the design load multiplier μ_d, determined according to the specific safety format (Eq.(4.3), Eq.(4.4) and Eq.(4.5)), to the partial safety factor $\gamma_G = \gamma_{QT} = 1.35$ for the permanent load multiplier and the traffic load multiplier or $\gamma_W = 1.5 * 0.6 = 0.9$ wind load multiplier.

Table 4-17 shows the results in terms of μ_d, while Table 4-18 shows the safety margin for the two decks according to the three different safety formats.

The GRF method produces the highest safety levels. The PF method leads to the lowest deck safety. This result is consistent with [98],[105],[106] and can be related to the fact that using design values of material properties to perform the non-linear analysis significantly changes the redistribution of internal stresses during the damage process (i.e., cracking and yielding) and the excursion of the ductility of the structural system compared to the case of adopting average values of material properties (which, in principle, leads to a more realistic prediction of the actual structural response) [106]. The ECoV method leads to intermediate safety results between the GRF and PF methods.

Table 4-15: Load multipliers obtained from non-linear analyses.

		μ_{NLFEA} Permanent		μ_{NLFEA} LM1		μ_{NLFEA} Wind	
		20.8m deck	**50m deck**	**20.8m deck**	**50m deck**	**20.8m deck**	**50m deck**
Model a	Beam 1	1.76	2.21	1.76	2.21	1.17	1.48
	Beam 4	1.67		1.67		1.12	
Model b	Beam 1	1.54	1.93	1.54	1.93	1.03	1.29
	Beam 4	1.49		1.49		0.99	
Model c	Beam 1	1.69	2.09	1.69	2.09	1.13	1.40
	Beam 4	1.61		1.61		1.07	
Model d	Beam 1	1.35	1.62	1.35	1.62	0.90	1.08
	Beam 4	1.35		1.35		0.78	

The safety margins shown in Table 4-18 for the 50 m deck refer to the deck modelled taking into account the stiffness of the two 17.5 m cantilevers on which it rests. For the sake of completeness, if the same deck had been modelled without taking the cantilevers into account, the values of the safety margins would have been approximately 5% lower for all three safety formats applied. Once again, this consideration demonstrates the importance of adequately modelling the boundary conditions of the structure.

the results for the two edge beams (beam 1 and 4) are shown in Table 4-15 to Table 4-18 for the 20.8 m deck, since the amount of post-tensioning reinforcement is different for the two beams and therefore the deck is not perfectly symmetrical in the transverse direction. Only one result is shown for the 50 m deck, as the amount of post-tensioning reinforcement is the same for the two edge beams.

Table 4-16: Global resistance safety factor γ_R , global safety factor of the model uncertainties γ_{Rd} and global safety factor γ_{Gl} used for the calculation of the design load multiplier.

		γ_R		γ_{Rd}		γ_{Gl}	
		20.8m deck	**50m deck**	**20.8m deck**	**50m deck**	**20.8m deck**	**50m deck**
PF	Beam 1	1.00	1.00	1.15	1.15	-	-
	Beam 4	1.00		1.15		-	
ECoV	Beam 1	1.30	1.29	1.15	1.15	-	-
	Beam 4	1.25		1.15		-	
GRF	Beam 1	-	-	-	-	1.27	1.27
	Beam 4	-		-		1.27	

Table 4-17: Design load multipliers obtained from the application of the different safety formats.

		μ_d **Permanent**		μ_d **LM1**		μ_d **Wind**	
		20.8m deck	**50m deck**	**20.8m deck**	**50m deck**	**20.8m deck**	**50m deck**
PF	Beam 1	1.17	1.42	1.17	1.42	0.78	0.94
	Beam 4	1.17		1.17		0.68	
ECoV	Beam 1	1.19	1.50	1.19	1.50	0.80	1.00
	Beam 4	1.17		1.17		0.78	
GRF	Beam 1	1.33	1.65	1.33	1.65	0.89	1.10
	Beam 4	1.26		1.26		0.84	

Table 4-18: Results of global verifications with the safety formats.

		Safety margin Permanent		**Safety margin LM1**		**Safety margin Wind**	
		20.8m deck	**50m deck**	**20.8m deck**	**50m deck**	**20.8m deck**	**50m deck**
PF	Beam 1	0.87	1.05	0.87	1.05	0.87	1.04
	Beam 4	0.87		0.78		0.75	
ECoV	Beam 1	0.88	1.11	0.88	1.11	0.89	1.11
	Beam 4	0.86		0.86		0.86	
GRF	Beam 1	0.98	1.22	0.98	1.22	0.99	1.22
	Beam 4	0.94		0.94		0.94	

Results Discussion

In this subsection, the results obtained from the local and global analyses are compared and discussed.

The most penalising results in terms of deck safety are obtained from the local analysis with the Courbon theory, which represents the simplest modelling that can be used for decks.

An increase in the safety coefficient of the deck can be achieved by increasing the complexity of the model. The gains of the different safety margins compared to those obtained by local analysis with Courbon theory are shown in Table 4-19.

A local analysis based on the results of a linear FEA leads to an increase in the safety margin between 13.2% and 18.7%. A global non-linear analysis under the PF method leads to an increase in the safety margin between 13.0% and 15.4%. A global non-linear analysis under the ECoV method leads to an increase in the safety margin between 15.8% and 24.6%. A global non-linear analysis under the GRF method leads to an increase in the safety margin between 28.9% and 36.2%.

The GRF method leads to the highest results in terms of safety margin, with an average gain of 33%; the PF method leads to the lowest results, with an average gain of 14%; the ECoV method leads to intermediate results between the PF and GRF methods, with an average gain of 21%.

Furthermore, for the case study, the results obtained with the PF method are in agreement with those obtained with the local analysis based on the linear FEA results.

The differences between the three safety formats result from the different material properties implemented in the 3D numerical models, which influence the redistribution of stresses with different inelastic deformations. This leads to a different utilisation of ductility resources in the numerical models.

Table 4-19: Safety margin variation starting from the solution using Courbon theory.

		Variation with respect to Courbon Theory	
		20.8m deck	50m deck
Linear FEA	Beam 1	+13.2%	+18.7%
	Beam 4	+14.5%	
PF	Beam 1	+14.5%	+15.4%
	Beam 4	+13.0%	
ECoV	Beam 1	+15.8%	+22.0%
	Beam 4	+24.6%	
GRF	Beam 1	+28.9%	+34.1%
	Beam 4	+36.2%	

In general, safety results obtained with a local approach are more conservative than those obtained with a global approach. With a local approach, safety assumptions are implemented in the material strengths and modelling assumptions and fall within the epistemic uncertainties. A safety choice can be useful to identify the worst-case scenario within a less sophisticated approach. By using a global approach, it is possible to appreciate aspects of structural behaviour that are

generally lost with a local approach, such as the redistribution of internal actions. This leads to a gain in the assessment of structural safety.

On the other hand, applying different safety formats to NLFEA results can lead to considerable variations in structural safety results. These variations are consistent with [106] and can be related to the use of different material property values (i.e. average, characteristic or design) within the nonlinear analysis, which significantly alter the redistribution of internal actions during the damage process.

The adoption of average material property values, in general, leads to a more realistic prediction of the actual structural response.

Chapter 5

Case study: Safety assessment of an existing bridge deck subject to different damage scenarios through the global safety format ECoV

5.1. Chapter introduction

3D NLFEAs are developed to assess the safety of a bridge deck in presence of concrete degradation and corrosion of the reinforcing steel.

The level of safety is calculated as a function of the damage by means of non-linear global 3D numerical analyses.

The effect of the real damage scenario, found during visual inspections of the structure, on the structural safety is assessed and its magnitude/extent is varied to generate a family of similar damages with different intensities.

Nine different damage scenarios are studied: the first one represents the real one observed on the structure, seven scenarios are derived from the real case by varying the magnitude and or the extent of the real one. The last damage scenario represents the ultimate limit damage for the safety of the bridge with respect to the ultimate limit state (ULS).

Different damages at different locations are not studied as they were not observed during the inspections and can be a further development of this study.

The safety of the bridge deck is assessed against the ULS in its intact condition by developing 3D NLFEAs with mean and characteristic material properties, respectively. Subsequently, the safety of the deck is numerically evaluated against the ULS for the nine different damage scenarios to assess the sensitivity of the structure to the extent and intensity of structural degradation.

Finally, damage thresholds on certain static parameters are determined for the structure under investigation.

5.2. Deck description and material characterisation

The viaduct belongs to an Italian highway and was built in the 1960s, it is shown in Figure 5-1. The viaduct deck is made of several simply supported pre-stressed RC girders having a length of 45m with net longitudinal spans of 42m. Each girder is 19.10m wide and counts six longitudinal double-tee beams. The slab is 20cm thick

and four transverse beams are present. The beams and slab are prefabricated elements, jointed in-situ by concrete casting.

Figure 5-1: Picture of the viaduct.

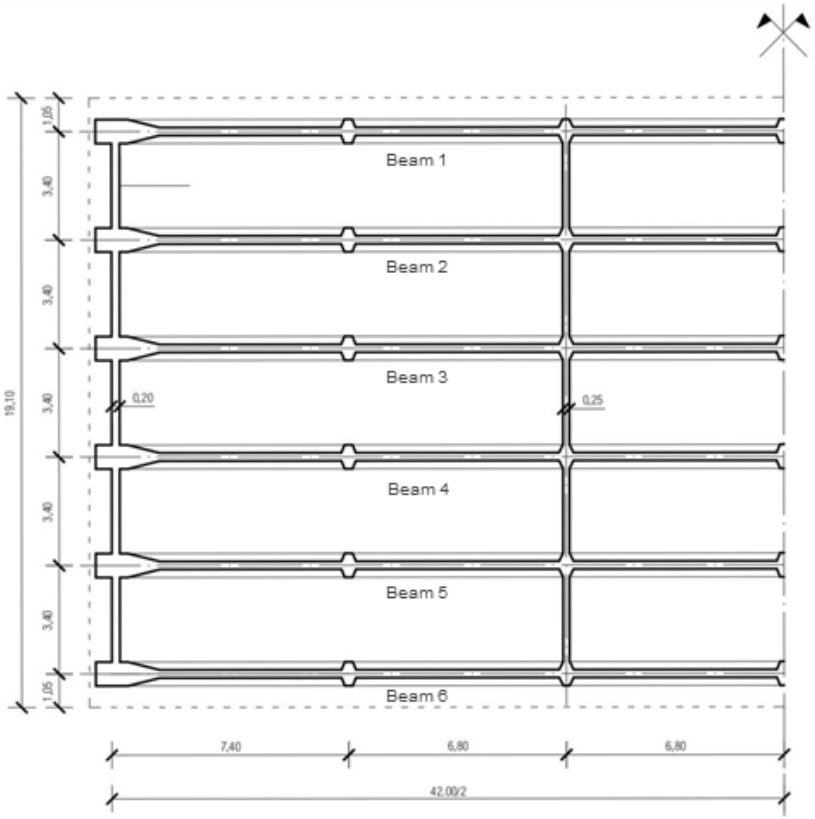

Figure 5-2: Geometry of the deck: planimetry. Measurements are in meters.

The longitudinal beams interaxis is 3.40m, as shown in Figure 5-3. All the longitudinal beams have the same cross-section with a depth of 2.60m and a 25cm thick web. The transverse beams are at the ends and at the thirds of each span. They

have a rectangular cross-section with a depth of 2.30m and a thickness variable from 25cm (end ones) to 20cm (span ones), as illustrated in Figure 5-4.

Ordinary, pre and post tensioning reinforcements are present in the deck, details on the arrangement of the reinforcement are provided in Annex B. In the longitudinal beams, there are 94 half-inch diameter strands and one post-tensioned cable with 32 wires of 7mm diameter. Transverse post-tension reinforcements are present in the transverse beams and in the slab above them. Two cables having 24 wires of 7mm diameter and 22 wires of 7mm diameter, respectively, lie in the transverse beams. One transverse cable made of 32 wires of 7mm diameter is placed in the slab.

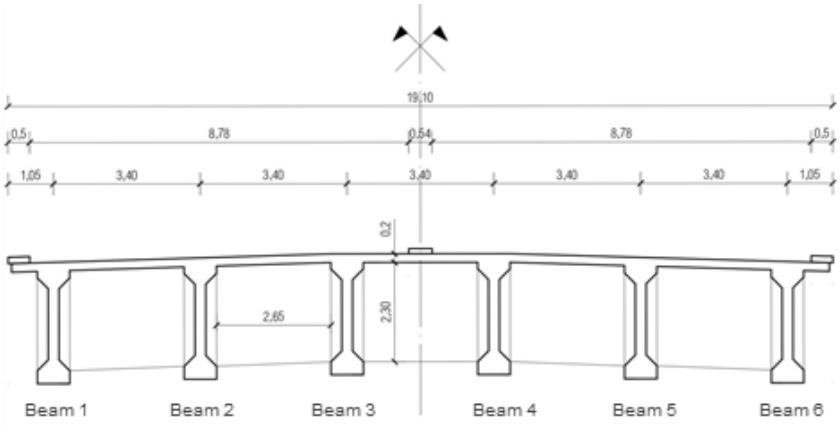

Figure 5-3: Geometry of the deck: cross-section. Measurements are in meters.

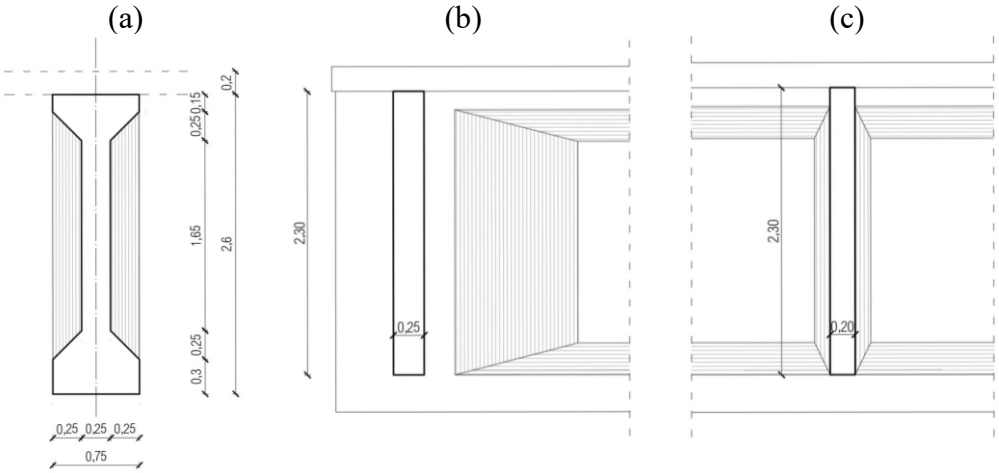

Figure 5-4: Geometrical details: (a) longitudinal beam cross-section, (b) transverse beams at the ends of the spans, (c) span transverse beams. Measurements are in meters.

Material properties characterisation

The approach shown in Section 4.2 is followed for the determination of the mechanical properties of materials. Here, the most significant information on the mechanical properties of materials is given.

The mechanical properties of the materials used in the original design of the deck are listed in Table 5-1. At the original time of the design of the deck and

according to the standards in force at the time, the values of the minimum material strengths had to be guaranteed (Table 5-1).

Table 5-1: Mechanical properties of materials used in the original design of the deck.

Description	Value
Minimum compressive strength of concrete [MPa]	46
Minimum tensile strength of ordinary reinforcing steel [MPa]	440
Minimum tensile strength of pre-tension reinforcing steel [MPa]	1750
Minimum tensile strength of post-tension reinforcing steel [MPa]	1650

Concrete and reinforcement specimens were sampled in-situ from the bridge deck for safety assessment. The average and CoV values of the concrete compressive strength were measured on 15 cylindrical cores of 10cm diameter: 12 taken from the longitudinal beams and 3 from the slab.

It should be noted that the CoVs in Table 5-2- Table 5-3 are lower than 10% since both beams and slab are prefabricated (with factory quality control).

Four specimens of ordinary steel bars were taken from Φ8 and Φ10 bars as well as five prestressing steel specimens were taken from the strands.

The comparison of the strength values used in the original design of the deck (Table 5-1) with the results of the laboratory tests on in-situ specimens (Table 5-2- Table 5-6) shows that both mean and characteristic ultimate strength values obtained from in-situ tests are higher than the minimal values assumed in the original design of the deck for concrete and ordinary reinforcement steel.

Table 5-2: Mechanical properties for the concrete of longitudinal beams.

Description	Symbol	Mean value	CoV	Characteristic value
Cylindrical compressive strength [MPa]	f_{cc}	57.0	9.0%	48.0
Tensile strength [MPa]	f_{ct}	4.0	*	3.5
Elastic modulus [MPa]	E_c	38340	*	36218

* Value of CoV not available. Creep and shrinkage parameters were calculated with formulations according to [11].

Table 5-3: Mechanical properties for the concrete of transverse beams and slab.

Description	Symbol	Mean value	CoV	Characteristic value
Cylindrical compressive strength [MPa]	f_{cc}	49.0	4.0%	44.0
Tensile strength [MPa]	f_{ct}	3.5	*	3.3
Elastic modulus [MPa]	E_c	36400	*	35320

* Value of CoV not available. Creep and shrinkage parameters were calculated with formulations according to [11].

Table 5-4: Mechanical properties for the ordinary reinforcing steel.

Description	Symbol	Mean value	CoV	Characteristic value
Yield tensile strength [MPa]	σ_{ys}	425	6.0%	383
Ultimate tensile strength [MPa]	σ_{su}	575	3.0%	543
Ultimate strain [-]	ε_{su}	0.117	12.0%	0.098
Elastic modulus [MPa]	E_s	200000	*	200000

* Value of CoV not available.

Table 5-5: Mechanical properties for the pre-tension reinforcing steel.

Description	Symbol	Mean value	CoV	Characteristic value
Yield tensile strength [MPa]	σ_{yp}	1636	5.0%	1466
Ultimate tensile strength [MPa]	σ_{up}	1818	5.0%	1629
Ultimate strain [-]	ε_{up}	0.05	*	0.045
Elastic modulus [MPa]	E_{sp}	195000	*	195000

* Value of CoV not available. Relaxation parameters were calculated with formulations according to [11].

Table 5-6: Mechanical properties for the post-tension wire steel.

Description	Symbol	Mean value	CoV	Characteristic value
Yield tensile strength [MPa]	σ_{yp}	1530	3.0%	1412
Ultimate tensile strength [MPa]	σ_{up}	1700	3.0%	1569
Ultimate strain [-]	ε_{up}	0.05	*	0.045
Elastic modulus [MPa]	E_{sp}	195000	*	195000

* Value of CoV not available. Relaxation parameters were calculated with formulations according to [11].

5.3. Definition of the 3D NLFE model

The 3D NFEL model definition is analogous to that shown in Chapter 4. Figure 5-5 shows the numerical model.

(a)

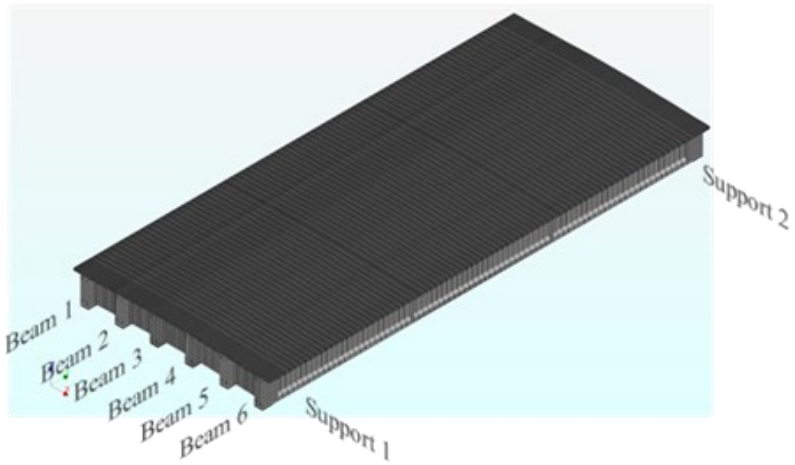

(b)

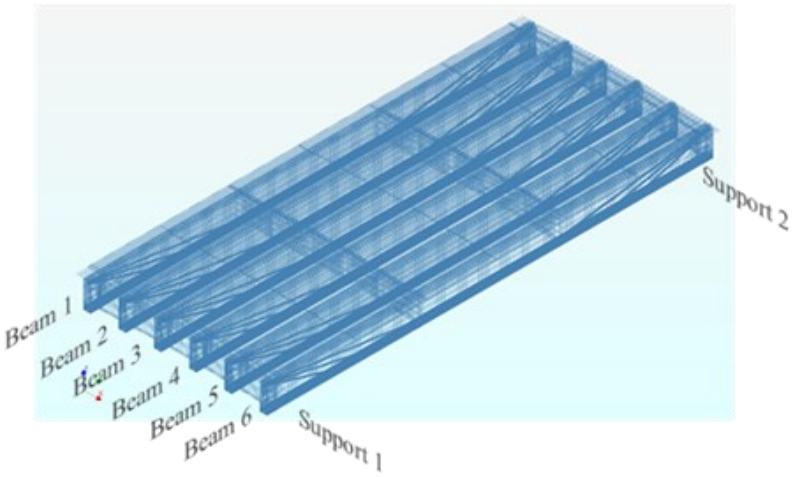

Figure 5-5: 3D FE model with annotation of the beams: (a) concrete elements, (b) reinforcement elements.

5.4. Preparatory simulations for the global safety assessment

The methodology adopted in the modelling and non-linear analysis is similar to that shown in Section 4.4, with some differences that will be explained here.

Visco-elastic analysis of the construction stage until the current age

The deck was built in different construction phases. A viscous-elastic analysis was performed in phases from the time of construction to the current age of the deck (49 years). Shrinkage, creep and relaxation of the pre/post-tensioned steel are considered. The construction phases considered are: precast, pre-tensioning, slab and transverse beam casting and post-tensioning.

Some results of the viscous-elastic analysis are shown in Figure 5-6 and Figure 5-7, considering both average and characteristic values of the material properties. In particular, the stresses in the concrete at the upper and lower fibres of the six longitudinal beams of the deck in the mid-height cross-section are presented in Figure 5-6, while the stresses in the post-tensioned and prestressed strands are shown in Figure 5-7.

The construction phases of the deck last from 0 to 130 days, while in the following 49 years (17885 days) only rheological effects occur. The most important effects of the construction phases on the concrete stresses in the beams occur at 60 days, when the self-weigh of the slab is introduced, and at 90 days with the tensioning of the post-tensioned cable. These times were taken from the original calculation report. The stresses in the cross-section are reduced over time due to creep, shrinkage and relaxation.

In detail, the variation of concrete stress in the upper fiber of the beam due to prestressing losses are 20.7% considering the average material properties, while they are 4.9% higher in the case of characteristic material properties. At the lower fibre, losses of 14.7% are recorded when applying the average material properties, while these losses are 2.5% higher in the case of the characteristic material properties. In addition, losses of 6.8% can be appreciated in both the post-tensioned tendon and prestressed strands when assuming the average material properties, while these losses are 0.7% higher in the case of the characteristic material properties.

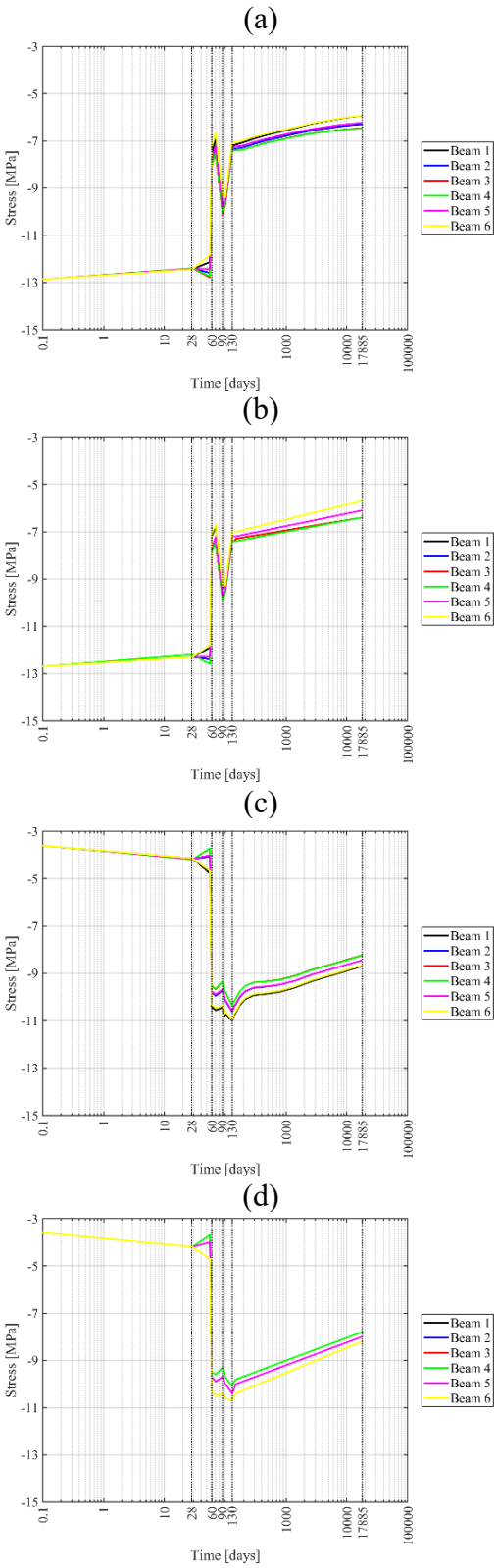

Figure 5-6: Results of viscous-elastic analysis for concrete: (a) stresses at the bottom fiber of the beams with mean materials properties, (b) stresses at the bottom fiber of the beams with characteristic materials properties, (c) stresses at the top fiber of the beams with mean materials properties, (d) stresses at the top fiber of the beams with characteristic materials properties.

(a)

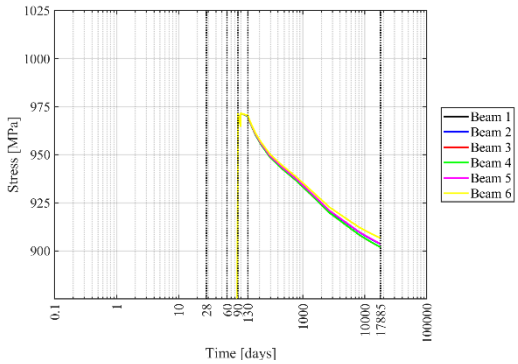

(b)

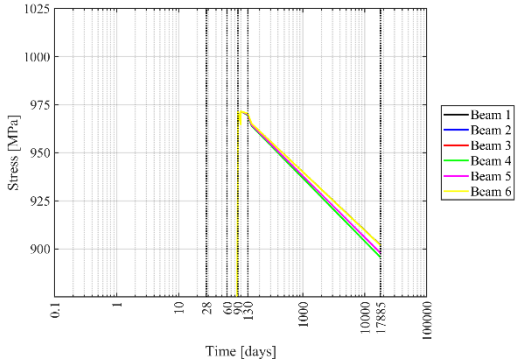

(c)

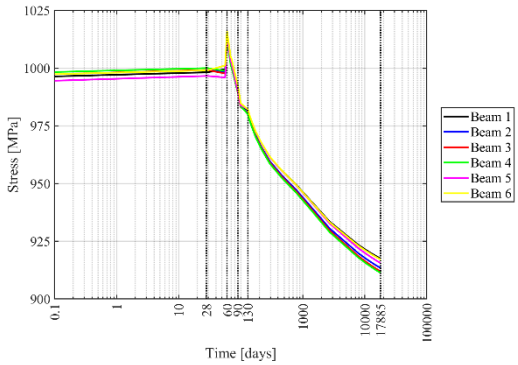

(d)

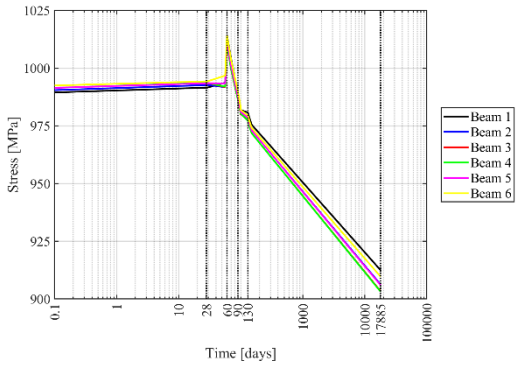

Figure 5-7: Results of viscous-elastic analysis: (a) stresses in post-tensioned cables with mean materials properties, (b) stresses in post-tensioned cables with characteristic materials properties, (c) stresses in pre-stressed strands with mean materials properties, (d) stresses in pre-stressed strands with characteristic materials properties.

The application of loads on the model follows the approach used in Section 4.4. Table 5-7 describes the different typologies of the loads considered in the phased analysis and Table 5-8 reports the construction time-stepping followed.

Table 5-7: Loads from the time of construction to the current age of the deck.

Description	Symbol	Value
Self-weight of longitudinal beams [kN/m^3]	$G_{1,LB}$	25
Self-weight of transverse beams [kN/m^3]	$G_{1,TB}$	25
Self-weight of slab [kN/m^3]	$G_{1,S}$	25
Pavement weight [kN/m^2]	$G_{2,P}$	3
Barriers weight [kN/m]	$G_{2,B}$	2
Tensioning stress of the pre-tensioned strands of the longitudinal beams [MPa]	P_S	1240
Tensioning stress of the post-tensioned tendon of the longitudinal beams [MPa]	P_{CLB}	1190
Tensioning stress of the post-tensioned tendon of the transverse beams [MPa]	P_{CTB}	1190
Traffic load [kN/m^2 or kN]	Q	According to [24]
Wind load [kN/m^2]	W	According to [24]

Table 5-8: Loads from the time of construction to the current age of the deck.

Phase	Time [days]	Active elements	Active loads
1	0	Longitudinal beams	$G_{1,LB} + P_S$
2	28	Longitudinal + Transverse beams	$G_{1,LB} + P_S + G_{1,TB}$
3	56	Longitudinal + Transverse beams	$G_{1,LB} + P_S + G_{1,TB} + P_{CTB}$
	60	Longitudinal + Transverse beams + slab	$G_{1,LB} + P_S + G_{1,TB} + P_{CTB} + G_{1,S}$
4	70	Longitudinal + Transverse beams + slab	$G_{1,LB} + P_S + G_{1,TB} + P_{CTB} + G_{1,S}$
5	90	Longitudinal + Transverse beams + slab	$G_{1,LB} + P_S + G_{1,TB} + P_{CTB} + G_{1,S} + P_{CLB}$
6	100	Longitudinal + Transverse beams + slab	$G_{1,LB} + P_S + G_{1,TB} + P_{CTB} + G_{1,S} + P_{CLB}$
	130	Longitudinal + Transverse beams + slab	$G_{1,LB} + P_S + G_{1,TB} + P_{CTB} + G_{1,S} + P_{CLB} + G_{2,P} + G_{2,B}$
⋮	⋮	⋮	⋮
7	>17885	Longitudinal + Transverse beams + slab	$G_{1,LB} + P_S + G_{1,TB} + P_{CTB} + G_{1,S} + P_{CLB} + G_{2,P} + G_{2,B} + Q + W$

Validation of the NLFE model

The validation of the 3D FE model is based on the results of a load test performed on the deck in terms of rotations measured in the supports regions of longitudinal beams [107].

The arrangement of the load test is shown in Figure 5-8.

The loads of the load test are introduced in the model after the viscous-elastic phased analysis (lasting from 0 to 49 years).

The rotations near the supports of the NLFE model caused by the lorries are computed and compared with the ones measured by an in-situ monitoring system of sensors.

Note that the measured rotations of the deck under investigation are assumed as reference values since the experimental monitoring campaign on the viaduct revealed that the rotations measured on damaged decks are almost identical to the rotations measured on undamaged decks of the same viaduct (with identical geometry).

The results of the comparison are shown in Table 5-9 for the beams, instrumented with inclinometers, (beam 2, 3, 4 and 5, see Figure 5-3). The differences between measured and numerical rotations are low and this validates the numerical model.

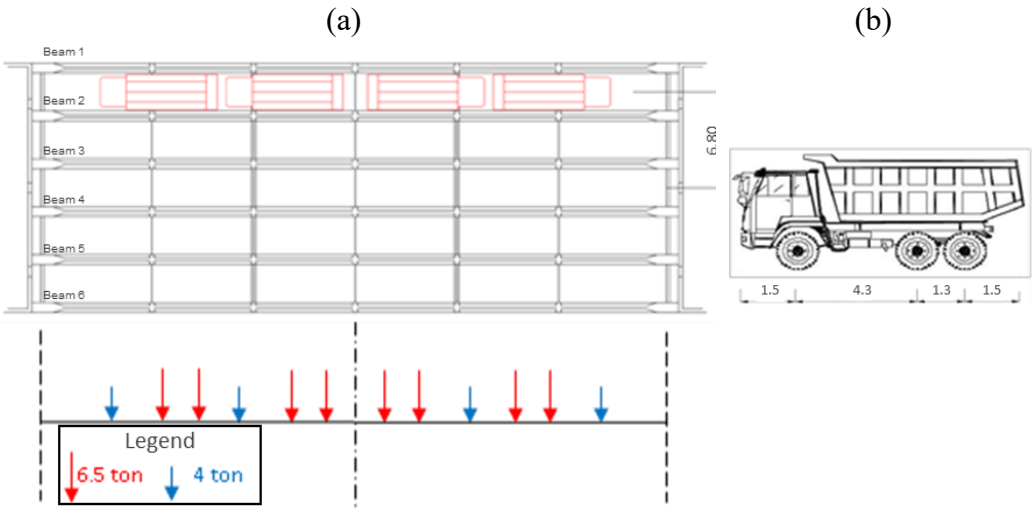

Figure 5-8: Details of the arrangement of loads during the load test: (a) position, (b) lorries silhouette. Measurements in metres.

Table 5-9: Measured vs. NLFE model rotations.

Beam	Measured rotation [mrad]	FE model rotation [mrad]	Difference [%]
Beam 2 support 1	0.53	0.56	6.73
Beam 3 support 1	0.36	0.36	0.29
Beam 4 support 1	0.15	0.18	5.35
Beam 5 support 1	≈ 0	0.01	-
Beam 2 support 2	0.52	0.56	8.49
Beam 3 support 2	0.32	0.36	7.33
Beam 4 support 2	0.20	0.18	3.45
Beam 5 support 2	≈ 0	0.01	-

Damage scenarios

The side beam of the deck has been suffering from reinforcement corrosion as can be appreciated in Figure 5-9: 19 out of 94 prestressing strands, 8 out of 32 wires of the prestressing tendon and 4 longitudinal ordinary reinforcement bars were broken and, therefore, ineffective in the midspan of the beam.

The information about the damage is taken from the reports written by the highway authorities through periodic visual inspections. During the inspections, the entire deck is examined, but only damage in the midspan of the structure was observed and described in the technical report. Other damages in different positions are not herein hypothesised since were not observed during the inspections.

The evaluation of the safety level of the existing bridge with respect to the undamaged condition is the first step of this research. Afterwards, the real and other different damage scenarios are simulated on the deck, mainly concerning corrosion of the reinforcement varying its extension and magnitude.

Preliminary numerical tests, simulating both concrete cover spalling and consequential loss of bond between concrete and reinforcements in the damaged areas, revealed the negligible effect of the concrete cover on the global resistance of the structure due to its nil tensile contribution in the bottom bulb of the beam at ULS.

The stress-strain relationship of the corroded bars can vary from the one of uncorroded steel, especially, with regard to the ductility of steel. Several studies in the literature show that ductility is unchanged for low corrosion levels [108],[109] and in absence of pitting corrosion [110],[111]. Ductility of steel is the most variable parameter in case of severe uniform corrosion or in presence of pitting, as yield stress and ultimate strength change slightly or negligibly.

In this case study, the information available about the damage is taken from standard reports written by highway inspectors through visual inspections without any quantitative technical or experimental measurements. Therefore, since any evaluation of ductility or bond variation according to the formulation proposed in the literature is not possible, the prestressing and/or ordinary reinforcements marked as “not effective” in the above-mentioned reports are completely removed from the numerical model to be on safety side (Damage 1).

The different other damage scenarios (Damages 2-8) are not real by derived from the real one (see Table 5-10). The damages derived from the real one are defined by varying the extent and intensity of the real one to take into account some uncertainties highlighted during the qualitative inspections and to assess the effects of different intensities and extensions of the observed damage.

The scenario “Damage 9” represents the ultimate limit condition, when the structure collapses exactly for the load level suggested by Italian standard [24] for the ULS.

Figure 5-9: Real damage on the side beam.

Table 5-10: Damage scenarios description.

Damage	Loss of pre-tension strands	Loss of wires in the post-tension cable	Loss of ordinary reinforcement bars	Damage extension
Damage 1	19/94 (-20%)	8/32 (-25%)	4/6 (-67%)	2 m
Damage 2	19/94 (-20%)	32/32 (-100%)	4/6 (-67%)	2 m
Damage 3	-	32/32 (-100%)	-	2 m
Damage 4	-	32/32 (-100%)	-	4 m
Damage 5	19/94 (-20%)	-	-	2 m
Damage 6	38/94 (-40%)	-	-	2 m
Damage 7	19/94 (-20%)	-	-	4 m
Damage 8	38/94 (-40%)	-	-	4 m
Damage 9	55/94 (-59%)	32/32 (-100%)	-	2 m

Table 5-11: Displacement of the structure when damage is introduced: cross-section at midspan of Beam 1.

Case	Displacement [mm]
Undamaged	1.61
Damage 1	1.64
Damage 2	1.90
Damage 3	1.62
Damage 4	2.28
Damage 5	1.65
Damage 6	2.06
Damage 7	2.18
Damage 8	3.41
Damage 9 (ultimate condition)	7.51

In any scenario, the damage was considered only in the central area of the beam for an extension ranging from 2 or 4 metres by removing pre-tension strands and/or post-tension wires. Outside this area, the reinforcement remains fully effective.

The extent of the simulated damage (2 or 4 metres) implicitly considers an approximate length required for the re-anchorage and full effectiveness of the wires and/or strands as the damages are typically localised with a smaller extension, according to the reports written by the highway authorities. This assumption is realistic also with respect to the grouting of the post-tension wires since they are considered ineffective in the area where the cable is corroded. Outside this area, in the absence of more accurate inspections, it can be reasonable to assume no effect on the grouting.

The damage is modelled as an instantaneous event occurred at the 49th year during the structure lifetime. Table 5-11 shows the displacements of the cross-section at midspan of Beam 1 at the 49th year in presence of the damage under the permanent loads only.

The effects in terms of increased deformability with respect to the undamaged scenario are very small (1.8mm of difference between undamaged and damage 8). The maximum increase in deformation (5.9mm) occurs for Damage 9, which is the limit condition of bridge collapsing exactly at design loads.

5.5. Results and discussion

This section presents the results in terms of damage-dependent safety assessment of the deck and provides the definition of the damage thresholds in terms of specific static parameters for the type of structure under investigation.

Safety results with respect to the ULS

This subsection describes the results obtained from the safety assessment of the deck through the ECoV safety format considering both the undamaged and the other nine damaged configurations.

For all the scenarios Table 5-12 reports the ultimate load multipliers achieved carrying out the 3D NLFEAs with the mean and characteristic material strengths, (to be able to apply the ECoV methodology shown in the following).

In any scenario, the damage was considered only in the central area of the beam for an extension ranging from 2 or 4 metres by removing pre-tension strands and/or post-tension wires. Outside this area, the reinforcement remains fully effective.

The extent of the simulated damage (i.e., 2 or 4 metres) implicitly considers an approximate length required for the re-anchorage and full effectiveness of the wires and/or strands as the damages are typically localised with a smaller extension, according to the reports written by the highway authorities. This assumption is realistic also with respect to the grouting of the post-tension wires since they are considered ineffective in the area where the cable is corroded. Outside this area, in the absence of more accurate inspections, it can be reasonable to assume no effect on the grouting.

The damage is modelled as an instantaneous event occurring at the 49th year of the structure age.

Table 5-11 shows the displacements of the cross-section at midspan of Beam 1 at the 49th year in presence of the damage under the permanent loads only. The effects in terms of increased deformability with respect to the undamaged scenario are very small. The most pronounced effect occurs for Damage 9, which is the limit condition.

Table 5-12: Ultimate load multipliers.

Case	Permanent and traffic load multiplier with mean materials strength	Wind load multiplier with mean materials strength	Permanent and traffic load multiplier with characteristic materials strength	Wind load multiplier with characteristic materials strength
Undamaged	2.73	1.82	2.46	1.64
Damage 1	2.30	1.53	2.08	1.39
Damage 2	2.13	1.42	1.92	1.28
Damage 3	2.46	1.64	2.24	1.49
Damage 4	2.19	1.46	2.03	1.35
Damage 5	2.35	1.57	2.13	1.42
Damage 6	2.08	1.39	1.92	1.28
Damage 7	2.19	1.46	2.03	1.35
Damage 8	1.97	1.31	1.81	1.21
Damage 9 (ultimate condition)	1.76	1.17	1.59	1.06

Figure 5-10 shows stresses at the failure time for the undamaged scenario with the mean strength values.

Figure 5-10 (a) shows stress in concrete and Figure 5-10 (b) in pre-stressed strands and post-stressed tendons. The maximum compressive stresses, leading to collapse, are reached in the concrete slab above external longitudinal beams (Beam 1 and Beam 2 of Figure 4).

In the beams called “Beam 2 and Beam 3”, the pre-stressing and post-tensioning reinforcement reaches yield stress, whereas for the “Beam 1” the values are close to the ultimate tensile strength.

In all other models analysed, there are similar stress distributions at the collapse step with modifications in terms of failure mode, which can be steel-side or concrete-side as a function of the material properties, as explained in the following.

The results from the 20 3D NLFEAs (considering both the mean and characteristic strength values) referred to the midspan section are shown in the following figures (Figure 5-11-Figure 5-20).

Figure 5-11and Figure 5-12 show the stresses at the bottom fiber of the edge beam (Beam 1). Figure 4-13 and Figure 5-14 show the stresses at the top fiber of the same edge beam (maximum compressive stress). Figure 5-15 and Figure 5-16 show the stresses in the post-tensioned tendon for some damage scenarios since the post-tensioned tendon in that section is completely removed for the models

"Damage 2, 3, 4 and 9". Figure 5-17 and Figure 5-18 show the stresses in the pre-stressed strands.

Collapse occurs with different resistance mechanisms in the different models with variable ductility. No brittle failure modes are observed due to the configurations of both loads and simulated damages.

In the scenarios with lower damage (i.e., Damage 3 and Damage 5), collapse occurs on the concrete-side reaching the ultimate compressive stress in the slab above the edge beam.

In presence of a more severe damage (i.e., Damage 1,2,4,6,7 and 9), collapse occurs on the steel-side reaching the ultimate strength of the pre-stressed strands and/or post-tensioned tendon. In these last cases, the non-linear ductile capacities of the structural system are used to a further extent.

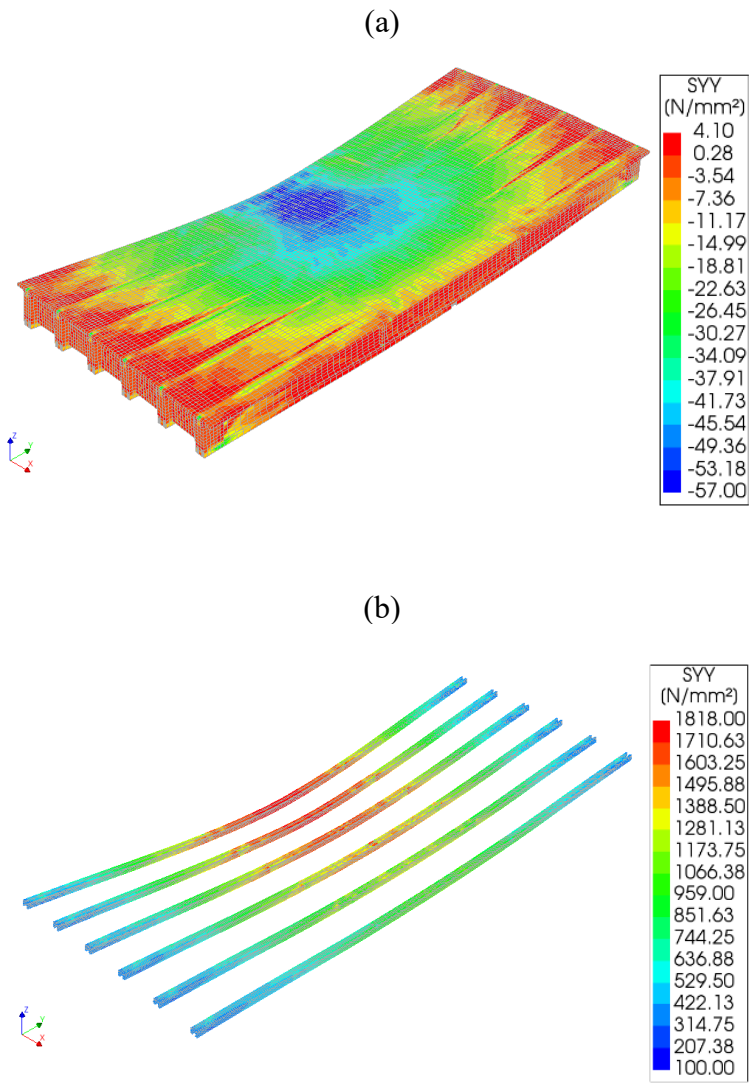

Figure 5-10: Failure mode: (a) stresses in longitudinal directions in concrete, (b) stresses in pre-stressed strands.

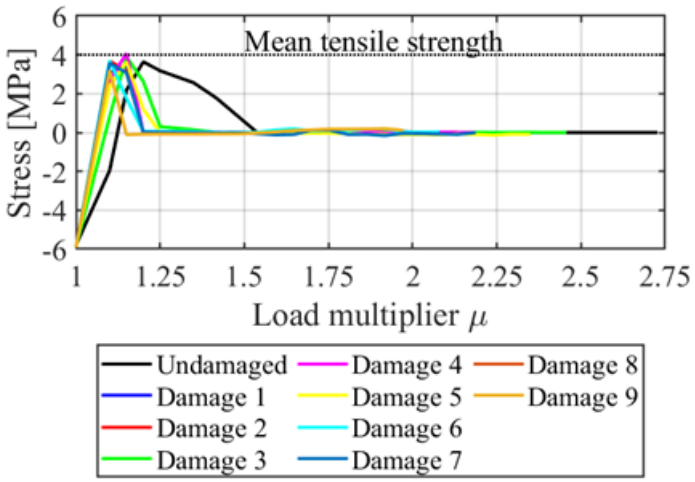

Figure 5-11: Stresses in the bottom fiber of the edge beam: model with the mean strengths of materials.

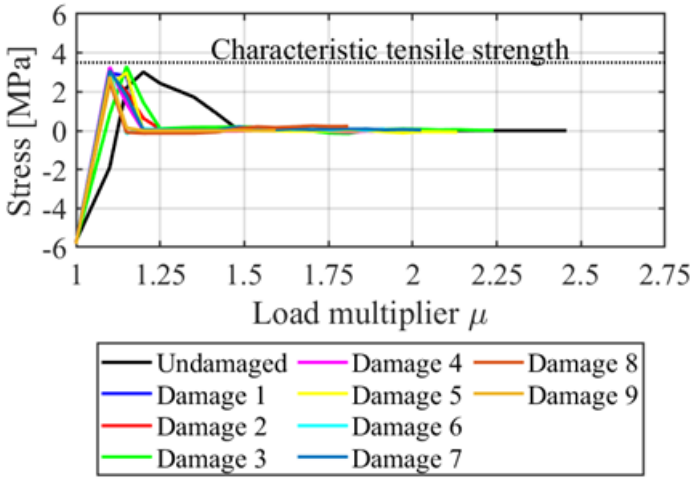

Figure 5-12: Stresses in the bottom fiber of the edge beam: model with the characteristic strengths of materials.

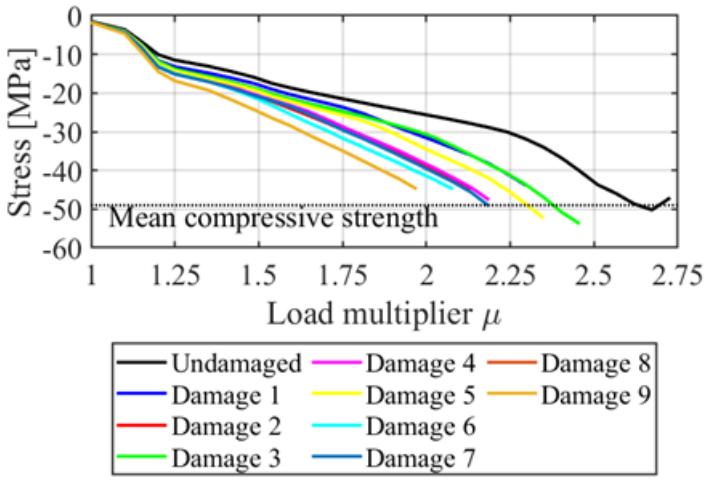

Figure 5-13: Stresses at the top fiber of the edge beam: model with the mean strengths of materials.

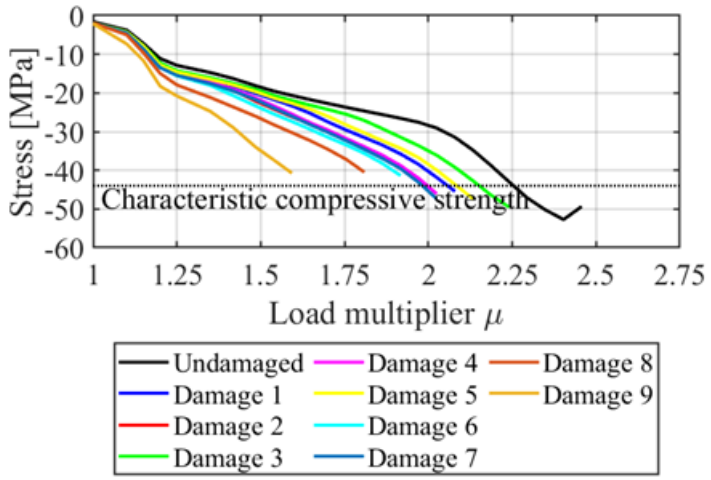

Figure 5-14: Stresses at the top fiber of the edge beam: model with the characteristic strengths of materials.

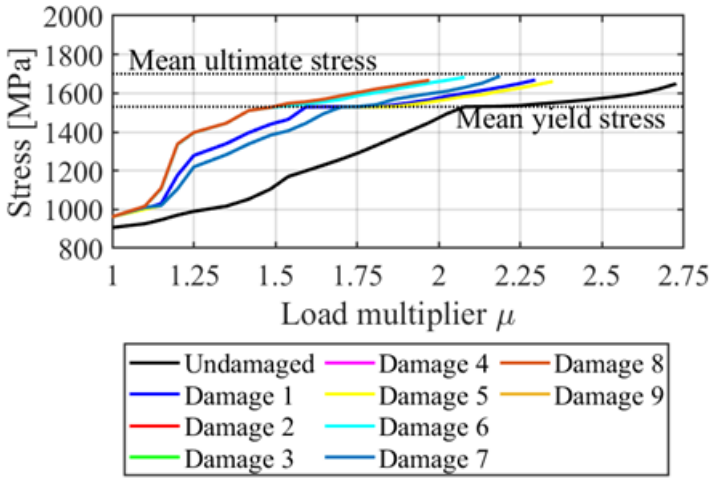

Figure 5-15: Stresses in the post-tensioned cable: model with the mean strengths of materials.

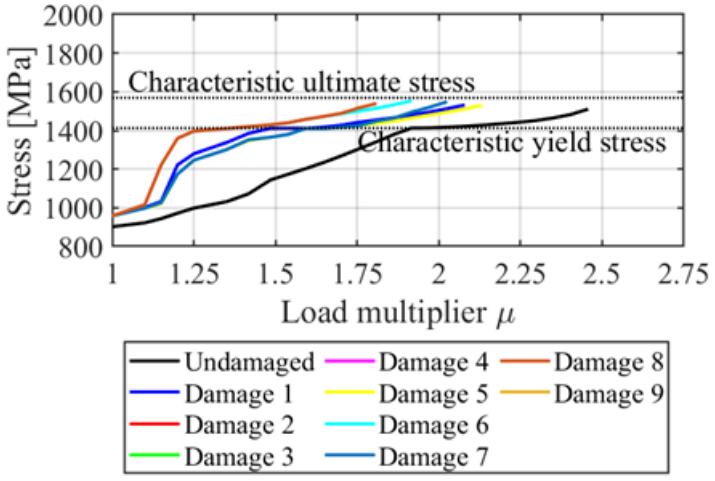

Figure 5-16: Stresses in the post-tensioned cable: model with the characteristic strengths of materials.

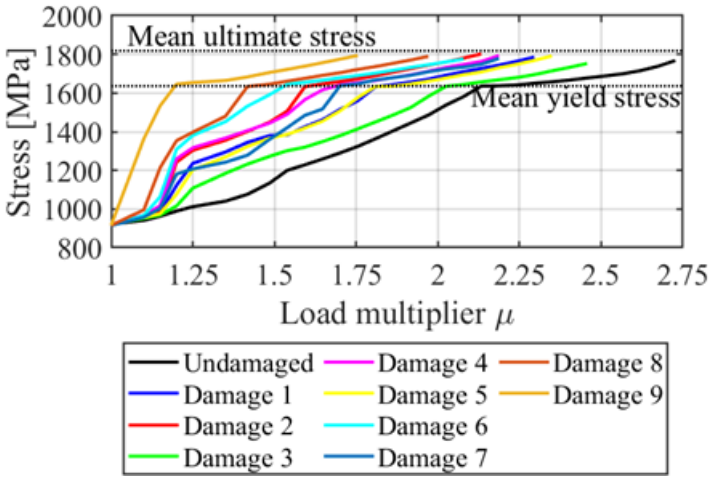

Figure 5-17: Stresses in the pre-stressed strands: model with the mean strengths of materials.

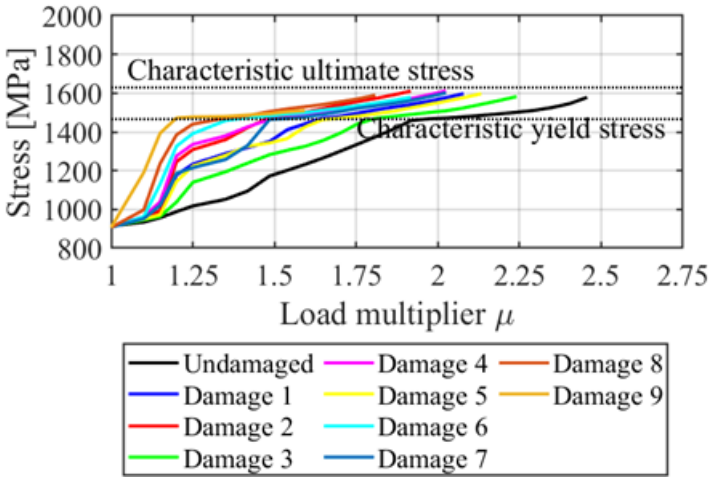

Figure 5-18: Stresses in the pre-stressed strands: model with the characteristic strengths of materials.

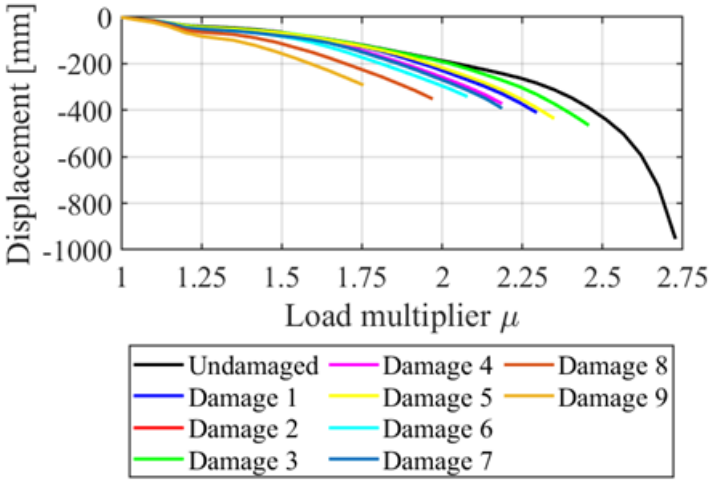

Figure 5-19: Load-displacement curve for the longitudinal edge beam: model with the mean strengths of materials.

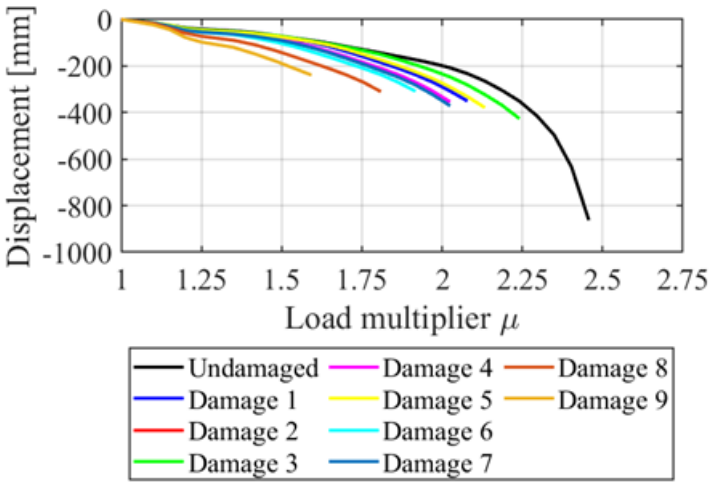

Figure 5-20: Load-displacement curve for the longitudinal edge beam: model with the characteristic strengths of materials.

Figure 5-19 and Figure 5-20 show the structural behaviour for the different scenarios considered. It is possible to note that, for low load multipliers, the structural behaviour between undamaged and damaged decks is almost the same. The most marked differences appear when the load multiplier increases, therefore, when the material non-linearity field is reached.

The undamaged deck shows great ductility, with an ultimate displacement of the edge beam bigger than 90cm (i.e., 1/46 of the span). When the simulated damage level increases, this global ductility is lost, and the ultimate displacement is reduced to 50% less than the one in the sound condition.

Table 5-13 reports the design load multipliers following the application of the ECoV safety format calculated according to Equation (4.5) on the basis of the results of Table 5-12.

The variation with respect to the ultimate limit state condition imposed by the current standards is also listed in Table 5-13. These results show that the damaged structure still ensures good safety margins against the ULS.

Table 5-13: Variation in load-bearing capacity compared to the ULS condition by standards.

Case	ECoV design permanent and traffic load multiplier	ECOV design wind load multiplier	Safety margin with respect to code design
Undamaged	2.05	1.36	+51.9%
Damage 1	1.74	1.16	+28.9%
Damage 2	1.59	1.06	+17.8%
Damage 3	1.89	1.26	+40.0%
Damage 4	1.73	1.15	+28.1%
Damage 5	1.79	1.19	+32.6%
Damage 6	1.63	1.09	+20.7%
Damage 7	1.73	1.15	+28.1%
Damage 8	1.53	1.02	+13.3%
Damage 9 (ultimate condition)	1.35	0.90	0.0%

The comparison in terms of safety factor is shown in Figure 5-21. There are two limit scenarios: undamaged deck with an available safety factor of 100% with respect to the ULS condition; “Damage 9” has 0% available safety compared to the ULS condition.

All the other damage scenarios (real and hypothesized ones) are in an intermediate condition. Damage 3 shows the smallest safety reduction (i.e., 77.1% available safety), whereas Damage 8 shows the highest effect on the safety of the deck (i.e., 25.7% available safety).

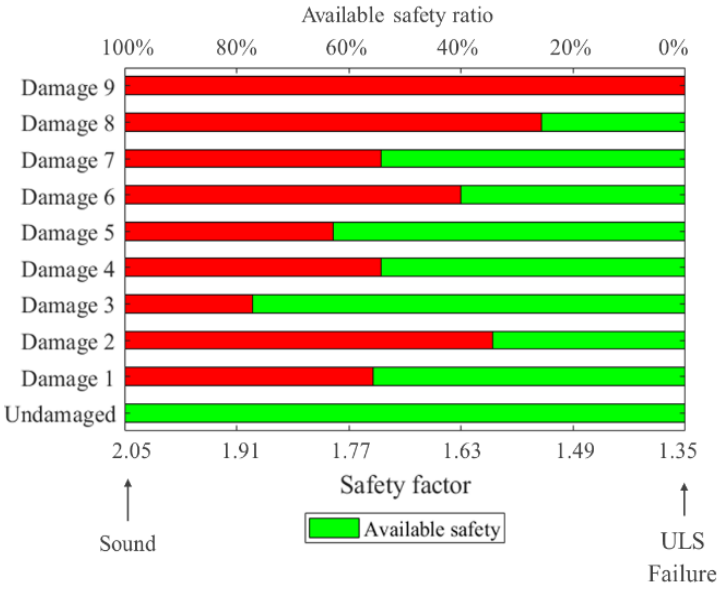

Figure 5-21: Safety factor comparison for the damage scenarios.

Damage thresholds

For each damage scenario, a 3D NLFEA is also carried out with the mean strengths of the materials applying the loads of the load test shown in Figure 5-8 (test lorries) used for the validation of the model. The test load represents a simulation of traffic load close to the frequent serviceability limit state combination.

This analysis is performed to define damage thresholds in terms of measurable static parameters on the structure and is useful to detect the degradation phenomena and their possible evolution on the existing bridges similar to the system under investigation. These damage thresholds are represented in terms of rotations near the supports and displacements at the midspan.

The limit rotation and displacement damage thresholds are evaluated on the model “Damage 9”. In fact, the application of ULS factorized LM1 loads on this model leads it to the collapse.

Table 5-14 shows the rotations in the support zones (supports 1 and 2 present the same rotations due to the symmetry of the load) and the displacements in the midspan of the Beam 1 for the different damage scenarios under the loads of the load test.

Figure 5-22 shows a comparison of the different models in terms of displacements, Figure 5-22 (a), and rotations, Figure 5-22 (b).

The two limit conditions are: undamaged deck with an available displacement and rotation capacity of 100% and model “Damage 9” with 0% available displacement and rotation capacity. All other damage scenarios represent an intermediate condition.

Table 5-14: Rotation and displacement under test loads.

Case	Rotation at support [mrad]	Displacement at midspan of Beam 1 [mm]
Undamaged	0.757	13.1
Damage 1	0.777	13.4
Damage 2	0.791	13.9
Damage 3	0.770	13.2
Damage 4	0.801	14.1
Damage 5	0.774	13.3
Damage 6	0.796	14.0
Damage 7	0.805	14.2
Damage 8	0.829	14.9
Damage 9 (ultimate condition)	1.180	25.5

Depending on the importance of the structure, the displacement and rotation results from the load test with respect to specific simulated damage scenarios can represent thresholds to derive the damage on the structure.

This procedure is useful for the evaluation of thresholds based on the damage level. In fact, during the in-situ test, with test loads lower than the load of the LM1, if the measured displacements/rotations are equal to those obtained with model “Damage 9”, the deck would have no margin of safety at the ULS.

If the displacements/rotations during the in-situ test are the same as the one of the "Undamaged" model, no deterioration of the bridge stiffness is observed. The measurement of a displacement/rotation during an in-situ load test can be compared to the displacement/rotation of a NLFEA model with a damage simulation, and if the two results are similar, an estimation of the damage level can, in theory, be deduced.

It is important to emphasize that damage thresholds based on localized parameters may not capture other critical forms of deterioration occurring in different areas of the structure—such as a reduction in shear capacity near a beam bearing—which can nonetheless significantly affect the overall load-bearing capacity. Furthermore, the rotation and displacement values associated with a specific damage scenario may, in reality, result from damage located elsewhere in the structure.

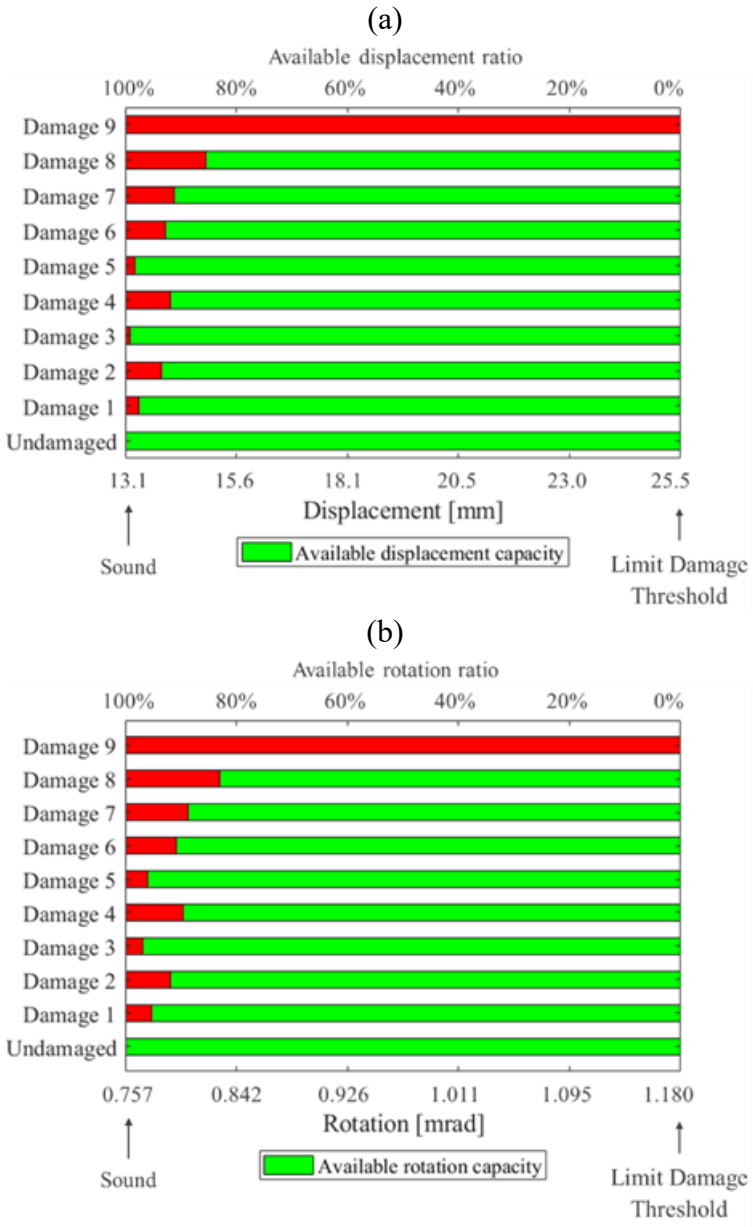

Figure 5-22: Comparison of the different damage scenarios under the test load: (a) displacements, (b) rotations.

Notably, the displacements and rotations measured under test loads (Figure 5-22) do not vary linearly with the reduction of the safety coefficient observed as damage progresses (Figure 5-21). This implies that a damage condition leading to a substantial reduction in the safety coefficient may not correspond to an equally significant change in the measured static displacements. This finding is particularly relevant for structures with a high ratio of permanent to variable loads—such as the one analysed in this study—where the effects of slight to moderate damage under service load conditions may be masked by the residual effects of prestressing. In such cases, the use of static parameters to detect damage proves largely ineffective.

Chapter 6

Case study: SHM of existing bridges

6.1. Chapter introduction

This chapter will present the results of dynamic monitoring activities on different types of viaducts.

A first case study is presented on a viaduct made of six girder decks and 3D frame piers (the viaduct is the same of the one examined in Chapter 4 for the safety assessment). For this viaduct, modal identification is performed by means of the SSI-Cov method (Section 3.3), after manual model updating is carried out on the viaduct's digital-twin taking into account some of the fundamental parameters that govern the structural response of the system. This first case study is used to investigate the influence of some structural parameters on the dynamic response of the digital-twin.

A second case study focuses on a historic arch bridge. For this structure, modal identification is carried out using the PolyMAX method and compared with results obtained from the SSI-Cov method (Section 3.3), in order to assess the consistency and reliability of the two identification techniques. A parametric analysis is then conducted to investigate the influence of various modelling parameters and to define the physical range of the problem. Once the most influential parameters are identified, the digital twin is calibrated through optimization using genetic algorithms.

The third case study examines a viaduct with a continuous box-girder deck. Modal identification is again performed using the PolyMAX method (Section 3.3). This is followed by a parametric study to determine the key modelling parameters and their physical bounds. As with the previous case, the digital twin is subsequently optimized using genetic algorithms, based on the identified parameters.

Across the three case studies—each representing a distinct structural typology—the modelling parameters most significantly affecting the dynamic behaviour of the digital twins are analysed. While some parameters exhibit a consistent influence across all structural types, others are specific to particular configurations.

6.2. Modal identification and model updating of an existing viaduct. Case study 1

This section will present the results of the modal identification and digital-twin model updating of an existing highway viaduct. The viaduct under consideration was built in the late 1950s. To date it has exceeded its design life (i.e. 50 years) and the objective of the monitoring system is to understand its health condition.

In particular, modal identification is performed through the SSI-Cov method (Section 3.3). The modal identification algorithm was implemented within MATLAB environment [112].

Model updating is performed on the digital-twin of the structure using the software SAP2000 after identifying the experimental modal parameters of the structure using the OMA method, [102].

Model updating is performed manually in this case by varying structural parameters that may have an influence on the dynamic behaviour of the structure. The structural parameters taken into account are:

- Modal masses of the structural system. Namely, weights of structural permanent loads and weights of non-structural permanent loads (especially road pavement, safety barriers and kerbs);
- Stiffness of bearing devices between decks and piers;
- Mechanical properties of the foundation soil and interaction between foundation and soil;
- Mechanical properties of materials.

Description of the Monitoring System

The viaduct consists of 50 m and 20.8 m prestressed reinforced concrete girder decks simple supported on 3D frame piers. Figure 6-1 (a) is a plan view and Figure 6-1 (b) is a side view of the viaduct. Red dots in the figure indicate the location of the accelerometers. All accelerometers are triaxial.

Only a part of the viaduct is monitored: the sensors are installed on one 50 m span and the two 3D frame piers with hammerhead supporting it.

On the 50 m span there are two triaxial accelerometers in the midspan section, one for each of the edge beams. At the ends of the hammerhead cantilevers of the piers there are two triaxial accelerometers, one on each side.

Accelerometers sampling rate is $f_s = 125\ Hz$.

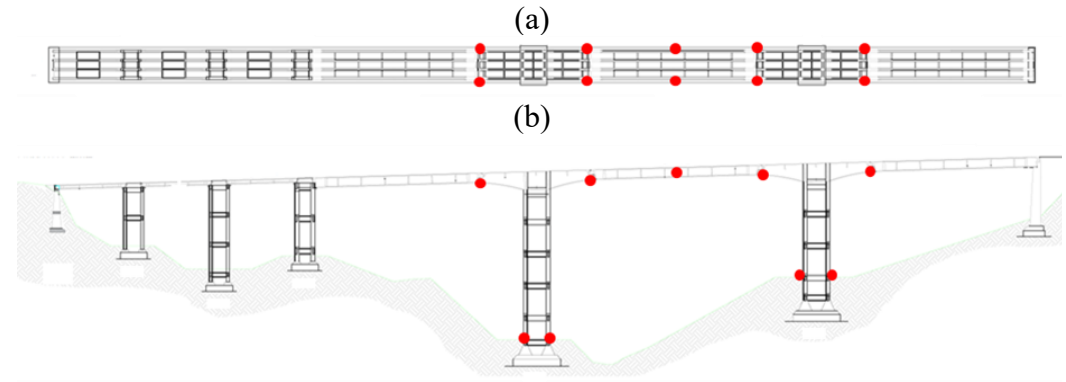

Figure 6-1: Geometry and sensors positions. (a) Plan view. (b) Side view.

Dynamic identification

Dynamic identification is performed with the OMA SSI-Cov method on a 34-minute acquisition performed on 23/05/2022 from 9:38 a.m. to 10:12 a.m. Traffic is the main source of excitement provided to the structure.

In the application of the SSI-Cov method, two parameters play a key role in the accuracy of identification: the maximum model order and the number of block rows. Ranges for choosing these two parameters are given in [113]. Following a sensitivity analysis to these parameters, the most appropriate pair of values provides the stabilisation diagram shown in Figure 6-2. With a maximum model order of 250 and a number of block rows of 300.

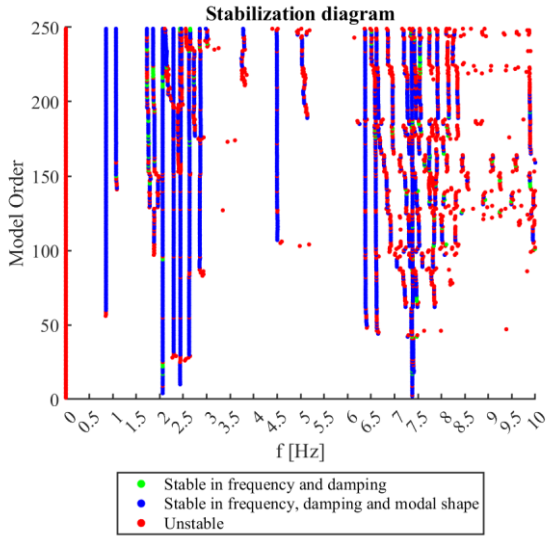

Figure 6-2: Stabilisation diagram for the viaduct under investigation.

Once the stabilisation diagram is obtained, the modal parameters of the system (i.e. frequencies, damping and modal forms of vibration modes) should be extrapolated.

The modes of the system are represented by the alignment of the stable poles in the stabilisation diagram (blue dots alignment). A density-based clustering algorithm

[114] is used for the extraction of modal parameters. The algorithm is usually named DBSCAN.

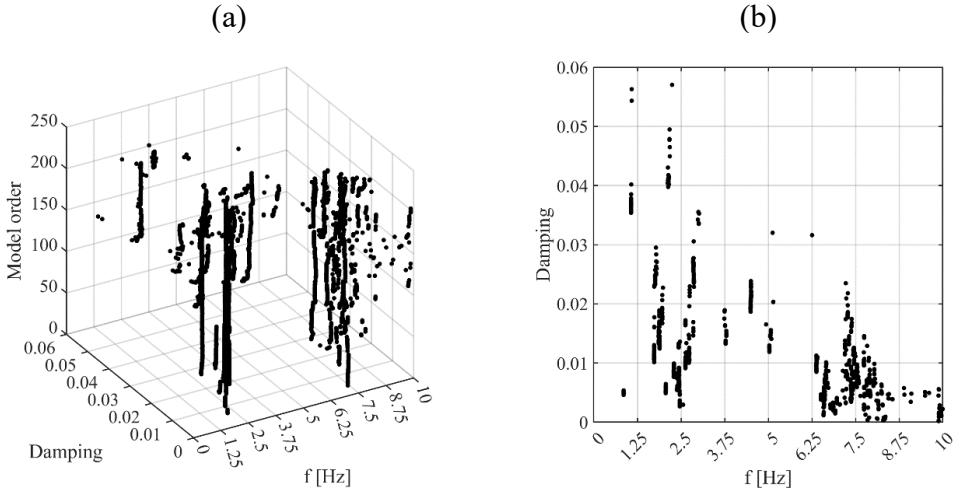

Figure 6-3: Visualisation of stable poles: (a) in 3D space frequency - damping - model order; (b) in 2D space frequency - damping.

Figure 6-3 shows the stable poles (blue dots in Figure 6-2) plotted in two different domains: Figure 6-3 (a) in the 3D frequency-damping-model order domain; Figure 6-3 (b) in the 2D frequency-damping domain.

Figure 6-3 (a) shows that the frequency alignments exhibit engineering-irrelevant changes in identified damping as the model order changes. Based on this last observation, the clustering algorithm can be applied to the 2D domain (Figure 6-3 (b)) imposing that at least 50% of the maximum order of the model is present in the cluster density.

Table 6-1: Identified frequencies and damping.

Mode	f [Hz]	Damping [%]	Description
1	0.86	0.49	Piers transverse flexional mode
2	2.06	0.59	Flexural mode of the deck
3	2.29	0.88	Piers longitudinal flexional mode
4	2.44	0.83	Flexural mode of the deck
5	2.63	1.22	Torsional mode of the deck
6	2.86	2.55	Torsional mode of the deck
7	4.50	2.01	Piers longitudinal flexional mode
8	6.38	0.95	Flexural mode of the cantilevers
9	7.38	0.58	Flexural mode of the cantilevers

Once the different clusters are obtained, each of them represents a mode of vibration of the investigated structural system. The mode frequency is the average of the pole frequencies and the mode damping is the average of the pole dampings within the cluster. The modal shape is the average of the modal shapes of the poles within the cluster, taking care to take all modal shape components in phase with each other.

Nine vibration modes are identified. Table 6-1 shows frequencies, damping and mode descriptions; Figure 6-4 shows the related modal shapes.

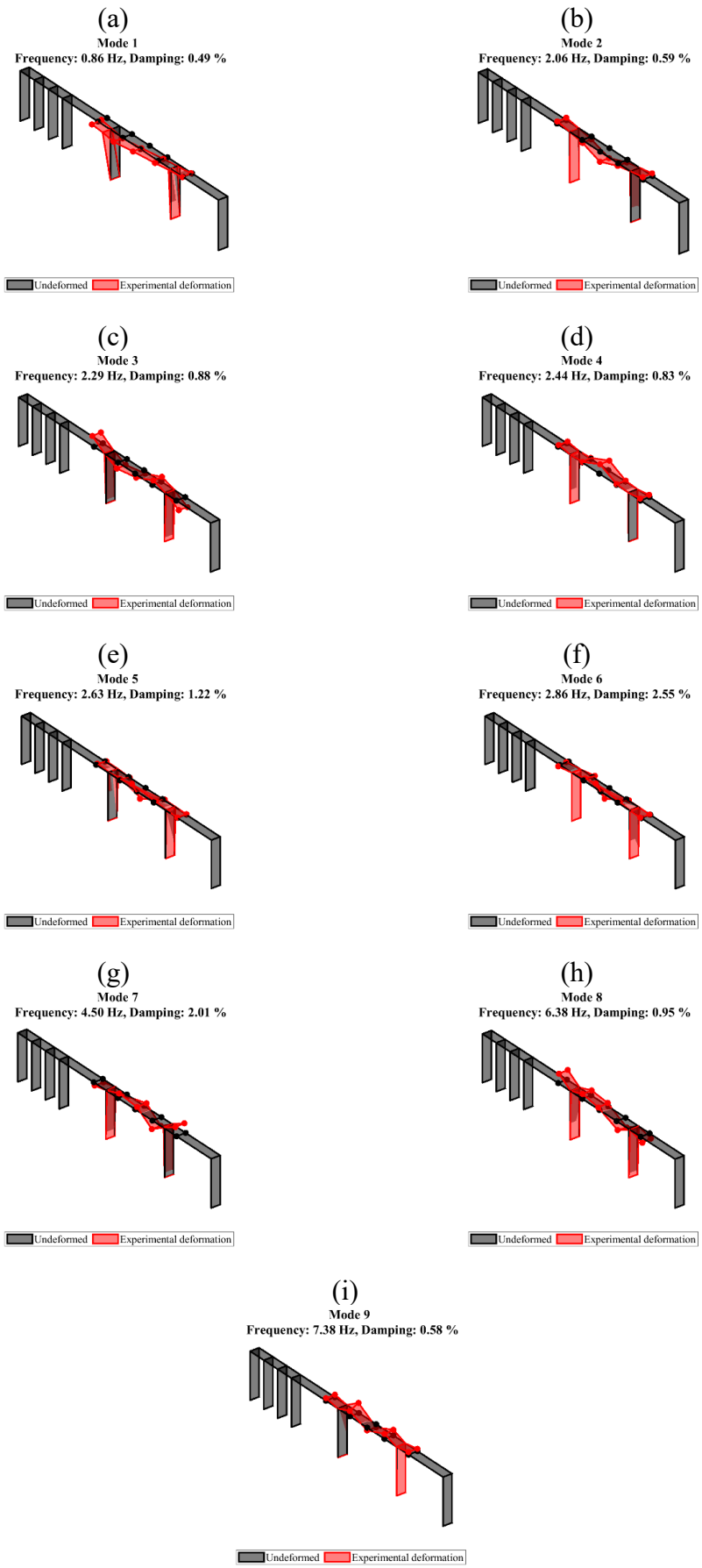

Figure 6-4: Identified modal shapes: (a) Mode 1; (b) Mode 2; (c) Mode 3; (d) Mode 4; (e) Mode 5; (f) Mode 6; (g) Mode 7; (h) Mode 8; (i) Mode 9.

Figure 6-5 shows the auto-MAC matrix; that is, the matrix comparing all identified modal shapes with each other. Ideally, this matrix contains unit values on the main diagonal and near-zero values outside the main diagonal. In identification, it is possible to find MAC values between 0 and 1 outside the main diagonal, as in the present case.

This problem is mainly due to an insufficient number of sensors on the structure. It is therefore difficult to detect the differences between two modes that might appear very similar due to under-instrumentation [45]. In the present case, this is the case for the mode pairs Mode 2-Mode 4; Mode 5-Mode 6 and Mode 7-Mode 3.

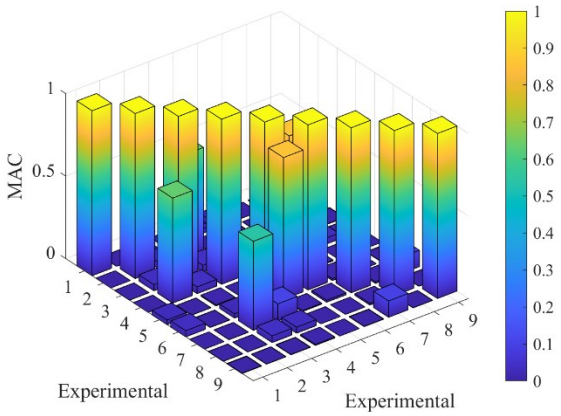

Figure 6-5: Auto-MAC matrix of identified modal shapes.

Digital-twin and model updating

This section provides details on the implementation of the digital-twin of the structure and the model updating performed on it.

Details on the realisation of the digital-twin FE model

The FE model is realised through the finite element software SAP2000 [102]. The modelling of the entire structure is realised with beam-type elements. A view of the FE model is shown in Figure 6-6.

Laboratory tests on concrete specimens are available for the decks and the cantilevers hammerheads. Therefore, the elastic modulus assigned to these elements is calculated from the values obtained from the laboratory tests.

No material investigations are available for the piers. According to design practice, the concrete used in the piers can have lower mechanical properties than the concrete used for the decks. Therefore, the modulus of elasticity of the concrete of the 20.8 metre decks (that showed the lowest mechanical properties) is assigned to the piers.

(a)

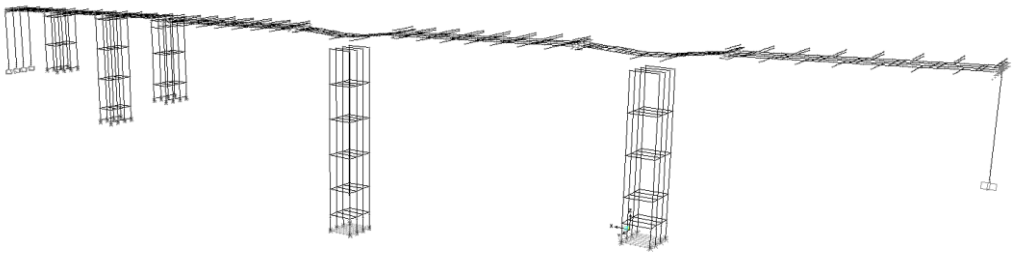

(b)

Figure 6-6: FE model of the structure under investigation. (a) Element view; (b) Extruded view.

A detail of the mechanical properties of the concrete assigned to the different elements is given in Table 6-2.

Table 6-2: Concrete properties.

Element	E_c [MPa]	f_{cm} [MPa]
50 m deck	34730	42
20.8 m deck	32945	36
Hammerhead cantilevers	34730	42
Piers	32945	36

No experimental evidence is available regarding permanent loads. Therefore, they were assumed in the first instance according to the current standard [24] for the design of a new structure. In detail, the following values of permanent structural and permanent non-structural loads were assumed:

- **Structural permanent loads** are represented by the self-weight of all elements that have a structural function in the viaduct. Since the viaduct is only made of reinforced and prestressed concrete, a weight of the structural elements of 25 kN/m^3 is assumed.
- **Kerbs** are not taken into account in the definition of the geometry of the structural elements of the decks, as they were probably realised after the construction of the decks. A linear load of 2.13 kN/m is introduced into the model. This load was assigned to the outermost longitudinal beam elements of the model, this assumption was adopted for modelling simplicity;
- **Safety barriers**. Standard New Jersey-type safety barriers are assumed, their weight being approximately 4600 kg per element. Each element has a linear development of approximately 6 metres. Therefore, a linear load

value of 8 kN/m was assumed in the model. The load, as for the kerbs, was assigned to the outermost longitudinal beam elements of the model;
- **Road pavement**. A load of 3 kN/m^2 has been assumed for the pavement in accordance with the standard.

Another key parameter in the realisation of the digital-twin is the stiffness of the foundation soil to model the soil-structure interaction. This parameter is taken into account in the model by placing elastic spring type constraints on the vertical displacements at the base of the pile foundation slabs. As there is no information on the foundation soil present in situ, standard soil stiffness values were imposed to approximate the actual response.

The initial stiffness of the vertical springs representing the soil deformability is chosen in order to achieve a vertical displacement of 1mm for every kgf/cm^2 of pressure on the soil under permanent loads. This stiffness is only a starting point and will be modified during model updating.

The last parameter influencing the dynamic behaviour of the digital-twin is the stiffness of the bearing devices between the deck and the piers. Generally the stiffness of old elastomeric bearings is an unknown parameter. Its starting value is assumed on the basis of their geometric dimensions and rubber properties. The starting stiffnesses assumed for the bearing devices are: K_H=8.5 kN/mm in horizontal direction; K_V=9000 kN/mm in vertical direction. These values are then updated during the model updating process.

Model updating of the digital-twin FE model. Results and discussion

The study of the influence of the parameters considered essential for model updating of the digital-twin FE model is presented below. The procedure reaches its end when the variations between the frequencies and modal shapes identified by the OMA techniques and the results of the digital twin FE model are engineering-acceptable.

For the case study under consideration, the following parameters were modified:

- **Reduction of non-structural permanent loads**. Current standards suggest a road pavement weight of 3.0 kN/m^2 [24]. This weight corresponds to a pavement thickness of about 15 cm using common bituminous conglomerates. The pavement weight has been changed until convergence reaching 2.6 kN/m^2 (13% reduction from nominal value) corresponding to a pavement thickness of 12÷13cm.
- **Introduction of rotational stiffness of bearing devices**. The rotational stiffness in longitudinal direction, usually neglected, has been introduced. The convergence value is 26000 kNm/rad. The value corresponds to the following condition:

    - the average value of the vertical reaction due to permanent loads on the 50m deck support is 1300kN;
    - the size of the bearings in the longitudinal direction is 40cm;
    - a realistic value of the reaction eccentricity with respect to the support axis is ¼ of the bearing dimension (10cm); this value is obtained from more refined analyses where the bearing is modelled with 3D f.e.m;
    - the bending moment corresponding to this eccentricity is 130 kNm;
    - a deformation of the rubber pad equal to 1mm on one side and a rise of 1mm on the opposite side as a result of this moment (thus a rotation of 0.005 rad) is assumed;
    - the rotational stiffness of 130/0.005 = 26000 kNm/rad is obtained.
- **Variation of horizontal stiffness of rubber bearing devices**. The initial stiffness in the horizontal direction of the bearing devices is assumed to be 8.5 kN/mm which corresponds to the deformability of a new bearing device. The actual rubber bearing pads may have different mechanical characteristics due to aging and deterioration. The stiffness of the rubber bearings has thus been incremented until convergence was found for a value that is about one hundred times the original one. This value simulates almost complete interlocking of the decks. The possible presence of forces exchanged through the expansion joints in the slab is not considered in the analysis but could be introduced as the joints could present passive resistance due to aging and presence of dirt and debris within the joints.
  The possible forces exchanged in the joints can sum up with the ones exchanged within the bearings and therefore change the result obtained for the horizontal stiffness of the bearings.
- **Increase in elastic modulus of concrete** to consider the homogenization of sections for the presence of reinforcement. The increase in the area and inertia properties of the section due to reinforcement is taken implicitly into account by the increase in elastic modulus. Elastic modulus of homogenized section is increased up to 10% for decks and piers' hammerheads and up to 5% for vertical elements of the piers. This variation enables accounting for the stiffening effect of reinforcement in a simplified way in a purely elastic f.e.m. model where reinforcement bars are not modelled.
- **Variation of the stiffness of the foundation soil**. In the starting model the springs placed under the foundation of the piers to simulate the deformability of the foundation soil are assumed to allow a displacement equal to 1 mm under a load of 10N/cm^2 applied after consolidation under permanent loads. At convergence this stiffness is doubled.

Table 6-3 shows the results of model updating in terms of frequency whereas Table 6-4 shows the same results in terms of modal shape, comparing the modal shapes of the starting FE model to the ones at the end of the process when convergence is reached (model f).

In finite element (FE) model a, the first modification to the original model is introduced by reducing the non-structural permanent loads. FE model b is derived from model a by incorporating rotational stiffness in the elastomeric bearings. FE model c builds on model b by tripling the horizontal stiffness of the elastomeric bearings. In FE model d, the elastic modulus of concrete is increased—relative to model c—to account for the homogenization effect due to reinforcement. FE model e is obtained from model d by increasing the stiffness of the foundation soil. Finally, FE model f is derived from model e by increasing the horizontal stiffness of the elastomeric bearings by a factor of 100, thereby simulating near-complete interlocking between the decks.

The potential interaction through expansion joints in the deck slab is not considered in the analysis. However, such forces could be introduced, as the joints may offer passive resistance due to aging, accumulated debris, or other obstructions.

Table 6-3: Results of model updating in terms of frequency.

		FE model						
Mode	Frequency identified with OMA [Hz]	Starting [Hz]	a [Hz]	b [Hz]	c [Hz]	d [Hz]	e [Hz]	f [Hz]
1	0.86	0.48	0.48	0.48	0.52	0.53	0.52	0.67
2	2.06	1.80	1.80	1.80	1.78	1.83	1.86	1.87
3	2.29	1.93	1.93	1.94	1.93	2.01	2.03	2.03
4	2.44	1.99	1.99	2.00	2.01	2.08	2.11	2.12
5	2.63	2.34	2.34	2.34	2.17	2.23	2.25	2.31
6	2.86	2.28	2.28	2.28	2.24	2.32	2.34	2.41
7	4.50	3.77	3.77	3.78	3.81	3.91	3.92	3.72
8	6.38	5.70	5.70	5.70	5.70	5.87	6.02	6.28
9	7.38	6.44	6.44	6.45	6.45	6.63	6.73	7.10

a) Original + Reduced non-structural permanent weight.
b) a + Rotational stiffness bearing devices.
c) b + Horizontal stiffness of rubber bearings triplicated.
d) c + Homogenization effect of ordinary and prestressing reinforcement.
e) d + Increased foundation soil stiffness.
f) e + Rigid rubber bearings in horizontal direction.

Figure 6-7 shows the evolution of the MAC matrix between experimental and numerical modal shapes. It can be seen that by switching from the original FE model to the end of the model updating process (from starting model to model f) there is an increase in the average MAC between experimental and numerical modal shapes. The average MAC increase is 13.9%.

Figure 6-8 shows the trend in frequencies and MAC following the changes in the FE model. A trend of increasing frequencies (Figure 6-8 (a)) can generally be seen as the model changes. This trend is most evident in Mode 1 (transverse horizontal) and in Modes 8 and 9 (bending of cantilevers). With regard to MAC (Figure 6-8 (b)), there are modes that are not clearly influenced by changes in the

different FE models and they are generally bending modes. On the other hand, the transverse horizontal modes and torsional modes of the deck are most affected by the variation of structural parameters in the FE model. The most impactful parameter is the stiffness of the bearing devices.

Table 6-4: Results of model updating in terms of modal shape. Comparison of modal forms between original FE model and f FE model.

	Starting FE model	f FE model
1	**Mode 1** **Frequency: 0.86 Hz, Damping: 0.49 %** 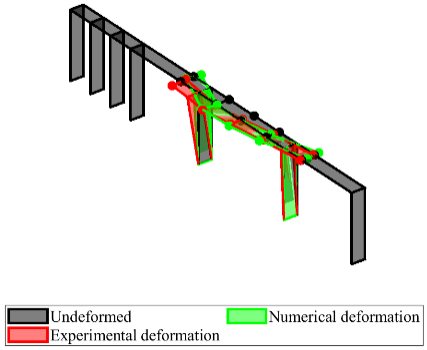	**Mode 1** **Frequency: 0.86 Hz, Damping: 0.49 %** 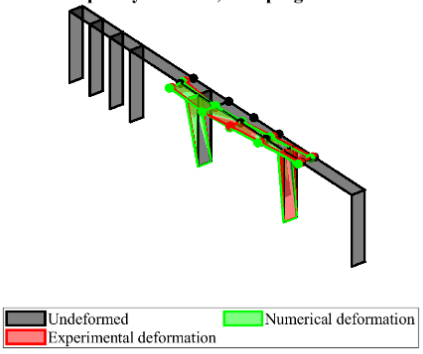
2	**Mode 2** **Frequency: 2.06 Hz, Damping: 0.59 %** 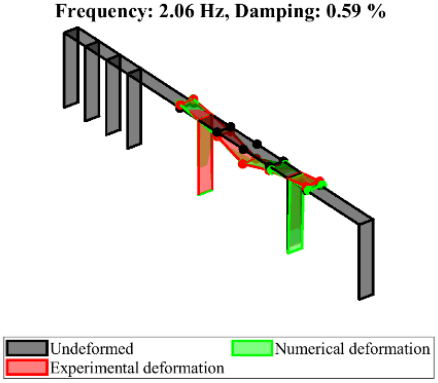	**Mode 2** **Frequency: 2.06 Hz, Damping: 0.59 %** 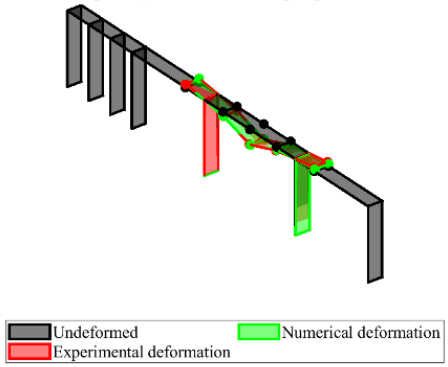
3	**Mode 3** **Frequency: 2.29 Hz, Damping: 0.88 %** 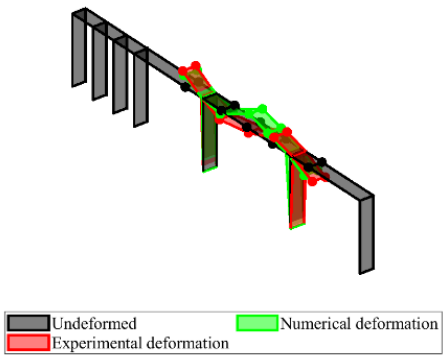	**Mode 3** **Frequency: 2.29 Hz, Damping: 0.88 %** 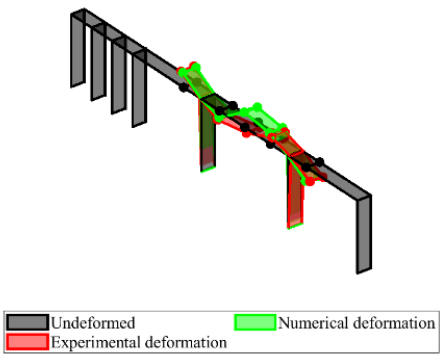

4	**Mode 4** **Frequency: 2.44 Hz, Damping: 0.83 %** 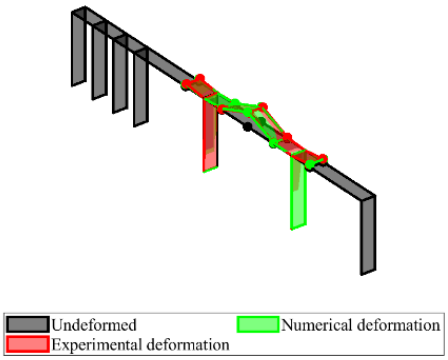 	**Mode 4** **Frequency: 2.44 Hz, Damping: 0.83 %** 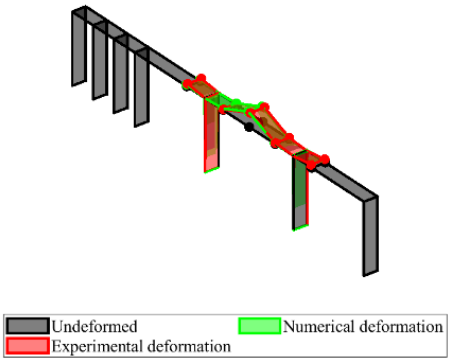
5	**Mode 5** **Frequency: 2.63 Hz, Damping: 1.22 %** 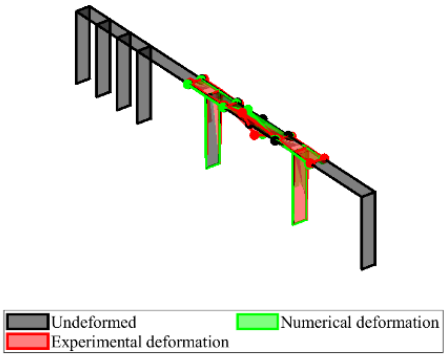 	**Mode 5** **Frequency: 2.63 Hz, Damping: 1.22 %** 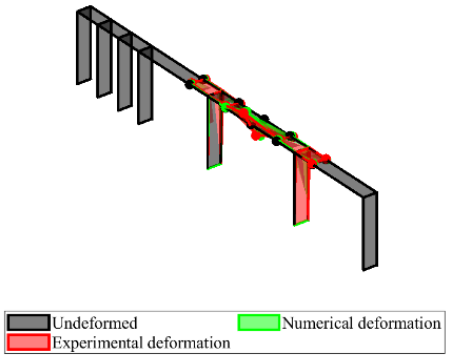
6	**Mode 6** **Frequency: 2.86 Hz, Damping: 2.55 %** 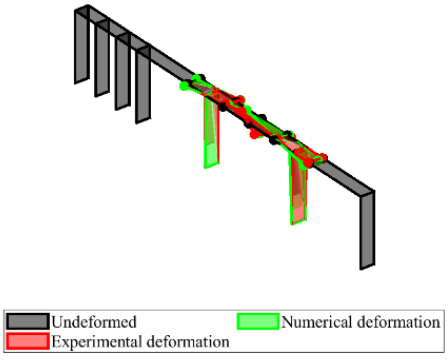 	**Mode 6** **Frequency: 2.86 Hz, Damping: 2.55 %** 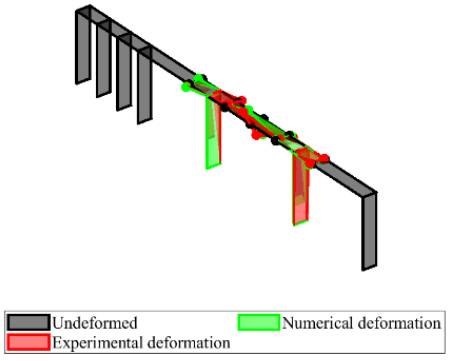
7	**Mode 7** **Frequency: 4.50 Hz, Damping: 2.01 %** 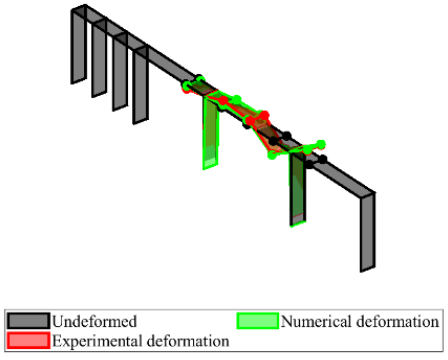 	**Mode 7** **Frequency: 4.50 Hz, Damping: 2.01 %** 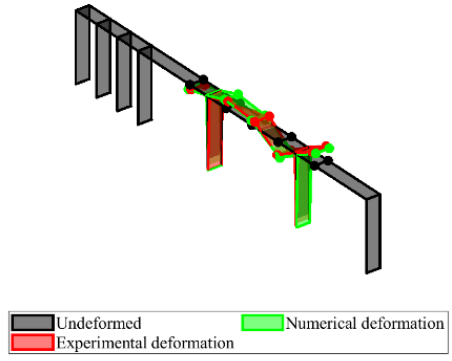

8	**Mode 8** **Frequency: 6.38 Hz, Damping: 0.95 %** 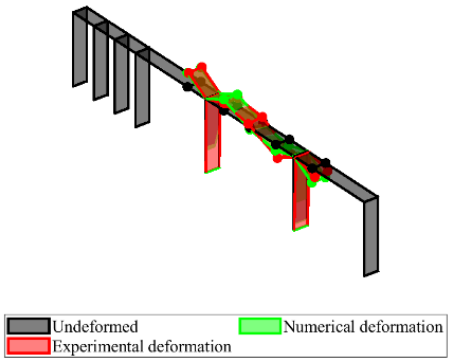 	**Mode 8** **Frequency: 6.38 Hz, Damping: 0.95 %** 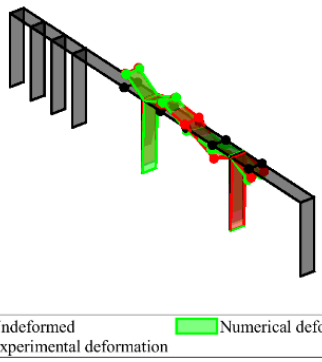
9	**Mode 9** **Frequency: 7.38 Hz, Damping: 0.58 %** 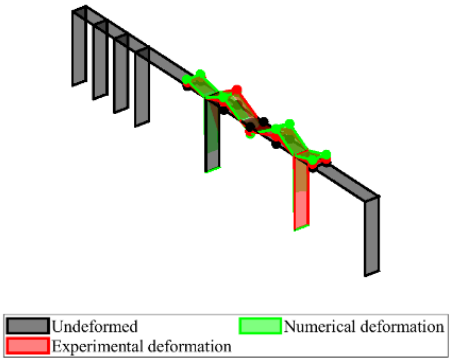 	**Mode 9** **Frequency: 7.38 H %** 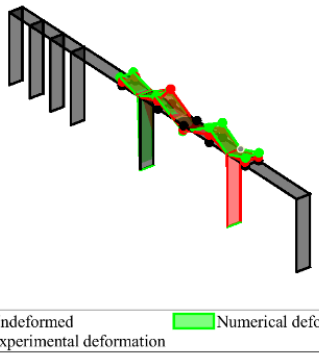

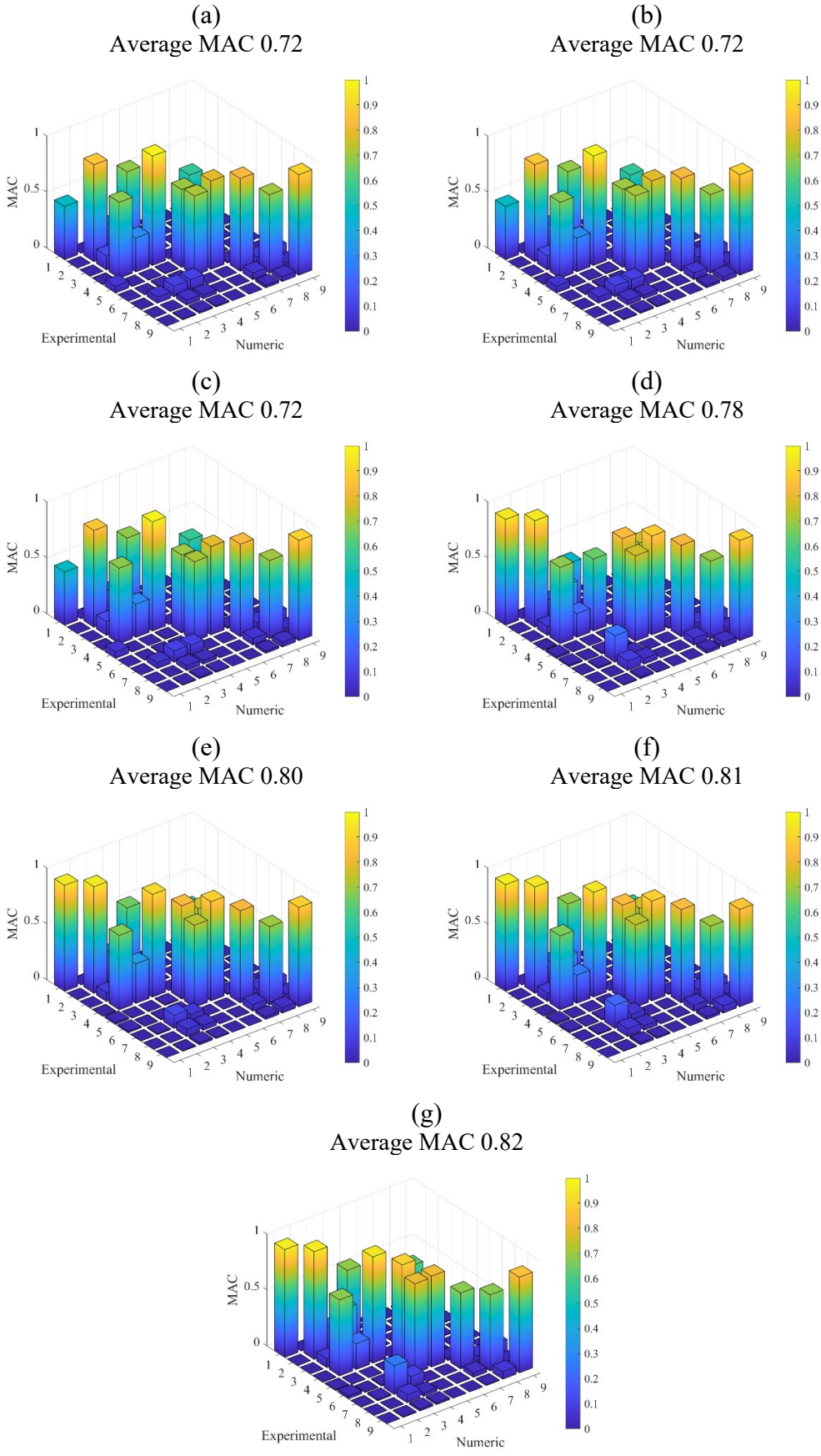

Figure 6-7: MAC between identified modal forms and FE models. (a) Original FE model; (b) a FE model; (c) b FE model; (d) c FE model; (e) d FE model; (f) e FE model; (g) f FE model.

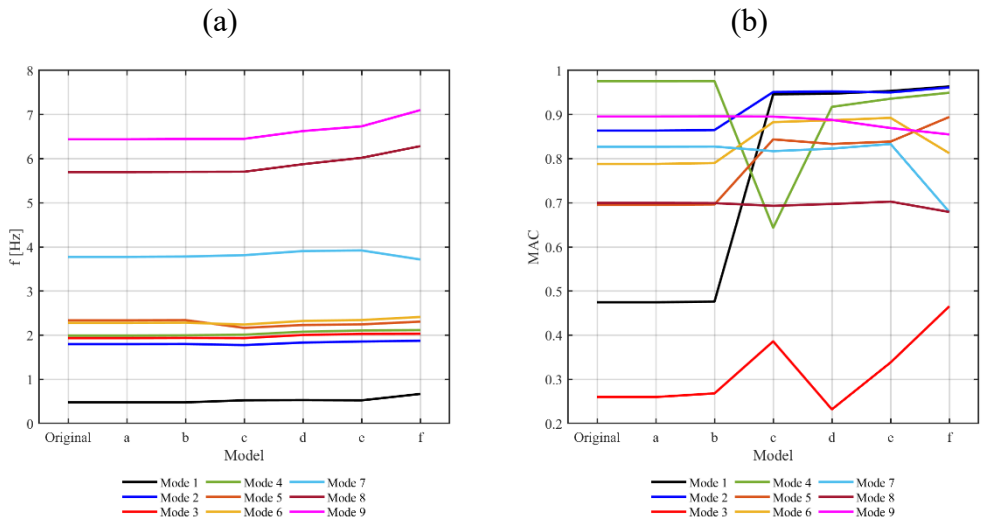

Figure 6-8: Trends varying the model. (a) Frequencies; (b) MAC.

Figure 6-9 shows variations between different FE models frequencies and identified frequencies (Figure 6-9 (a)) and between different FE models modal shapes and identified modal shapes (Figure 6-9 (b)).

The starting FE model has an overall average error of -18.0% (Figure 6-9 (a)) with respect to the identified frequencies. The largest error is related to horizontal modes, which amounts to -44.1%, whereas the error on bending modes amounts to -14.4% and the error on torsional modes amounts to -15.7%.

In general, the starting f.e.m. model is more deformable than the real structure. FE model f is considered in this study the ultimate result of model updating, nevertheless it still shows a global error from the identified frequencies of -11.7%: -21.8% for horizontal modes; -9.4% for bending modes and -13.9% for torsional modes. It basically halved the error between starting FE model results and identified frequencies for horizontal modes.

The effect of model updating was weaker for bending and torsional modes. It still shows an average global error slightly higher 10% but can be considered engineeringly a fair tool for evaluating and interpreting monitoring data and understanding the structural behaviour.

The most impactful effects on the matching of modal shapes (Figure 6-9 (b)) is covered by the stiffness of the bearing devices placed between decks and piers and the stiffness of the foundation soil. These two parameters play a fundamental role especially on transverse horizontal modes and torsional modes.

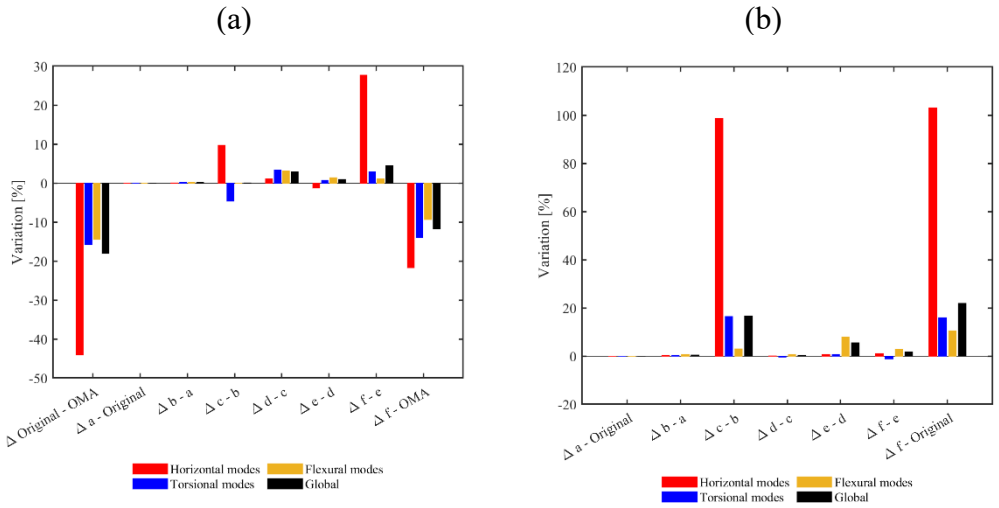

Figure 6-9: Variations between different models. (a) Frequency variations; (b) MAC variations.

From the above results, the following considerations can be made:

- Starting FE model, which is similar to common design model, is about 20% more deformable than the actual structure when it is subjected to environmental vibration.
- The most important stiffening effect in model updating is achieved by varying the stiffness of the bearing devices, especially their horizontal stiffness. It is common design practice to use the horizontal stiffness of these devices provided by the producer; but due to aging, deterioration, or malfunction it can be significantly higher.
- Foundation deformability is another impactful parameter. It is common practice in design phase to consider a full restraint at the base of the piers. This modelling choice may be far from the actual behaviour of the structure even in the case of deep foundations.
- Permanent loads estimation and actual stiffness of sections/materials play a less impactful but still not negligible effect. it is common practice to use parameters suggested by design standards for both parameters in the absence of in situ testing.

6.3. Modal identification and model updating of an historic bridge. Case study 2

This section will present the results of the modal identification and digital-twin model updating of an historic concrete bridge shown in Figure 6-10. The approach used is similar to that followed in Section 6.2 for case study 1, but with the following differences:

- The method of identification. The OMA PolyMAX method [60] (Section 3.3) implemented commercially in the Siemens TestLab software [115] is used in this case study.
- Model updating is performed with the support of a genetic algorithm (Section 3.5) implemented in MATLAB [112].

The structure was built in 1915. It is entirely made of ordinary reinforced concrete. It consists of two central arches 37.5 m long and a girder deck of 14 spans, with a total length of 129.5 m.

The superstructure has been subjected to several maintenance and retrofitting interventions over time. The original one consists of four longitudinal beams and three transverse beams.

As a result of retrofitting interventions, the slab was widened from 5.5 m to 8.65 m.

The slab was strengthened by adding a new 20 cm layer to the original one that was 15 cm thick.

Two longitudinal side beams, larger than the existing ones, were added. Cantilevers were to the transverse beams in order to support the additional slab.

The roadway is straight, the carriageway is 6.25 m wide and contains two traffic lanes, one in each direction. Figure 6-11 shows the pan view of the bridge.

Figure 6-12 and Figure 6-13 show the geometric details of the bridge.

Figure 6-10: Picture of the bridge.

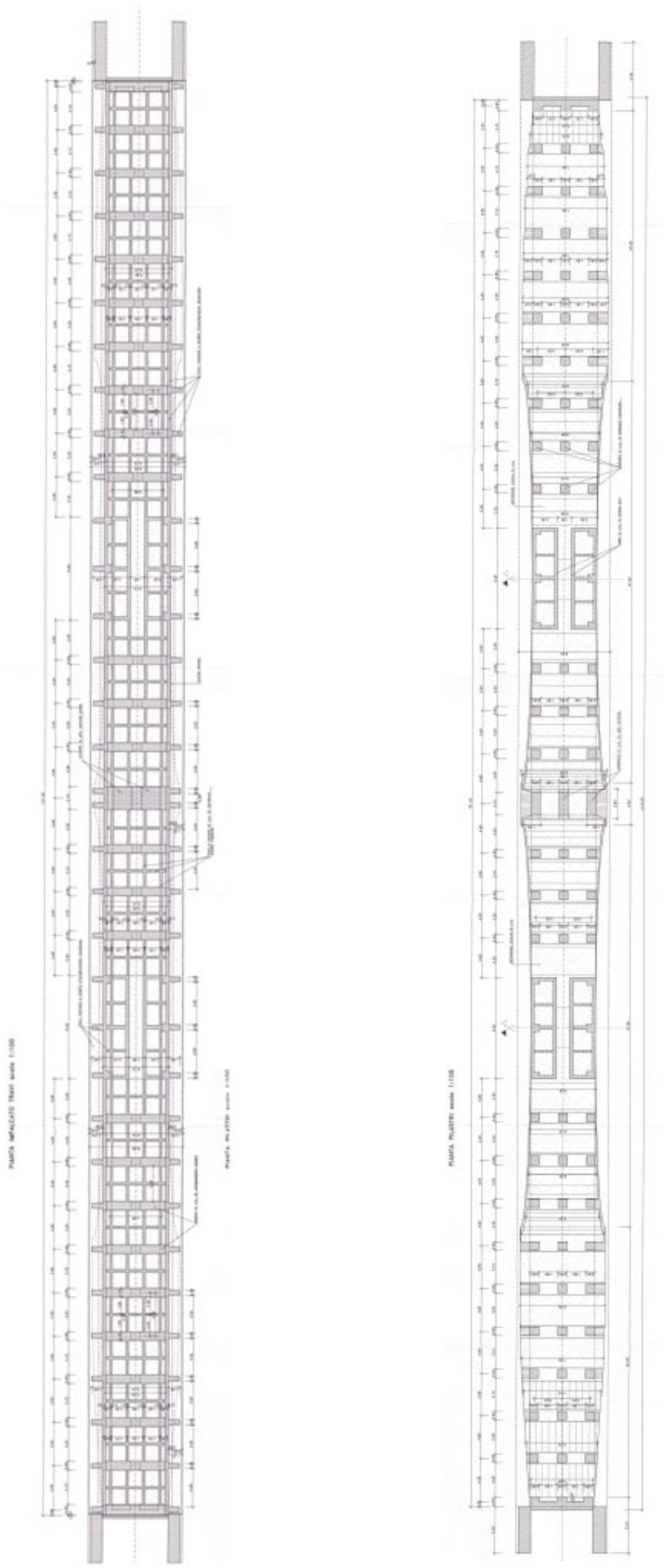

(a) (b)

Figure 6-11: Geometric details of the bridge. (a) Plan view of the deck; (b) Plan view of the substructure.

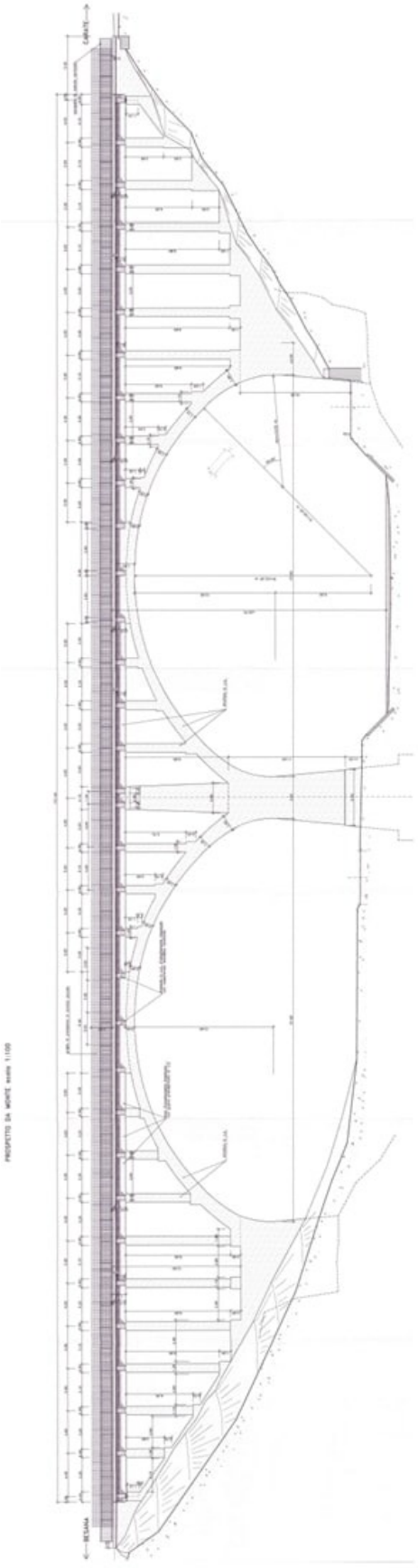

Figure 6-12: Side view of the bridge.

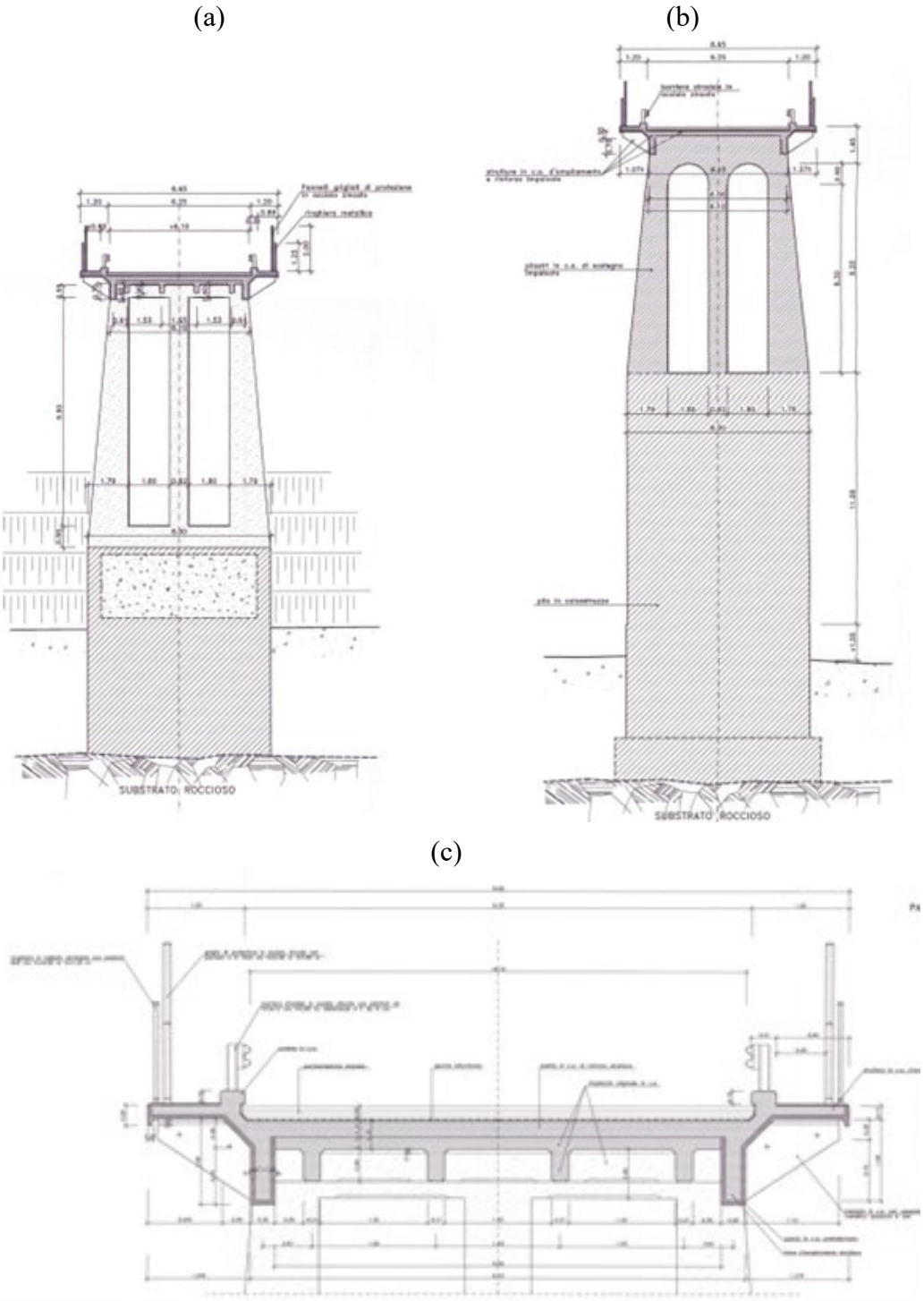

Figure 6-13: Geometrical details of the bridge. (a) Generic pier transverse section; (b) Central pier transverse section; (c) Bridge deck transverse section.

Description of the Monitoring System

The monitoring layout, shown in Figure 6-14, includes the installation of mono-axial and triaxial capacitive accelerometers. Mono-axial accelerometers (red dots in Figure 6-14) are uniformly positioned on the two arches, while the triaxial accelerometers (green dots in Figure 6-14) are installed in correspondence of the middle of the arches and in the central pillar.

A weather station is also placed at the centre of the bridge. In this case, due to the long service life of the structure, the purpose of the monitoring system is to evaluate the structural integrity of the most important structural elements (i.e. arches), which could be potentially compromised due to the loads generated by the current traffic conditions for which it was not originally designed.

For this structure, data for OMA analysis are recorded and saved in the cloud twice a day from February 2023: in a time window from 8:00 to 10:00 a.m. and in a time window from 7:00 to 8:00 p.m. Accelerometer recordings are sampled at a rate of $f_s = 200\ Hz$.

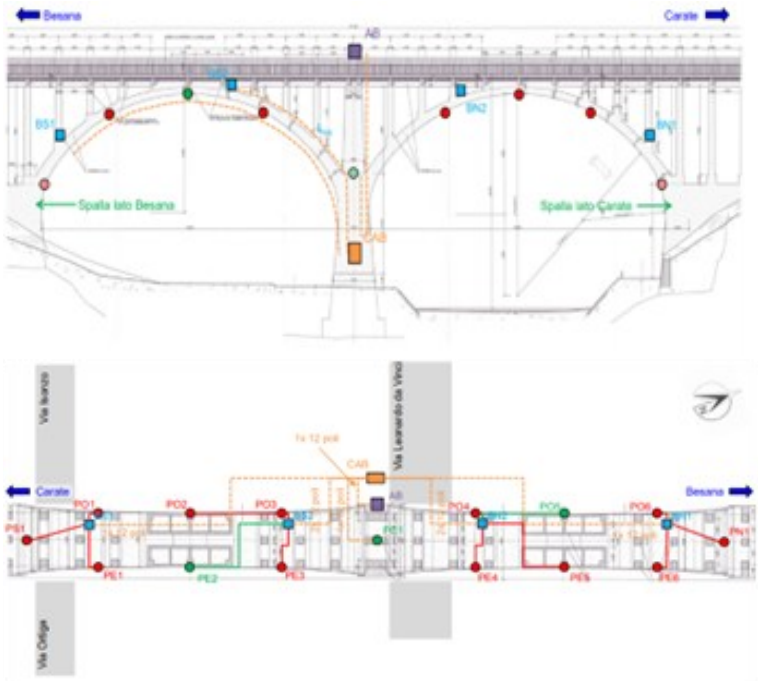

Figure 6-14: Monitoring system scheme.

Dynamic identification of the structure

As specified above, the dynamic identification in this case study is carried out using TestLab, a commercial software [115] in which the OMA PolyMAX identification algorithm is implemented.

A comparison between the dynamic identification performed with TestLab and the one performed with a code written in MATLAB environment (SSI-Cov) is shown, as an example, for the data regarding one day, the 28/02/2023.

The results in terms of frequency are shown in Table 6-5, in terms of damping are shown in Table 6-6, and in terms of modal shapes are shown in Figure 6-15. Good agreement between the two dynamic identification methods can be observed.

The identified modal shapes are shown in Figure 6-16.

Table 6-5: Comparison of identified frequencies. PolyMAX vs SSI-Cov.

Mode	$f_{PolyMAX}$ [Hz]	$f_{SSI-Cov}$ [Hz]	Variation [%]
1	3.36	3.34	+0.60%
2	4.12	4.13	-0.24%
3	4.61	4.62	-0.22%
4	6.48	6.49	-0.15%
5	7.72	7.72	0.00%
6	8.23	8.29	-0.72%
7	9.62	9.63	-0.10%
8	11.03	11.12	-0.81%

Table 6-6: Comparison of identified damping. PolyMAX vs SSI-Cov.

Mode	$\zeta_{PolyMAX}$ [%]	$\zeta_{SSI-Cov}$ [%]	Variation [%]
1	2.50%	3.06%	-18.30%
2	2.00%	2.14%	-6.54%
3	1.70%	1.78%	-4.49%
4	3.50%	3.57%	-1.96%
5	2.50%	2.42%	+3.31%
6	1.70%	2.89%	-41.18%
7	1.90%	2.09%	-9.09%
8	2.90%	3.16%	-8.23%

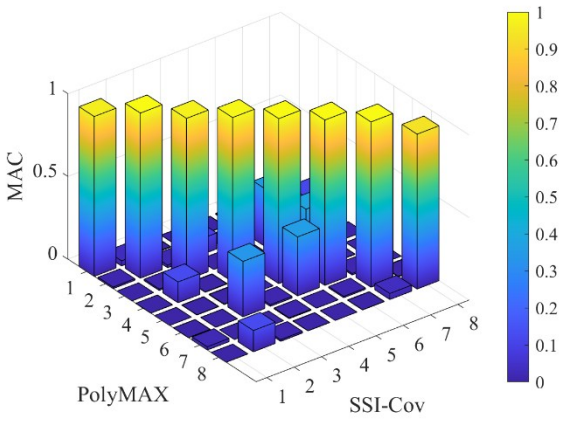

Figure 6-15: Comparison of identified modal shapes. PolyMAX vs SSI-Cov.

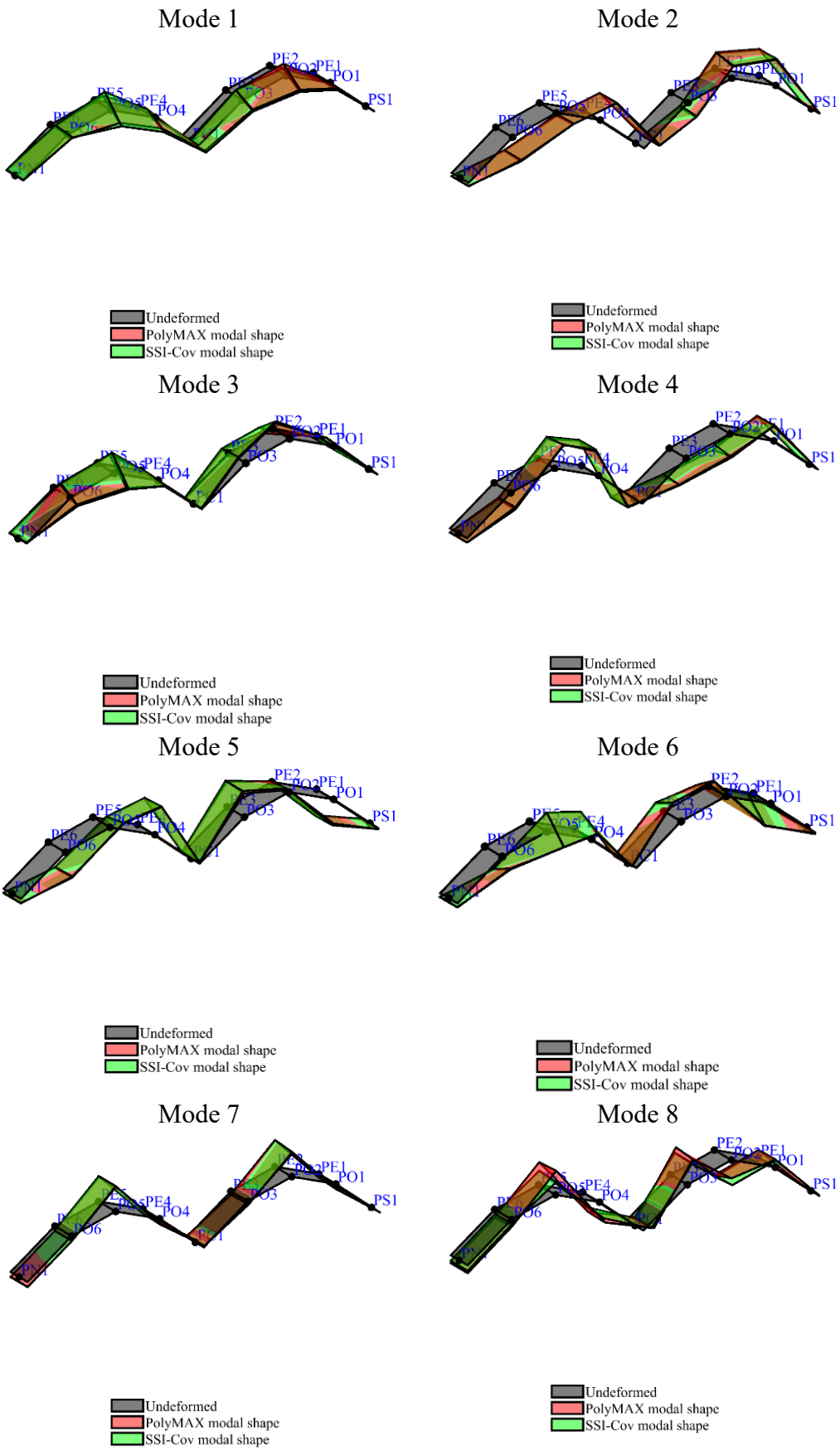

Figure 6-16: Identified modal shapes.

After comparing the two different OMA identification methods, dynamic identification is performed once a week from February 2023 to February 2024 with the PolyMAX method implemented in TestLab [115].

Figure 6-17. Figure 6-18 shows the linear regression between identified frequencies and temperatures. Some modes have a poor correlation between identified frequencies and temperatures (i.e. Mode 1 and Mode 6); some modes have a direct correlation between identified frequencies and temperatures (i.e. Mode 2 and Mode 5); all other modes have an inverse correlation between identified frequencies and temperatures.

The correlation between frequency and temperature is influenced by the viscous and temperature-dependent properties of the materials composing the structure - primarily concrete and bituminous pavement. The nature of this correlation (i.e., direct or inverse) depends on the specific vibration mode (i.e., modal shape), which can itself be affected by thermally induced deformation, thereby altering the frequency–temperature relationship.

In general, there is a correlation between identified frequencies and temperatures, but changes in frequency with changing temperature are marginal and engineering negligible.

The results in terms of identified damping and their trend over time compared to the temperature trend is shown in Figure 6-19. Damping is not clearly influenced by temperature variations. Furthermore, damping is one of the least stable dynamic identification parameters due to different random phenomena from which it is affected [116].

The results are summarised in Table 6-7.

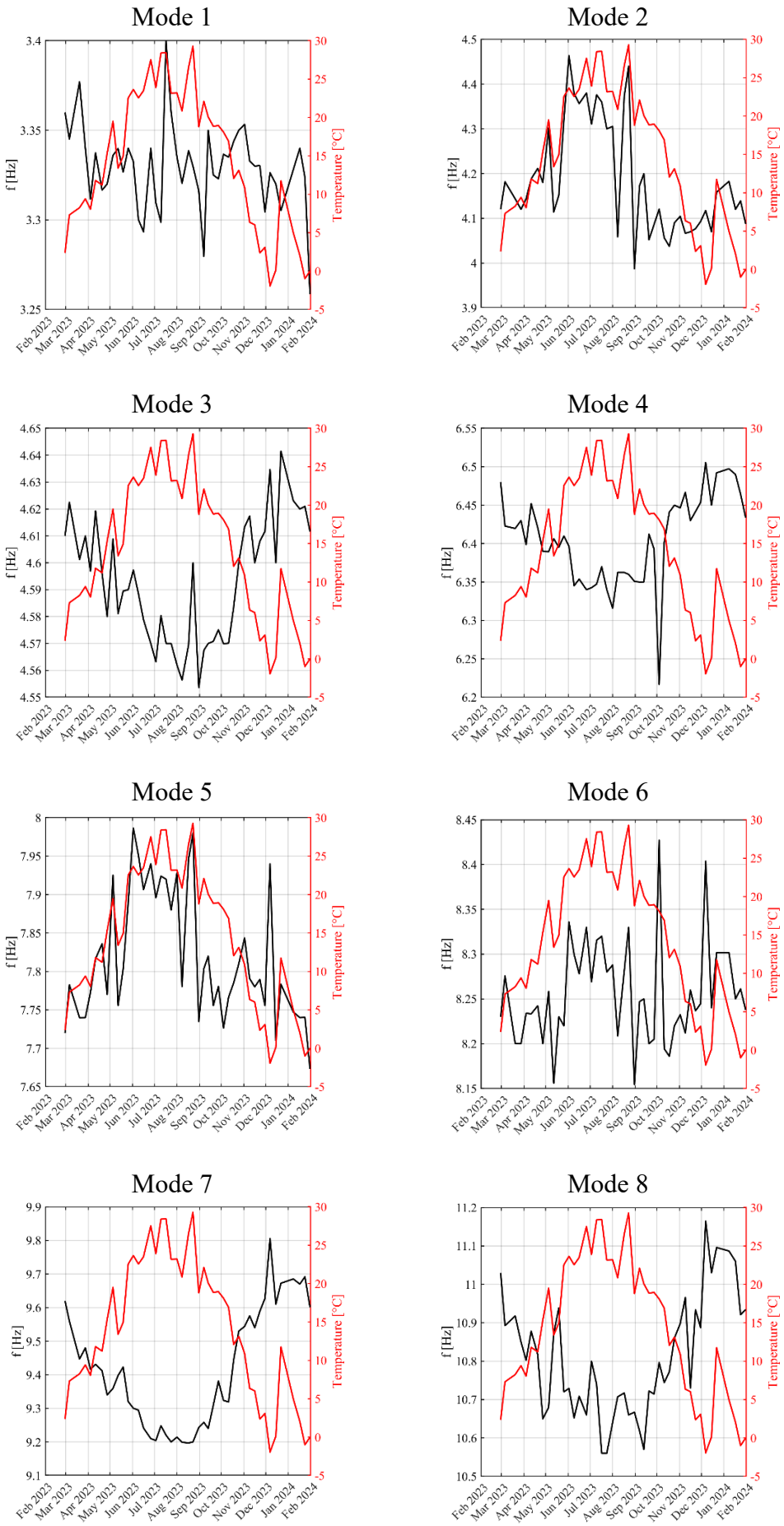

Figure 6-17: Trend of identified frequencies and comparison with the ambient temperature trend.

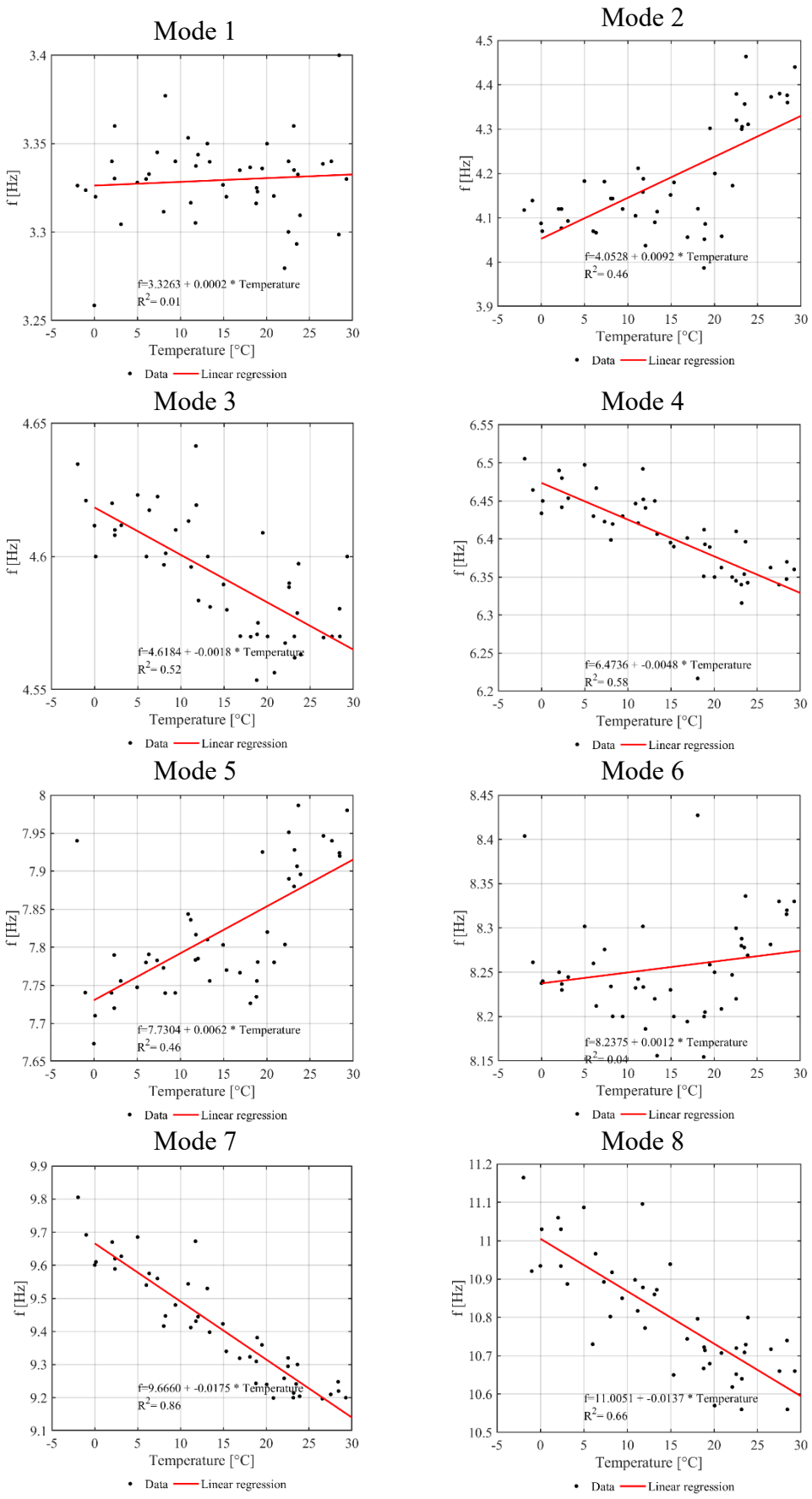

Figure 6-18: Linear regressions between identified frequencies and temperature.

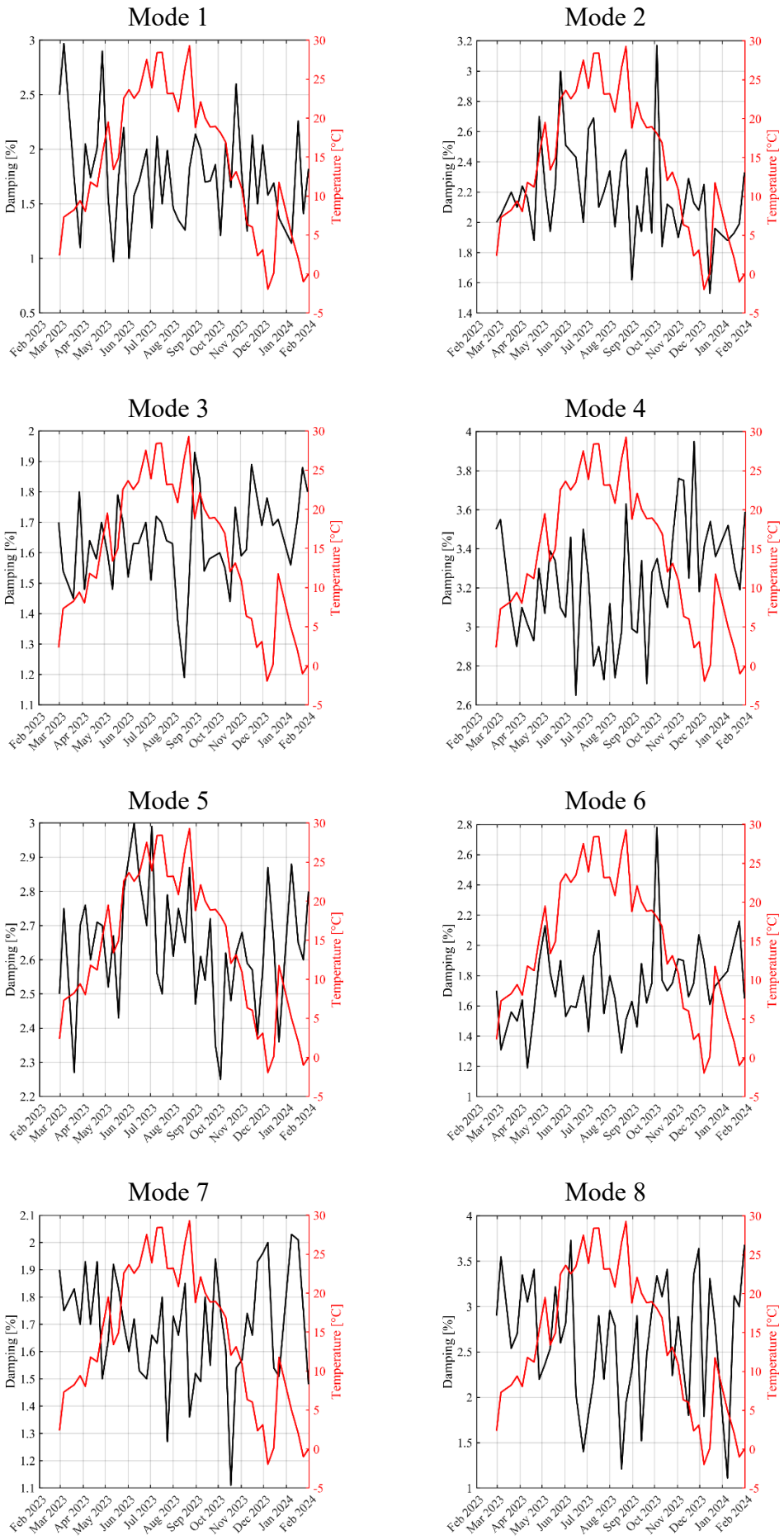

Figure 6-19: Comparison between identified damping trend and ambient temperature trend.

Table 6-7: Identified frequencies and damping.

Mode	f [Hz]	Damping [%]	Description
1	3.34	2.06	Transverse flexural mode
2	4.21	2.13	Longitudinal flexural mode
3	4.59	1.68	Torsional mode
4	6.39	3.19	Vertical flexural mode
5	7.82	2.65	Longitudinal flexural mode
6	8.25	1.76	Torsional mode
7	9.36	1.62	Vertical flexural mode
8	10.75	2.41	Longitudinal flexural mode

Figure 6-20 shows the auto-MAC matrix comparing all identified modal shapes with each other. Ideally, this matrix contains unit values on the main diagonal and near-zero values outside it.

Doing OMA it is possible to find high MAC values outside the main diagonal, as in the present case. This can be due to an insufficient number of sensors placed on the structure and therefore to the inability to pick up the differences between two modes that might appear very similar due to under-instrumentation. In the present case, this is the case for the mode pair 3-6.

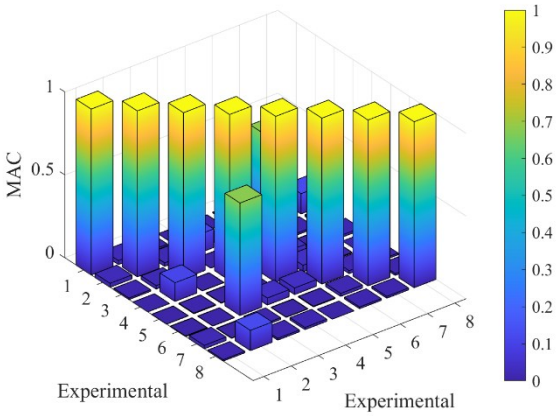

Figure 6-20: Auto-MAC matrix of identified modal shapes.

FE model digital-twin

In this section, the main details of the FE model creation are reported. The FE model is created with the commercial software SAP2000 [102] through the combined use of beam and shell type elements.

The deck is modelled through the combination of beam type elements used for longitudinal beams and transverse beams and shell elements for the slab.

Beams and slab have a vertical offset and are appropriately connected by rigid links.

The piers (shown in Figure 6-13) are modelled with beam-type elements and the abutments with shell type elements.

Foundations consist of transverse inverted T beams, modelled with shell elements. Arches are also modelled using shell elements.

The overall model is shown in Figure 6-21: beams are blue and shells are red.

The restraint conditions at the base of the structure are a crucial aspect, as they exert a significant influence on the dynamic behaviour of the bridge.

The soil-structure interaction is modelled through vertical Winkler-type spring beds. The calibration of the stiffness of these springs is obtained with the procedure shown for case study 1.

The mechanical properties of the concrete for this structure are unknown as no material investigations are available. The modulus of elasticity of concrete is therefore estimated in the ranges suggested in [117] as a function of the age of the structure. A first-attempt modulus of elasticity value is assumed to be 32310 MPa.

No experimental evidence is available regarding loads. Therefore, they are assumed in the first instance according to the current standard [24] for the design of a new structure. In detail, the following values of permanent structural and permanent non-structural loads are assumed:

- **Structural permanent loads** are represented by the self-weight of all elements that have a structural function in the bridge. Since the bridge is made in its entirety of ordinary reinforced concrete, a weight of the structural elements of 23 kN/m^3 is assumed. The weight is less than the usual 25 kN/m^3 as for historic ordinary concrete structures there is evidence of lower concrete weight than for today's weight [117].
- **Kerbs** are not taken into account in the definition of the geometry of the structural elements of the decks. A linear load of 1.15 kN/m is introduced into the model, as the geometry of the kerb consist of a rectangular cross section of 031m x 0.15m. This load is assigned at the external edge of the shell elements that model the deck slab.
- **Safety barriers**. Pedestrian parapet and guardrails are present on the bridge. For the pedestrian barriers a weight of 1 kN/m is assumed, for the guardrail a weight of 2 kN/m is assumed.
- **Road pavement**. A load of 3 kN/m^2 has been assumed for the pavement in accordance with the standard.

(a)

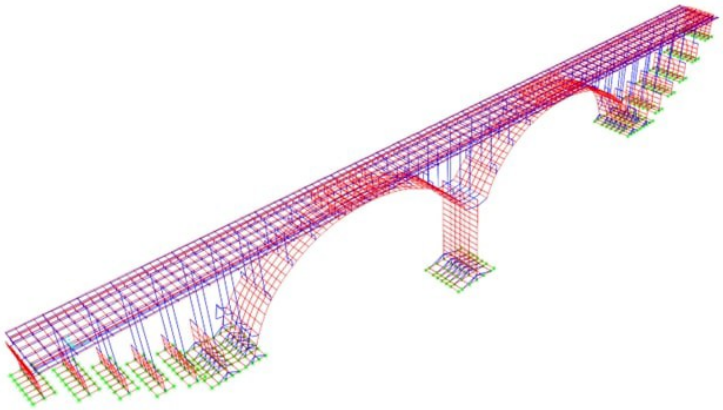

(b)

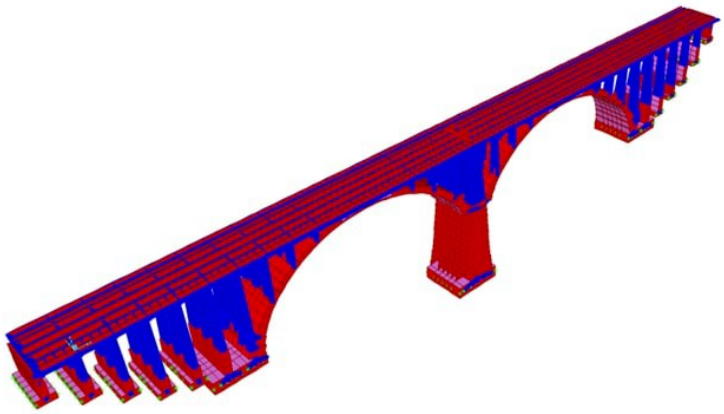

Figure 6-21: FE model of the structure. (a) wireframe view of the mesh. (b) 3D view of the mesh.

Model updating of the digital twin

As investigated in Case Study 1 (Section 6.2), the unknown parameters that can potentially influence the behaviour of the structure, and consequently the accuracy of the FE model, are the constraint conditions in the foundation and the mechanical characteristics of the material.

The stiffness the springs below the foundations in the starting FE model is set such that there is one millimetre of deflection under the action of structural permanent loads and non-structural permanent loads. Initial stiffnesses range from 8 kg/cm^2/cm to 48 kg/cm^2/cm. In particular, the stiffnesses vary from 8 kg/cm^2/cm to 15 kg/cm^2/cm for the approach piers from both sides. For the centre pier, there is a stiffness of 48 kg/cm^2/cm, and for the foundations of the impost of the arches, on both sides there is a stiffness of 25 kg/cm^2/cm.

The results of the starting FE model, in terms of frequencies, are shown in Table 6-8. It can be seen that on average the starting FE model is 11.6% more deformable than the real structure. In particular, it can be seen that modes involving the displacement of the central pier in the modal shape (Figure 6-16) have the highest error, modes not involving the central pier in the modal shape have very low error.

Table 6-8: comparison between frequencies of the starting FE model and the identified frequencies.

Mode	Frequency identified with OMA [Hz]	Frequency of the starting FE model [Hz]	Difference [%]
1	3.34	2.31	-30.8%
2	4.21	3.32	-21.1%
3	4.59	3.81	-17.0%
4	6.39	6.24	-2.3%
5	7.82	6.50	-16.9%
6	8.25	8.10	-1.8%
7	9.36	9.20	-1.7%
8	10.75	10.60	-1.4%
Average difference [%]			11.6 %

Preliminary "hand-made" analysis

The first approach conducted on the structure under investigation is a parametric analysis. The parameterisation evaluates all the combinations that can be performed within the set of possible solutions. The objective is to identify the optimal result and sensitivity to the change in the dynamic characteristics of the structure, i.e. frequencies and modal shapes, as the parameters studied vary. In particular, two hypotheses were initially assumed on the FE model:

- stiffness of the ground, and therefore of the springs under the foundation, constant throughout the development of the structure;
- stiffnesses of the ground divided into clusters, i.e. into subsets having the same deformability.

The hypotheses described are assumed to be simplified, since the precise evaluation of the deformability of the ground on each foundation element would entail a high computational burden and time. Furthermore, the results will not deviate significantly from the expected results, which, at the end of the model updating will prove to be already highly reliable.

The analyses were performed with the commercial f.e.m. software SAP2000 [102] and implemented using the numerical calculation programme MATLAB [112] to automate the input/output process. The performance of the results is assessed also using the MAC matrix, therefore, it is entered into the objective function in order to give an estimate of the model's conformity.

The parameterization was carried out over a range from a minimum foundation spring stiffness value of 8 kg/cm^2/cm to a maximum foundation spring stiffness value of 48 kg/cm^2/cm with a discretization of 4 kg/cm^2/cm for a total of 11 possible soil deformability input. The FE Model vibration modes, will be compared with the 8 identified modes. The best result is obtained with a stiffness value of 48 kg/cm^2/cm. In Table 6-9 the comparison between identified modal shapes and modal shapes of the FE model is shown for the soil stiffness equal to 48 kg/cm^2/cm.

In Table 6-10 the comparison between identified frequencies and frequencies of the FE model is shown. This first parametric analysis shows an improvement in overall error on frequencies compared to the starting FE model (Table 6-8).

Table 6-9: comparison between FE modal shape and identified modal shape.

	FE model modal shape	Identified modal shape
1	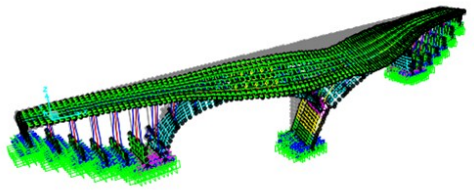	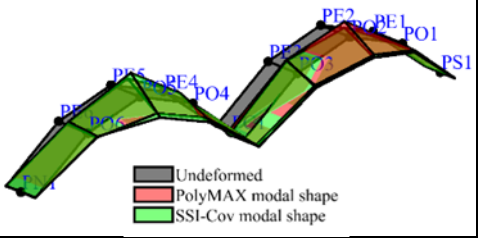
2	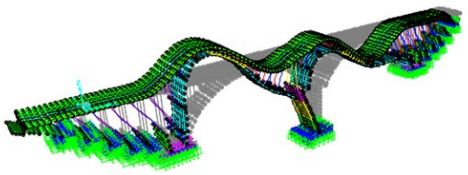	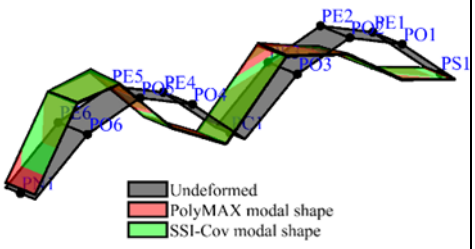
3	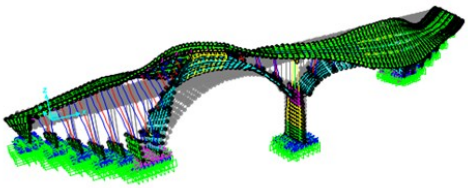	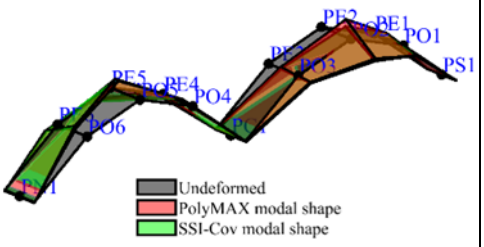
4	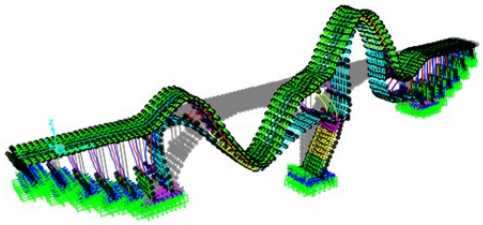	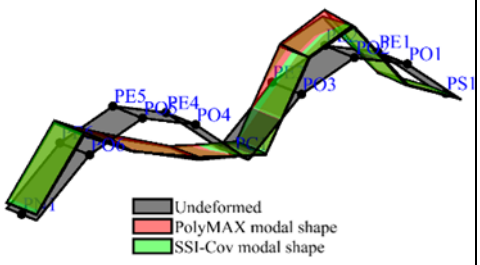
5	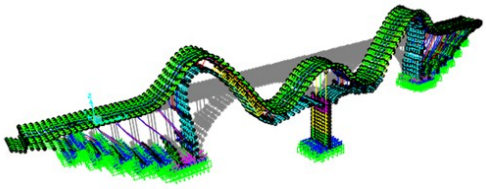	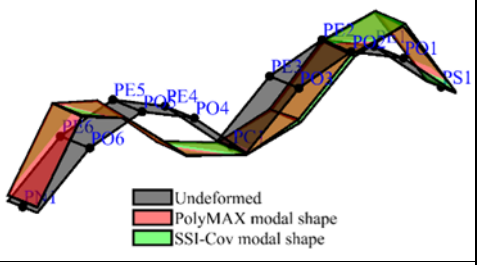
6	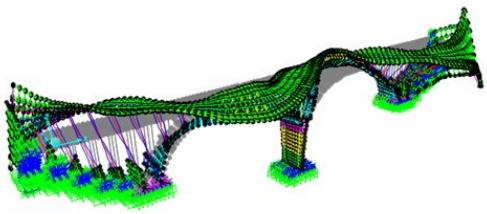	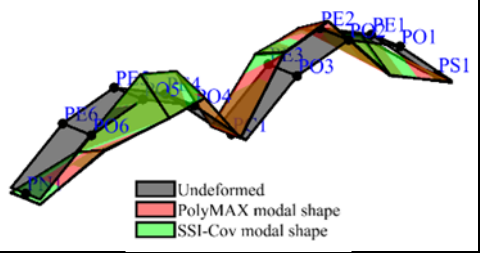

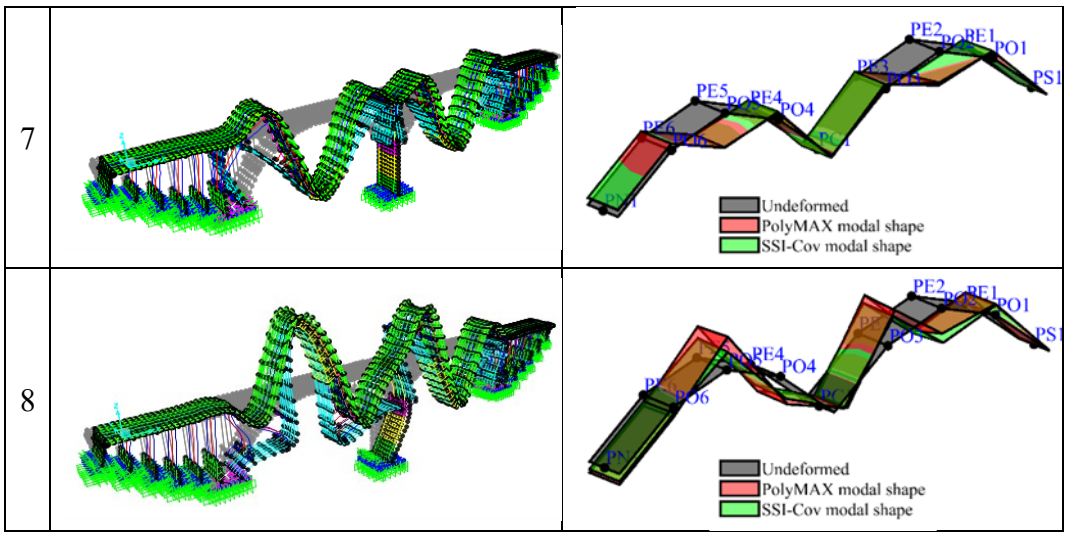

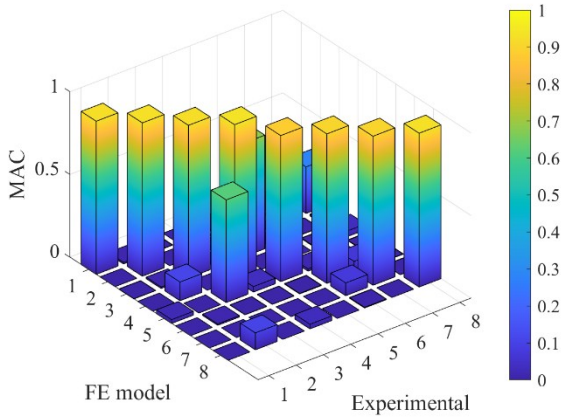

Figure 6-22: MAC matrix of the FE model with constant soil stiffness under all foundations.

Table 6-10: comparison between frequencies of the FE model with constant soil stiffness under all foundations and the identified frequencies.

Mode	Frequency identified with OMA [Hz]	Frequency of the starting FE model [Hz]	Frequency of the FE model 48 kg/cm²/cm [Hz]	Difference 48 kg/cm²/cm to OMA [%]
1	3.34	2.31	2.47	-26.08%
2	4.21	3.32	3.73	-11.43%
3	4.59	3.81	4.44	-3.16%
4	6.39	6.24	6.62	+3.58%
5	7.82	6.50	8.51	+8.81%
6	8.25	8.10	8.28	+0.35%
7	9.36	9.20	9.38	+0.19%
8	10.75	10.60	10.84	+0.83%
		Average difference [%]		6.80 %

The second step of the model updating consists into dividing the foundation soil into three clusters. Each cluster has different soil stiffnesses from the others, but the elements within the cluster have uniform characteristics:

- Soil under the foundation of the central pile (k_1);

- Soil under the foundation of the arches (k_2);
- Soil under the foundations of the approach side piers (k_3).

The bridge is situated within a narrow gorge. The two sides of the gorge are assumed to exhibit nearly identical mechanical properties; thus, the soil beneath the approach piles on both sides is considered to belong to a single geotechnical cluster. In contrast, the soil beneath the central pier—located at the base of the rocky gorge and near the river—may possess different mechanical characteristics compared to the soils on either side. Additionally, the soil supporting the foundations of the arches on both sides of the gorge may differ from that beneath the approach piers, likely due to a higher degree of consolidation.

This analysis considers three clusters with the same range of stiffness variability used in the previous step (4 to 48 kg/cm^2/cm).

In this case, the number of possible combinations of the algorithm becomes 11^3. The best result, obtained from the automatized parametric analysis, provides the following soil stiffnesses: k_1 =44 kg/cm^2/cm; k_2 =48 kg/cm^2/cm and k_3 =24 kg/cm^2/cm, as shown in Figure 6-23.

In terms of MAC, there are no engineering changes from the results shown in Figure 6-22. In terms of frequency, the results are shown in Table 6-11.

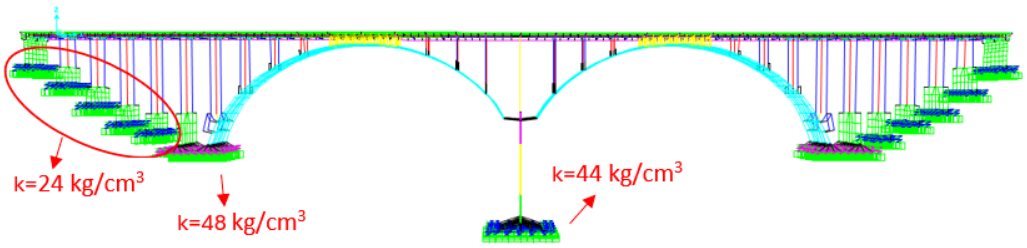

Figure 6-23: Stiffness of the three soil clusters.

Table 6-11: comparison between frequencies of the FE model with three clusters soil stiffness (upper bound 48 kg/cm²/cm) under foundations and the identified frequencies.

Mode	Frequency identified with OMA [Hz]	Frequency of the FE model 48 kg/cm²/cm [Hz]	Frequency of the FE model 24-48-44 kg/cm²/cm [Hz]	Difference 24-48-44 to OMA [%]
1	3.34	2.47	2.43	-27.27%
2	4.21	3.73	3.54	-15.94%
3	4.59	4.44	4.36	-4.91%
4	6.39	6.62	6.59	+3.11%
5	7.82	8.51	8.40	+7.41%
6	8.25	8.28	7.60	-7.89%
7	9.36	9.38	9.36	-0.02%
8	10.75	10.84	10.83	+0.74%
		Average difference [%]		8.41 %

The results of the two parametric analyses shown above present two problems. The first relates to the search set assigned to the parameterization, since the upper limit of the range is reached, so it is plausible that it may also exceed this value. The second relates to the outcome of the analysis, as it shows no improvement despite the level of detail being increased. It has therefore been chosen to extend the stiffness range by increasing the upper limit from 48 kg/cm^2/cm to 144 kg/cm^2/cm.

The best result obtained by the automatized parametric analysis provides the following soil stiffnesses: k_1 =24 kg/cm^2/cm; k_2 =52 kg/cm^2/cm and k_3 =144 kg/cm^2/cm,

In terms of frequency, the results are shown in Table 6-12.

Table 6-12: comparison between frequencies of the FE model with three clusters soil stiffness (upper bound 144 kg/cm^2/cm) under foundations and the identified frequencies.

Mode	Frequency identified with OMA [Hz]	Frequency of the FE model 24-48-44 kg/cm^2/cm [Hz]	Frequency of the FE model 24-52-144 kg/cm^2/cm [Hz]	Difference [%]
1	3.34	2.43	2.72	-18.59%
2	4.21	3.54	3.69	-12.38%
3	4.59	4.36	4.94	+7.74%
4	6.39	6.59	6.78	+6.08%
5	7.82	8.40	8.58	+9.71%
6	8.25	7.60	7.61	-7.77%
7	9.36	9.36	9.56	+2.12%
8	10.75	10.83	10.10	-6.05%
		Average difference [%]		8.81 %

To further refine the correspondence between the FE model and identified frequencies, the further considerations are made.

An additional stiffness cluster is added. The results obtained indicate that the first FE model vibration modes require additional stiffness to reach the experimental ones.

In particular, the north and south foundation of the arch, placed on the two sides of the valley (the abutments) may have different geometry or soil stiffness.

They are assumed equal in the first FE model as no information from in situ test are available and the original drawings did not provide explicit dimensions, but now they may have different soil stiffnesses. Furthermore, the upper limit of the range is increased to 164 kg/cm^2/cm.

At the end of the automatized parametric analysis, the stiffnesses of the four new clusters are:

- 24 kg/cm^2/cm for the foundation of the central pier;
- 124 kg/cm^2/cm for the foundation of the north arch;
- 144 kg/cm^2/cm for the foundation of the north and south approach piers;
- 164 kg/cm^2/cm for the foundation of the south arch.

Table 6-13: comparison between frequencies of the FE model with four clusters soil stiffness (upper bound 164 kg/cm^2/cm) under foundations and the identified frequencies.

Mode	Frequency identified with OMA [Hz]	Frequency of the FE model [Hz]	Difference [%]
1	3.34	3.23	-3.33%
2	4.21	3.99	-5.25%
3	4.59	4.94	+7.74%
4	6.39	7.18	+12.34%
5	7.82	8.63	+10.35%
6	8.25	7.61	-7.77%
7	9.36	9.60	+2.54%
8	10.75	11.36	+5.67%
Average difference [%]			6.87 %

From the results obtained, it can be seen that there are no clear improvements between the various analyses conducted, despite the increase in the parameters studied. Consequently, it is necessary to conduct further, more sophisticated analyses aimed at optimizing the results in an intelligent and effective manner. Indeed, the objective of a parametric analysis is not to identify an optimal result, but rather to study the sensitivity of the parameters and their influence on the results. The use of this technique has proved advantageous in identifying the search space of possible solutions, on which the study of the optimum can be conducted using specific algorithms, such as genetic algorithms. Parametric analysis, moreover, has limitations in that the greater the variables examined, or the range of variation of them, the greater the computational burden and execution time. This is why it is necessary to use an algorithm that can derive reliable results in significantly less time. Genetic algorithms may be a good solution to the required problem.

Model updating through genetic algorithms

This section reports the basis of the genetic algorithm used and the results of the model updating obtained from the application of the genetic algorithm.

Theoretical background of the genetic algorithm used

The algorithm used is the standard one provided by the numerical calculation software MATLAB [112], which, has been fitted, implemented and calibrated for the solution of the specific problem. In particular, the following settings were defined to improve the algorithm's performance:

- **Number of variables**. The number of design variables represents the number of unknown parameters to be derived by the algorithm. In the case study, these are the stiffnesses of each foundation soil cluster and the elastic moduli of the material composing the structure. The number of variables will be indicated later

- **Constraints**. The algorithm must follow constraints to be able to orient itself within the search range. In particular, the extremes of the set of possible solutions that can be obtained are defined as constraints. When the problem has integer or linear constraints (including the limits of the interval), the algorithm modifies its evolutionary characteristics so that they are compatible with the predefined constraints. In this case study, the parameters relating to the stiffnesses of the springs to simulate the behaviour of the soil under the foundation have positive integer constraints, which will be indicated in the next section.
- **Population Options**. The following option allows the characteristics of the population to be defined for each generation. This option represents an important detail, as the effectiveness of the algorithm is influenced by the size of the population and the genetic diversity that individuals possess. An incorrect configuration of characteristics leads to non-homogeneity between individuals or early convergence of results. Therefore, trial and error is the only way to interpret the results and determine the best solution. In order to derive the right result, a compromise often has to be made, taking into account the goodness of the solution and the computational burden. In fact, fast but less powerful algorithms are often preferred. Subject to constraints, the genetic algorithm randomly creates an initial population using a creation function. In this case study, individuals are randomly generated.
- **Fitness Scaling Options**. The selection function chooses the parents of each next generation. In fact, individuals with a higher weight will have a higher probability of being selected. An incorrect allocation of the range can alter the functioning of the algorithm. In particular, high variations in the manipulated values lead to a higher consideration of only those individuals with a higher scaled fitness, preventing the search for solutions on other areas of the set of possible solutions. Conversely, low variations generate similar selection probabilities, leading to a greater number of potential parents to be analysed, and thus very high computation times. The scalar fitness function used is 'fitscalingrank'. It modifies the raw values according to the rank of each individual instead of his or her score, then considers his or her position in the order of the scores. The rescaling of the fitness values takes place in the following way: the scaled value of an individual with rank n is proportional to $1/\sqrt{n}$. Hence, the element with the highest manipulated score is equal to 1, the next one to $1/\sqrt{2}$ and so on; The sum of the scaled values of the entire population is equal to the number of parents needed to create the next generation.
- **Selection options**. They give information on how the algorithm chooses parents for the next generation. As mentioned above, this is done via the fitness scaling function. The selection option used is 'selectiontournament'. It compares 'size' random individuals and chooses the best scoring element as the parent;

- **Reproduction options**. They specify how the algorithm creates new individuals (children) for the next generation. Each element can:
    - remain unchanged in the next generation as it already possesses very good characteristics that do not need to be improved. Such items are also called 'elite children' as they possess the best fitness values;
    - cross (crossover) with other individuals by selecting vector voices, or genes, and combining them to form a child;
    - generate a new child without crossing by mutating its own genotype.
- **Mutation options**. Mutation options describe how the system creates new individuals (children) by making small changes in the genetic code of one existing element (parent). Through mutation, the genetic algorithm is able to search a larger set.
- **Crossover options**. The crossover options specify how the genetic algorithm combines two individuals, or parents, to form a crossover child for the next generation.

As with the preliminary parametric analyses, the goodness of the results determined with the genetic algorithm depends on the discrepancy between numerical and identified modal shapes, assessed through the MAC matrix. The aim of the algorithm is to identify the optimal solution to the problem, defined as the combination of parameters that minimises the objective function. The ideal result yields a MAC matrix equal to the identity matrix; consequently, the sum of the diagonal of the matrix will be equal to the number of modal pairs present (8). Therefore, the objective function is described as:

$$Of = -sum[diag(MAC)] \tag{5.1}$$

In the next section the limitations of the objective function expressed only in terms of MAC will be demonstrated. For this reason, the objective function will also take into account the frequencies.

Results of the application of the genetic algorithm

The first analysis performed considers the structure model with soil divided into 3 clusters with ranges from 8 to 164 kg/cm^2/cm. This is a first calibration attempt for the algorithm. Therefore the code is be very simple, with a small number of iterations and arbitrary properties. These will then be corrected according to the solutions obtained. The characteristics of the analysis are as follows:

- nvars=3. Corresponding to the three stiffness values of the three clusters;
- PopulationSize=10;
- MaxGeneration=10;
- Objective Function. MAC matrix, Equation (5.1).

The solutions of this test analysis are: k=26 kg/cm^2/cm for the soil under the foundation of the approach side piers; k=134 kg/cm^2/cm for the soil under the

foundation of the arches; k=53 kg/cm^2/cm for the soil under the foundation of the central pier.

The results indicate that the stiffnesses obtained are comparable to those obtained with the parametric analysis with three clusters, thus confirming the performance of the code. The results of the analysis in terms of frequencies is shown in Table 6-14.

Table 6-14: comparison between frequencies of the FE model with three clusters soil stiffness under foundations and the identified frequencies. Genetic algorithm results.

Mode	Frequency identified with OMA [Hz]	Frequency of the FE model [Hz]	Difference (FE-OMA)/OMA [%]
1	3.34	2.68	-19.79%
2	4.21	3.69	-12.38%
3	4.59	4.92	+7.31%
4	6.39	6.76	+5.77%
5	7.82	8.58	+9.71%
6	8.25	7.71	-6.56%
7	9.36	9.54	+1.90%
8	10.75	11.08	+3.06%
Average difference [%]			8.31 %

After the validation of the algorithm, further investigations can be conducted in more detail to assess its robustness. In particular, the further investigation considers the division of the ground under the foundations into four clusters and the introduction of the frequency parameter in the search for the optimal solution in order to refine the result.

In fact, it was observed that evaluating the system only in terms of modal forms does not lead to accurate results in terms of frequency. Within the objective function, therefore, in addition to the sum of the values on the diagonal of the MAC matrix, the sum of the differences between numerical and identified frequencies is be added. The function will have to consider both contributions equally, whereby one of the two values will be weighted so as to have a similar order of magnitude to the other. In particular, high MAC values correspond to better outcomes, while high differences in frequencies correspond to less consistent outcomes. With this in mind, the Objective Function is described as:

$$Of = 8 - sum[diag(MAC)] + sum((f_{id} - f_{FEM})/f_{id}) \qquad (5.2)$$

where 8 is the number of modal pairs compared, thus also the maximum value that the diagonal sum of the MAC matrix can obtain; $(f_{id} - f_{FEM})/f_{id}$ is the frequency difference between experimental and numerical modes.

In the new analysis the soil is divided into 4 clusters with a range from 8 to 164 kg/cm^2/cm. In particular: k=43 kg/cm^2/cm for the soil under the approach side piers; k=85 kg/cm^2/cm for the soil under the North side arch foundation; k=69 kg/cm^2/cm for the soil under the central pier; k=84 kg/cm^2/cm for the soil under the South side

arch foundation. The results of the analysis in terms of frequencies are shown in Table 6-15.

Table 6-15: comparison between frequencies of the FE model with four clusters soil stiffness under foundations and the identified frequencies. Genetic algorithm results.

Mode	Frequency identified with OMA [Hz]	Frequency of the FE model [Hz]	Difference (FE-OMA)/OMA [%]
1	3.34	2.76	-17.40%
2	4.21	3.87	-8.10%
3	4.59	4.76	+3.82%
4	6.39	6.83	+6.86%
5	7.82	8.65	+10.60%
6	8.25	8.21	-0.50%
7	9.36	9.50	+1.48%
8	10.75	11.07	+2.97%
Average difference [%]			6.47 %

Several considerations can be made from the reported results:

- The MAC values obtained continue to be optimal and do not undergo any engineering change;
- Considering both MAC values and frequencies in the objective function, the variations in frequencies between identified and numeric modes decrease from an average value of 8.81% (preliminary parametric analysis) to a value of 6.47% (genetic algorithm).

From the various analyses conducted up to now, it can be seen that a higher level of detail in the numerical model improves the numerical result. Therefore, an appropriate analysis should also be carried out on the material characteristics, which up to now have been assumed a priori. In particular, since the FE model evaluates the elastic behaviour of the structure, the material parameter to be investigated will be the elastic modulus of concrete. The extremes of variation of the elastic modulus of the material within the algorithm are set to vary from a minimum of 15 GPa to a maximum of 35 GPa. Consequently, the analysis considers the model of the structure with soil divided into 4 clusters, with a range varying from 8 to 164 $kg/cm^2/cm$, and constant material characteristics for the entire structure changing within the range illustrated. Therefore, the study presents the following characteristics:

- nvars=5. Corresponding to the four stiffness values of the four foundation soil clusters and the modulus of elasticity;
- PopulationSize=30;
- MaxGeneration=25;
- Objective Function. MAC matrix and difference between frequencies.

This analysis provides the following results: k=60 kg/cm^2/cm for the soil under the approach side piers; k=140 kg/cm^2/cm for the soil under the North side arch foundation; k=82 kg/cm^2/cm for the soil under the central pier; k=128 kg/cm^2/cm for the soil under the South side arch foundation and E=30.3 GPa for concrete.

The results of the analysis in terms of frequencies are shown in Table 6-16. A reduction in the average error on frequencies from 6.47% to 5.42% can be observed if compared to the results shown in Table 6-15 (genetic algorithm with four clusters for the stiffness of the foundation soil). In terms of MAC, there are not relevant engineering variations.

Table 6-16: comparison between frequencies of the FE model with four clusters soil stiffness under foundations and one cluster for elastic modulus of concrete and the identified frequencies. Genetic algorithm results.

Mode	Frequency identified with OMA [Hz]	Frequency of the FE model [Hz]	Difference (FE-OMA)/OMA [%]
1	3.34	2.87	-14.10%
2	4.21	3.95	-6.20%
3	4.59	4.88	+6.43%
4	6.39	6.75	+5.61%
5	7.82	8.51	+8.81%
6	8.25	8.22	-0.38%
7	9.36	9.29	-0.77%
8	10.75	10.86	+1.02%
Average difference [%]			5.42 %

A further analysis is performed by considering five different clusters for the concrete's modulus of elasticity of:

- the arches;
- the piers;
- the deck;
- the central pier;
- the foundations.

The analysis is performed considering these characteristics:

- nvars=9. Corresponding to the four stiffness values of the four foundation soil clusters and the five clusters for the elastic modulus of concrete;
- PopulationSize=30;
- MaxGeneration=25;
- Objective Function. MAC matrix and difference between frequencies.

This analysis provides the following results: k=102 kg/cm^2/cm for the soil under the approach side piers; k=88 kg/cm^2/cm for the soil under the North side arch foundation; k=112 kg/cm^2/cm for the soil under the central pier; k=90 kg/cm^2/cm for the soil under the South side arch foundation; E=32.7 GPa for the concrete of the arches; E=25.5 GPa for the concrete of piers; E=27.6 GPa for the

concrete of the deck; E=26.6 GPa for the concrete of the central piers and E=33.8 GPa for the concrete of the foundations.

The results of the analysis in terms of frequencies is shown in Table 6-17.

A reduction in the average error on frequencies from 5.42% to 3.93% can be observed if compared to the results shown in in Table 6-16 (genetic algorithm with four clusters for the stiffness of the foundation soil and only one cluster for the elastic modulus of concrete). In terms of MAC, there are not relevant engineering variations.

The elastic moduli of concrete show an average of 30 GPa. The observed inhomogeneity of the elastic moduli between the different clusters can probably be attributed to the use of different mixtures, not certified at the time, for the construction of the main elements of the structure.

Furthermore, it is possible that some elements of the structure like (deck and slender piers) are subjected to cracking, which leads to a reduction in the stiffness of the cross sections. Consequently, the results obtained indicate that genetic algorithms, compared to manual or parametric analyses, allow to obtain a better solution in considerably less time, 8.3 hours instead of 26 hours in the most sophisticated parametric analysis, and with greater accuracy.

Table 6-17: comparison between frequencies of the FE model with four clusters soil stiffness under foundations and five cluster for elastic modulus of concrete and the identified frequencies. Genetic algorithm results.

Mode	Frequency identified with OMA [Hz]	Frequency of the FE model [Hz]	Difference (FE-OMA)/OMA [%]
1	3.34	2.95	-11.71%
2	4.21	4.13	-1.93%
3	4.59	4.73	+3.16%
4	6.39	6.75	+5.61%
5	7.82	8.38	+7.15%
6	8.25	8.19	-0.74%
7	9.36	9.36	-0.02%
8	10.75	10.87	+1.11%
Average difference [%]			3.93 %

Summary of results

This section provides a summary of the results reported previously.

Table 6-18 shows the comparison between the identified frequencies and the frequencies of the different FE models considered. When the refinement of the optimization and the number of parameters to be optimised increases, the average error on frequencies decreases.

Table 6-19 shows the comparison between the MAC between identified modal shapes and modal shapes of the different FE models considered. The variations in modal shape, and therefore in MAC, as the level of analysis refinement varies are almost nil.

Table 6-18: Summary of results obtained in terms of frequencies.

Mode	f_{ID} [Hz]	Original FE model [Hz]	Parametric analysis 1 [Hz]	Parametric analysis 2 [Hz]	Parametric analysis 3 [Hz]	Parametric analysis 4 [Hz]	Genetic Algorithm 1 [Hz]	Genetic Algorithm 2 [Hz]	Genetic Algorithm 3 [Hz]	Genetic Algorithm 4 [Hz]
1	3.34	2.31	2.47	2.43	2.72	3.23	2.68	2.76	2.87	2.95
2	4.21	3.32	3.73	3.54	3.69	3.99	3.69	3.87	3.95	4.13
3	4.59	3.81	4.44	4.36	4.94	4.94	4.92	4.76	4.88	4.73
4	6.39	6.24	6.62	6.59	6.78	7.18	6.76	6.83	6.75	6.75
5	7.82	6.50	8.51	8.40	8.58	8.63	8.58	8.65	8.51	8.38
6	8.25	8.10	8.28	7.60	7.61	7.61	7.71	8.21	8.22	8.19
7	9.36	9.20	9.38	9.36	9.56	9.60	9.54	9.50	9.29	9.36
8	10.75	10.60	10.84	10.83	10.10	11.36	11.08	11.07	10.86	10.87
Mean error [%]		11.6	6.80	8.41	8.81	6.87	8.31	6.47	5.42	3.93

Parametric analysis:
- **1**. Single soil stiffness cluster with an upper limit of 48 kg/cm^2/cm;
- **2**. Three soil stiffness clusters with an upper limit of 48 kg/cm^2/cm;
- **3**. Three soil stiffness clusters with an upper limit of 144 kg/cm^2/cm;
- **4**. Four soil stiffness clusters with an upper limit of 164 kg/cm^2/cm.

Genetic Algorithm:
- **1**. Three soil stiffness clusters with an upper limit of 164 kg/cm^2/cm. Objective function only with MAC;
- **2**. Four soil stiffness clusters with an upper limit of 164 kg/cm^2/cm. Objective function with MAC and frequencies;
- **3**. Four soil stiffness clusters with an upper limit of 164 kg/cm^2/cm and only one cluster for concrete elastic modulus with upper limit 35 GPa. Objective function with MAC and frequencies;
- **4**. Four soil stiffness clusters with an upper limit of 164 kg/cm^2/cm and five clusters for concrete elastic modulus with upper limit 35 GPa. Objective function with MAC and frequencies.

Table 6-19: Summary of results obtained in terms of MAC.

		Parametric analysis				Genetic Algorithm			
Mode	Original FE model	1	2	3	4	1	2	3	4
1	0.915	0.918	0.921	0.924	0.923	0.923	0.923	0.923	0.929
2	0.918	0.915	0.919	0.926	0.926	0.926	0.926	0.925	0.925
3	0.926	0.929	0.928	0.933	0.935	0.933	0.935	0.936	0.929
4	0.932	0.941	0.938	0.941	0.943	0.943	0.943	0.944	0.931
5	0.882	0.896	0.895	0.893	0.894	0.893	0.894	0.893	0.883
6	0.938	0.943	0.945	0.955	0.956	0.953	0.956	0.954	0.955
7	0.961	0.966	0.968	0.976	0.978	0.972	0.977	0.972	0.958
8	0.929	0.934	0.932	0.942	0.944	0.942	0.944	0.941	0.936

Parametric analysis:
- **1**. Single soil stiffness cluster with an upper limit of 48 kg/cm^2/cm;
- **2**. Three soil stiffness clusters with an upper limit of 48 kg/cm^2/cm;
- **3**. Three soil stiffness clusters with an upper limit of 144 kg/cm^2/cm;
- **4**. Four soil stiffness clusters with an upper limit of 164 kg/cm^2/cm.

Genetic Algorithm:
- **1**. Three soil stiffness clusters with an upper limit of 164 kg/cm^2/cm. Objective function only with MAC;
- **2**. Four soil stiffness clusters with an upper limit of 164 kg/cm^2/cm. Objective function with MAC and frequencies;
- **3**. Four soil stiffness clusters with an upper limit of 164 kg/cm^2/cm and only one cluster for concrete elastic modulus with upper limit 35 GPa. Objective function with MAC and frequencies;
- **4**. Four soil stiffness clusters with an upper limit of 164 kg/cm^2/cm and five clusters for concrete elastic modulus with upper limit 35 GPa. Objective function with MAC and frequencies.

6.4. Modal identification and model updating of an existing highway viaduct subjected to works. Case study 3

This section will present the results of the modal identification and digital-twin model updating of a highway viaduct, shown in Figure 6-24, subject to structural changes because of construction works of new junctions nearby.

The approach used is similar to that followed in Section 6.3 for case study 2, but with the exclusive application of a genetic algorithm for model updating without prior parametric analysis.

The structure consists of a continuous beam deck with a box section in pre-stressed reinforced concrete with a curvilinear development in plan with a radius of curvature of approximately 535 m. The viaduct has a total length of 600 m, and consists of two 50 m semi-spans at the entrance, from abutment SP2 to pier P6, and at the exit, from pier P1 to abutment SP1, and five intermediate spans of 100 m each. The viaduct side view is shown in Figure 6-25. The deck rests on six square hollow-section piers up to a certain elevation, after which they continue as vertical parallel plates up to the support axis.

Deep foundations are present under the piers, unlike what happened in the two case studies examined previously.

Figure 6-24: Picture of the viaduct.

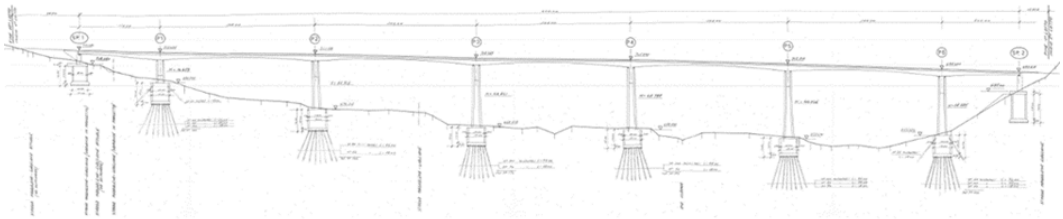

Figure 6-25: Side view of the viaduct.

Description of the Monitoring System

The monitoring system installed on the structure is shown in Figure 6-26.

It consists of monaxial accelerometers (blue dots in the picture) and triaxial accelerometers (green dots in the picture).

Uniaxial high precision accelerometers are primarily used, oriented in vertical direction, they are positioned in the centre of each span. Three piers over six are equipped with triaxial accelerometers.

The monitoring objectives for this viaduct is the control of the effects of the construction of two new junctions providing a new exit and a new entrance for the highway in correspondence with the bridge.

New deep foundations for the piers of the new junctions needs to be drilled close to the foundations of the existing bridge. Big soil excavations and realizations of new embankments are also foreseen in the project. Heavy construction equipment and machinery will be placed on the existing bridge during the construction of the new ones.

For this structure, data for OMA analysis are recorded and saved in the cloud once a day: in a time window from 8:00 to 9:00 a.m. Accelerometer recordings are sampled at a rate of $f_s = 200\ Hz$.

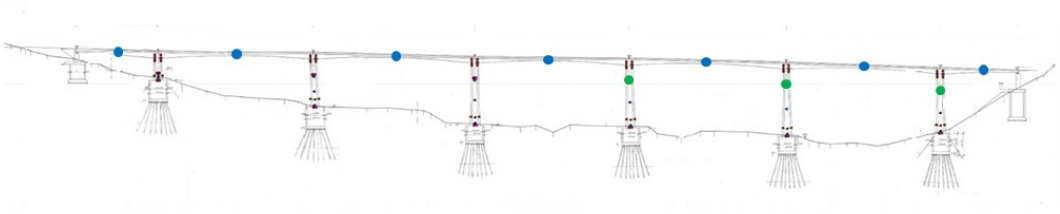

Figure 6-26: Monitoring system scheme of the viaduct.

Dynamic identification of the structure

Dynamic identification is performed once a week from March 2023 to Novembre 2024 with the PolyMAX method implemented in commercial software [115].

The results in terms of identified frequencies and their trend over time compared to the temperature trend are shown in Figure 6-27. Figure 6-28 shows the linear regression between identified frequencies and temperatures. In general, there is a moderate inverse correlation between identified frequencies and temperature trends. Changes in frequency with changing temperature are marginal and engineering negligible.

The results in terms of identified damping and their trend over time compared to the temperature trend is shown in Figure 6-29. Damping is not clearly influenced by temperature variations. Furthermore, damping is one of the least stable dynamic identification parameters due to different random phenomena from which it is affected [116].

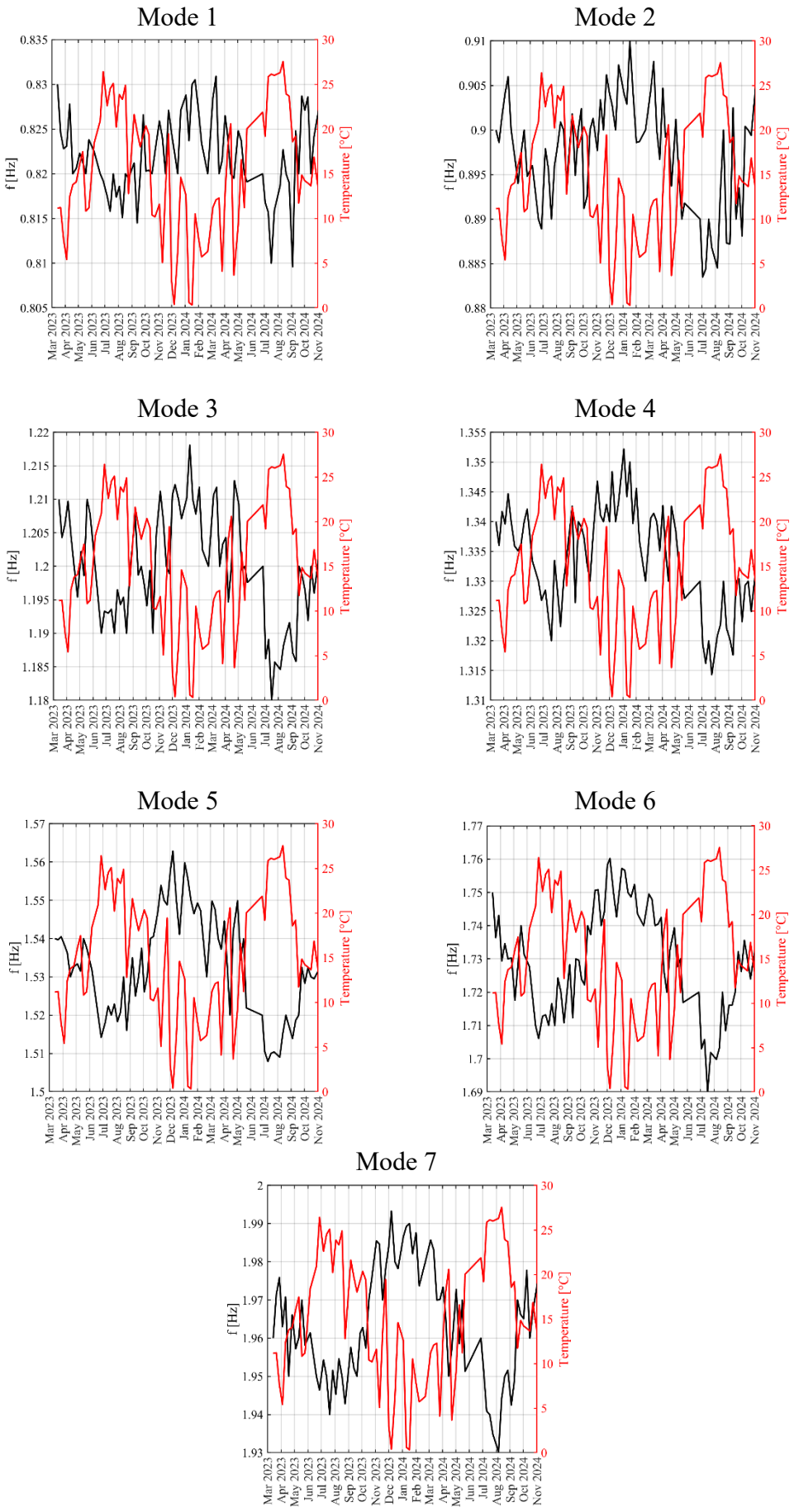

Figure 6-27: Trend of identified frequencies and comparison with the ambient temperature trend.

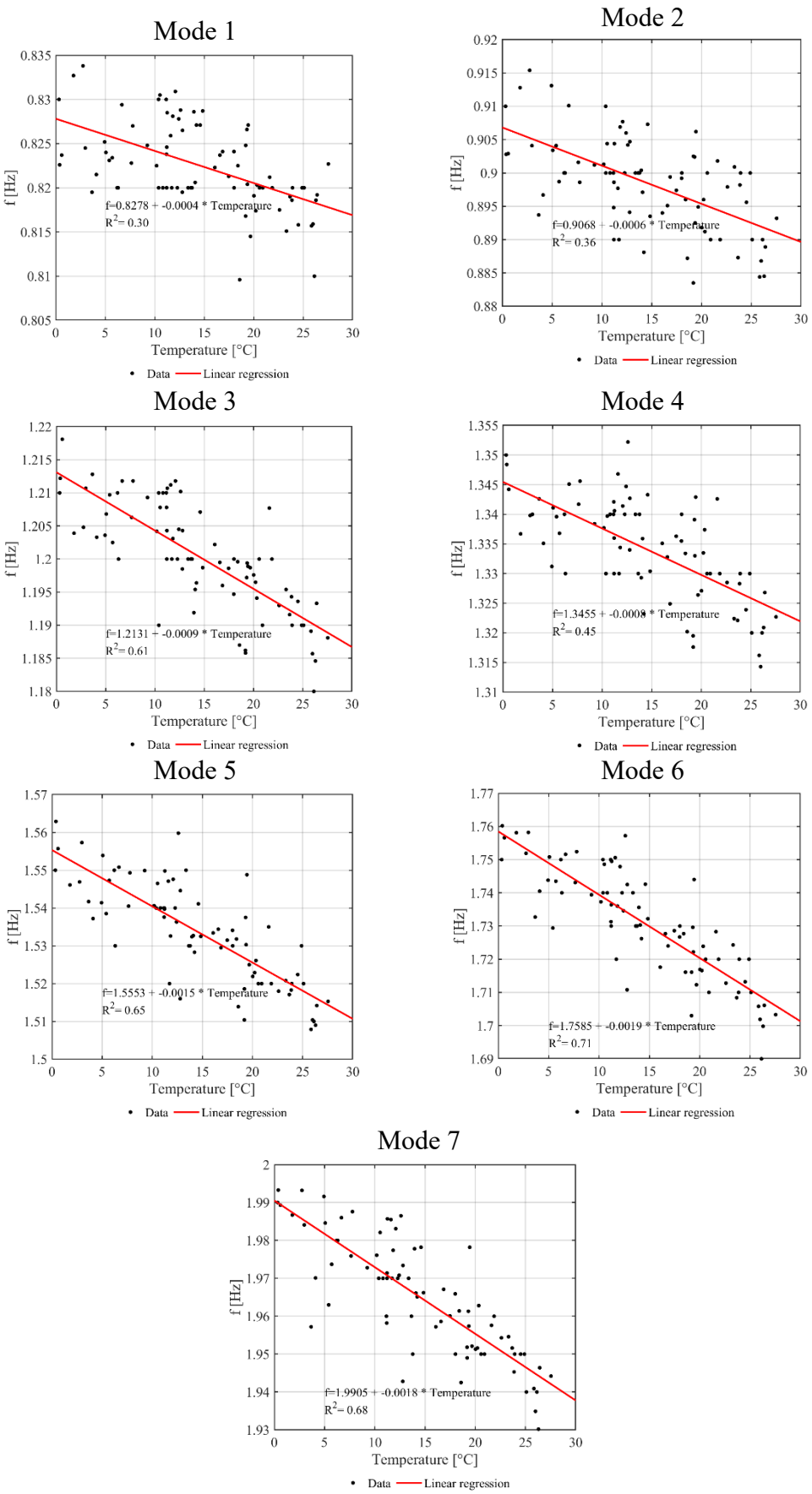

Figure 6-28: Linear regressions between identified frequencies and temperatures.

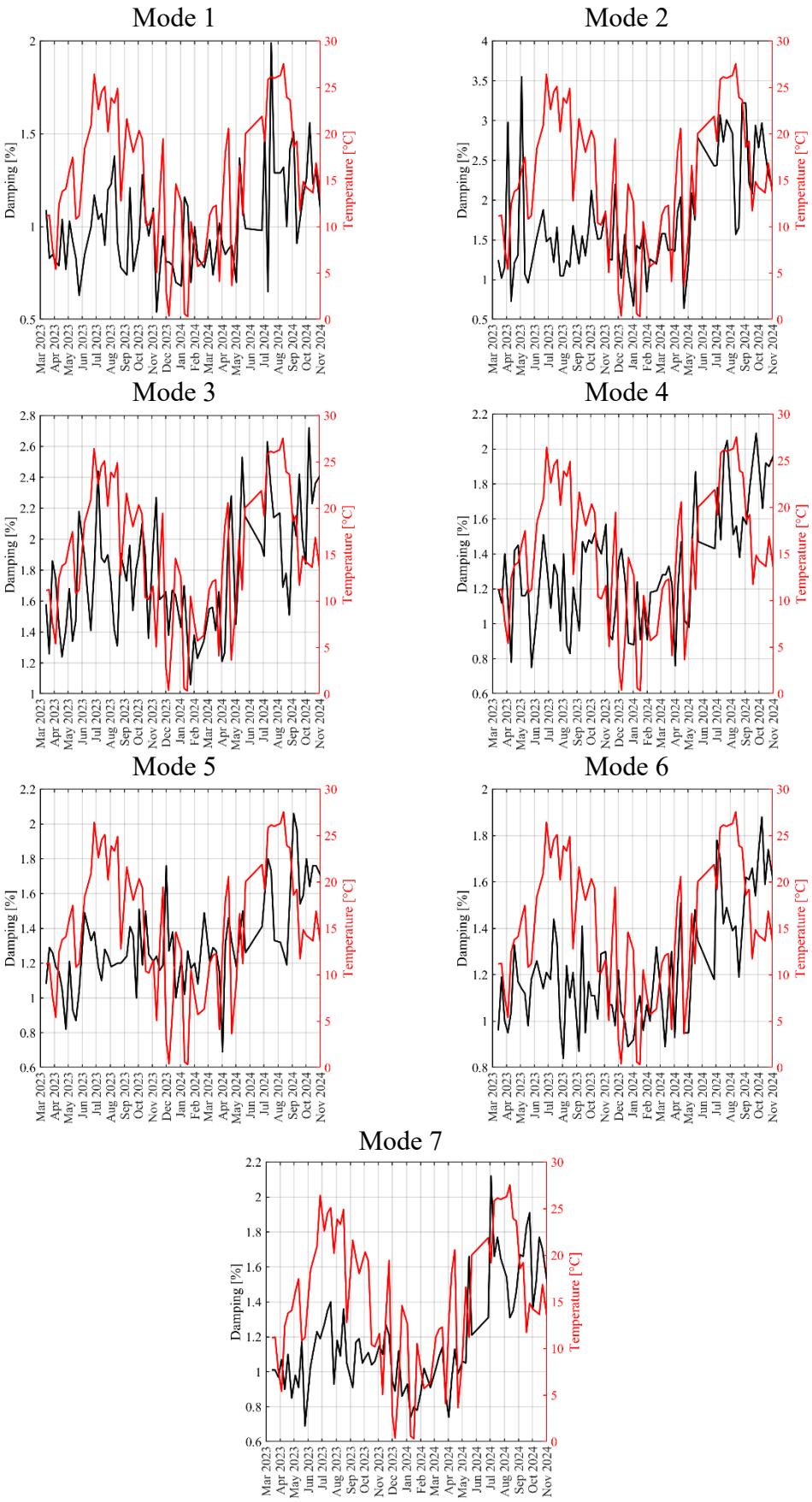

Figure 6-29: Trend of identified damping and comparison with the ambient temperature trend.

The results in terms of identified modal shapes is shown in Figure 6-30. The results are summarised in Table 6-7.

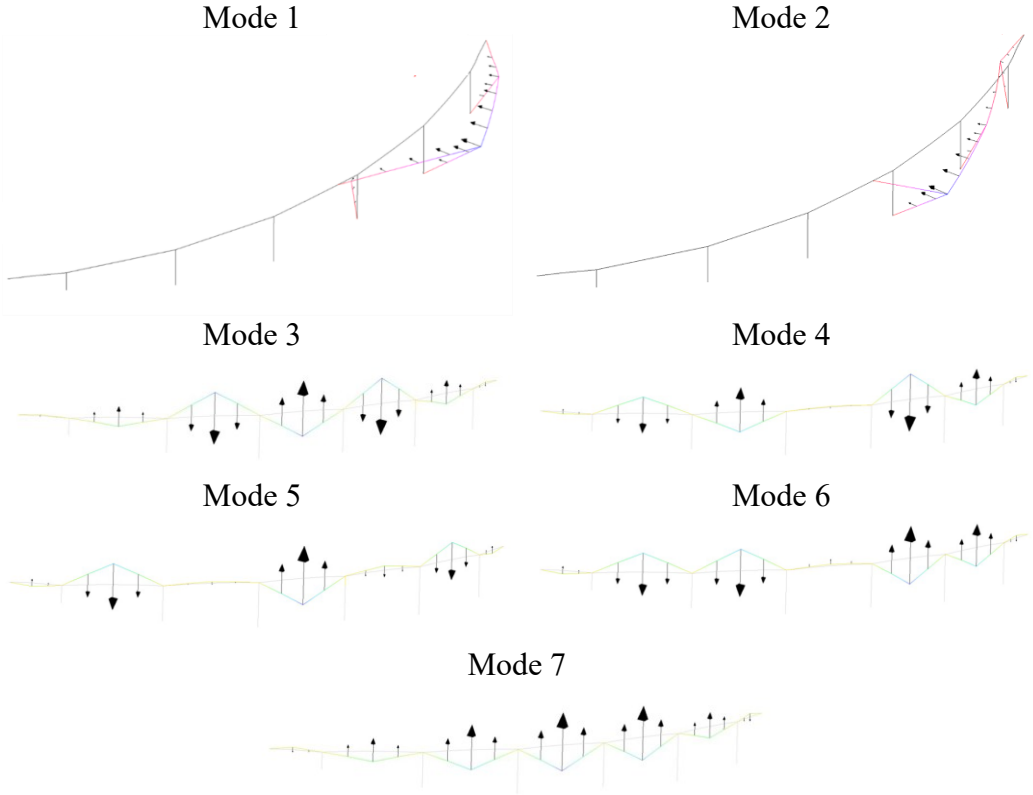

Figure 6-30: Identified modal shapes.

Table 6-20: Identified frequencies and damping.

Mode	f [Hz]	Damping [%]	Description
1	0.82	0.99	Transverse flexural mode
2	0.90	1.57	Transverse flexural mode
3	1.20	1.68	Vertical flexural mode
4	1.33	1.33	Vertical flexural mode
5	1.53	1.31	Vertical flexural mode
6	1.73	1.18	Vertical flexural mode
7	1.96	1.21	Vertical flexural mode

FE model digital-twin

The numerical model was created with the finite element modelling software SAP2000 [102]. The purpose of the FE model is to create a simple numerical model that reproduces the real dynamic behaviour of the structure. The FE model consists of a unifilar model, shown in Figure 6-31. The use of beam elements to model the deck and piers is also justified because torsional effects cannot be captured by the arrangement of accelerometers (that are placed along the axis of the deck), therefore will not be provided as an output of the OMA.

(a)

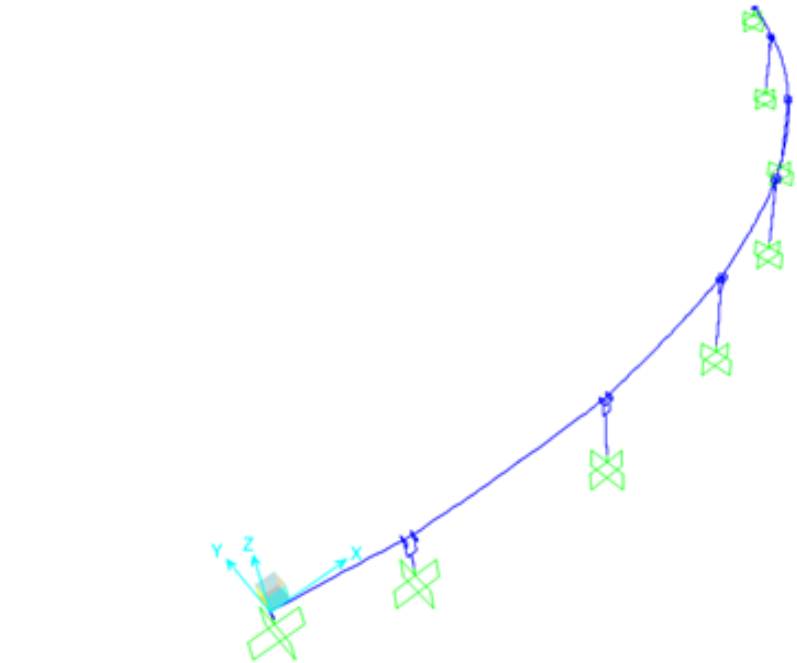

(b)

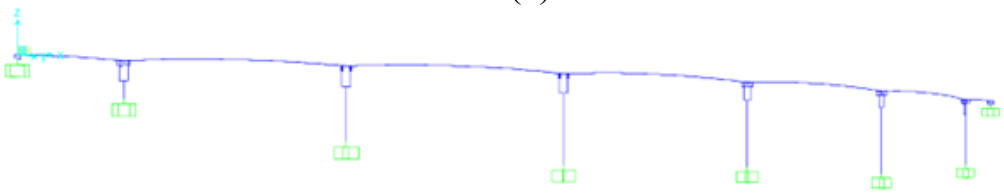

Figure 6-31: FE model of the viaduct. (a) 3D view; (b) Side view.

Some parameters that can affect the numerical dynamic response are highlighted by comparing numerical results with experimental results:

- Restraint condition between pier and deep foundation. In the original FE model assumed as perfect full restraint at the base.
- Constraint condition between deck and piers and between deck and abutments. In the original FE model all bearings devices are assumed to have the ideal behaviour considered in design.
- Mechanical properties of the material.

The mechanical properties of the concrete for this structure are unknown as no material investigations are available.

No experimental evidence is available regarding loads. Therefore, they were assumed in the first instance according to the current standard [24] for the design of a new structure. In detail, the following values of permanent structural and permanent non-structural loads were assumed:

- **Structural permanent loads** are represented by the self-weight of all elements that have a structural function in the bridge. Since the bridge is

made in its entirety of ordinary reinforced concrete, a weight of the structural elements of 25 kN/m^3 is assumed;
- **Kerbs** are not taken into account in the definition of the geometry of the structural elements of the decks. A linear load of 11.25 kN/m is assigned;
- **Safety barriers**: a weight of 15 kN/m is assumed.
- **Road pavement**: a load of 3 kN/m^2 has been assumed in accordance with the standard.

Table 6-21 compares the results, in terms of frequencies, between the original FE model and identified. It can be seen that the original FE model is on average 18.4% more deformable than the real structure.

Table 6-21: comparison between frequencies of the original FE model and the identified frequencies.

Mode	Frequency identified with OMA [Hz]	Frequency of the FE model [Hz]	Difference (FE-OMA)/OMA [%]
1	0.82	0.71	-13.41%
2	0.90	0.80	-11.11%
3	1.20	0.92	-23.33%
4	1.33	1.07	-19.55%
5	1.53	1.24	-18.95%
6	1.73	1.42	-17.92%
7	1.96	1.48	-24.49%
Average difference [%]			-18.40 %

Model updating through genetic algorithms

From the preliminary analysis of the parameters that may influence the dynamic response of the structure, the following parameters are chosen to be optimised through model updating:

- Rotational stiffness, in the two main direction (M2 and M3), of the fully restraint constraint in the foundation.
- Axial stiffness (P) of bearings between deck and substructure.
- Horizontal stiffness, in the two main directions (V2 and V3), of the bearings between deck and substructure.
- Elastic modulus of concrete.
- Concrete weight.
- Winkler axial stiffness (K_x) of springs in lateral abutment knots.
- Winkler axial stiffness (K_x) of springs in central abutment knots.

The search intervals of the genetic algorithm were calibrated following the results of the preliminary analyses and are shown in Table 6-22

The variation range of the parameters to be optimised was established as follows:

- Rotational stiffness, in the two main direction (M2 and M3), of the fully restraint constraint in the foundation. For the highest pile of the viaduct, under the design wind action in the transverse direction of the viaduct axis, a rotation of the foundation block is assumed such that the difference in vertical displacement between the two edges of the block is 1 mm. This assumption results in a stiffness of 1.0E8 kNm/rad, which corresponds to the lower limit. The upper limit is 32 times higher to account for the greater stiffness of the shorter piers and the greater assumed stiffness for rotation about the other main axis
- Axial stiffness (P) of bearings between deck and substructure. Lower limit set so as to have a 1 mm sag for the smallest vertical constraint reaction. Upper limit established so as to have a slope of 1 mm for the largest vertical constraint reaction.
- Horizontal stiffness, in the two main directions (V2 and V3), of the bearings between deck and substructure. Lower limit set so as to have a horizontal displacement of 1 mm for a horizontal action equal to 3% of the vertical reaction. Upper limit 100 times greater than the lower limit to take into account possible deterioration of the supporting devices and thus an increase in their stiffness.
- Elastic modulus of concrete. Lower limit equal to the minimum value of a structural concrete. Upper limit 10% higher than the modulus of elasticity of the design concrete to take into account the beneficial effect of ageing on the modulus of elasticity of the concrete.
- Concrete weight. Lower limit 10% lower than the value generally used in the design of 25 kN/m^3 to allow for any variability in weight [117]. Upper limit 2% higher than the value generally used at the design stage.
- Winkler axial stiffness (K_x) of springs in lateral abutment knots. Lower limit obtained in such a way that the horizontal reaction value corresponds to a displacement of 1 mm. 10-times upper limit to take account of any higher soil stiffness.
- Winkler axial stiffness (K_x) of springs in central abutment knots. Lower limit obtained in such a way that the horizontal reaction value corresponds to a displacement of 1 mm. 10-times upper limit to take account of any higher soil stiffness.

Table 6-22: Range of variation of parameters in the genetic algorithm.

Parameter	Lower boundary	Upper boundary
M2 and M3 [kNm/rad]	1.0E8	3.2E9
P [kN/m]	5.0E6	3.0E7
V2 [kN/m]	1.0E4	1.0E6
V3 [kN/m]	1.0E4	1.0E6
K_x lateral nodes [kN/m]	2.5E4	2.5E5
K_x central node[kN/m]	5.0E4	5.0E5
E_{deck} [GPa]	25.0	40.0
E_{piers} [GPa]	25.0	40.0
$\gamma_{concrete}$ [kN/m^3]	22.5	25.5

The first analysis with the genetic algorithm was performed considering these characteristics:

- nvars=9: Table 6-22;
- PopulationSize=35;
- MaxGeneration=25;
- Objective Function. MAC matrix.

The results of the first analysis are shown in Table 6-23.

Table 6-23: Results of the first analysis with genetic algorithm.

Parameter	Result from genetic algorithm
M2 and M3 [kNm/rad]	1.0E8
P [kN/m]	10.0E6
V2 [kN/m]	9.0E4
V3 [kN/m]	79.0E4
K_x lateral nodes [kN/m]	12.0E4
K_x central node[kN/m]	27.0E4
E_{deck} [GPa]	37.6
E_{piers} [GPa]	25.6
$\gamma_{concrete}$ [kN/m^3]	25.2

Table 6-24 compares the results, in terms of frequencies, between the first analysis with genetic algorithm and the identified ones. Figure 6-32 shows the MAC matrix between the experimental modal shapes and the modal shapes of the FE model upgraded with the first analysis through genetic algorithm.

The correspondence in terms of modal form is optimal, but there is only 4% improvement in terms of frequencies compared to what is shown in Table 6-21 (original FE model).

Table 6-24: comparison between frequencies of the first analysis of FE model updated with genetic algorithm and the identified frequencies.

Mode	**Frequency identified with OMA [Hz]**	**Frequency of the FE model [Hz]**	**Difference (FE-OMA)/OMA [%]**
1	0.82	0.79	-3.66%
2	0.90	0.61	-32.22%
3	1.20	1.03	-14.17%
4	1.33	1.15	-13.53%
5	1.53	1.32	-13.73%
6	1.73	1.52	-12.14%
7	1.96	1.71	-12.76%
Average difference [%]			-14.60 %

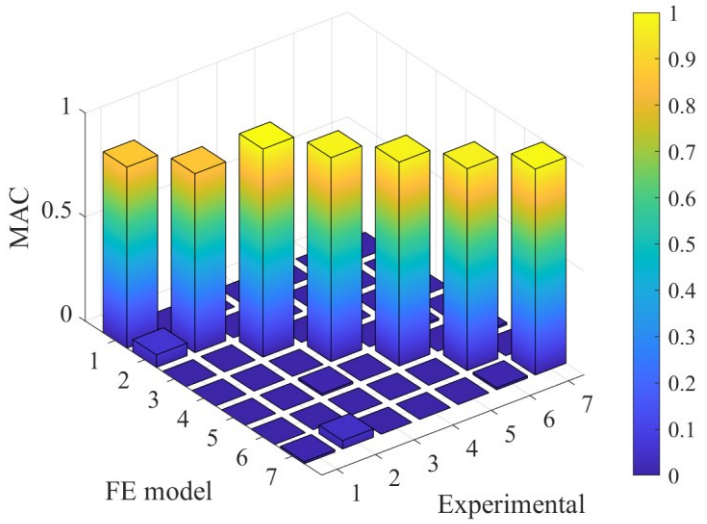

Figure 6-32: MAC matrix between identified and FE model updated with the first analysis with genetic algorithm.

The second analysis performed has similar characteristics to the first, but with the following partial modifications, the Population Size is set equal to 30. Furthermore, as the stiffness M2 and M3 at the base of the piers reaches the lower limit of the range, it is therefore appropriate to change the search range. In particular, it is assigned: lower bound 1.0E6 kNm/rad and upper bound 100.0E6 kNm/rad.

The results of the second analysis are shown in Table 6-25.

Table 6-25: Results of the second analysis with genetic algorithm.

Parameter	Results of 1st g.a. run	Results of 2nd g.a. run
M2 and M3 [kNm/rad]	100 E6	20 E6
P [kN/m]	10 E6	11 E6
V2 [kN/m]	9 E4	6 E4
V3 [kN/m]	79 E4	74 E4
K_x lateral nodes [kN/m]	12 E4	6 E4
K_x central node[kN/m]	27 E4	8 E4
E_{deck} [GPa]	37.6	38.1
E_{piers} [GPa]	25.6	28.4
$\gamma_{concrete}$ [kN/m^3]	25.2	25.1

Table 6-26 compares the results, in terms of frequencies, between the second analysis with genetic algorithm and the identified ones. In terms of MAC, there are no engineering variations from the results shown in Figure 6-32. The error on the frequencies increases showing that the method is unfit.

Table 6-26: comparison between frequencies of the second analysis of FE model updated with genetic algorithm and the identified frequencies.

Mode	Frequency identified with OMA [Hz]	Frequency of the FE model [Hz]	Difference (FE-OMA)/OMA [%]
1	0.82	0.61	-25.61%
2	0.90	0.44	-51.11%
3	1.20	1.04	-13.33%
4	1.33	1.16	-12.78%
5	1.53	1.33	-13.07%
6	1.73	1.53	-11.56%
7	1.96	1.70	-13.27%
Average difference [%]			-20.10 %

Based on the results reported for the first two analyses with the genetic algorithm, it is considered appropriate to also include the difference between identified frequencies and frequencies of the numerical model in the objective function, similarly to case study 2, as follow:

$$Of = 7 - sum[diag(MAC)] + sum((f_{id} - f_{FEM})/f_{id}) \quad (5.2)$$

where 7 is the number of modal pairs compared, thus also the maximum value that the diagonal sum of the MAC matrix can obtain; $(f_{id} - f_{FEM})/f_{id}$ is the normalised difference between numeric frequency and identified frequency.

The results of the third analysis are shown in Table 6-27.

Table 6-27: Results of the third analysis with genetic algorithm.

Parameter	Results of 1st g.a. run	Results of 3rd g.a. run
M2 and M3 [kNm/rad]	100 E6	79 E6
P [kN/m]	10 E6	28 E6
V2 [kN/m]	9 E4	9 E4
V3 [kN/m]	79 E4	78 E4
K_x lateral nodes [kN/m]	12 E4	18 E4
K_x central node[kN/m]	27 E4	32 E4
E_{deck} [GPa]	37.6	40.0
E_{piers} [GPa]	25.6	39.2
$\gamma_{concrete}$ [kN/m^3]	25.2	22.5

Table 6-28 compares the results, in terms of frequencies, between the second analysis with genetic algorithm and identified. In terms of MAC, there are no engineering variations from the results shown in Figure 6-32. With the exclusion of the second mode of vibration, a good match was also obtained in terms of frequencies with the identified modes; therefore, the optimisation of the model can be considered completed. Mode 2 is a horizontal transverse mode of the viaduct. It is identified through the three triaxial accelerometers positioned on three of the total six piers. Therefore, the reconstruction of the mode is partial, which could have

caused an association of the identified mode with a numerical mode that partially has the same shape, but lower frequency.

Table 6-28: comparison between frequencies of the third analysis of FE model updated with genetic algorithm and the identified frequencies.

Mode	Frequency identified with OMA [Hz]	Frequency of the FE model [Hz]	Difference (FE-OMA)/OMA [%]
1	0.82	0.84	+2.44%
2	0.90	0.66	-26.67%
3	1.20	1.21	+0.83%
4	1.33	1.33	0.00%
5	1.53	1.49	-2.61%
6	1.73	1.68	-2.89%
7	1.96	1.87	-4.59%
Average difference [%]			-4.78 %

Summary of the results

This section provides a summary of the results reported previously. Table 6-29 shows the comparison between the identified frequencies and the frequencies of the different FE models considered. It can be seen that as the refinement of the optimisation increases, therefore, the number of parameters to be optimised, there is a decreasing trend in the average error. With regard to modal shapes these remain more or less unchanged, showing engineering changes that are not relevant between the different analyses, as shown in Table 6-30.

Table 6-29: Summary of results obtained in terms of frequencies.

			Genetic Algorithm		
Mode	f_{ID} [Hz]	Original FE model [Hz]	1 [Hz]	2 [Hz]	3 [Hz]
1	0.82	0.71	0.79	0.61	0.84
2	0.90	0.80	0.61	0.44	0.66
3	1.20	0.92	1.03	1.04	1.21
4	1.33	1.07	1.15	1.16	1.33
5	1.53	1.24	1.32	1.33	1.49
7	1.73	1.42	1.52	1.53	1.68
Mean error [%]		18.40	14.60	20.10	4.78

Genetic Algorithm:
- **1**. Nine optimisation parameters. Objective function only with MAC;
- **2**. As analysis 1, but with decreased Population Size;
- **3**. As analysis 2, but with an objective function that includes both MAC and frequencies.

Table 6-30: Summary of results obtained in terms of MAC.

Mode	Original FE model [Hz]	Genetic Algorithm 1 [Hz]	Genetic Algorithm 2 [Hz]	Genetic Algorithm 3 [Hz]
1	0.87	0.87	0.87	0.87
2	0.85	0.86	0.94	0.88
3	0.99	1.00	1.00	1.00
4	0.97	0.98	0.99	0.98
5	0.96	0.97	0.97	0.98
6	0.94	0.95	0.95	0.96
7	0.97	0.99	0.99	0.98

Genetic Algorithm:
- **1**. Nine optimisation parameters. Objective function only with MAC;
- **2**. As analysis 1, but with decreased Population Size;
- **3**. As analysis 2, but with an objective function that includes both MAC and frequencies.

Conclusions

This thesis investigates two critical aspects of existing infrastructure: the safety assessment of structures and the interpretation of their structural behaviour through dynamic monitoring.

Various modelling approaches were explored for both safety assessment and the interpretation of monitoring data. Among these, three-dimensional nonlinear finite element (3D NLFE) models represent the most accurate, realistic, and detailed option. They can be applied to both design- and safety-related assessments as well as to the interpretation of structural monitoring data. However, their use entails significant computational and economic costs. For this reason, such high-fidelity models should be reserved for cases where the complexity of the structure or the required level of accuracy justifies the effort.

Linear models, on the other hand, offer greater versatility and can also be employed for both safety assessment and monitoring interpretation. Due to their relatively low computational demands and reduced cost, they are particularly well-suited for the analysis of monitoring data. Nevertheless, their effective use requires specific modelling assumptions, which will be discussed in detail in the following sections.

Safety Assessment of Existing Structures

Various methodologies for evaluating structural safety were compared, utilizing five distinct approaches. The first two approaches relied on linear analyses, including Courbon theory and linear finite element (FE) models with beam elements. The remaining three approaches employed global safety formats - GRF, PF, and ECoV - based on results from three-dimensional nonlinear finite element analyses (3D NLFEAs). Additionally, the evolution of structural damage was correlated with changes in structural safety by evaluating damage thresholds derived from static parameters that can be monitored on the structure.

The following conclusions were drawn:

- Increasing the complexity of analysis and modelling can enhance the safety margin; however, the extent of this improvement varies depending on the type of analysis and the theoretical assumptions underlying the chosen safety assessment method.
- The lowest safety margin was observed when modelling the deck using Courbon theory. By employing a linear FE model, the safety margin increased by 13.2% to 18.7% compared to Courbon results. This gain is comparable to more conservative nonlinear approaches, such as the PF method, which yielded a safety margin increase of 13.0% to 15.4%. The GRF method provided the highest gain, ranging from 28.9% to 36.2%,

while the ECoV method produced intermediate results with a safety margin increase between 15.8% and 24.6%.

- Proper modelling of boundary conditions (e.g., support types) is essential for accurately capturing structural behaviour. Incorrect evaluation of boundary conditions can significantly reduce the structure's safety margin.
- Material strength plays a fundamental role in safety assessment. Therefore, whenever possible, it is essential to obtain a sufficient number of material test results. Equally important is the need to perform an appropriate statistical analysis of the available test data to ensure that the material properties are reliably characterized for structural evaluation purposes.
- Applying safety formats to results obtained from 3D NLFEAs can lead to substantial gains in safety margins compared to traditional checks based on linear analyses.
- Prestressed concrete girder decks demonstrate considerable transverse load redistribution capacity, which can only be assessed through detailed 3D NLFEAs that account for all structural members working together. This capacity depends on each structure's geometry and reinforcement ratios. Simplified analyses underestimate this redistribution capacity, leading to overly conservative assessments regarding ultimate limit states (ULS). Therefore, refined analyses are crucial for accurate structural safety evaluations.
- From an operational perspective, if simplified methods meet safety requirements, further sophisticated approaches may not be necessary. However, if these methods fail to meet safety standards, switching to advanced techniques like 3D NLFEAs with safety formats is recommended before imposing traffic restrictions on the structure. The ECoV format is particularly advantageous as it provides a realistic prediction of structural behaviour based on mean material strength.
- Structural damage reduces the load-bearing capacity of a structure relative to its undamaged condition, with the extent of the reduction depending on the severity and distribution of the damage. However, changes in load-bearing capacity due to damage typically exceed the corresponding variations in stiffness. As a result, measurements based on static parameters are often ineffective for detecting damage. This issue is particularly significant in structures with a high ratio of permanent to variable loads—such as the one analysed in this study—where the effects of slight to moderate damage under service load conditions are largely masked by residual prestressing. Consequently, the detection of damage through static parameter monitoring proves to be an unreliable strategy in such cases.

Interpretation of Structural Behaviour Through Dynamic Monitoring

Dynamic identification was performed for three different structural typologies, followed by model updating of their digital twins. The conclusions are as follows:

- The availability of a digital model is essential for interpreting structural health monitoring (SHM) data of complex structures like bridges and viaducts.
- Structural models used for SHM data interpretation differ from design models due to their distinct purposes. Design models prioritize safe construction and may deviate from actual structural behaviour as long as they remain conservative whereas SHM models should simulate the behaviour of the structure as close as possible.
- During long-term monitoring, the average intensity of actions on structures falls between unloaded conditions (permanent loads only) and quasi-permanent combination limit state. Simulation models for monitoring must maximize adherence to real structural behaviour within this range.
- Key differences between design models and simulation models include:
    - **Bearings friction and deformability characterization**: bearing device friction is typically neglected in design but must be accounted for in simulation models; correct bearings deformability should also be taken into account.
    - **Soil Deformability**: in the project, short and long-term parameters (undrained and drained conditions) are used to calculate the maximum initial and final displacements of the structures. If a monitoring system is installed decades after the construction of the structure, the deformability of the soil on which the foundations rest due to variable loads (traffic, wind, etc.) is generally smaller than the one used in the project, as the consolidation processes have already partially or completely taken place.
    - **Global System deformability**: Design often uses simplified decoupled analyses for main bridge components like decks or piers or foundations. However, SHM simulation models must account for overall system deformability. The characterization of the deformability of the soil-foundation-substructure-superstructure system can be correctly performed only on global models.
    - **Permanent loads estimation**: Structural and non-structural weights may vary from design assumptions. Old concretes may be lighter than the ones used today. Pavement thickness may be changed (increased) during renovations; it may also be variable

along the bridge as thicker layers may be placed to compensate deck deformation.

- **Material Properties**: Mechanical characteristics like elastic modulus often lack sufficient investigation .

Among these parameters, bearing device stiffness has the greatest impact on model updating. These devices, due to aging, deterioration or malfunction, and due to the significantly low level of actions during normal operation of the structure, can be much stiffer than what assumed. Soil deformability under foundations also plays a significant role; even deep foundations (piles and shafts) cannot be considered fully rigid restraints, especially for rotations.

Less impactful but still relevant parameters include permanent loads estimation and material mechanical properties. Pavement thickness may have a crucial role as it can be higher than expected and non-uniform. Current standards often overestimate old concrete mass; hence, in situ tests are strongly recommended.

Optimizing a larger number of parameters generally yields better results; however, preliminary analysis is critical to define realistic parameter ranges and reduce computational burdens. Genetic algorithms are particularly effective for optimization due to their reduced computation times.

Future prospects

The findings highlight the need for further investigation into shear actions, which may, in certain cases, govern the safety verification of older under-reinforced beams. Applying the methodology developed in this thesis to shear failure scenarios—particularly within the context of nonlinear analyses—requires a deeper exploration of modelling uncertainties, given the inherent complexity of brittle failure mechanisms.

Moreover, the safety assessment approach proposed here could be extended to other structural typologies, such as box girders and composite bridges.

Future research could also explore the integration of mixed monitoring strategies—combining static and dynamic measurements—for the calibration of digital twins. A particularly promising avenue involves calibrating numerical models based on environmental effects, such as temperature variations, which may offer a novel means of improving model accuracy and reliability.

References

[1] Petti L., Lupo C., De Gaetano C. M. "*A Methodological Framework for Bridge Surveillance*". Applied Sciences. 2023; 13 (8): 4975.

[2] Bazzucchi F., Restuccia L., Ferro G. A. "*Considerations over the Italian road bridge infrastructure safety after the Polcevera viaduct collapse: past errors and future perspectives*". Frattura ed Integrità Strutturale. 2018; 46; Pages 400-421.

[3] Anania L., Badalà A., D'Agata G. "*Damage and collapse mode of existing post tensioned precast concrete bridge: The case of Petrulla viaduct*". Engineering Structures. 2018; Volume 162; Pages 226-244.

[4] Di Prisco M., Colombo M., Martinelli P. "*Structural Aspects of the Collapse of a RC Half-Joint Bridge: Case of the Annone Overpass*". Journal of Bridge Engineering. 2023; Volume 28; Number 11.

[5] Wolff M., Starossek U. "*Robustness assessment of a cable-stayed bridge*". 4th International Conference on Bridge Maintenance, Safety, and Management. 2008.

[6] Ghosn M., Moses F., Frangopol D. M. "*Redundancy and robustness of highway bridge superstructures and substructures*". Structure and Infrastructure Engineering. 2010; Volume 6(1-2); Pages 257-278.

[7] Martinez Y., Cabrera F., Pisani F. "*Rehabilitation of stays of the Polcevera Viaduct*". Proceedings of the Int. Symp. on Cable Stayed Bridges. 1994; Pages 640-665.

[8] Scattarreggia N., Salomone R., Moratti M., Malomo D., Pinho R., Calvi G. M. "*Collapse analysis of the multi-span reinforced concrete arch bridge of Caprigliola, Italy*". Engineering Structures. 2022; Volume 251, Part A.

[9] Repubblica Italiana - Ministero delle Infrastrutture e della Mobilità Sostenibili Consiglio Superiore dei Lavori Pubblici. "*Linee guida per la classificazione e gestione del rischio, la valutazione della Sicurezza ed il monitoraggio dei ponti esistenti*". Decreto numero 578 del 17-12-2020.

[10] Repubblica Italiana - Ministero delle Infrastrutture e della Mobilità Sostenibili Consiglio Superiore dei Lavori Pubblici. "*Linee guida per la classificazione e gestione del rischio, la valutazione della Sicurezza ed il monitoraggio dei ponti esistenti*". Decreto numero 204 del 01-07-2022

[11] "*fib Model Code for Concrete Structures 2010*". fib. 2013; Lausanne.

[12] Muttoni A., Ruiz M. F. "*Levels-of-approximation approach in codes of practice*". Struct Eng Int J Int Assoc Bridge Struct Eng. 2012; Volume 22 (2); Pages190-4.

[13] Cornell C. A. "*Bounds on the reliability of structural systems*" J. Struct. Div. 1967; Pages 171–200.

[14] Hasofer A., Lindt N. "*An exact and invariant first order reliability format*". Proc. ASCE, J. Eng. Mech. Div. 1974; Pages 111-121.

[15] CEN EN 1990 Eurocode. 2002. "*Basis of structural design*." Brussels.

[16] Konig G., Hosser D. "*The simplified level II method and its application on the derivation of safety elements for level I*". CEB Bulletin no.147. 1982.

[17] Madsen H. O., Krenk S., Lind N. C. "*Methods of Structural Safety*". Prentice-Hall. 1986.

[18] fib Bulletin N°80. "*Partial factor methods for existing concrete structures*". Lausanne; 2016.

[19] Chem H. P., Ni Y. Q. "*Structural Health Monitoring of Large Civil Engineering Structures*". John Wiley & Sons Ltd. 2018

[20] Gino D., Castaldo P., Bertagnoli G., Giordano L., Mancini G. "*Partial factor methods for existing structures according to fib Bulletin 80: Assessment of an existing prestressed concrete bridge*". Structural Concrete. 2020; Volume 21; Pages 15–31.

[21] CEN EN 1992-1- Eurocode 2 – "*Design of concrete structures, Part 1: General rules for buildings*". CEN Brussels; 2005.

[22] Steenbergen R. D. J. M., Rozsas A., Vrouwenvelder A. C. W. M. "*Target reliability of new and existing structures-A general framework for code making*". 2018.

[23] Diamantidis D., Holický M., Sýkora M. "*Reliability and risk acceptance criteria for civil engineers structures*". Civil Engineers Series. 2016; Volume 16 (2).

[24] Repubblica Italiana - Ministero delle Infrastrutture e della Mobilità Sostenibili Consiglio Superiore dei Lavori Pubblici. "*Aggiornamento delle «Norme tecniche per le costruzioni»*". Supplemento ordinario n. 8 alla Gazzetta ufficiale del 20-2-2018. 2018; Italy.

[25] Cosenza E., Losanno D. "*Assessment of existing reinforced-concrete bridges under road-traffic loads according to the new Italian guidelines*". Structural Concrete. 2021; Volume 22.

[26] fib Bulletin N°45. "*Practitioner's guide to finite element modelling of reinforced concrete structures – State of the art report*". Lausanne; 2008.

[27] DIANA FEA BV. "*DIANA – Finite Element Analysis – Users Manual Release 10.1 – Theory*". DIANA FEA BV. 15-02-2017.

[28] DIANA FEA BV. "*DIANA – Finite Element Analysis – Users Manual Release 10.1 - Element Library*". DIANA FEA BV. 15-02-2017.

[29] DIANA FEA BV. "*DIANA – Finite Element Analysis – Users Manual Release 10.1 - Material Library*". DIANA FEA BV. 15-02-2017.

[30] CEN EN 1992-2- Eurocode 2 – "*Design of concrete structures, Part 2: General rules for buildings*". Brussels: CEN. 2005..

[31] Cervera M., Chiumenti M. "*Smeared crack approach: back to the original track*". Int. J. Numer. Anal. Meth. Geomech. 2006; Volume 30; Pages1173–1199.

[32] Vecchio F. J., Collins M. P. "*The modified compression field theory for reinforced concrete elements subjected to shear*". ACI Journal 83. 1986; Volume 22, Pages 219-231.

[33] Selby R. G., Vecchio F. J. "*Three-dimensional Constitutive Relations for Reinforced Concrete*". Technical report 93-02, University of Toronto, dept. Civil Engineering. 1993.

[34] Castaldo P., Gino D., Bertagnoli G., Mancini G. "*Partial safety factor for resistance model uncertainties in 2D non-linear finite element analysis of reinforced concrete structures*". Engineering Structures. 2018; Volume 176; Pages 746-762.

[35] Vecchio F. J., Collins M. P. "*Compression response of cracked reinforced concrete*". *J. Str. Eng. ASCE 119*. 1993; Volume 12; Pages 3590-3610.

[36] Selby R. G., Vecchio F. J. "*A constitutive model for analysis of reinforced concrete solids*". Can. J. Civ. Eng. 1997; Volume 24; Pages 460–470.

[37] Bertagnoli G., La Mazza D., Mancini G. "*Effect of concrete tensile strength in non –linear analysis of 2D structures: a comparison between three commercial finite element softwares*". 3rd International conference on advances in civil, structural and construction engineering – CSCE. 2015; Pages 104-111.

[38] Mises R. V. "*Mechanik der festen Körper im plastisch- deformablen Zustand*" Nachrichten von der Gesellschaft der Wissenschaften zu Göttingen, Mathematisch-Physikalische Klasse. 1913; Pages 582-592.

[39] Ford H., Alexander J. M. "*Advanced Mechanics of Materials"*. London: Longmans. 1963.

[40] Engen M., Hendriks M. A. N. , Köhler J., Øverli J. A, Åldtstedt E. "*A quantification of modelling uncertainty for non-linear finite element analysis of large concrete structures*". Structural Safety. 2017; Volume 64; Pages 1-8.

[41] Kadlec L., Červenka V. "*Model Uncertainties of FEM Nonlinear Analyses of Concrete Structures*". Solid State Phenomena. 2016; Volume 249; Pages 197-202.

[42] Gino D., Castaldo P., Giordano L., Mancini G. "*Model uncertainty in non-linear numerical analyses of slender reinforced concrete members*", Structural Concrete, 2021; Volume 22 (2); Pages 845-870.

[43] Engen M., Hendriks M. A. N., Monti G., Allaix D. L. "*Treatment of modelling uncertainty of NLFEA in fib Model Code 2020*". Structural Concrete. 2021; Volume 22 (3); Pages 202–212.

[44] Gino D., Miceli E., Castaldo P., Recupero A., Mancini G. "*Strain-based method for assessment of global resistance safety factors for NLNAs of reinforced concrete structures*". Engineering Structures. 2024; Volume 304.

[45] Ranieri C., Fabbrocino G. "*Operational Modal Analysis of Civil Engineering Structures*". Springer. 2014.

[46] Doebling S. W. et al. "*Damage identification and health monitoring of structural and mechanical systems from changes in their vibration characteristics: a literature review*". Technical Report. Los Alamos National Lab. NM (United States). 1996.

[47] Peeters B., De Roeck G. "*One-Year Monitoring of the Z24 Bridge: A Case Study*" Journal of Structural Engineering. 1999; Volume 125 (8); Pages 853-863.

[48] Brincker R., Zhang L., Andersen P. "*Modal Identification of Output-Only Systems*" Proceedings of the 18th International Modal Analysis Conference (IMAC). 2000.

[49] DeWolf J. T. et al. "*Bridge monitoring network-Installation and operation*". Connecticut Department of Transportation, Report No. CT-2217-F-06-10. 2006.

[50] Franklin G. F. , Powell J. D., Workman M. L. "*Digital control of dynamic systems*", 3rd edn. Ellis-Kagle Press, Half Moon Bay, CA. 2006.

[51] Van Overschee P., De Moor B. "*Subspace identification for linear systems: theory - implementation – applications*". Kluwer Academic Publishers, Dordrecht. 1996.

[52] Juang J. N. "*Applied system identification*". PTR Prentice Hall, Englewood Cliffs, NJ. 1994.

[53] Juang J. N., Pappa R. S. "*An eigensystem realization algorithm for modal parameter identification and model reduction*". AIAA J Guid Contr Dynam. 1985; Volume 8; Pages 620–627.

[54] Andersen P., Brincker R., Kirkegaard P. H. "*Theory of covariance equivalent ARMAV models of civil engineering structures*". Proc XIV international modal analysis conference. 1996.

[55] Ibrahim S. R., Brincker R., Asmussen J. C. "*Modal parameter identification from responses of general unknown random inputs*". Proc 14th international modal analysis conference. 1996.

[56] Ho B. L., Kalman R. E. "*Effective construction of linear state variable models from input/output data*". Regelungstechnik. 1996; Volume 14; Pages 545–548.

[57] Juang J. N. "*Applied system identification*". PTR Prentice Hall, Englewood Cliffs, NJ. 1994.

[58] Hush D. R. "*Mathematics of Signal Processing*". Wiley. 1979.

[59] Yi J. H. , Yun C. B. "*Comparative study on modal identification methods using output-only information*". Struct Eng Mech. 2004; Volume 17 (3–4); Pages 445–466.

[60] Peeters B., Van der Auweraer H. "*PolyMAX: a revolution in operational modal analysis*". Proc 1st international operational modal analysis conference. 2005.

[61] Cauberghe B. "*Applied frequency-domain system identification in the field of experimental and operational modal analysis*", Ph.D. thesis. Vrije Universiteit Brussels, Brussels. 2004.

[62] De Troyer T., Guillaume P., Steenackers G. "*Fast variance calculation of polyreference least-squares frequency-domain estimates*". Mech Syst Signal Process. 2009; Volume 23; Pages 1423–1433.

[63] Chopra A. K. "*Dynamics of structures - theory and applications to earthquake engineering*". 2nd edn. Prentice Hall, Upper Saddle River, NJ. 2000.

[64] Ewins D. J. "*Modal testing: theory, practice and application*". 2nd edn. Research Studies Press Ltd., Baldock. 2000.

[65] Catbas F. N, Kijewski-Correa T., Aktan A. E. "*Structural Identification of Constructed Facilities: Approaches, Methods, and Technologies for Effective Practice of St-Id*". ASCE, Reston, VA. USA. 2012.

[66] Ni Y. Q. "*Sensing Solutions for Assessing and Monitoring Supertall Towers*". Sensor Technologies for Civil Infrastructures: Applications in Structural Health Monitoring, Wang, Lynch and Sohn (ed.), Woodhead Publishing, Cambridge, UK. 2014.

[67] Glisic B., Inaudi D. "*Fibre Optic Methods for Structural Health Monitoring*". John Wiley & Sons, Chichester, UK. 2007.

[68] Casas J. R., Cruz J. S. "Fibre optic sensors for bridge monitoring". Journal of Bridge Engineering ASCE. 2003; Volume 8 (6); Pages 362–373.

[69] Doebelin E. O. "*Measurement Systems: Application and Design*" McGrawHill, New York, NY, USA. 1990.

[70] Farrar C. R., Sohn H., Hemez F. M., Anderson M. C., Bement M. T., Cornwell P. J., Doebling S. W., Lieven N., Robertson A. N., Schultze J. F. "*Damage Prognosis: Current Status and Future Needs*". Los Alamos National Laboratory report LA14051MS. 2003.

[71] Sohn H., Farrar C. R., Hemez F. M., Shunk D. D., Stinemates D. W., Nadler B. R. "*A Review of Structural Health Monitoring Literature: 1996–2001*". Report LA13976MS. Los Alamos National Laboratory. 2004.

[72] Bertagnoli G., Antognelli C., Ciccone E., Ferrara M. "*Structural health monitoring of a prestressed concrete girder bridge deck using clinometers*". *AIP Conf. Proc.* 2023.

[73] Tan P. N., Steinbach M., Kumar V. "*Introduction to data mining*". Addison-Wesley, Boston, MA. 2006.

[74] Witten I., Frank E. "*Data mining: Practical machine learning tools and techniques with java implementations*". Morgan Kaufman Publishers, San Francisco, CA. 2005

[75] Zinno R., Haghshenas S. S., Guido G., Rashvand K., Vitale A., Sarhadi A. "*The State of the Art of Artificial Intelligence Approaches and New Technologies in Structural Health Monitoring of Bridges*". Applied Sciences. 2023; Volume 13 (1).

[76] Mottershead J. E., Friswell M. I. "*Model updating in structural dynamics: a survey*". Journal of Sound and Vibration. 1993; Volume 167 (3); Pages 347–375.

[77] Friswell M. I., Mottershead J. E. "*Finite Element Model Updating in Structural Dynamics*". Kluwer Academic Publishers, Dordrecht, The Netherlands. 1995.

[78] Kabe A. M. "*Stiffness matrix adjustment using modal data*". AIAA Journal. 1985; Volume 23 (9); Pages 1431– 1436.

[79] Link M. "*Updating of analytical models – Review of numerical procedures and application aspects*". Proceedings of Structural Dynamics Forum SD2000, Los Alamos, USA. 1999.

[80] Modak S. V., Kundra T. K., Nakra B. C. "*Comparative study of model updating methods using simulated experimental data*". Computers and Structures. 2002; Volume 80; Pages 437–447.

[81] Mottershead J. E., Link M., Friswell M. I. "*The sensitivity method in finite element model updating: A tutorial*". Mechanical Systems and Signal Processing. 2011; Volume 24; Pages 2275–2296.

[82] Chen H. P., Maung T. S. "*Regularised finite element model updating using measured incomplete modal data*". Journal of Sound and Vibration. 2014; Volume 333 (21); Pages 5566–5582.

[83] Brownjohn J. M. W., Xia P. Q. "*Dynamic assessment of curved cable stayed bridge by model updating*". Journal of Structural Engineering ASCE. 2000; Volume 126 (2); Pages 252–260.

[84] Palmonella M., Friswell M. I., Mottershead J. E., Lees A. W. "*Finite element models of spot welds in structural dynamics: review and updating*". Computers and Structures. 2005; Volume 83; Pages 648–661.

[85] Simoen E., Papadimitriou C., Lombaert, G. "*On prediction error correlation in Bayesian model updating*". Journal of Sound and Vibration. 2013; Volume 332 (18); Pages 4136–4152.

[86] Simoen E., De Roeck G., Lombaert G. "*Dealing with uncertainty in model updating for damage assessment: A review*". Mech Syst Signal Process. 2015; Volume 56; Pages 123–49.

[87] Sun L., Li Y., Zhang W. "*Experimental Study on Continuous Bridge-Deflection Estimation through Inclination and Strain*". J Bridg Eng. 2020; Volume 25.

[88] Ereiz S., Duvnjak I., Jiménez-Alonso J. F. "*Review of finite element model updating methods for structural applications*". Structures. 2022; Volume 41.

[89] Faraonis P., Sextos A., Chatzi E., Zabel V. "*Model Updating of a Bridge-Foundation-Soil System Based on Ambient Vibration Data*". Eccomas Proceedia. 2015.

[90] Hester D., Koo K., Xu Y., Brownjohn J., Bocian M. "*Boundary condition focused finite element model updating for bridges*". Engineering Structures. 2019; Volume 198.

[91] Polanco N. R., May G., Hernandez E. M. "*Finite element model updating of semi-composite bridge decks using operational acceleration measurements*". Engineering Structures. 2016; Volume 126; Pages 264-277.

[92] Levin R. I, Lieven N. A. J. "*DYNAMIC FINITE ELEMENT MODEL UPDATING USING SIMULATED ANNEALING AND GENETIC ALGORITHMS*". Mechanical Systems and Signal Processing. 1998; Volume 12 (1).

[93] Bertagnoli G., Anerdi C., Ferrara M. "*Structural Health Monitoring Issues Using Inclinometers on Prestressed Concrete Girder Bridge Decks*". 2021. IOP Conference Series: Materials Science and Engineering, Volume 1203.

[94] Sassano A. "*Modelli e algoritmi della ricerca operativa*". Franco Angeli. 2004.

[95] Castillo E., Mínguez R., Castillo C. "*Sensitivity analysis in optimization and reliability problems*". Reliability Engineering and System Safety 17th European Safety and Reliability Conference. 2008; Pages 1788–1800.

[96] Michalewicz Z. "*Evolution Programs for Various Discrete Problems*". Genetic Algorithms + Data Structures = Evolution Programs. 1996; Pages 239–266.

[97] Courbon J. "*Application de la résistance des matériaux au calcul des ponts. Dunod*". 1950.

[98] Castaldo P., Gino D., Mancini G. "*Safety formats for non-linear finite element analysis of reinforced concrete structures: discussion, comparison and proposals*". Engineering Structures. 2019; Volume 193: Pages 136-153.

[99] Comité Européen de Normalisation (CEN) "EN 13791:2021: *Assessment of in situ compressive strength in structures and precast concrete components*". CEN. 2021.

[100] Consiglio Superiore dei Lavori Pubblici. "*Linee Guida per la Valutazione delle Caratteristiche del Calcestruzzo in Opera*". 2017.

[101] Holicky M., Materna A., Sedlacek G., Arteaga A., Sanpaolesi L., Vrouwenvelder T., Kovse I., Gulvanessian H. "*Implementation of Eurocodes: Handbook 2: Reliability backgrounds*". Leonardo Da Vinci Pilot Project CZ/02/B/F/PP-134007.

[102] Computers & Structures, Inc. "*CSI Analysis Reference Manual: For SAP 2000*". Etabs, Safe and CSI Bridge; Berkeley California U.S.A.

[103] Comité Européen de Normalisation (CEN) "EN 1337-3:2005: *Structural bearings - Part 3: Elastomeric bearings*". CEN. 2005.

[104] Castaldo P., Gino D., Bertagnoli G., Mancini G. "*Resistance model uncertainty in non-linear finite element analyses of cyclically loaded reinforced concrete systems*". Engineering Structures. 2020; Volume 211.

[105] Cervenka V. "*Reliability-based non-linear analysis according to fib Model Code 2010*". Structural Concrete. 2013; Volume 14; Pages 19-28.

[106] Allaix D. L., Carbone V. I., Mancini G. "*Global safety format for non-linear analysis of reinforced concrete structures*". Structural Concrete. 2013; Volume 14 (1); Pages 29-42.

[107] Bertagnoli G., Ciccone E., Ferrara M. "*Structural Health Monitoring of a prestressed concrete bridge deck*". Proceedings of Italian Concrete Conference Ed. By Aiello M. A., Bilotta A., Springer Nature. 2022.

[108] Du Y. G., Clark L. A. Chan A. H. C. "*Effect of corrosion on ductility of reinforcing bars*". Magazine of Concrete Research. 2005; Volume 57 (7); Pages 407-419.

[109] Apostolopoulos C. A., Papadakis V. G. "*Consequences of steel corrosion on the ductility properties of reinforcement bar*". Construction and Building Materials. 2008; Volume 22 (12); Pages 2316-2324.

[110] Hingorani R., Fullea J., Sanchez J., Andrade C. "*Loss of ductility and strength of reinforcing steel due to pitting corrosion*". VIII International Conference on Fracture Mechanics of Concrete and Concrete Structures.

[111] Franceschini L., Belletti B., Tondolo F., Montero J. S. "*A simplified stress–strain relationship for the mechanical behavior of corroded prestressing strands: The SCPS-model*". Structural Concrete. 2022; Volume 24 (1); Pages 189-210.

[112] The MathWorks Inc. MATLAB version: R2021b, Natick, Massachusetts: The MathWorks Inc.

[113] Rainieri C., Fabbrocino G. "*Influence of model order and number of block rows on accuracy and precision of modal parameter estimates in stochastic subspace identification*". International Journal of Lifecycle Performance Engineering. 2014; Volume 10 (1); Pages 317-334.

[114] Ester M., Kriegel H. P., Sander J., Xiaowei X. "*A density-based algorithm for discovering clusters in large spatial databases with noise*" Proceedings of the Second International Conference on Knowledge Discovery in Databases and Data Mining. 1996; Pages 226-231.

[115] Siemens. (2023). Simcenter TestLab 2206.

[116] Cara J., Caetano E., Magalhaes F., Alarcon E. "*Uncertainty of Damping Ratios Estimated in a Multi-Setup OMA of a Cable-Stayed Bridge*" 6th International Operational Modal Analysis Conference. 2015.

[117] Ferraro E., Chiaia B., Fantilli A. P. "*Stima della resistenza a compressione del calcestruzzo in ponti storici in funzione dell'anno di costruzione*". Ingenio. 2018.

Annex A

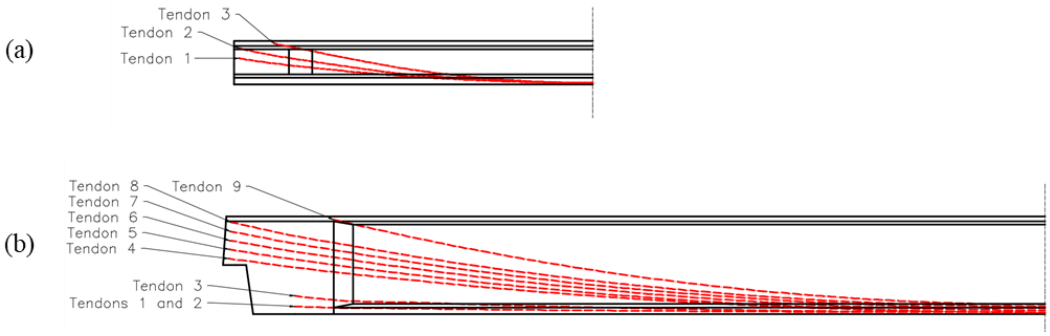

Figure A - 1: Post-tensioned tendon layout: (a) 20.8 m deck; (b) 50 m deck.

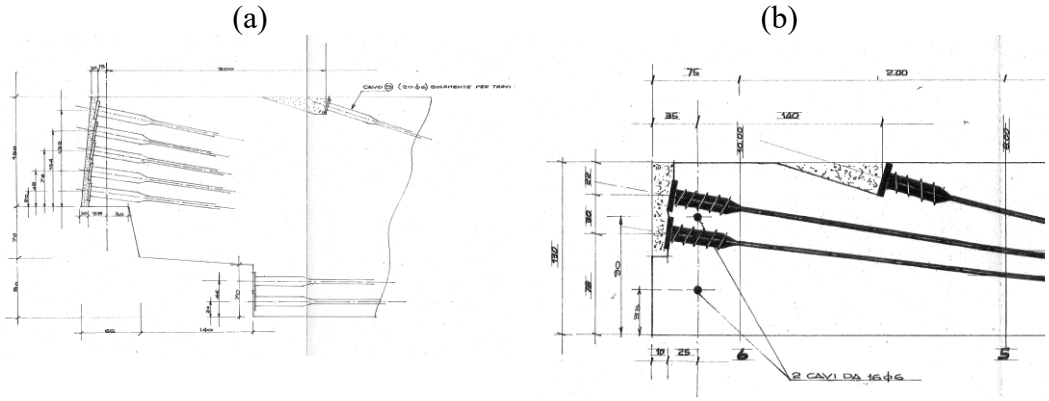

Figure A - 2: Detail of cable anchor heads: 50 m deck (a), 20.8 m deck (b). Measurements in centimeters with diameters in millimetres.

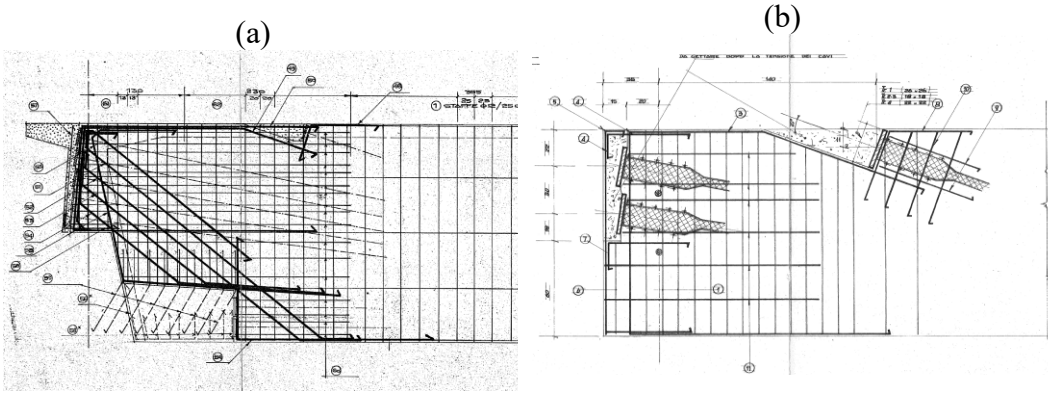

Figure A - 3: Ordinary reinforcement in the beam head: 50 m deck (a), 20.8 m deck (b). Measurements in centimeters with diameters in millimetres.

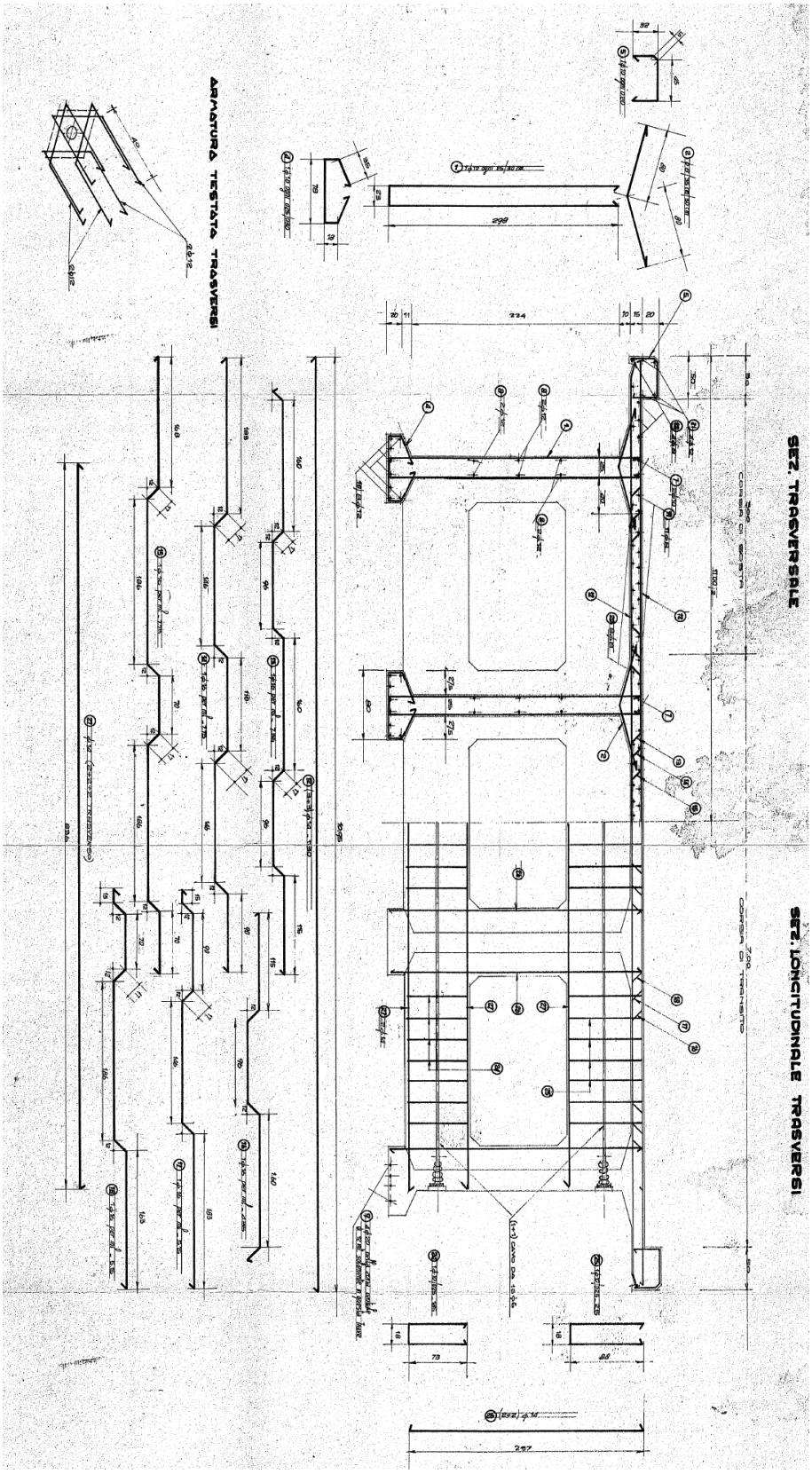

Figure A - 4: Arrangement of ordinary reinforcement in transverse direction in the 50 m deck. Measurements in centimeters with diameters in millimetres.

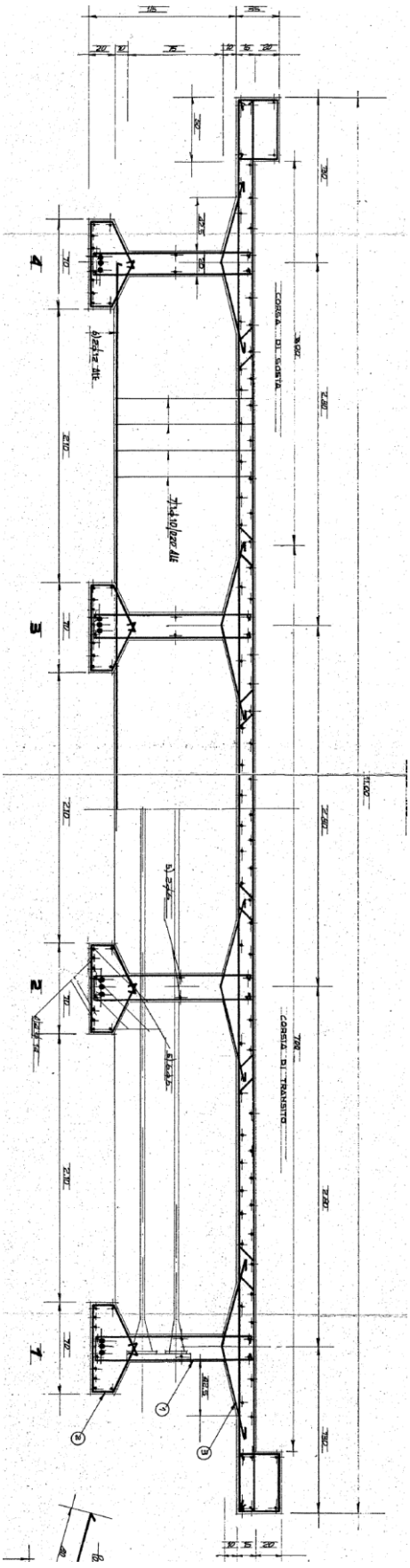

Figure A - 5: Arrangement of ordinary reinforcement in transverse direction in the 20.8 m deck. Measurements in centimeters with diameters in millimetres.

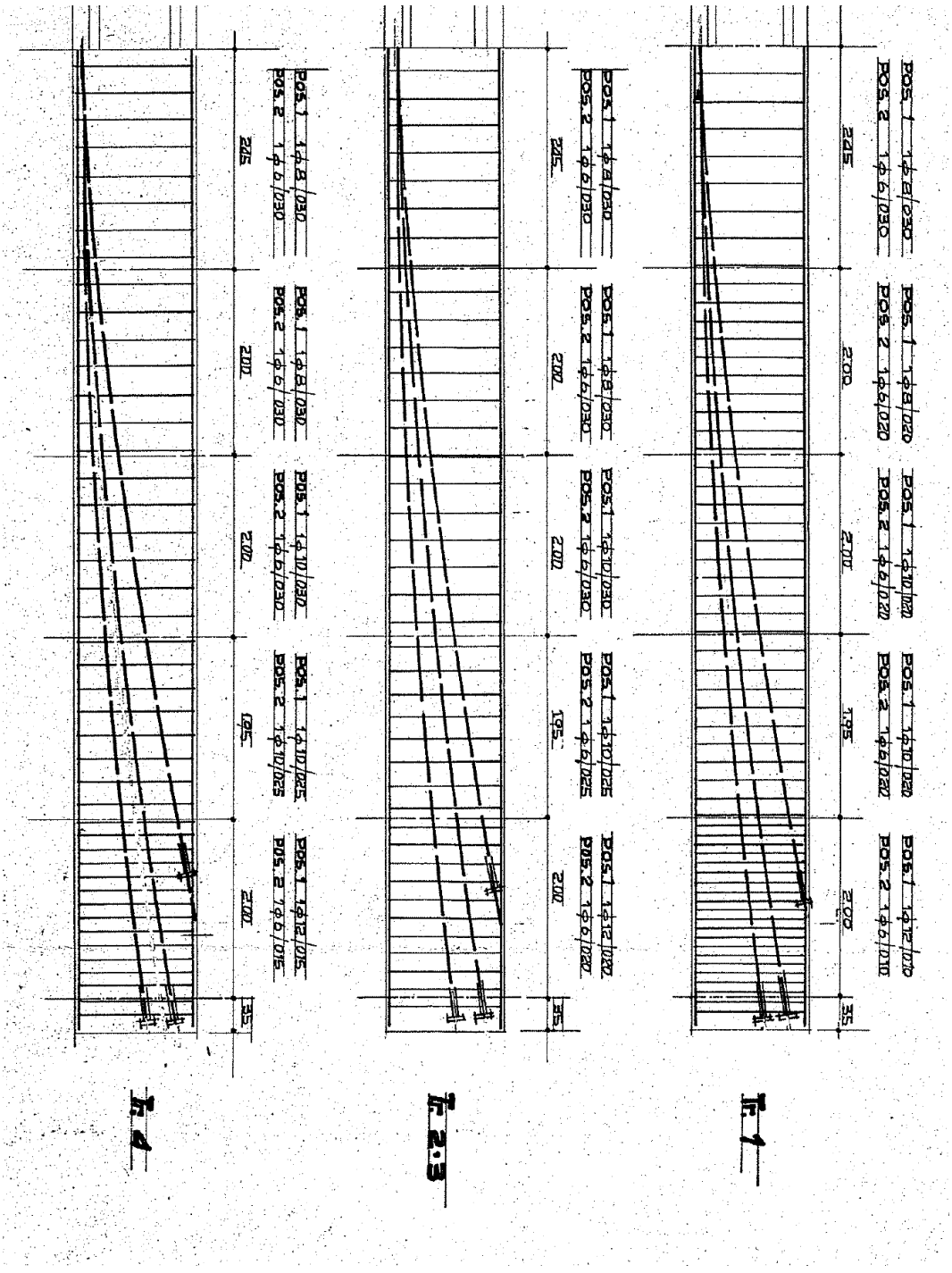

Figure A - 6: Arrangement of stirrups in the 20.8 m deck. Measurements in centimeters with diameters in millimetres.

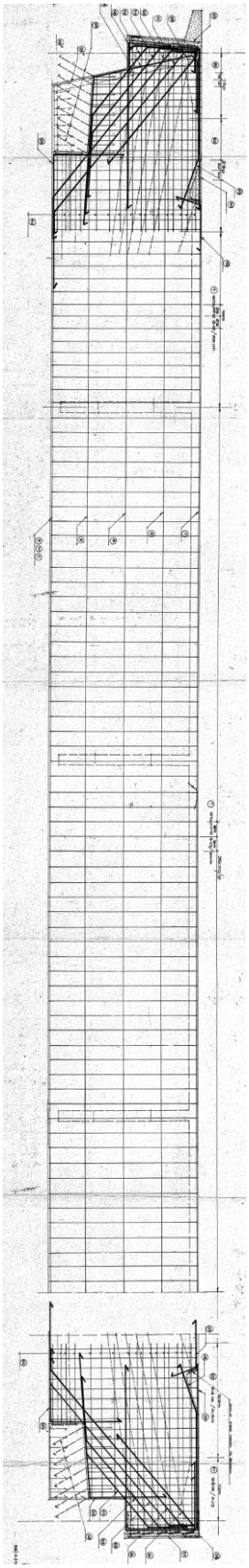

Figure A - 7: Arrangement ordinary reinforcement in the 50 m longitudinal beam. Measurements in centimeters with diameters in millimetres.

Annex B

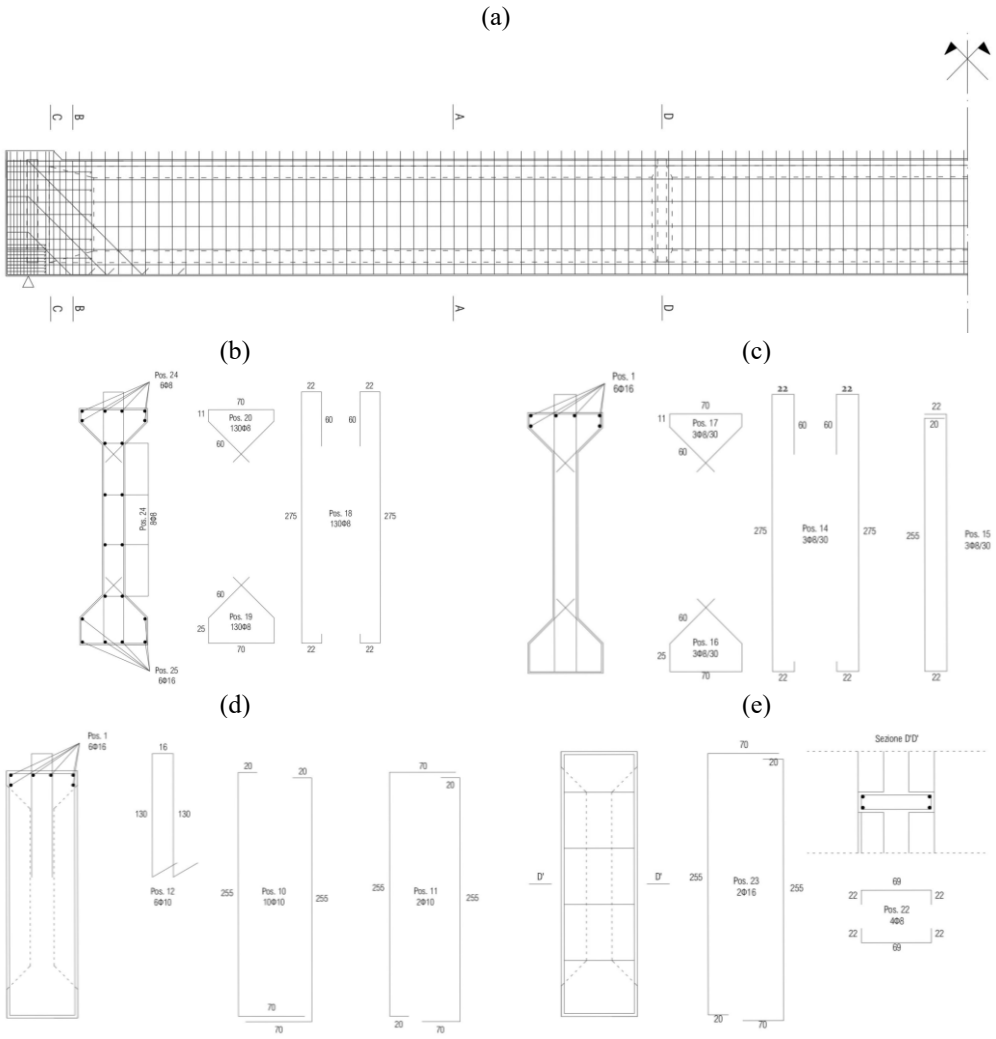

Figure B - 1: Ordinary reinforcement arrangement in longitudinal beam: (a) longitudinal view, (b) cross-section A-A, (c) cross-section B-B, (d) cross-section C-C, (e) cross-section D-D. Measurements in centimetres with diameters in millimetres.

(a)

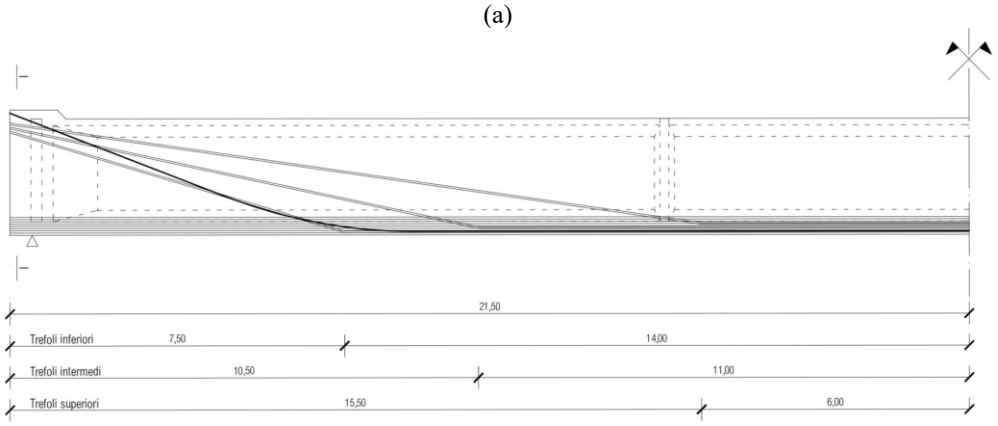

(b)

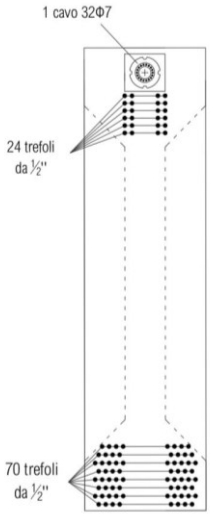

Figure B - 2: Ordinary reinforcement arrangement in longitudinal beam: (a) longitudinal view, (b) cross-section A-A, (c) cross-section B-B, (d) cross-section C-C, (e) cross-section D-D. Measurements in centimetres with diameters in millimetres.

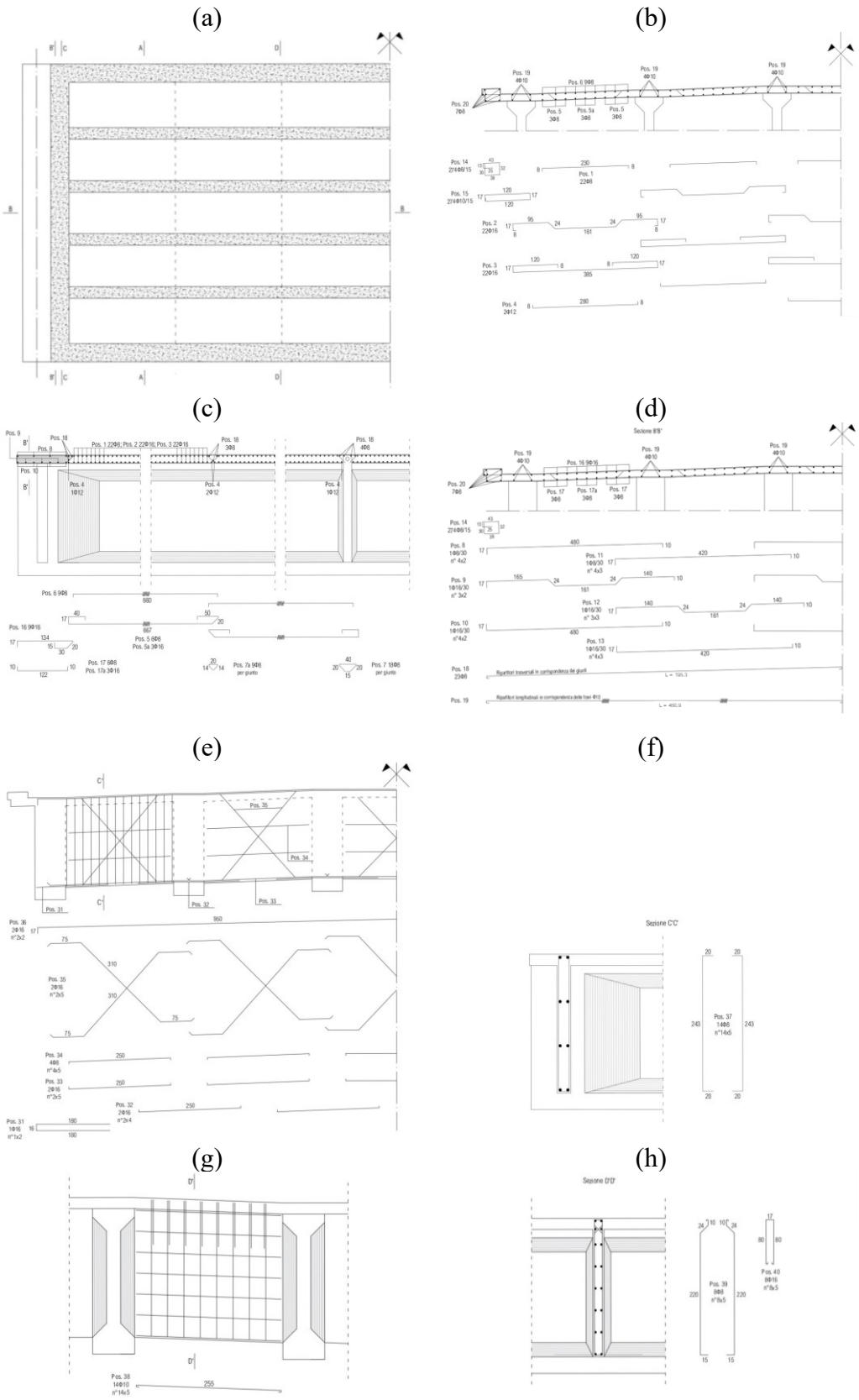

Figure B - 3: Ordinary reinforcement arrangement in the slab and transverse beam: (a) planimetry, (b) section A-A, (c) section B-B. (d) section B'-B', (e) section C-C, (f) section C'-C', (g) section D-D, (h) section D'-D'. Measurements in centimetres with diameters in millimetres.

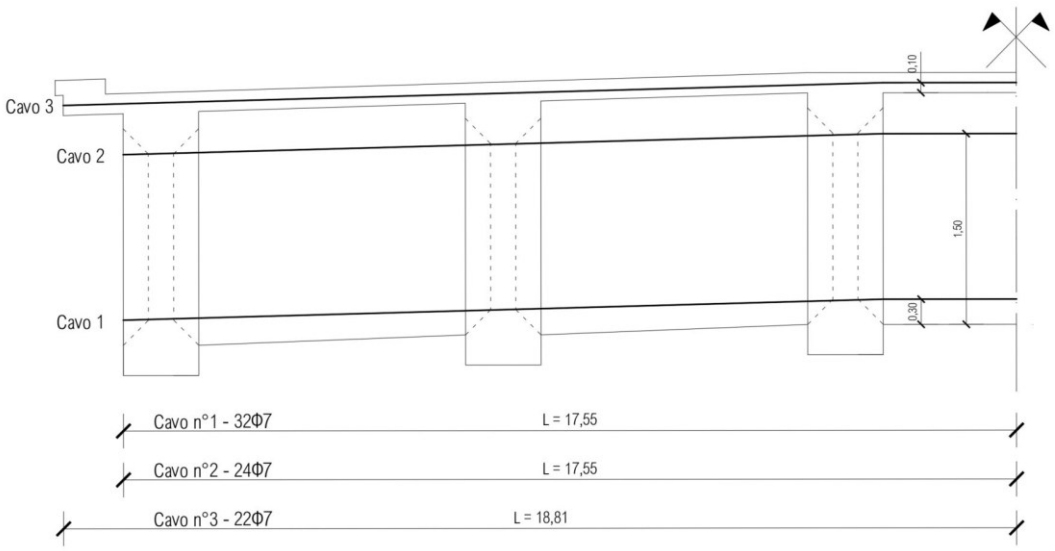

Figure B - 4: Post-tension reinforcement arrangement in transverse beam and slab. Measurements in meters with diameters in millimetres.